Calcium Carbonate Crystallization Kinetics in Relation to Surface Scale Formation in Oil and Gas Pipelines

Miriam Barber

Submitted in accordance with the requirements for the degree of
Doctor of Philosophy

The University of Leeds
Institute of Particle Science and Engineering
School of Chemical and Process Engineering

January 2018

The candidate confirms that the work submitted is her own and that appropriate credit has been given where reference has been made to the work of others.

This copy has been supplied on the understanding that it is copyright material and that no quotation from the thesis may be published without proper acknowledgement.

__Dedicated to my beloved Family__

I'm very grateful for all the encouragement, affection, support, love, guidance and prayers from each of you throughout this challenging PhD accomplishment.

Acknowledgements

Abstract

Calcium carbonate (CaCO$_3$) mineral scale is one of the major problems faced by the oil and gas industry; as its deleterious crystallisation process causes serious flow assurance problems in oilfield facilities.

In this thesis, a suitable methodology based on experimental and modelling approaches was developed for assessing the crystallisation mechanisms and kinetics of CaCO$_3$ precipitating spontaneously in a bulk solution and at metallic surfaces. Several parameters have been assessed during the simultaneous crystallization at bulk and surface: supersaturation, temperature, flow rate, nature of metal substrate and time.

Bulk nucleation kinetics revealed interfacial tension values in the range 0.92 – 25.46 mJ/m^2, suggesting homogeneous nucleation for higher supersaturation (11 ≤ σ ≤ 55), and heterogeneous nucleation for the lower supersaturation brines (1.52 ≤ σ ≤ 4.77). These interfacial tension values calculated for 25°C, 40°C and 80°C are in good agreement with literature for calcite and vaterite. Bulk growth rate varied from $5*10^{-13}$ m/s to $1.25*10^{-15}$ m/s over a range of supersaturation and temperatures. The mechanisms obtained for bulk crystallisation suggested spiral growth is predominant at lower saturation ratio and 2D nucleation at high saturation ratio at 25°C.

A de-saturation profile was obtained via direct measurements of solution speciation and validated using MultiScale for scale predictions. These results supported the crystal evolution approach proposed based on experiments.

Surface crystallization results have shown that in presence of corrosion, a localized supersaturation at the metal of steel enhances surface kinetics and there is a competition between CaCO$_3$ and ferrous corrosion products to occupy the surface nucleation sites. At higher temperature FeCO$_3$ was more likely to co-precipitate with CaCO$_3$, whilst at lower temperature mostly CaCO$_3$ polymorphs and Fe$_2$O$_3$ were formed. The bulk crystallization kinetics and mechanisms observed in absence of corrosion (i.e., stainless steel) showed to be identical to the spontaneous crystallization process.

This thesis delivers an appraisal of the engineering science around the crystal formation (scaling) in oil and gas relevant conditions. The mechanisms and rates of formation of CaCO$_3$ in the solution and at the surface of a corroding substrate are discussed.

Table of Contents

List of Figures

xviii

List of Tables

Nomenclature

(Alphabetical order)

Latin Letters	Explanation	Units
A_0	Pre-exponential factor	[-]
A	Surface area	[m^2]
	Aragonite	[-]
a	Unit cell parameter	[nm]
b	Unit cell parameter	[nm]
	Constant	[-]
B	Secondary nucleation rate	[g/m^{3}s]
C	Concentration	[g/l]
	Calcite	[-]
c	Unit cell parameter	[nm]
C* C$_{eq.}$	Concentration at equilibrium	[g/l]
d	Diameter	[m]
D	Diffusion coefficient	[-]
D$_{0.5}$	Mean size diameter	[m]
D$_{[1,0]}$	Number mean diameter	[m]
D$_{[2,0]}$	Number-surface mean diameter	[m]
D$_{[3,0]}$	Number-volume mean diameter	[m]
D$_{[3,2]}$	Surface mean diameter	[m]
D$_{[4,3]}$	Volume mean diameter	[m]
E$_A$	Activation energy	[J/mol]
E$_{att}$	Attachment energy	[kcal/mol]
E$_{opt}$	Optimisation energy	[Kcal/mol]
F	Faraday constant = 9.649×10^4	[C mol^{-1}]
fv, fs	Shape factors	[-]
G	Gibbs free energy	[KJ/mol]
H	Enthalpy	[KJ/mol]
hkl	Miller index	[-]
I$_L$	Levich current	[A]
J or J$_n$	Nucleation rate	[kg/m^{3}s]
K$_B$	Boltzmann constant = 1.3805×10^{23}	[J/K]
k$_n$	Nucleation rate constant	[-]
k$_g$ or k$_G$	Growth rate constant	[-]
L	Characteristic particle size	[mm]
M$_w$	Molecular weight	[kg/mol]
n	Growth rate order	[-]
N$_A$	Avogadro constant = 6.023×10^{23}	[mol^{-1}]
R	Universal gas constant = 8.314	[J/mol K]
r$_{C*}$	Critical size of nucleus	[Å]
Re	Reynolds number	[-]
R$_G$	Overall growth rate constant	[Kg/m^{2}s]
R$_{wp}$	Structural disorder factor	[-]
R^2	Regression coefficient	[-]
S	Supersaturation	[-]
T	Temperature	[^{o}C] or [K]
u or v	Velocity	[m/s] or [rpm]
V	Vaterite	[-]
V$_m$	Molecular volume	[m^3]

| X_i | Molar fraction | [-] |

Greek Letters	**Explanation**	**Units**
α	Cell parameter angle (b and c axes)	[-]
β	Cell parameter angle (a and c axes)	[-]
μ	Chemical potential	[-]
Δ	Delta/Difference in	[-]
γ	Interfacial tension energy	[J/m^2]
	Cell parameter angle (a and b axes)	[-]
τ	Induction time	[s]
θ	Contact angle	[^{o}] degree
ρ	Density	[kg/m^3]
δ	Thickness of boundary layer	[m]
σ	Relative Supersaturation	[-]
	Standard deviation for of crystal size	[μm]

Subscripts	**Explanation**	**Units**
l	Liquid	[-]
G	Crystal growth	[-]
Ind.	Induction time	[-]
Max.	Maximum	[-]
Min.	Minimum	[-]
p	Particle	[-]
s or surf.	Surface	[-]
T	Total	[-]
V or vol	Volume	[-]

Abbreviations	**Explanation**	**Units**
ACC	Amorphous calcium carbonate	[-]
BCF	Burton, Cabrera and Frank	[-]
BFDH	Bravais, Friedel, Donnay,Harker	[-]
B&S	Birth and spread	[-]
CSD	Crystal size distribution	[-]
	Cambridge structural database	[-]
CS	Carbon steel	[-]
EDXS	Electron dispersion X-ray spectroscopy	[-]
HPHT	High pressure high temperature	[-]
ICP	Inductively coupled plasma	[mg/L]
ICSD	Inorganic crystal structure database	[-]
ID	Internal diameter	[m]
LPR	Linear polarisation resistance	[Ω]
MSZW	Metastable zone width	[-]
OCP	Open circuit potential	[A]
OD	Outer/External diameter	[-]
PSD	Particle size distribution	[um] or [m]
PXRD	Power X-ray diffraction	[-]
QCM	Quartz crystal microbalance	[-]
RIG	Rough Interface Growth	[-]
RCE	Rotating cylinder electrode	[-]

RDE	Rotating disc electrode	[-]
SEM	Scanning electron microscope	[-]
SI	Supersaturation index	[-]
SR	Saturation ratio	[-]
S – 1	Relative Saturation ratio	[-]
SS	Stainless Steel	[-]
XRD	X-ray diffraction	[-]
XPS	X-ray photoelectron spectroscopy	[-]

Chapter 1 - Introduction

Summary

This chapter introduces the background to the oil and gas industry and highlights the main aims and objectives of this PhD thesis. It shows how the work aligns to both science and industrial processes and how it was managed. An outline of the thesis is presented via a diagrammatic route map.

1.1 Industrial Background

1.1.1 Oil and Gas Industry

The oil and gas industry is crucial for energy and as a source for the petroleum production industries (1). The importance of its usage is highly significant and therefore any impact relating to petroleum and gas production can directly affect our society with respect to development, economy and politics.

Changes in human living habits and the subsequent necessity of new technologies have led to extremely high demand for energy consumption. Nowadays, the oil and gas industries supply about 40% of the world's energy, of which 63% corresponds to the transportation energy sector and 47% to other industrial sectors (2). World energy consumption is expected to keep increasing up to year 2040 (Figure 1.1).
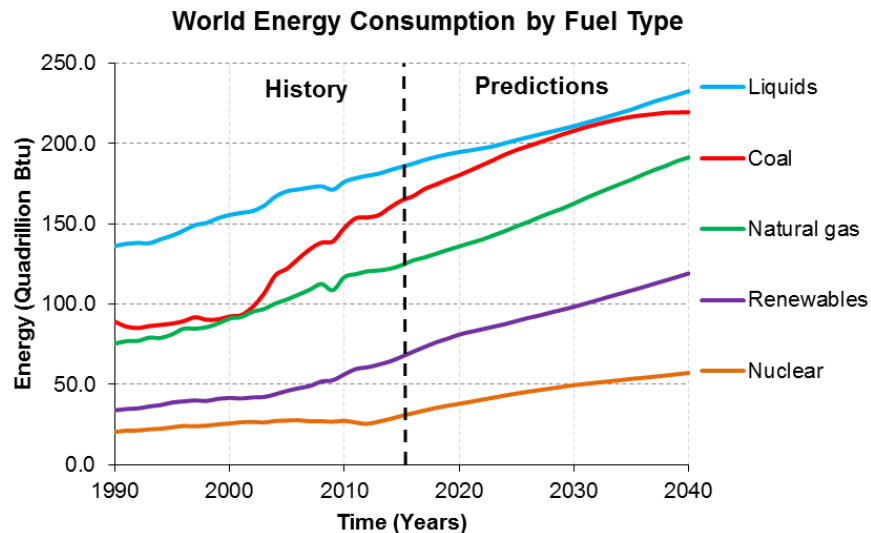
Figure 1.1: World energy consumption prediction up to year 2040 based on the overall expected global population and economic growth (2)

According to the U.S. administration energy information, the global energy consumption will continue to increase, thus, the oil and gas industry is required to produce constantly more, innovate its current exploration techniques and face extremely challenging geographical conditions such as deeper sea water, Arctic drilling, unconventional oil and gas, etc (3) (4). Nonetheless, there are some issues involved during the extraction, production and recovery stages: flow obstruction caused by organic (waxes, asphaltenes, gas hydrates) and inorganic scales (carbonates, sulphides, iron), corrosion, bio-fouling and sand erosion (5).

1.1.2 Formation of Inorganic Scale and its Impact on the Oilfield

Inorganic scale and corrosion are two common processes occurring in the oil and gas installations and can cause failure and breakdown of oilfield equipment [6] [7]. Both of these processes will depend on the water composition (i.e. complex mixture of ions present in surface seawater and reservoir water) and environment conditions such as pH, temperature, pressure, organic matter, dissolved gases [7] [8].

The deleterious crystallisation of calcium carbonate typically occurs during the enhanced oil recovery (EOR) stage, when surface water containing dissolved CO_2 gas is injected to the reservoir to stimulate the production of crude oil [7] [8] [9]. Furthermore, $CaCO_3$ scale can also be formed due to sudden changes in temperature and pressure within the tubing, pumps, tanks, heat exchangers or valves, making its removal a very difficult process [7] [8] [10].

The flow chart in Figure 1.2 shows a schematic representation of areas in which $CaCO_3$ mineral scale can be found in the oilfield installations.
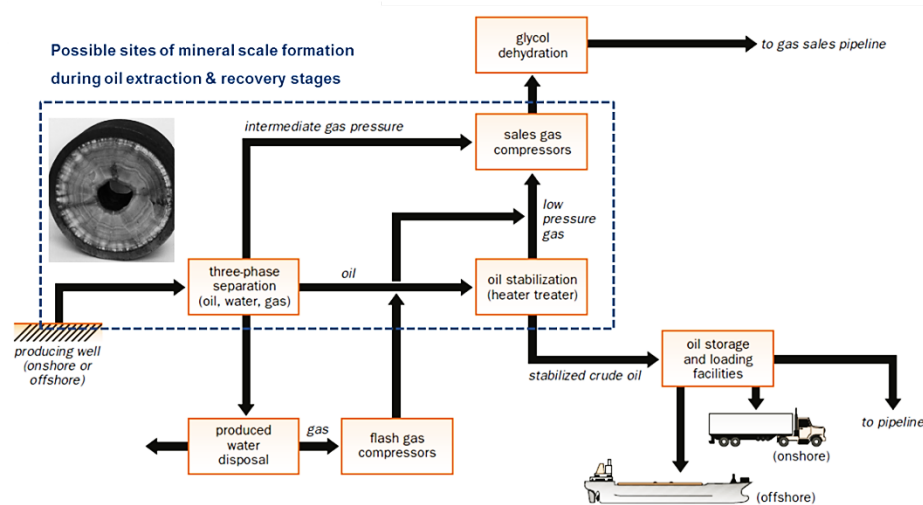
Figure 1.2: Typical crude oil processing flow diagram with possible sites for inorganic scale formation during enhanced oil recovery (EOR) [11]

Current removal techniques are still quite expensive and limited because of the extreme sub-sea conditions, and trouble in controlling every single parameter of a flowing system travelling thousands of kilometres. These techniques can be classified as mechanical and chemical treatments. Chemical remedial solutions are the most common and suitable for both scale and corrosion treatments [7] [12].

However, there is still lack of in-depth understanding of the kinetics and mechanisms of $CaCO_3$ crystallisation happening simultaneously in the bulk solution and at the

surface of oilfield facilities. Hence, this is reflected by the scarcity of adequate scale kinetic prediction models incorporated into thermodynamic prediction tools.

Furthermore scale and corrosion are often assessed separately, despite the apparent relationship in their formation and kinetics, as often these two phenomena appear in the same field locations (Figure 1.3).
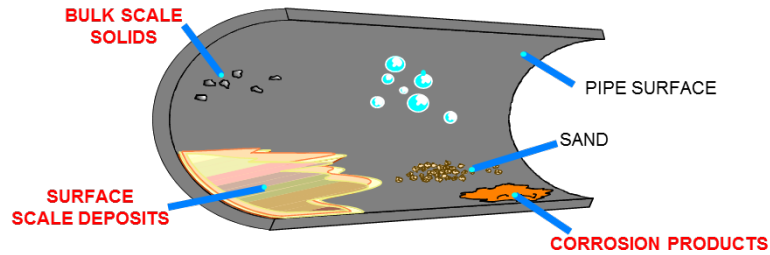
Figure 1.3: Schematic representation of scale and corrosion problems affecting the flow in a pipeline (13)

This whole scenario (Figure 1.2 – Figure 1.3) sets the backdrop to this PhD study. The research work presented in this thesis is focused on calcium carbonate ($CaCO_3$) crystallisation processes happening simultaneously in bulk solutions and at surfaces, using representative oilfield brines. To achieve this, a robust methodology has been developed to assess nucleation and crystal growth kinetics, the crystal growth mechanisms, the changes in crystal morphology and thermodynamic stability over a range of supersaturation and different temperature conditions. In addition, the effect of surface scaling on corrosion has also been investigated, as these two processes can occur simultaneously (due to the ionic brine content) but are frequently studied individually.

1.2 Research Aims and Objectives

The research question underlying this PhD study is as follows:

What is the influence of solution chemistry (e.g. composition and pH) on the formation, transformation and structure of calcium carbonate phases crystallising simultaneously in bulk solution (i.e. precipitation) and at metal surfaces (i.e. deposition)?

The above question will be delivered through the following core objectives:

1. To understand the basic science and engineering with respect to previous bulk crystallisation studies and surface deposition of $CaCO_3$ in corrosion environments.

2. To develop a robust methodology which enables assessing and characterising the crystallisation process of $CaCO_3$ from representative field brines, under different conditions (e.g., supersaturation, temperature, flow rates and pH).

3. To establish a quantitative approach for assessing the nucleation kinetics, including the determination of the induction times (τ) and the estimation of the interfacial energy (γ) for bulk solution precipitation and metal surface deposition.

4. To determine the crystal growth mechanisms and kinetics of calcium carbonate particles precipitated from bulk solutions and deposited at metallic surfaces.

5. To understand the relationship between formation mechanisms of $CaCO_3$ *surface crystallisation* and corrosion processes.

6. To assess the validity of existing thermodynamic scale prediction software (i.e., MultiScale™) with experimentally collected kinetic data from bulk crystallisation analysis.

In order to address this research question and investigate the synergy of $CaCO_3$ crystallisation processes at bulk and at surfaces (in presence of corrosion processes), an appropriate selection of computational and experimental methods was required. Therefore, the general inter-relationship between the various parts of this study which aim to answer the research questions are outlined in Figure 1.4.
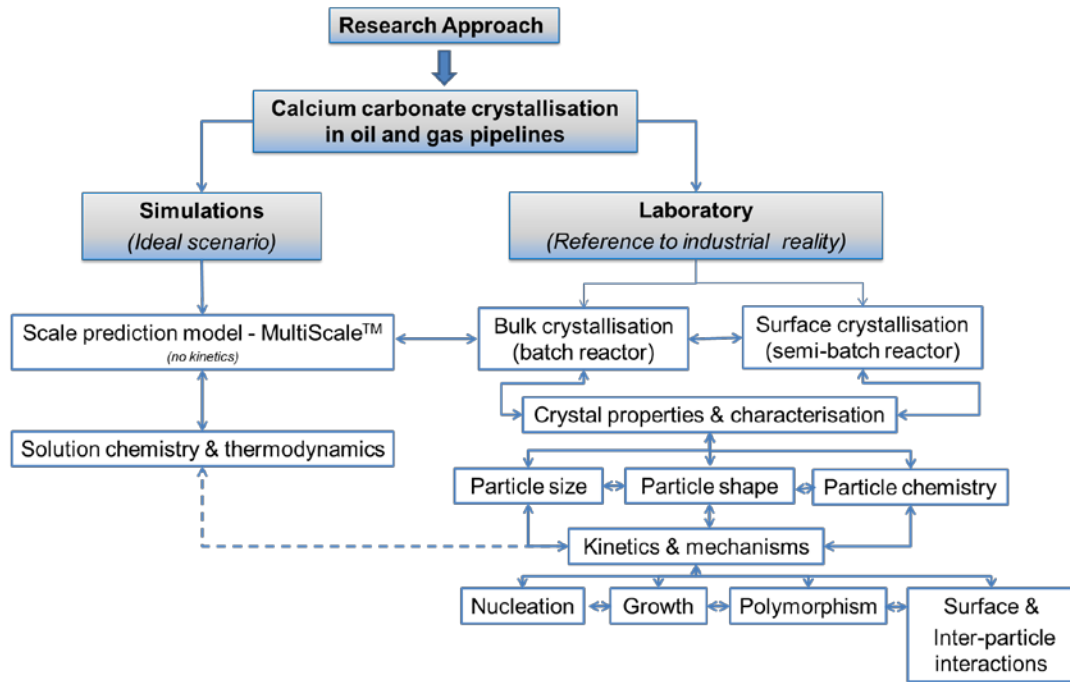
Figure 1.4: Flow diagram illustrating the integration of experimental and computational techniques to investigate the crystallisation process of $CaCO_3$ in a representative manner

The integration of kinetic data with thermodynamic predictions will contribute to describe a realistic non-equilibrium process taking place in the oilfield facilities. Currently, there are no thermodynamic tools which incorporate kinetic data for mineral scale simulations. The MultiScale™ scale prediction software is widely used within the oil and gas industry but does not consider factors such as crystal size, shape (i.e., polymorphism) and kinetics in their predictions.

1.3 Project Management

This PhD project was funded by the Engineering and Physical Sciences Research Council (EPSRC) Doctoral Training Award. The research work was carried out in the Institute of Particle Science (School of Chemical and Process Engineering) & Engineering and in the Institute of Functional Surfaces (School of Mechanical Engineering) at University of Leeds, under supervision of Professor Kevin J. Roberts and Professor Anne Neville.

Collaboration with EXPRO International© (Terje Ostwald and Annette Pang) and BP© (Hugh Bourne and Bill Smith) was established for facilitating training on the commercial thermodynamic scale prediction software, MultiScale™ (v.7). The preliminary kinetic data obtained for $CaCO_3$ scale precipitation was used to support

the Technology Strategy Board (TSB) project on prediction of scale deposition kinetics.

1.4 Thesis Delivery Plan and Layout

This PhD thesis consists of eight chapters as shown in layout from Figure 1.5.

Chapter 1 is the introductory one. It provides the background to the study, highlighting the research question set with clear aims and objectives for this research work and providing project management and route map of the overall thesis.

Chapter 2 presents an overview of crystallization science and engineering coupled with the various aspects of crystallography and crystal properties. Theories of nucleation and crystal growth are briefly summarised along with further discussion of their relationship with the crystal's morphology, size and purity.

Chapter 3 provides a general background and literature of calcium carbonate crystallisation, highlighting the basic principles of mineral scale formation in the oil and gas industry.

Chapter 4 provides some fundamentals and literature review on oilfield corrosion processes with focus on sweet or CO_2 corrosion.

Chapter 5 contains a detailed description of all experimental and analytical methods (including methods developed for determining induction times). This also includes some computational approaches used for thermodynamic scale predictions.

Chapter 6 presents the results and discussions for $CaCO_3$ bulk crystallization studies. It includes the induction time methods development, nucleation kinetics and derivation of models for assessing the crystal growth mechanisms and kinetics. A detailed characterisation of crystals evolution in solution with respect to their shape and size is also presented as well as the re-assessment of MultiScale^{TM} software used for thermodynamic predictions. Finally, discussions on key outcomes and comparison to previously reported studies on spontaneous crystallisation of $CaCO_3$ are done.

Chapter 7 provides the results and discussions for the $CaCO_3$ surface crystallization and corrosion processes. It includes results obtained from a novel in-situ approach which enabled monitoring of scale deposition kinetics on metal surfaces. The nucleation and growth kinetics were derived through models and crystals were

characterised to understand the effect of factors such as temperature and flow rate on the polymorphic stability and evolution. The scale and corrosion film characterisation was completed, discussed and compared to published literature. Finally, the differences in growth mechanisms and kinetics from $CaCO_3$ crystals forming in bulk and at surface of the metal are presented and discussed.

Lastly, Chapter 8 summarises the main outcomes from this work and makes some future work recommendation. The overall layout of this PhD thesis is summarised in Figure 1.5.
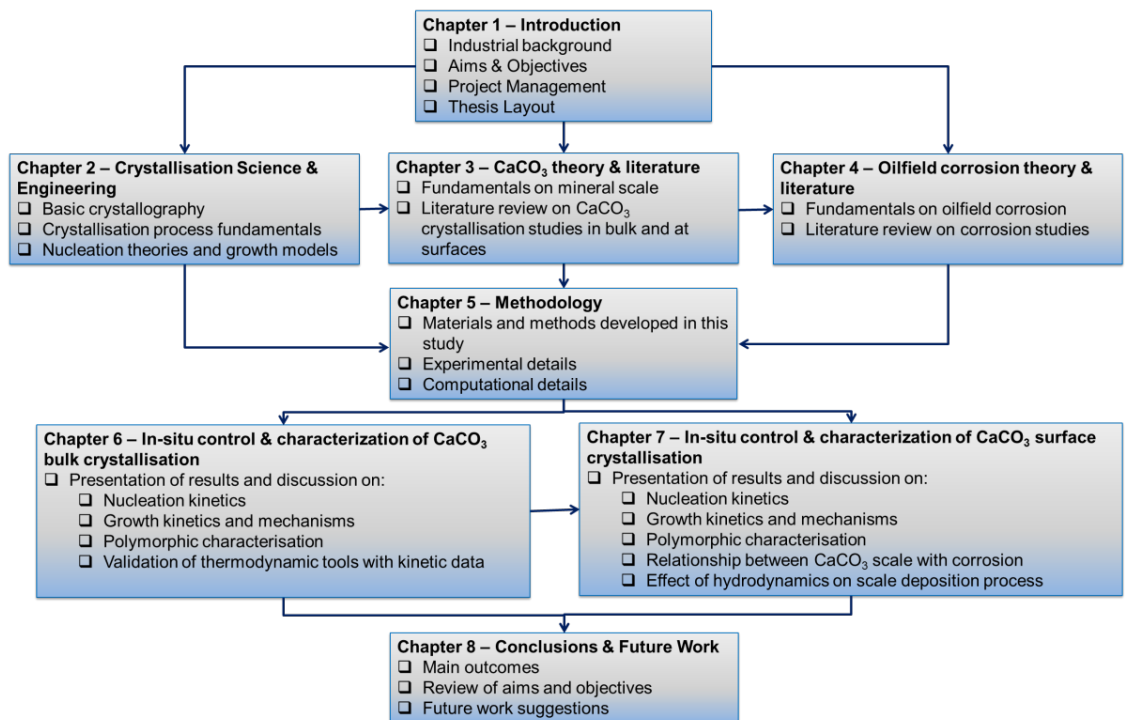
Figure 1.5: Thesis Layout – brief description of each chapter's content

Chapter 2 - Fundamentals of Crystallization Science and Engineering

Summary

This chapter provides an introduction to crystallization science with the aim of bringing together chemistry, material science and chemical engineering related to crystallization phenomena. It reviews fundamental principles, basics concepts and the hypotheses relevant to this study such as nucleation and crystal growth models.

2.1 Introduction

The aim of this chapter is to provide the basic theoretical understanding of crystallization science and engineering. This objective is achieved with the review of fundamentals, concepts and theories broadly applied in crystallisation processes.

The chapter starts with a brief introduction of crystal's concept, followed by an overview of crystallography science, notably of crystal chemistry, systems, Bravais lattices, Miller indices, and a thorough review of the theories of nucleation, crystal growth and polymorphism, which are applied for assessing the kinetics and mechanisms involved in crystallising systems. Lastly, the reviewed fundamentals and concepts are discussed and analysed to understand how crystallising conditions can affect the solution thermodynamics, crystal's properties and nucleation and growth kinetics.

A summary of the key areas presented and discussed in this chapter can be found in Figure 2.1:
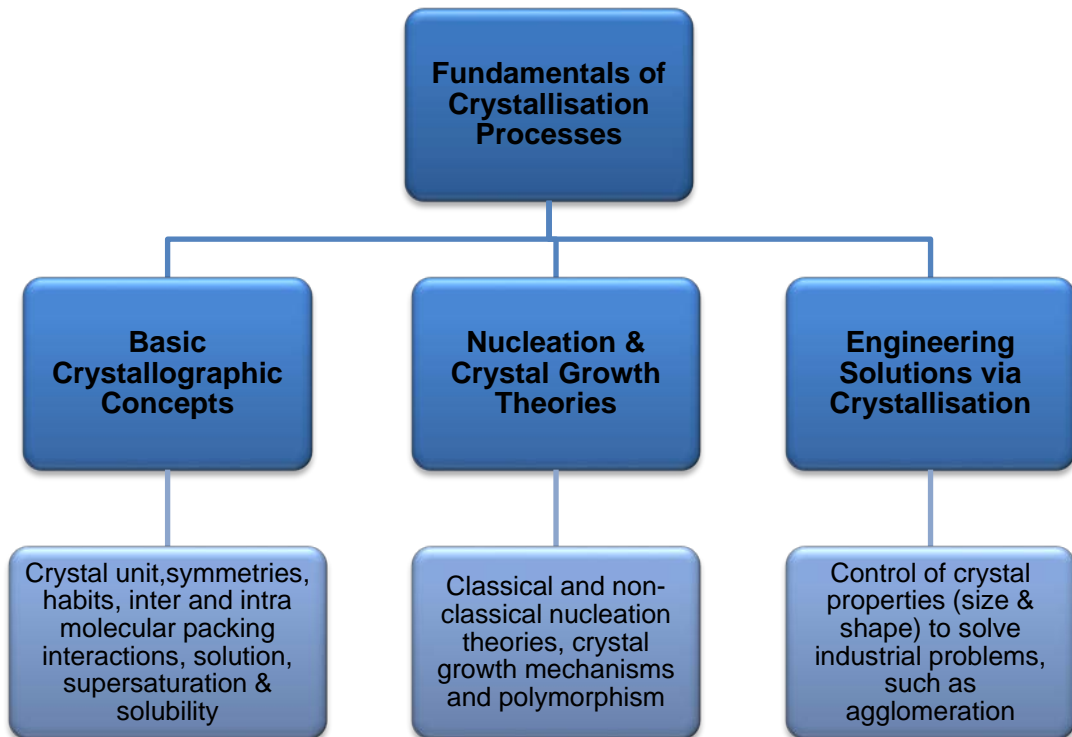
Figure 2.1: Overview of main topics covered in this crystallisation science and engineering chapter. Most of the fundamentals reviewed have been published by Mullin (14)

2.2 Crystals, Crystallography and Crystal Chemistry

2.2.1 Basic Crystallography

2.2.1.1 Crystalline and Amorphous Solid

Solids in nature are sub-divided into amorphous or crystalline solids (14). Amorphous can be defined as any material which lacks long range of order (typically similar to liquid structures), whilst crystalline matter is constituted by an internally ordered structure, made up of crystals which in essence have atoms, ions and molecules arranged in a regularly ordered and repeating pattern which extend in all spatial dimensions (15).

2.2.1.2 Crystal Lattices, Lattice Points and Unit Cell

Each crystal lattice contains an infinite number of lattice points (also known as nodes), which have the same geometrical arrangement as all of the others. Usually, each lattice point corresponds to an atom or molecule (15). A crystal's motif is the 3D repeating pattern which sits near the intersections (i.e. lattice points) of an imaginary grid (i.e. the lattice or repeating sequence of the motif). Within the lattice (repeating scheme) a single repetition of the constituent scheme is known as a unit cell (14). Figure 2.2 illustrates a crystal unit cell with its lattice points and vector directions.
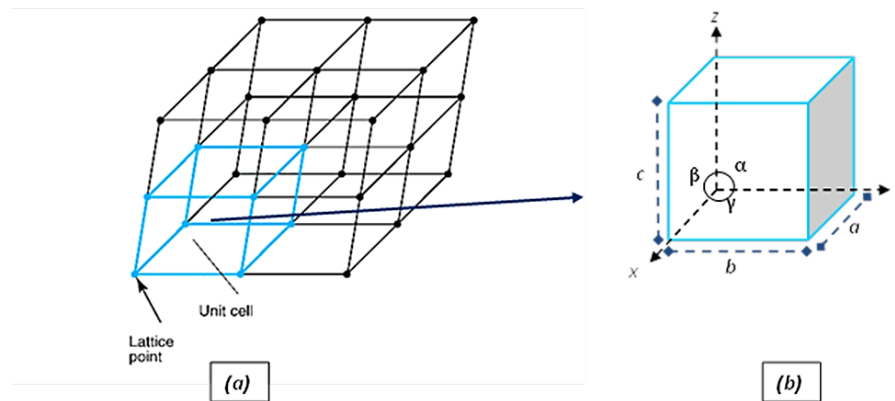
Figure 2.2: *(a)* Schematic illustration of the crystal lattice and a unit cell within the same lattice *(b)* Crystal unit cell with its respective vectors (*x, y* and *z*), inter axial angles (*α, β* and *γ*) and edge lengths (*a, b* and *c*) (14).

2.2.1.3 The Seven Crystal Systems and Directions

Unit cells can take any of the seven possible dimensional shapes, namely: cubic, tetragonal, orthorhombic, rhombohedra, hexagonal, monoclinic and triclinic (14).

These different shapes can be characterised through the relationship between their axial lengths and angles (Table 2.1).

Table 2.1: Seven crystal systems (14)

System	Angles between axes	Length of axes	Typical examples
Cubic (Regular)	$\alpha = \beta = \gamma = 90$	$a = b = c$	NaCl, CaO
Tetragonal	$\alpha = \beta = \gamma = 90$	$a = b \neq c$	SnO_2, TiO_2, urea
Orthorhombic	$\alpha = \beta = \gamma = 90$	$a \neq b \neq c$	K_2SO_4, KNO_3, Iodine
Monoclinic	$\alpha = \beta = 90 \neq \gamma$	$a \neq b \neq c$	Sucrose
Triclinic	$\alpha \neq \beta \neq \gamma \neq 90$	$a \neq b \neq c$	$CuSO_4 . 5H_2O$
Trigonal	$\alpha = \beta = \gamma \neq 90$	$a = b = c$	Sodium Nitrate
Hexagonal	$\alpha = \beta = 90, \gamma = 120$	$a = b \neq c$	Water (ice)

Atomic or molecular packing within a crystal lattice varies according to their crystallographic directions and can be defined with respect to an indexing system (16).

2.2.1.4 Miller Indices

Two dimensional crystal planes are a set of parallel and equally spaced faces that have an infinite periodic array of lattice points and sit within the 3D axial system (*x, y and z*). Each lattice plane can be described by its Miller index, (i.e. the extent to which a plane intercepts the three principle axes), holding the notation (*hkl*) while representing the crystallographic form that comprises all faces that can be derived from *hkl,* by symmetrical operation of the crystal.

Miller indices are the most common system of describing planes of a crystal, suggested by Miller in 1839 (14). Each crystal face can therefore be represented by the *h, k* and *l* indices:

$$h = \frac{a}{X}; \quad k = \frac{b}{Y}; \quad\quad l = \frac{c}{Z} \tag{2.1}$$

The example shown in Equation (2.1) presents a plane with axial intercepts which are a, b and c, so the indices *h*, *k* and *l* are a/a, b/b and c/c, i.e. 1, 1 and 1, representing (111) crystal plane.

2.2.1.5 Fourteen Crystal Bravais Lattices

Crystals of different substances vary in their elementary lengths and angles. There are 14 possible Bravais lattices in three dimensional space (14). These 14 distinct lattices have resulted from additional lattice points encountered either in the centre of the unit cell, centre of each face or even the centre of two basal faces. For instance, a primitive unit cell (P) contains one lattice point, one at each corner of the unit cell, which is shared with eight other unit cells. Other types involving lattice points at the centre of the cell are the body-centred (I), the face-centred (F) has lattice points at opposite pairs of faces, and finally the base centred (C) has a lattice point at the centre of the basal planes of the cell (14) (17).

2.2.1.6 Point Groups, Space Groups and Symmetry Operations

The seven crystal systems classification can be re-established in terms of the symmetry elements. There are 32 possible combinations of the symmetry elements and these are called the 32 point groups (18). The combination of all available symmetry operations with the Bravais translations leads to exactly 230 combinations, the 230 space groups. The International Tables for crystallography (19) list those by symbol and number, together with symmetry operators, origins, reflection conditions, and space group projection diagrams.

2.2.2 Crystal Defects

Theoretically, there should be no variation in a crystal's structure and its pattern should be perfectly repeated from the atomic to the macroscopic scales (20). However, in reality, crystals are neither perfect internally or externally, as when they grow, a range of lattice imperfections or inconsistencies can appear, due to thermal motion and the fact that crystal growth is not an equilibrium process. These imperfections are identified as defects (21) and will have an impact upon physical and chemical properties of crystalline matter (22).

Figure 2.3 represents the schematic growth of a polyhedron in which growth is affected by the presence of impurities which may interfere with the growth of certain crystal faces. Hence, it can be observed a competition between fast and slow growing faces marked by different striations (defects) in the crystal (21).
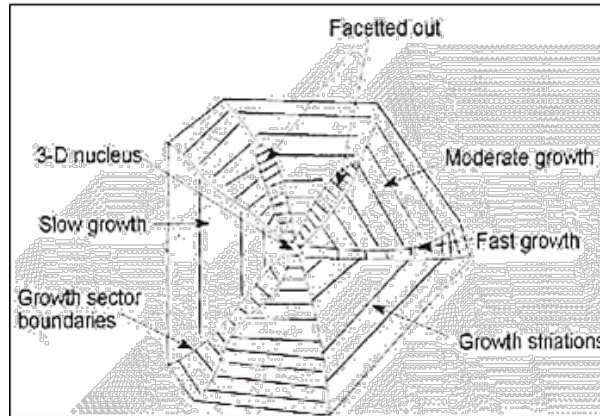
Figure 2.3: A schematic sketch of a slice cut through a grown crystal, revealing the growth history of the crystallization process (21)

2.2.3 Crystal Chemistry

2.2.3.1 Bonding in the Solid State

The overall structure and crystallographic properties of solid materials is highly dependent upon the relationship between the crystal lattices and crystal chemistry. Within solid-state materials, the variety in strength and nature of inter-molecular bonding yields to five main interaction groups: covalence, ionic, hydrogen, molecular or Van der Waals and metallic (Figure 2.4) (23).
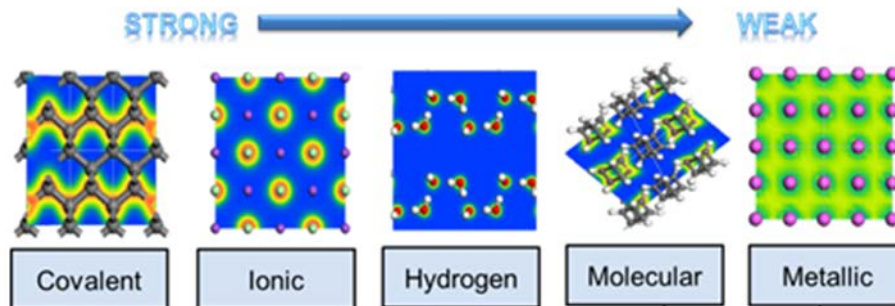
Figure 2.4: Different types of inter-molecular forces for solid matter. The strength and direction of these interactions affects the crystal internal structure (23)

Considering $CaCO_3$ mineral scale, its intermolecular interactions are classified as ionic. In this case, the ions are held in the lattice by electrostatic forces and separated from the opposite charged ions (i.e. Ca^{2+} and CO_3^{2-}). The electrostatic forces holding the ions together are very strong and require a large energy to break up the lattice. Therefore, ionic compounds have typically high melting and boiling points and are usually very soluble in water or other liquid solvents.

2.2.3.2 Polymorphism

Polymorphism can be defined as the ability of a chemical compound to have more than one possible crystal structure, whilst enclosing different physical properties (24): crystal shape, colour, density, hardness, melting point, refractive index, vapour pressure, solubility, dissolution rate, heat capacity, thermal conductivity and melting point (25).

The increasing awareness and importance of polymorphism in industry is due to the advantages of controlling particles shape in order to obtain the best properties and behaviour out of them. However, in order to obtain the desired polymorphic modification, one has to search for optimal conditions of nucleation and crystal growth, and consider the transformation pathways. A prerequisite for this is an understanding of the thermodynamic stability of the polymorphic modifications, which can be expressed by a Gibbs energy relationship (26). Compounds with polymorphic systems are able to crystallise in a number of structures that will subsequently have different free energies (27). The structure with the lowest free energy, at given temperature and pressure conditions is known as the stable form. All others having higher free energies can be the metastable and unstable forms, respectively (24).

2.2.3.3 Ostwald's Rule of Stages

It is quite common for an unstable polymorph to appear first and then transform into a stable form. Ostwald proposed a rule of stages theory (28) to describe the observed appearance of thermodynamically metastable phases. This theory stated that an unstable system does not necessarily transform directly into the most stable state, but into another transient state, whose formation is accompanied by the smallest loss of free energy (28) (29). Even though this theory lacks fundamental support, it is easy to understand that if many reactions are possible, the resulting reaction is not necessarily the one that is thermodynamically most likely to occur, but yet the one that has the fastest rate (30).

2.2.3.4 Crystal Habit and Morphology

Both morphology and habit are terms used to describe the external shape and appearance of a crystal (14). Even though crystals are in the same crystal system, they may have different external shape or morphology, due to the relative growth of the different crystal faces (14). Furthermore, the growth of an individual crystallographic face can be affected by the crystallising environment conditions (i.e., supersaturation, temperature, solvent type and impurities), crystal structure and

defects (31). Figure 2.5 illustrates that an example of a snowflake (ice) crystal in which the hexagonal crystal can exhibit three different crystal habits (14) under different crystallising conditions. The elongated growth of the hexagonal prismatic habit gives a needle-shaped (equivalent to the acicular habit) or dendritic (branched) crystals at higher supersaturation, whilst a stunted growth gives a flat plate-like crystal (tabular, platy or flaky habit).
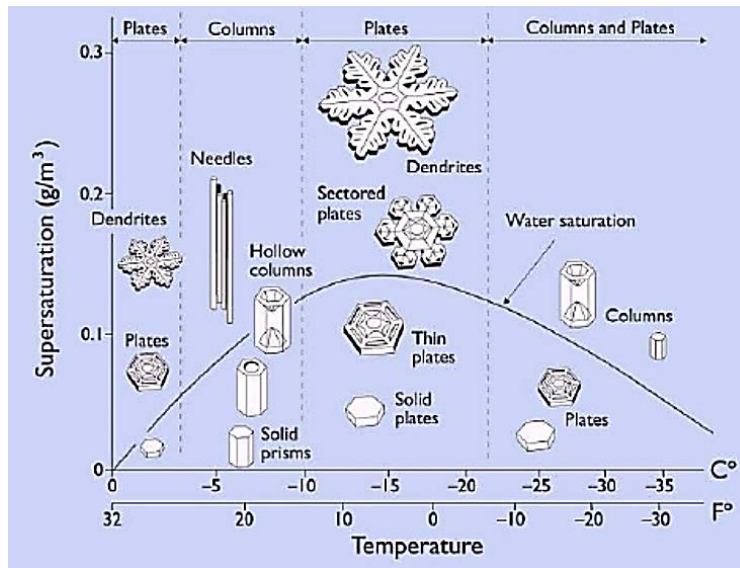
Figure 2.5: Morphology diagram of snow crystals showing different morphologies under different crystallising environments with very specific shapes at specific temperature conditions (32)

2.3 Solution Crystallization

The crystallization process comprises two main stages: nucleation and crystal growth. During this process (Figure 2.6.), the molecules in solution form clusters, which in turn, form nuclei, because of the increased concentration of the solute, and the further the nuclei grow to form stable crystals is known as the crystal growth stage. In order to understand and control any crystallization process, some key concepts of crystallisation such as solution properties, solubility, supersaturation, nucleation and crystal growth must be fully understood.
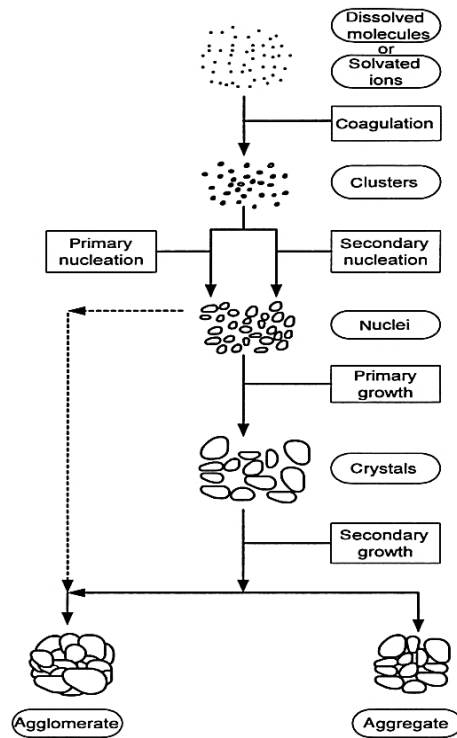
Figure 2.6: Diagram showing the sequence of particle formation from solution in which solvated ions coagulate to form clusters and stable nuclei which then start growing in solution and may form aggregates (33)

2.3.1 Solutions, Solubility and Ideality

Solutions are commonly defined as homogeneous mixtures of two or more substances (14). Solutions can be classified into undersaturated, saturated and oversaturated, according to the nature of the thermodynamic equilibrium between solvent and solute. A saturated solution is always in thermodynamic equilibrium with the solid phase. Thus, the majority of solutes will proceed to dissolve in their near-saturated solution via absorption of heat. This type of heat is referred to as heat of solution and is endothermic in the near saturated solution.

Solubility is typically defined by the maximum amount of a substance (solute) that can be dissolved in a solvent (liquid) at a given temperature (34). In most cases, but not always, the solubility of a substance increases with temperature, whereas the equilibrium solubility concentration will increase exponentially as a function of temperature (14). Whenever there is a phase change, it will be observed as a discontinuity in the solubility profile and a transition point is the point at which the solubility curves of two phases cross.

In reaction crystallization (i.e., precipitation), two soluble materials are added together in solution and react to form a product with a lower solubility. Once the

solubility of the product exceeds the saturation point of the solution, the system becomes supersaturated and the material crystallises. This method is commonly used for slightly soluble substances and also in the production of inorganic materials. There are many factors influencing solubility, there is no current robust model which can predict solubility to a high degree of accuracy, so solubility is often estimated experimentally (14).

2.3.2 Supersaturation

Supersaturation is the essential driving force of all crystallization processes and has a significant influence on mechanisms occurring during the nucleation and crystal growth stages.

A solution that contains an excess of concentration over the saturated (equilibrium) value at a given temperature is described as being supersaturated. The supersaturation driving force allows the system to initiate nuclei formation and maintain growth until the degree of supersaturation is relieved.

Understanding the principle of supersaturation is fundamental not only to characterise the kinetics but also to relate the crystallization outcomes to the parameters that can control crystallization (35). The rate of crystallization is often determined by the degree of supersaturation. Supersaturation subsequently can be defined as the concentration driving force Δc, or saturation ratio S or even as relative supersaturation S*, all three are expressed in the following Equations (36):

$$\Delta c = c - c^* \tag{2.2}$$

$$S = \frac{c}{c^*} \tag{2.3}$$

$$S^* = \frac{\Delta c}{c^*} = S - 1 \tag{2.4}$$

where, c is the actual solution equilibrium concentration, c* is the saturation solution concentration at a given temperature. In this report supersaturation will be defined as shown in Equation (2.2). Supersaturation can also be represented as a saturation ratio (SR or S) which is defined as the square root of the ratio between chemical activities of components and the product solubility constant.

$$S = \sqrt{\frac{[(a_X)(a_Y)]}{K_{sp,XY}}} \tag{2.5}$$

where (a_x) and (a_y) represent the chemical activities of components *x* and *y*; and K_{sp} is the solubility product constant of compound *xy*.

Alternatively, the saturation ratio (SR) can be denoted a saturation index (SI) which is simply defined by:

$$SI = \log_{10}(SR) \tag{2.6}$$

Theoretically, crystals will form in any solution that is supersaturated, i.e. when the solute concentration exceeds the solubility forming the first nuclei. However, in reality, this might not always happen, as a large supersaturation is required to overcome the activation energy barrier which exists when forming the crystal (29). This energy barrier represents the free energy required to create the nucleus, from which the crystal will eventually grow.

2.4 Nucleation

Nucleation is the first stage of crystallisation process, and can happen once a certain degree of supersaturation is reached in the system, subsequently leading to the formation of stable clusters via a process which involves the agglomeration of solute molecules (Figure 2.6). This process can occur very rapidly, especially in local regions of high supersaturation, but only clusters that grow beyond a certain critical size become stable under the average conditions of supersaturation obtained in the bulk of the fluid (14). Depending on the mechanisms involved for the nuclei formation and growth, the nucleation can be classified by two main categories: primary and secondary, as shown in Figure 2.7. Primary nucleation can be sub-categorised into homogenous and heterogeneous, and does not involve the adhesion of any crystals to induce nucleation in the crystallising solution; while in the secondary occurs in presence of seeds which serve as a template for the solute molecule to aggregate and grow within the metastable zone (14).
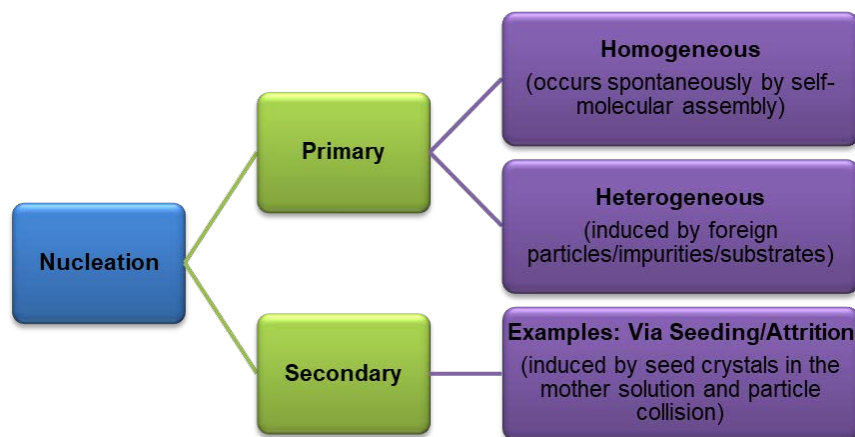
Figure 2.7: Schematic characterisation of nucleation mechanisms (14)

2.4.1 Primary Nucleation

Theories of primary nucleation are based on the sequences of bi-molecular collisions and interactions within a supersaturated fluid, which result in the build-up of a lattice structured crystal, which is likely to be metastable. This type of interaction is known as homogeneous primary nucleation (14). Primary nucleation may also be initiated by suspending particles of foreign substances within the system, and is known as heterogeneous nucleation (14). One of the differences between homogenous and heterogeneous primary nucleation is that there is a displacement of the nucleation rate against the supersaturation curve as can be seen in Figure 2.8:
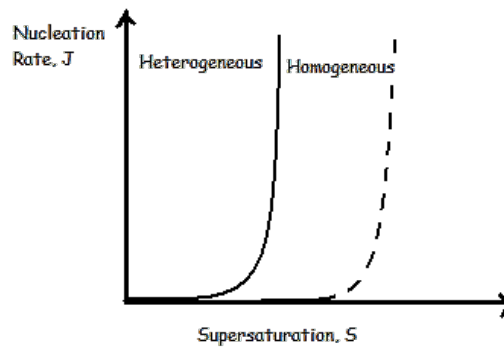
Figure 2.8: Schematic plot of nucleation rate versus supersaturation, showing the nucleation rates increase significantly when approaching the critical supersaturation for both homogeneous and heterogeneous nucleation types (37)

In nature, there are many examples in which crystal formation will be dependent on mechanical work to overcome the barrier imposed by the solution chemistry (36). This mechanical work, needed to bring the system to the unstable state, corresponds to the overall Gibbs free energy (ΔG). Overall, with the assumption that the nucleus is a spherical particle, the excess free energy between a small solid particle of solute and the solute in solution is equal to the sum of surface excess free energy ΔG_s and the volume excess free energy ΔG_v (36).

2.4.1.1 Homogeneous Nucleation

The classical theory of nucleation (36) can be described by the thermodynamic approaches of Gibbs (29) and Volmer (38), with modification by others (39), which considers the growth of clusters via saturation fluctuations within the vapour-state and considers solutions where liquid systems are treated as very compressed gases. Thus a growing cluster must overcome a free energy barrier in order to become stable (Figure 2.9).
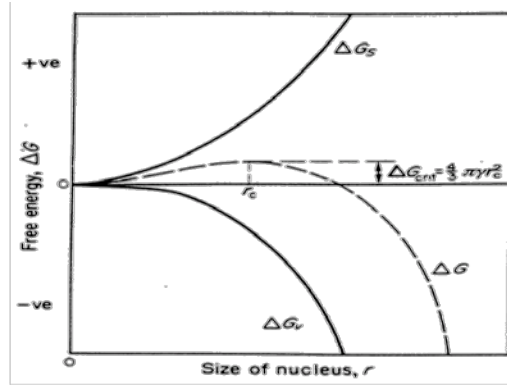
Figure 2.9: Free energy diagram mapping the energy range during the formation of critical spherical cluster (14)

The cluster growth occurs in the metastable zone region where the condition of supersaturation is achieved. The number of molecules in a stable crystal nucleus can vary from about ten to a thousand. Similarly, ions or molecules in a solution can interact to form short-lived clusters. Short chains may be formed initially or flat monolayers and eventually a crystalline lattice structure is built up. The crystal development process occurs very rapidly in the regions of very high supersaturation and many of the sub-nuclei fail to achieve maturity because of their instability and they simply re-dissolve.

2.4.1.2 Nucleation Rate

The rate of nucleation is defined as the number of nuclei formed per unit time as shown by the Equation (2.7).

$$J_n = A \times exp\left(\frac{-N}{lnS^2}\right) \qquad (2.7)$$

where A is a pre-exponential factor, S is the saturation ratio and N is a parameter related to the basic Gibbs-Thomson expression and includes other crystallization parameters shown in Equation (2.8) (40):

$$N = \frac{16\pi\gamma^3 V_m{}^2}{3k^3T^3} \qquad (2.8)$$

where v is the molar volume ($v = V_m = 2$ for $CaCO_3$ molecule), γ is the interfacial tension and k is the Boltzmann constant= $1.3805 \times 10^{-23} J/K$, and T is the absolute temperature in Kelvin. Rearranging equations (2.7) and (2.8), the nucleation rate expression becomes:

$$J = J_n = A \times \exp\left[-\frac{16\pi\gamma^3 V_m{}^2}{3k^3 T^3 (\ln S)^2} \right]$$

$$(2.9)$$

The pre-exponential factor A is defined as A=zf*C$_o$; where f* is a collision factor, z is the Zeldowich factor which corrects for the fact that not all super nuclei grow out to larger sizes and C$_o$ is the concentration of nucleation sites (14).

The nucleation rate equation (2.9) provides the key variables governing nucleation, such as temperature, supersaturation, molar volume and interfacial tension of the crystal. In addition, it highlights the enormous rapid increase in nucleation rate once a certain degree of critical supersaturation is achieved. However, the experimental trend displays decay in the nucleation rate associated to very high solubility levels, leading to the physical instability of the solution (Figure 2.10).
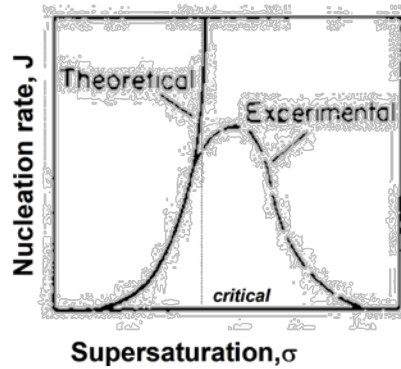
Figure 2.10: Nucleation rate as a function of supersaturation. The critical supersaturation is associated with rapid increase of the rate of nucleation. Experimentally this rate decreases after reaching the peak (14)

When the crystallising material is sparingly soluble (e.g. CaCO$_3$), nucleation is more difficult and occurs only when at high supersaturation. In this case, the supersaturated solution may stay in a meta-stable state over a very long period. But as soon as a critical supersaturation is exceeded (Figure 2.10) the nucleation rate increases dramatically (41). However, it has been experimentally shown that the nucleation rate decreases at high supersaturation (14).

2.4.1.3 Induction Time

The period of time usually elapsed between achievement of supersaturation and the appearance of crystal is usually referred as to an induction period (14). This time is a measure of the ability of the system to remain in metastable equilibrium. Given the small size expected for a critical nucleation cluster, the nucleation rate can be hard to measure experimentally. Hence, for practical purposes, the induction time (τ or

$t_{ind.}$) is often employed to estimate the nucleation rate J using the following expression:

$$\tau = \frac{1}{J} \tag{2.10}$$

Mullin (14) proposed relating Equation (2.10) with equation (2.9) to elucidate the relationship between the induction time and nucleation rate taking into account the interfacial tension as shown by:

$$\ln(\tau) \propto \left[\frac{\gamma^3}{T^3 (\ln S)^2} \right] \tag{2.11}$$

$$\ln J = \ln\left(\frac{1}{\tau}\right) = \ln(A) - \left[-\frac{16\pi\gamma^3 V_m^2}{3k^3} \right]\left[\frac{1}{T^3 (\ln S)^2} \right] \tag{2.12}$$

Rearranging Equation (2.12), it becomes:

$$\ln \tau_{ind} = \ln A + \frac{16\pi\gamma^3 v_m^2}{3k^3 \left[T^3 (\ln S)^2 \right]} \tag{2.13}$$

The interfacial tension and supersaturation can then be quantified within Equation (2.13) to give the critical cluster radius. Hence, a plot of $\ln \tau_{ind}$ against $T^{-3}(\ln S)^{-2}$ yields a straight line. The value of the interfacial surface energy is then easily estimated from the slope and the intercept gives the pre-exponential factor A of note is the significance of A to the nucleation process. It is a temperature independent constant that indicates the probability of molecular collision. Thus, higher collision rates result from higher kinetic energy, which has an important effect on the amount of energy required (or activation energy) to ensure that a reaction happens.

Assuming that nucleation is homogenous and the critical nuclei are spherical, then the minimum size of a stable nucleus (r_c) is given by Equation (2.14), and the number of molecules in a critical nucleus (N*) can be estimated using Equation (2.15).

$$r_c = \frac{2\gamma v}{kT \ln S} \tag{2.14}$$

$$N^* = \frac{\left(4\pi \times r^{*3}\right)}{3V_m} \tag{2.15}$$

Where, r_c is the radius of the critical nucleus, k is the Boltzmann constant (k= 1.3805 $\times 10^{-23}$ J/K) and V_m is the molar volume (V_m=2 for $CaCO_3$ molecule).

Collectively, all of these parameters are sufficient to characterise any crystallization system. From these mathematical expressions (i.e., Equations (2.13) and (2.14)), it can be observed that as the supersaturation increases (i.e., or the interfacial energy decreases), the free energy of the particle will decrease. Therefore, any nuclei smaller than the critical nuclei size, can be expected to re-dissolve, and generate larger nuclei than the expected r_c, therefore, initiating the crystal growth stage (14). A drawback of the classical theoretical development of crystals is that it assumes only spherical shaped nuclei (14). However, more specific expressions can be derived through the use of volume and area shape factors when nuclei adopt different shapes.

Furthermore, Kashchiev (42) (43) and Rosmalen (20) have also proposed a general expression for determining τ , which is valid for any number of nuclei appearing and growing in the solution, as shown in Equation (2.16). This formula considers variables such as nucleation and growth rates, assuming that the induction time can be experimentally characterised by techniques which detect the appearance of a certain overall volume of nuclei crystals.

$$\tau = t_{ind} = \left(\frac{\alpha}{\alpha_4 J G^3} \right)^{\frac{1}{4}} = \left(\frac{3\alpha}{\pi J G^3} \right)^{\frac{1}{4}} \tag{2.16}$$

Or expressed by the nucleation rate, J, Equation (2.16) becomes:

$$J = J_n = \left(\frac{3 \times \alpha}{\pi \times G^3 \times t_{ind}^4} \right) \tag{2.17}$$

where J and G are the nucleation and the growth rates, α is a ratio between the macroscopic volume of the new phase (i.e. precipitate particle volume) and the volume of the liquid phase (α=V_{min}/V) and usually takes on values in the range of $10^{-6} - 10^{-8}$. Lastly, α_4 considers the shape of the nuclei, which is (π/3) for a spherical nuclei particle.

2.4.1.4 Heterogeneous Nucleation

Homogeneous nucleation is normally rarely observed in crystallization from solution, except in cases of very high supersaturation obtained by chemical reaction or addition of miscible anti-solvent. In most solutions, nucleation occurs at much a lower supersaturation (γ > $γ_s$) and it is usually due to the interaction of foreign particles such as dust or dirt contained in the walls of equipment. Hence, when a foreign particle such as impurities or added seed crystals exist in the solution, heterogeneous

nucleation is said to be occurring. This is generally associated with lower free energy barrier, thus enhancement of nucleation rates which depend on the contact (wetting) angle (θ) of the solute phase as shown in Figure 2.11:
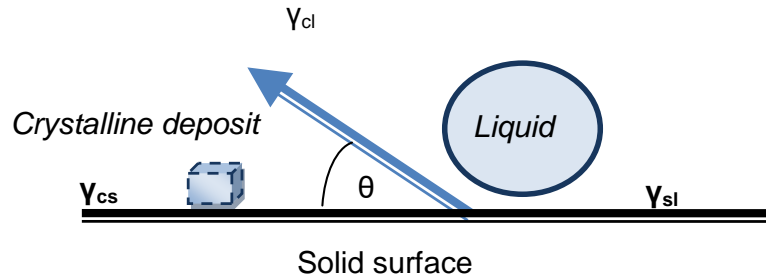
Figure 2.11: Interfacial tensions at the boundaries between a solid and liquid (14)

where, θ is the angle of contact between the crystal and the foreign solid surface (angle of wetting in liquid-solid systems), γ_{cl}: Interfacial tensions between the crystalline phase and mother liquor, γ_{sl}: Interfacial tensions between the solid foreign-body surface and mother liquor and γ_{cs}: Interfacial tensions between the solid crystalline phase and a foreign body.

2.4.1.5 Interfacial Tension Energy

The concept of surface energy is best explained by drawing a distinction with the volume energy associated with molecules that reside within the bulk of a crystal lattice, where these are subjected to forces exerted by surrounding molecules in 3D (44). When a crystalline particle is surrounded by a wetting mother-liquor, the surface molecules will differ from those in the vacuum case, because they are also attracted by the liquor phase molecules. Therefore, the energy of the intermolecular interactions between surface active molecules is reduced. For example, the specific surface energies for the major faces of $CaCO_3$ have been investigated (45) and results showed these tend to range from 1089 mJ/m^2 to 1787 mJ/m^2, whilst experimental values for solution crystallization are considerably lower e.g. 100 mJ/m^2.

Some predictions of the specific surface energy have been made by applying molecular dynamic calculations (46) whilst Walton has reported a simple method to calculate the surface energies using a bond-breaking model (47). Thermodynamic considerations have led to a proportional relationship between the cluster size and the surface energy in a manner which takes into consideration the significant contribution made by the crystal corners and edges particularly at small particle sizes (47). However, as its variation decreases quite rapidly with the increase of the crystal size (48) (49), surface energy is assumed size-independent in the classical

nucleation theory (42). Molecular modelling studies aiming to calculate the interfacial energy for small particles of sizes (300 – 750 atoms) near the nucleus size claimed that the interfacial energy will decrease with increasing the particle size (50).

2.4.2 Secondary Nucleation

Secondary nucleation can only take place if crystals of the species under consideration are already present. Thus, the productive interactions with the (seed) crystals introduced and new crystal clusters are the main causes of crystal growth (51). During seeding, secondary nucleation of new crystals can be considered due to contact between original crystals and growing crystals themselves and/or with internal parts of the equipment. Therefore, seeds can reduce the interfacial tension favouring nucleation and hence act as a template for nuclei formation (14).

2.4.3 Non Classical Nucleation Approaches – New Pathways

The classical nucleation theory approach does not consider the exact shape, structure and densities of small molecular clusters. New theoretical approaches indicate that small nucleation clusters could differ drastically from the final crystal phase both in composition and structure (52). However, the accuracy of assuming independent surface energy on a specific cluster size is not discussed (53), as well as the meaning of the surface energy for clusters having less bulk than surface molecules (54).

The mechanism of nucleus formation is extremely challenging (55). Vekilov and co-workers (56, 57) suggested that nucleation from solution proceeds via two steps: first a droplet of dense liquid is formed and then secondly molecules order within the droplet to form a crystalline nucleus. Simulation studies (58) supported this assumption that nucleation of crystals from solution involves a two-stage process with the first stage consisting of the formation of disordered clusters of solute and the second stage involving the nucleation of the crystal from this solute dissolution.

Colfen (59) (60), DeYoreo (61) and Meldrum (62) supported other pathways for bio-mineralization nucleation. Terminologies such as pre-nucleation (63) (64), mesocrystallization (59) (65) and polymer induced liquid precursor (PILP) (66) had emerged from other approaches, giving an insight completely different from the formal classical nucleation theory. Figure 2.12 displays a summary of approaches proposed to understand the stages of crystallization, especially the nucleation.
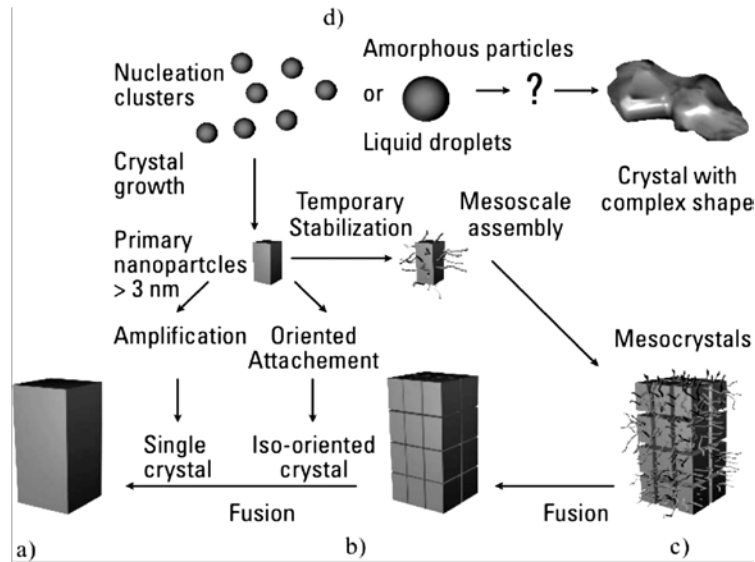
Figure 2.12: Schematic illustration of crystallization pathways from a classical approach to several non-classical ones (63)

In Figure 2.12, pathway (a) represents a typical crystallisation pathway to a single crystal. Pathway (b) shows that primary nano-particles can arrange into an iso-oriented crystal, in which the nano-crystal units form a single oriented crystal. Pathway (c) illustrates that if nano-particles are covered by a polymer or additive before they undergo a mesoscale assembly, then a mesocrystal is formed. Pathway (d) shows the possibility of amorphous nano-particle formation before or after their assembly to much more complicated structures (63).

2.5 Crystal Growth

2.5.1 Stages of Crystal Growth from Solution

The structure of a supersaturated solution is highly transient and complex. The occurrence of spontaneous nucleation in inactive supersaturated solutions depends on their concentration gradients upon mixing and formation of unstable molecular clusters. Studies have provided indirect evidence of the existence of solute clusters given by numerous experiments (34) (67) involving the diffusion properties of solutes (68) (diffusion of clusters and formation of saturated solutions) and spectroscopic measurements (69). Additionally, researchers have also investigated the chemical activity of supersaturated solutions, solution's critical cluster size and the degree of association via electrodynamics increase of single solution droplets (70).

When growth of a crystal is described, it can be approached as a macroscopic problem by discussing the overall change in some dimensions of the crystal. However, this description will provide knowledge about process kinetics without giving the relevant information about the actual mechanism of crystal growth (71). Therefore, it is necessary to understand the mechanistic approaches for crystal growth. The key stages involved during crystal growth process (72) (73) are illustrated in Figure 2.13 and can be summarised as:

- Bulk transport, when solute molecules move from the bulk of the solution towards the boundary layer surrounding the crystal surface;
- Diffusion through the boundary layer to the surface of the crystal, according to Fick's Law due to the concentration gradient;
- Adsorption onto the surface and partial or total desolvation;
- Diffusion along the crystal surface to energetically favourable incorporation sites;
- Diffusion away from the crystal surface;
- Attachment to the surface step and partial or total desolvation;
- Diffusion along the surface step;
- Integration into the crystal at a kink and total desolvation;
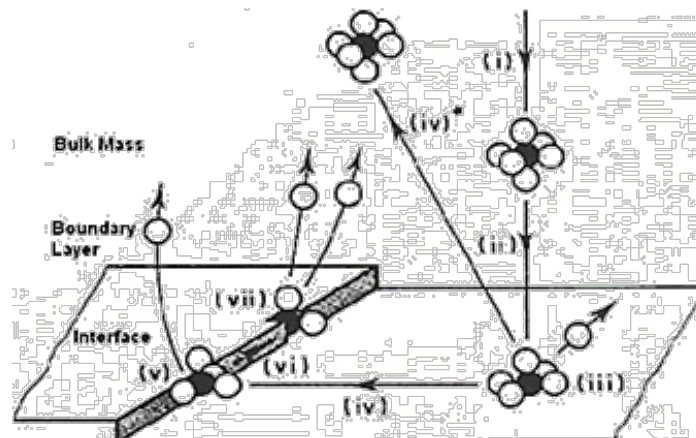
Figure 2.13: Schematic representation of several steps involved in crystal growth: diffusion (i, ii, iv, iv*, vi), adsorption (iii), attachment (v), integration (vii) and de-solvation (iii, v, vii) (72)

Each of these steps can be affected by changes in the crystal growth conditions. The structure of the crystal growth interface depends on the supersaturation, which in turn gives rise to three types of growth mechanisms.

2.5.2 Diffusion Layer Theories

To characterise the bulk crystal growth, two main processes have been suggested: the diffusion and surface adsorption (deposition) as illustrated in Figure 2.14.
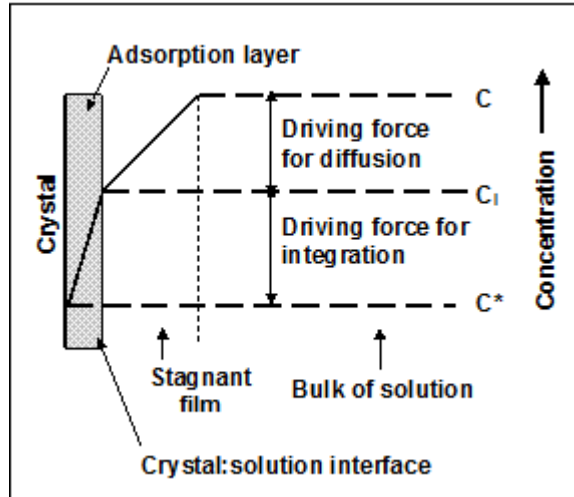
Figure 2.14: Pictorial representation of concentration driving forces in crystallization from solution (14)

In the diffusion process, solute molecules are transported from the bulk of the supersaturated mother liquid through the solution boundary layer which is adjacent to the surface of the crystal. In the adsorption process, the solute molecules are incorporated into the crystal surface extending the crystal lattice (adsorption).

Both of these processes (i.e. diffusion and adsorption) considered that the driving force for crystallisation is the difference between the concentration in the bulk of solution and at the crystal surface, as represented by the following equations:

$$\frac{\mathrm{d}m}{\mathrm{d}t} = k_d A (C - C_i) \text{ (diffusion through the boundary layer)}$$

(2.18)

$$\frac{\mathrm{d}m}{\mathrm{d}t} = k_r A (C_i - C^*) \text{ (surface reaction/adsorption)}$$

(2.19)

where m is the mass of solute deposited in time t, k_d is the mass transfer coefficient associated with diffusion, k_r is the rate constant associated with the surface reaction (integration) process, A is the surface area of the crystal, C is the solute concentration in the bulk, Ci is solute concentration in the solution at the crystal-solution interface, C* is the equilibrium saturation concentration.

2.5.3 Growth Rate Expressions

The measurement of the crystal growth rate can be carried out either as a direct measurement of the linear growth rate on a specific face of crystal {hkl} or by an indirect method by estimating an overall linear growth rate from mass deposition rates measured on a single crystal or a population of crystals. Growth rate estimation will always depend on the crystallization conditions, such as supersaturation, temperature, crystal size, crystal habit, pH and impurities (72).

The crystal growth rate can be expressed in terms of overall mass deposition rate, R_G (kgm^{-2}s^{-1}) or overall linear growth rate G (ms^{-1}) considering the following empirical correlation:

$$R_G = k_G (C - C^*)^g = k_G (\Delta C)^g = \frac{1}{A} \frac{dm}{dt} = \frac{3\alpha}{\beta} \rho_c G = \frac{3\alpha}{\beta} \rho_c \frac{dL}{dt} \quad (2.20)$$

$$\therefore R_G = \frac{6\alpha}{\beta} \rho_c \frac{dr}{dt} = \frac{6\alpha}{\beta} \rho_c \bar{V} \quad (2.21)$$

Where R_G is the overall growth rate, k_G is the growth rate constant, ΔC is the concentration gradient, g is the overall growth order, m and A are the mass and area of the crystal, L is the characteristic crystal size, r is the radius of the spherical crystal, ρ_c is the crystal density, α and β are the volume and surface factors ($\beta/\alpha=6$ for spherical or cubic crystals).

In the literature (72) (73) (74), three main methods have been established to express the crystal growth rate, and these are:

a. Face growth rate (R_{hkl} or v_{hkl}, m/s) which is the velocity of movement forward of the crystallographic faces in a direction perpendicular to the face (hkl) which can be measured on individual crystal faces. These face specific growth rates can be related to theories of crystal growth mechanisms and are considered as an effective measurement of the overall growth rate.

b. Overall mass growth rate, R_G (kg/m^{2}s) represents the total mass flux to the crystallographic face and is used to express the average growth rate of the whole crystal as shown in Equation (2.22).

$$R_G = \frac{1}{A_C} \times \frac{dM_C}{dt} \quad \leftrightarrow \quad R_G = \frac{\rho_c}{A_C} \sum v_{hkl} A_{hkl} \quad (2.22)$$

where M_c is the mass of crystal, A_C is the surface area of the whole crystal, ρ_c is the density of the crystal and A_{hkl} is the surface area of the face (hkl).

This approach considers also the weighing of the crystals (i.e., mass) over time.

c. Overall linear growth rate, G (ms^{-1}) is the rate of change of characteristic dimensions over time and is given by Equation (2.23). This method is commonly applied for population balance methods: The population balance methods are related to the bulk crystal size distribution (CSD) and was initially applied by Randolph and Larson (75) for kinetic analysis.

$$G = \frac{dL}{dt} \tag{2.23}$$

where G has the same dimensions as velocity (m/s).

This overall linear rate (G) can therefore be translated in terms of shape and size of crystal by the following R$_G$ expression:

$$R_G = \frac{1}{A_C} \times \frac{dM_C}{dt} = \frac{1}{\beta.L^2} \frac{d(\alpha \rho_c L^3)}{dt} = \frac{3\alpha \rho_c}{\beta} \frac{dL}{dt} = \frac{3\alpha \rho_c}{\beta} G \tag{2.24}$$

For spherical or cubic crystal particles, it can be assumed that β/α=6. Hence, the Equation (2.24) reduces to:

$$R_G = \frac{1}{2} \rho_C.G \tag{2.25}$$

2.5.4 Crystal Growth Mechanisms

The growth of individual crystal faces will depend on crystallisation parameters such as the supersaturation, temperature, impurities and solvents. Therefore, the crystal growth kinetics will vary according to the different changes in crystal size and morphology (76). Growth mechanisms can show the interaction between the crystal growth rates and supersaturation. Figure 2.15 shows the relationship between supersaturation and crystal growth over time, the size and shape evolution of the final crystals will depend on supersaturation and mechanisms involved during the growth process (14).
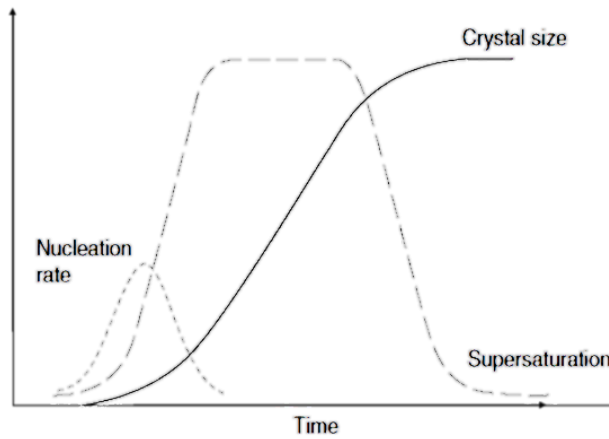
Figure 2.15: Relationship between nucleation rate, crystal growth and supersaturation (14)

The behaviour of crystal growth rate of a crystal face will depend on its growth mechanisms, which can control the molecular attachments onto the growing face (77) (78). As a result, three main crystal growth mechanisms are described as a function of supersaturation:

a. **Screw dislocation mechanism or Burton, Cabrera and Frank model**

This model was developed by Burton, Cabrera and Frank (BCF) (14) (24) to explain experiments where the transport of solute molecules from bulk to the surface of the crystal seemed unfavourable due to very low supersaturation. The model is based on the idea that screw dislocations on the surface of crystals provide a continuous source of kink sites which enable the incorporation of growth units onto the crystal surface and facilitate subsequent growth of the surface (14). This mechanism leads to a spiral growth as shown in Figure 2.16.
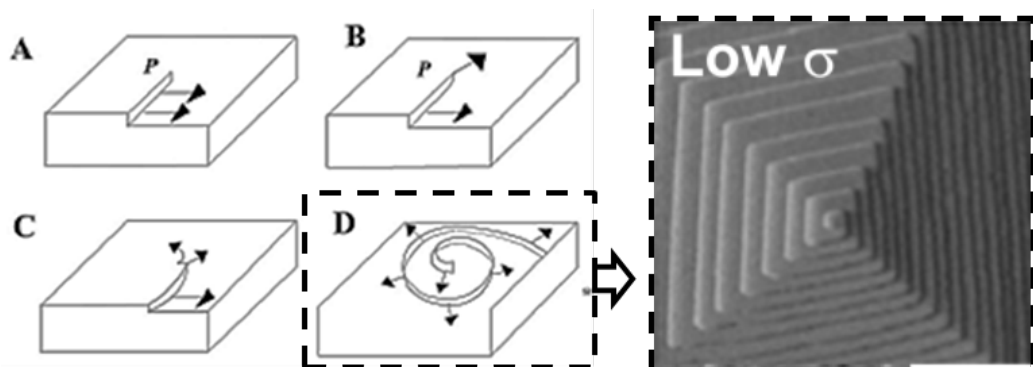
Figure 2.16: Crystal grow by BCF mechanism showing the stages for the development of a spiral (A to D) (14). The right hand image illustrates screw dislocations during calcite face growth at low supersaturation (79) (80)

The resulting BCF growth rate expression is given by:

$$R = A_1\sigma^2\tanh\left(\frac{A_2}{\sigma}\right)$$

(2.26)

where A_1 and A_2 are complex temperature-dependent constants and σ the relative supersaturation ($\sigma = S - 1$ where $S = C/C^*$).

The growth rate, R, dependency on the level of supersaturation, and different relationships between growth rate and supersaturation can be established as shown in Figure 2.17.
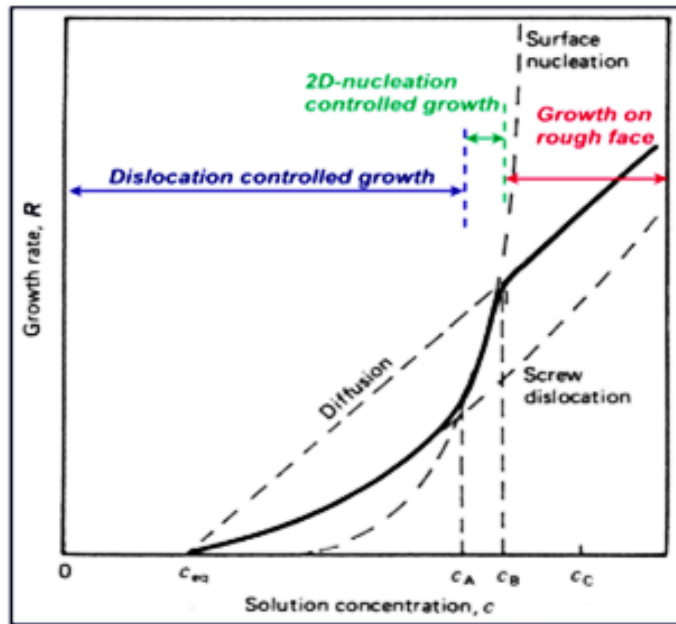
Figure 2.17: Relationship between the 3 interface kinetic mechanisms involved in the growth process – change of growth rates from linear to parabolic as supersaturation decreases (14)

From Figure 2.17 it can be observed that at low supersaturation levels ($<c_A$) the BCF from Equation (2.26) can be rewritten as:

$$R \propto \sigma^2$$

(2.27)

b. **Two-dimensional Birth and Spread (B+S) model**

In this model, crystal growth starts from surface nucleation once the supersaturation is sufficient to form surface nuclei without the need of steps (Figure 2.18). Further surface nuclei will then develop on the monolayer nuclei as they spread across the crystal face. Therefore, a 2D nucleus will appear on the surface of the crystal and then spread out with resultant growth normal to the crystal face.
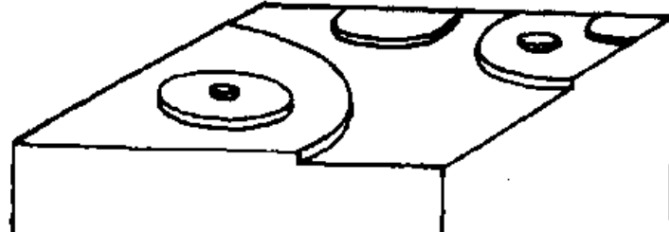
Figure 2.18: Two dimensional growth of surface with nucleation taking place at the edges or corners of the crystal face (14)

Each new layer will be dependent on the formation of a nucleus on the crystal surface which is therefore the rate-limiting step. When more than one nucleus is formed on a layer that is still spreading out, growth is referred to as polynuclear. Such growth usually occurs at moderate supersaturation levels and the growth rate R_{B+S} can be expressed as:

$$R_{B+S} = A_1\sigma^{5/6}\exp\left(\frac{A_2}{\sigma}\right)$$

(2.28)

where A_1 and A_2 are system-related constants.

c. **Rough interface surface (RIG) Model or continuous growth**

This mechanism describes the growth of faces at very high supersaturation region, where the growth units attach anywhere on the crystal surface (terraces, steps or kinks) making the crystal surface rough (Figure 2.19).
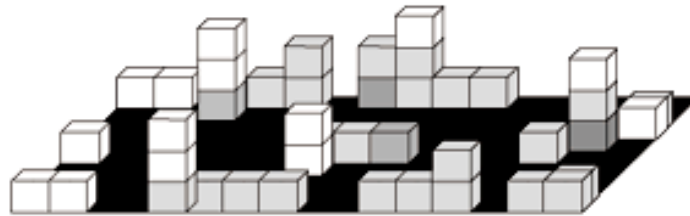
Figure 2.19: Schematic of growth mechanism of a rough surface crystal (14)

This growth mechanism typically produces spherulitic or dendritic crystals and can be expressed by:

$$R \propto \sigma$$

(2.29)

2.5.5 Crystal Agglomeration and Breakage

Agglomeration is the process in which individual particles are put together, probably by chemical forces and inter particle collisions, forming an assemblage of particles that lead to a bigger volume (Figure 2.20) (81) (82). The collision mechanisms involved will depend on the size of the crystals involved, their inter-particle interactions, electrostatic and repulsive forces. Supersaturation is the driving force

for agglomeration. However, the shear rate in a crystallising solution will determine the rate of collisions and therefore aggregation. If shear rate becomes too high, aggregates are disrupted before sufficient cementation can take place (83).
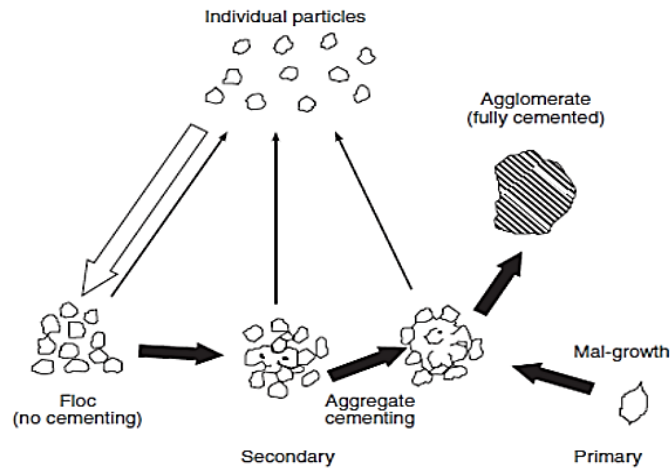
Figure 2.20: Mechanisms for particle agglomeration (14)

Similar to attrition, particle breakage can result from crystal-crystal collisions, crystal-pumps and wall-vessels. Breakage involves the fracture of a single particle into smaller fragments (reverse of agglomeration). But to accomplish total particle fracture, it needs more energy than that needed for attrition (75) (83).

2.6 Closing Remarks

This chapter reviewed and discussed several fundamental theories within crystallisation processes, including some basic crystallography, crystal chemistry and orientation, nucleation and growth stages with the emphasis on the influence of crystallisation conditions on crystal growth mechanisms, size and morphologies. All of the reviewed background provides the foundation for the study and understanding of $CaCO_3$ crystallisation processes which will be detailed in the results and discussion chapters (i.e., 6 and 7). Lastly, this chapter has elucidated the importance of crystal science and engineering to control and predict final crystals properties from a very early stage of crystallisation. Thus, the interrelation among crystal's structure, properties, performance and processing conditions is achieved by controlling the crystallisation process.

Chapter 3 - Mineral Scale Theory & Literature Review

Summary

This chapter provides the relevant background theory and literature review on mineral scale with particular focus on calcium carbonate crystallisation in the oil and gas industry. The literature reviewed covers aspects such as the solution chemistry, thermodynamics, kinetics, mechanisms, morphology and other factors which influence the crystallisation process.

3.1 Introduction

Calcium carbonate has been extensively studied in mineralogy (14) (84) (59) (85) (86) (87) and biomineralization (79) (88) (89) (90) (91) (92) (93) sectors. However, given the complexity of the $CaCO_3$ system, there are still uncertainties related to its formation (94), transformation mechanisms (95) (96) and kinetics (97), especially when this mineral precipitates within oil and gas industrial facilities. Hence, there is still a critical need to better understand $CaCO_3$ crystallisation phenomena and surface deposition (adhesion) to improve and optimise the current preventive and remedial industrial techniques, from simulation models to chemical treatments. A clear gap remains in the lack of a scale prediction model that can also provide simulations about the kinetics progression in the field.

The aim of this chapter is to provide background on $CaCO_3$ mineral scale and review the key scientific studies related to $CaCO_3$ crystallisation in bulk solution and at surfaces. A particular focus is given to the interactions of thermodynamic and kinetic aspects during $CaCO_3$ crystallization process. These research objectives come from sub-section 1.2 (Chapter 1) and aim to help understanding the previous science and engineering work done on $CaCO_3$ crystallisation (i.e., nucleation, crystal growth, growth mechanisms, polymorphism, kinetic parameters, properties, etc.). Furthermore, this chapter gives the grounding to create robust experimental methodologies, and to validate scale prediction models (e.g., MultiScale™) by understanding the theory and thermodynamic calculations behind the scale tendency predictions from aqueous water chemistries. Figure 3.1 displays a summary of the scope of this chapter.
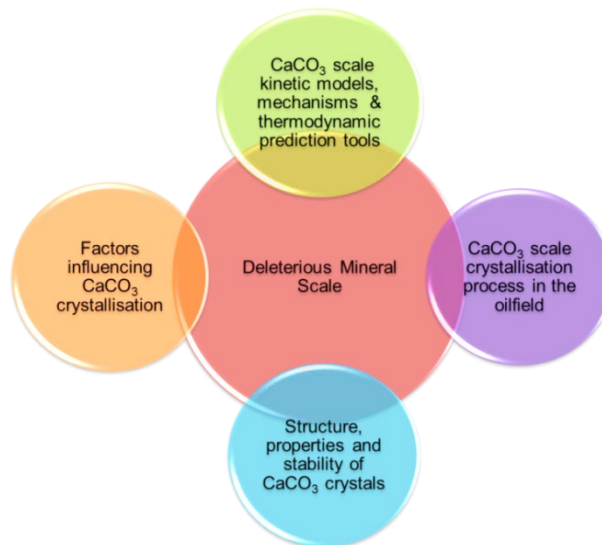
Figure 3.1: A summary of key topics to be reviewed and discussed in this fundamental chapter on $CaCO_3$ mineral scale

3.2 Overview on Deleterious Mineral Scale

Mineral scale is the terminology used for solid compounds that result from precipitation reactions in supersaturated solutions under specific conditions of temperature, pressure, pH and water chemistry (98). Inorganic scale may occur spontaneously in nature or in industry as a consequence of changes in the crystallising solution (i.e., supersaturation) and formation of stable crystal deposits that become insoluble in the mother solution. Typical inorganic scale examples include calcium carbonate ($CaCO_3$), barium sulphate ($BaSO_4$), calcium phosphate ($Ca_3(PO_4)_2$, ferric and aluminium hydroxides ($Fe(OH)_3$) and $Al(OH)_3$ (99).

Calcium carbonate is one the world's most abundant minerals and comprises about 4% of the earth's crust. Given its abundance and properties, it constitutes a popular topic of research. $CaCO_3$ low solubility in water promotes its spontaneous formation in nature (100), such as the limestone caves, in the form of stalagmites and stalactites. Furthermore, $CaCO_3$ can also be formed in unwanted places such as boilers, water taps, washing machines, heat exchangers (fouling) (101), inside oil and gas piping facilities, valves, water membranes (102), as shown in Figure 3.2.
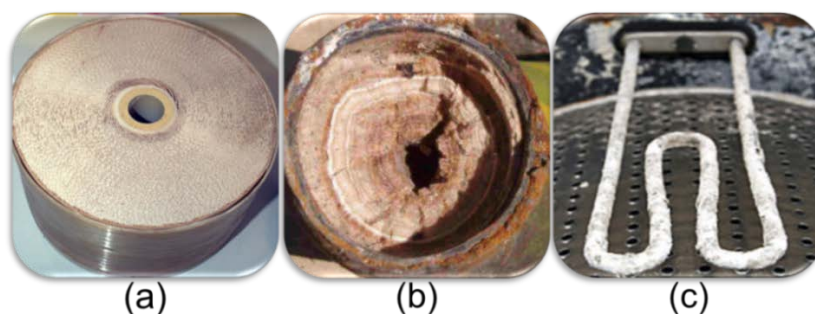
Figure 3.2: Examples of deleterious scale formed in different sectors: (a) – Water industry (e.g., membrane filter) (103) (104), (b) – Petroleum industry (e.g., scaled and corroded pipe) (105); (c) – Domestic industry (e.g., heat exchanger of a washing machine) (106) (107)

There is a global high demand for process optimisation to prevent scale formation in different industrial sectors, especially in the water treatment and oil and gas industries. This is generally due to the flow blockage issues which then lead to higher energy consumption, higher maintenance requirements, reduction of the production capacity and shorter lifetime of the process installation facilities.

In the oilfield, mineral scales can be found in both production and injection wells from down-hole to topside equipment facilities during the process of oil and gas extraction. Thus, the need for investigating the science underpinning $CaCO_3$ crystallization in

order to create scale prediction models based on both thermodynamic and kinetic components.

3.3 Calcium Carbonate Crystallisation in the Oilfield

During oil and gas exploration and transportation, calcium carbonate scale can be formed depending on factors such as supersaturation (i.e. brine's concentration), temperature, pressure, flow rate, metallic substrates and impurities (complex systems saturated with ions, oil and sand). Subsequently, $CaCO_3$ scale can form, grow and adhere to the walls of the pipelines blocking the fluid motions (Figure 3.3).

Figure 3.3: Calcium carbonate deposits in oil and gas pipes – Sample provided by private communication with BP, Sunbury, UK.

For the scale formation in the oilfield environment, water is the key parameter since it is a good solvent which can carry numerous ionic species of the scaling minerals which can crystallise once optimal conditions are provided. The identification of mineral scale deposition or location and composition is very important for the design of a cost effective remediation programme.

The main scale-related challenges encountered in the oilfield are due to long and narrow sub-sea wells, high pressure valves, temperature variance, pumps transportation of natural gas and condensate from offshore facilities and supersaturation of multiphase fluids. Subsequently, the main mechanisms involved for inorganic scale formation in the oilfield are schematized in Figure 3.4 and can be due to (8) (10) (108):

- Pressure reduction and/or increase in temperature in the formation brine at well bores, causing liberation of CO_2 gas and reduction of the solubility of $CaCO_3$ scale.

- Mixing of incompatible waters (high sulphate waters such as seawater or flooding water system mixed with brines containing high concentrations of divalent sulphate cations of (Ca^{2+}, Ba^{2+}, and Sr^{2+}) in the reservoir formation water. Typically sulphate scales such as $BaSO_4$ are formed under these conditions.

- Brine evaporation leading to an increase in salt concentration above the solubility limit. This causes salt precipitation due to possible high pressure and temperature conditions (HP/HT) in the gas wells where a dry gas stream may mix with a low rate brine stream provoking dehydration and most frequently precipitation of salts (e.g., NaCl).

- Temperature fluctuations through the flow system which will serve as a driving force for scale precipitation to occur in that environment.
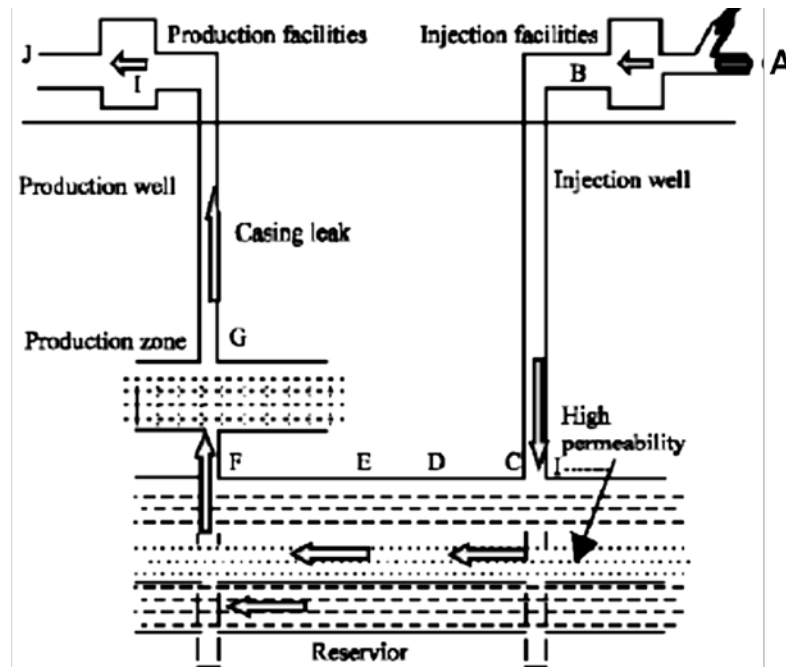
Figure 3.4: Schematic representation of areas (A – J) likely for inorganic scale formation within oil and gas production (10)

Overall, the diagram in Figure 3.4 illustrates that changes in pressure and temperature from the surface to the reservoir, will increase the likelihood of inorganic scale formation, which may deposit and block the tubing facilities in the oil and gas production installations (10) (109).

3.4 Calcium Carbonate Reactive Crystallisation Process

Calcium carbonate crystallization process takes place when a system has reached some level of supersaturation and is initially indicated by nucleation then followed by growth and subsequent agglomeration. External factors such as temperature, pressure and pH can trigger the start of precipitation and control the extent of the reaction kinetics.

The pH plays a critical role in carbonate scale crystallisation, as it can be related to the partial carbon dioxide pressure which is dependent on the concentration levels of carbonic acid. Hence, the carbonic system existing in aqueous solution comprises of different chemical forms, which are: dissolved carbon dioxide (CO_2), carbonic acid (H_2CO_3), bicarbonate ions (HCO_3^-), carbonate ions (CO_3^{2-}) and calcium carbonate ($CaCO_3$) [110] [111] [112]. The precipitation reaction will be triggered upon dissolution of carbon dioxide in water at specific conditions of pressure and temperature, favourable to the formation of mineral $CaCO_3$ [110]. The chemical reaction crystallisation process of $CaCO_3$ can be summarised by the following equations [110]:

$$CO_{2(g)} = CO_{2(aq.)} \tag{3.1}$$

$$CO_{2(aq.)} + H_2O_{(l)} \leftrightarrow H_2CO_{3\ (aq.)} \tag{3.2}$$

$$H_2CO_{3\ (aq.)} \leftrightarrow HCO_{3(aq.)}^- + H_{(g)}^+ \tag{3.3}$$

$$HCO_{3(aq.)}^- \leftrightarrow H_{(g)}^+ + CO_{3(aq.)}^{2-} \tag{3.4}$$

$$Ca_{(aq.)}^{2+} + CO_{3\ (aq.)}^{2-} \leftrightarrow CaCO_{3(s)} \tag{3.5}$$
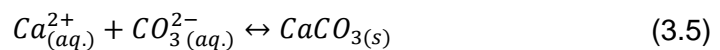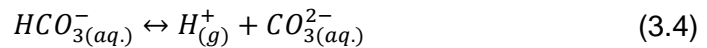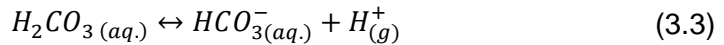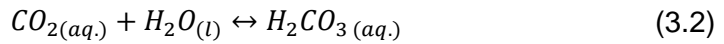
The CO_2 equilibrium constants at 25°C have been determined for the $CaCO_3$ spontaneous crystallization process in closed system and can be seen in Table 3.1.

Table 3.1: Calcium carbonate – CO_2 equilibrium reactions at 25°C

Equilibrium reaction	Constant, K	Reference
$H_2O \leftrightarrow H^+ + OH^-$	1.01×10^{-14}	[113]
$H^+ + HCO_3^- \leftrightarrow H_2CO_3$	2.25×10^6	[114]
$H^+ + CO_3^{2-} \leftrightarrow HCO_3^-$	2.13×10	[115]
$Ca^{2+} + CO_3^{2-} \leftrightarrow CaCO_{3\ (s)}$	1.41×10^3	[115]
$Ca^{2+} + HCO_3^- \leftrightarrow$ CaHCO$_3^+$	10.00	[115]
$Ca^{2+} + OH^- \leftrightarrow CaOH^+$	19.95	[115]

$H_2O + CO_2 \leftrightarrow H_2CO_3$	3.39×10^{-2}	(115)

Figure 3.5 illustrates the dependency of $CaCO_3$ crystallisation in CO_2 dissolution process into water.
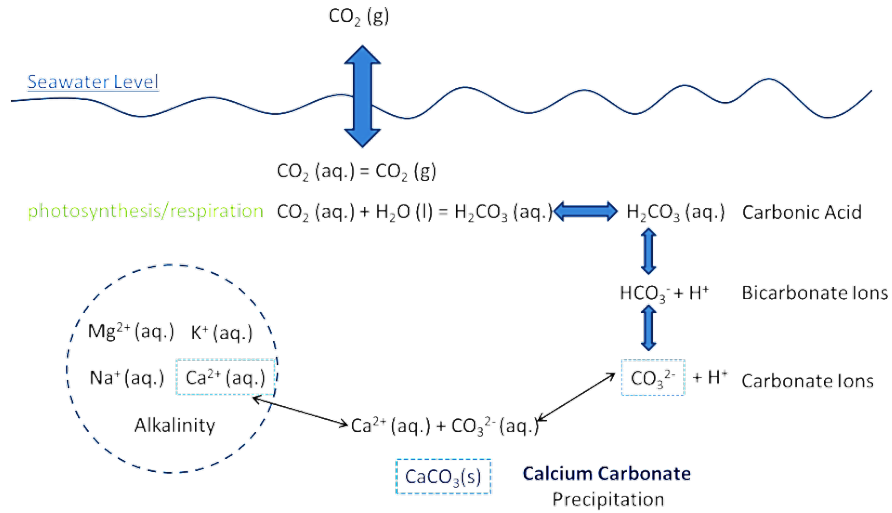
Figure 3.5: Schematic illustrations of the seawater carbonate equilibrium and its response to increased atmospheric CO_2 (116)

Figure 3.5 emphasises the fact that seawater chemistry at the surface of an ocean can change in response to an increase in atmospheric CO_2 gas, leading to $CaCO_3$ precipitation when the system is saturated with ions such as calcium from sedimentary rocks (117). Furthermore, the carbonate ion concentration can usually be approximated to the total alkalinity (A_T) when considering an open system as the main contribution to alkalinity depends on the CO_2 levels (116) (118). This is not the case when some strong organic acids are present in the solution, for example when these are added during the water injection stage to the oilfield facilities. This helps understanding that any losses of CO_2 to the atmosphere can also lead to an increase in pH (as less carbonic acid is produced) (119) and subsequently this will affect the solubility of calcium carbonate, i.e. it becomes less soluble (120). Furthermore, the state of CO_2 is highly dependent on temperature and pressure conditions (121).

3.5 Structure, Properties and Stability of Calcium Carbonate

3.5.1 Polymorphism

Calcium carbonate precipitates in six distinct solid phases (93), three anhydrous crystal modifications, vaterite, aragonite, calcite and one amorphous hydrated form

amorphous calcium carbonate (ACC). The other two additional forms are calcium carbonate monohydrate and hexahydrate (i.e. ikaite).

Calcite is generally regarded as the thermodynamically stable polymorph (122), but it will only be obtained directly at relatively low supersaturation. With a low solubility salt like calcium carbonate metastable phases or precursors are easily formed. The metastable phases (123) are kinetically favoured when two relatively concentrated solutions of calcium and carbonate ions are mixed (124) (125) . This often results in a mixture of polymorphs. The variation in polymorphic abundance is a result of supersaturation and/or impurities content leading to differences in growth and nucleation rates of the different polymorphs at varying conditions. Difference in solubility will cause the precursors species to dissolve, and eventually the precipitate stabilises as calcite. Table 3.2 shows the solubility products of different forms of calcium carbonate.

Table 3.2: Solubility products of $CaCO_3$ at 25°C

Polymorph	K_{sp} [M^2]	Reference
ACC	9.1×10^{-7}	Clarkson et al. (1992) (123)
	4.0×10^{-7}	Brecevic and Nielsen (1989) (126)
Vaterite	1.22×10^{-8}	Plummer and Busenberg (1982) (115)
Aragonite	1.68×10^{-9}	Nancollas and Sawada (1982) (127)
Calcite	1.29×10^{-9}	Nancollas and Sawada (1982) (127)

Previous studies (115) (128) (129) have shown that $CaCO_3$ polymorphs are strongly dependent of factors (130) such as temperature, pH, pressure, ion concentration and presence of impurities. However, temperature plays a critical role in the formation of calcium carbonate in oil and gas production systems, as it can vary strongly throughout the system. Figure 3.6 illustrates the relationship between $CaCO_3$ anhydrous polymorphs and temperature. In general, it is observed that an increase in temperature leads to a decrease in $CaCO_3$ solubility, thus more calcium carbonate scale tends to precipitate in the bulk (131) (132).

In addition, the diagram from Figure 3.6 also shows that vaterite is the least thermodynamically stable form, because it has a higher solubility than both aragonite and calcite (131). Aragonite, as the metastable form tends to be more thermodynamically stable at high temperature (131). Finally, calcite is the most thermodynamically stable at room temperature, hence it is the most common polymorph found from bulk precipitation reactions.
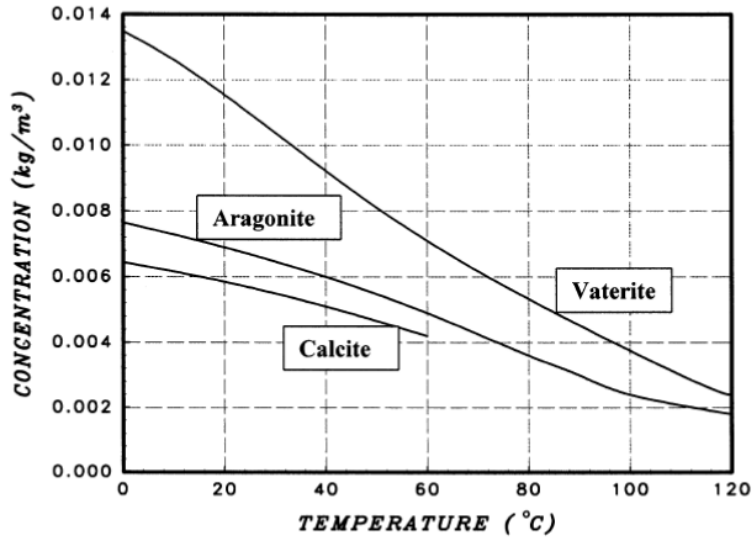
Figure 3.6: Solubility of $CaCO_3$ according to temperature (131)

Other studies (133) have also shown the temperature dependence on the polymorphic composition of calcite, vaterite and aragonite precipitated at the same supersaturation, as shown in Figure 3.7 (133).
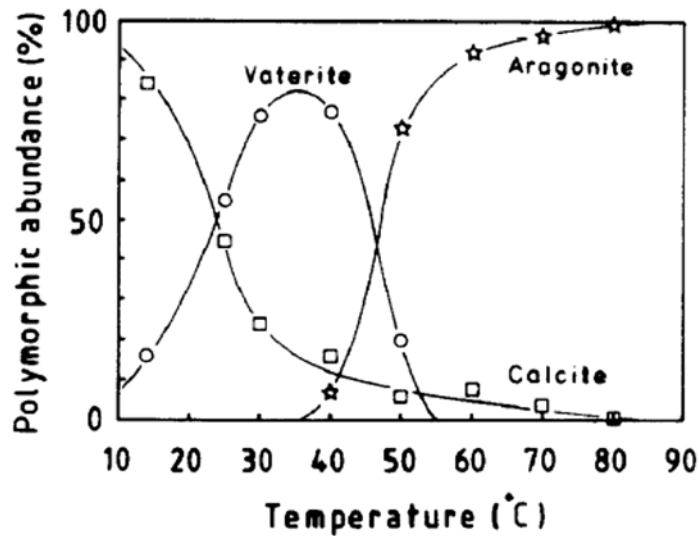
Figure 3.7: Abundance of $CaCO_3$ crystalline polymorphs at early metastable stages of precipitation (133)

Results suggested that during spontaneous crystallisation of $CaCO_3$, vaterite crystals tend to form at high levels of supersaturation at temperature range between 30°C and 70°C, when their ionic activity product (IAP) exceeds the solubility of this polymorph or transforms from the amorphous phase to a higher solubility phase such as calcite (133). On the other hand, aragonite crystals tend to precipitate directly in the bulk of solution or transform from the vaterite or calcite crystal phases (134) (135) (136) (137).

44

To summarise, crystallization studies (127) (138) (139) have shown similarities in the nucleation process of all $CaCO_3$ phases, at early stages of supersaturation. However, changes in morphology are also attributed to temperature and stirring conditions. It is worth noting that the potential solid-phase-transition mechanisms were excluded, and most authors concluded on a dissolution and re-crystallization process which induces phase transformation. Additionally, the nucleation process assumed this dissolution hypothesis and was also confirmed by Kralj et al., (140) in their study of vaterite transformation.

3.5.2 Physico – Chemical Characteristics

Among the anhydrous forms of $CaCO_3$, three different polymorphs can be distinguished: vaterite (unstable), aragonite (metastable) and calcite (stable), as seen in Figure 3.8.
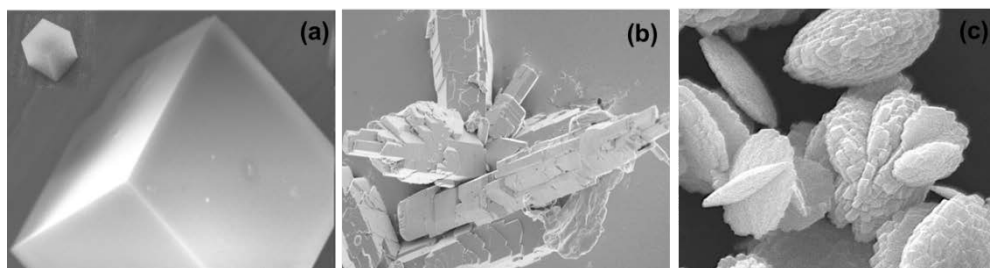
Figure 3.8: Calcium carbonate anhydrous polymorphs: (a) calcite (b) aragonite (c) vaterite

These different polymorphs can appear simultaneously depending on their crystallising conditions. They will exhibit the same chemical components (i.e. $CaCO_3$) but display different internal molecular arrangements which are reflected in their final morphologies. Since the intermolecular bonding between calcium ions (Ca^{2+}) and the carbonate group (CO_3^{2-}) varies from one polymorph to another (141), $CaCO_3$ polymorphs will have different physicochemical and mechanical properties. Vaterite crystals exhibit a hexagonal structure that typically results in spherical polycrystalline particles (142) with flower-like or spherulitic shapes. Aragonite crystals have an orthorhombic structure, often found as needle-like or prism-like particles and calcite has a trigonal-hexagonal structure which crystallises as rhombohedral particles. Table 3.3 summarises the physical properties of these polymorphs.

Table 3.3: Crystallographic properties of $CaCO_3$ polymorphs (143)

Parameters	Calcite	Aragonite	Vaterite
Crystal System	Trigonal – Hexagonal	Orthorhombic	Hexagonal
Unit Cell Parameters (Å/°)	**a** = **b** = 4.99, **c** = 17.06	**a** = 4.96, **b** = 7.97, **c** = 5.74	**a** = **b** = 7.14, **c** = 16.98
Cell Space Group	$R\overline{3}C$	Pmcn	$P6_3/mmc$
Morphology	Rhombohedral	Needle like	Spherical/Disc like
Density (g/cm³)	2.71	2.93	2.66
Hardness	3	3.5 - 4	3
Refractive Index	1.66	1.70	1.65
Thermodynamic Stability	Stable	Metastable	Unstable
Molar Weight (g/mol)	100.089	100.089	100.089

3.5.3 Crystallisation Pathways and Thermodynamic Stability

According to the Ostwald-Lussac rule of stages, a solution is supersaturated with respect to more than one phase, and the more soluble phase (i.e. least stable) is the first to appear. Then, given sufficient time and energy to the system, the more thermodynamically stable state is reached and therefore, products should ultimately transform into the lower energy level (123). This theory helps in explaining the existence of polymorphisms and their physical chemical differences. Figure 3.9 displays $CaCO_3$ crystallization pathways, where these are kinetically driven and depend on the relative heights of energy barriers between each of the metastable states (144).
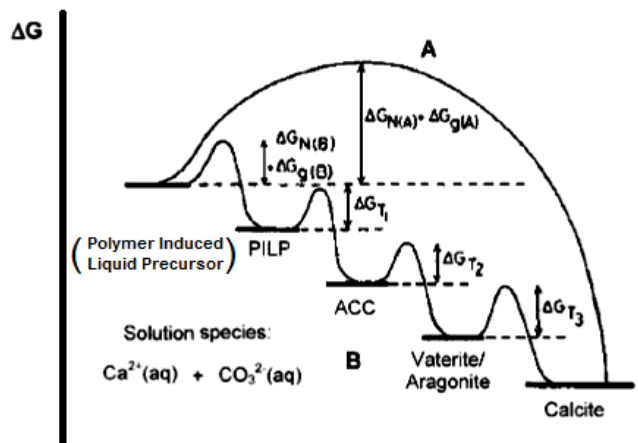
Figure 3.9: Stages of $CaCO_3$ transformation via pathways of lowering Gibbs free energy (144)

In Figure 3.9, pathway (A) refers to the crystallization from the solution without having to pass through any intermediate phase (s) that needs subsequent structural

changes. On the other hand, pathway (B) considers the crystallization from different metastable phases of different crystal structures or even from the amorphous phase (144). As an example, calcite is $CaCO_3$ most thermodynamically stable phase, so during its crystallisation it can be preceded by the less stable phases due to their lower energy barriers, which could be vaterite or aragonite or even unstable ACC under high supersaturation conditions. The ACC phase has a less organised structure and this suggests being the less dense phase, thus with the lowest surface energy (144).

Overall, these theories have shown that polymorphic evolution is related to the phase's stability. However, there are questions remaining that ACC can be a precursor of crystalline anhydrous forms such as vaterite or calcite. The classical approach does not consider the evolution from a non-crystalline form into a crystalline form.

3.6 Factors Influencing Calcium Carbonate Crystallisation

3.6.1 Supersaturation and Solubility

Calcium carbonate supersaturation can be expressed in terms of saturation ratio (SR or S), as shown in the following equation:

$$S_{CaCO_3} = \sqrt{\frac{(a_{Ca^{2+}} \times a_{CO_3^{2-}})}{K_{sp,CaCO_3}}} \tag{3.6}$$

where a_{Ca}^{2+} is the activity coefficient of calcium ions and a_{CO3}^{2-} is the activity coefficient of bicarbonate ions; K_{sp} is the thermodynamic solubility product (dependant on pressure and temperature).

The activity coefficients of z-valent ions can be determined by the modified Debye-Hückel equation proposed by Davies (145):

$$a_i = (f_i \times C_i) \tag{3.7}$$

where, f_i is the ionic activity coefficient, and C_i the concentration of the ions in the solution.

$$log f_i = \left(\frac{AZ^2\sqrt{I}}{1+\sqrt{I}}\right) + 0.1\,Z^2 I \tag{3.8}$$

where, *A* corresponds to the Debye-Hückel constant (which is temperature dependent and equivalent to 0.521 at 25 °C), *Z* is the charge of the ions in solution and *I* is the ionic strength calculated from Equation (3.9), where C_i corresponds to the concentration of species *i,* (146):

$$I = \frac{1}{2} \sum C_i Z_i^2 \qquad (3.9)$$

By assuming the same effect of solvent (i.e. water) on solubility of all polymorphs (147) (148) and considering that both calcium and carbonate activities are independent of the precipitating polymorphs, the supersaturation for vaterite (*vat.*) and aragonite (*arag.*) can be expressed as a function of calcite (*cal.*) supersaturation (149):

$$S_{Vaterite} = \sqrt{\frac{K_{sp,calcite}}{K_{sp,vaterite}}} \times S_{calcite} \qquad (3.10)$$

$$S_{Aragonite} = \sqrt{\frac{K_{sp,calcite}}{K_{sp,aragonite}}} \times S_{calcite} \qquad (3.11)$$

where, $S_{vaterite}$ *and* $S_{aragonite}$ corresponds to the saturation ratio of vaterite and aragonite, $K_{sp,calcite}$ is the solubility product constant of calcite and $K_{sp,vaterite}$ and $K_{sp,aragonite}$ represent the solubility product constant for vaterite or aragonite, and $S_{calcite}$ is the saturation ratio of calcite.

The solubility product constants of $CaCO_3$ polymorphs at a wide range of temperatures have been previously studied by Plummer and Busenberg (115) as shown in Table 3.2. On the other hand, the total alkalinity of the solution (i.e. sum of all ions in solution that may affect the pH) would strongly depend on bicarbonate concentration, thus an assumption of it being equivalent to twice the calcium concentration (i.e. 2 $[Ca^{2+}]$) has been considered for assessing the de-supersaturation process during calcium carbonate crystallization. This approach is shown by Equation (3.12) and was previously demonstrated in Ellen's studies (149):

$$Alk_i = Alk_o - 2 \times \left[Ca_o^{2+} - Ca_i^{2+} \right] \qquad (3.12)$$

Where Alk_i corresponds to the final alkalinity of the system. Alk_o is the initial alkalinity of the system and $[Ca^{2+}]_o$ is the initial calcium content and $[Ca^{2+}]_i$ is the final calcium ion content. Equation (3.12) shows that any decrease in calcium will correspond to a decrease in carbonate ions.

3.6.1.1 Growth mechanisms as a function of supersaturation

The impact of supersaturation in nucleation and crystal growth process for calcium carbonate has been previously highlighted (150) . Studies by Teng et al., (79) have shown the impact of supersaturation during calcite growth. In their work, an atomic force microscope (AFM) was used to show the growth mechanisms involved during calcite formation in bulk at low and high supersaturation levels. As shown in Figure

3.10, calcite growth was initiated by dislocations and when increasing the supersaturation it could be observed a transition from spiral to 2D surface nucleation mechanism.
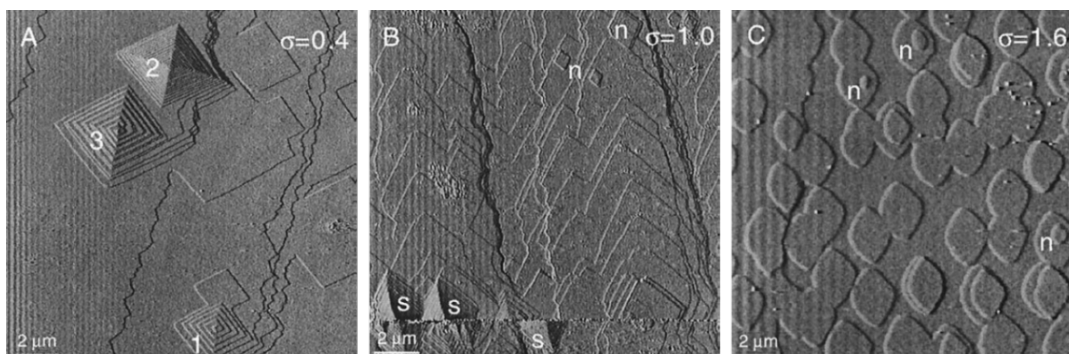
Figure 3.10: AFM images of calcite growth on a {104} face at a) low supersaturation (σ=0.4), b) high supersaturation (σ=1) and c) higher supersaturation (σ=1.6) (79)

Figure 3.10 illustrates the different growth mechanisms at different saturation levels for calcite {104} face. At low supersaturation, σ=0.4, the main growth mechanism is spiral. As the supersaturation increases to σ=1, there is co-existence of spiral (denoted by *s*) and homogenous surface nucleation growth (denoted by *n*). Finally, at highest supersaturation, σ=1.6, the only dominant growth mechanism is 2D surface nucleation.

Further studies (151) done on calcite using a scanning force microscope (SFM) have also shown a relationship between supersaturation and growth mechanisms. Observations from this work have found that when saturation with respect to calcite is greater than 1 or 2, the initial growth mechanism is by surface nucleation and then spiral growth was also observed.

Experiments by Turner and Smith (152) have shown that for the same heat exchanger temperature it is possible to obtain calcite and aragonite crystals simultaneously. However, results at higher supersaturation (σ=12 – higher temperature) showed that mostly aragonite tends to form, whilst calcite could also be found at lower supersaturation (σ=9.8 – lower temperature) as shown in Figure 3.11.
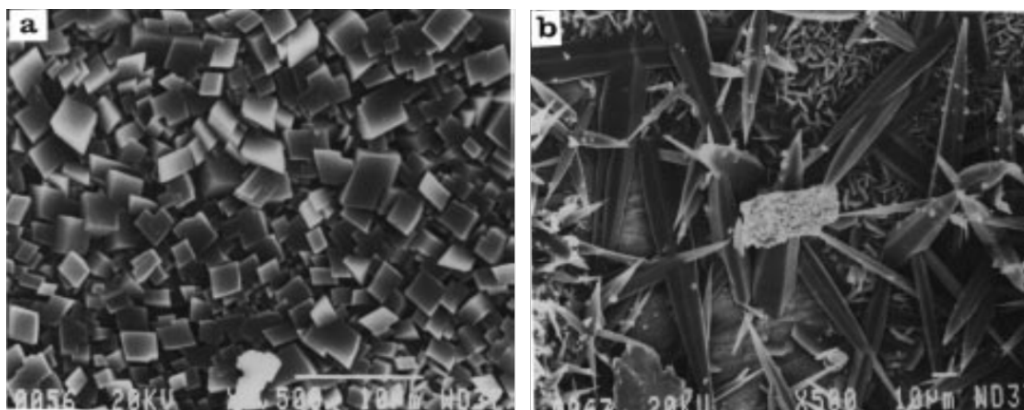
Figure 3.11: SEM micrographs of calcium carbonate precipitated as a) calcite at supersaturation of σ=9.8 and b) as aragonite at supersaturation of σ=12 (152)

$CaCO_3$ supersaturation is temperature dependant and subsequently this affects the mechanisms of scale formation and the final crystal appearance.

3.6.2 Temperature

Temperature is one of the prime parameters influencing crystallization of calcium carbonate, as it controls the supersaturation and thus formation and transformation stages. Han et al. (153) prepared calcium carbonate at 25°C and 60°C and showed that for the high temperature tested, only aragonite was formed. At low temperature the deposit was composed of calcite and vaterite. Kitamura (96) obtained similar results for an identical temperature range (25°C and 50°C). Kitamura used a combination of Brecevic and Nielsen's (154) study for determining solubility of ACC. This crystallization process involved three main steps: the formation of a precursor known as ACC, its dissolution and the formation of calcite and vaterite, followed later by the transformation into the most stable form calcite. Yu et al., (155) also found that temperature alters crystal solubility, however this effect was observed for the calcite and not the amorphous form. These studies (155) showed also the impact of temperature on the crystal particle size. So, at 25°C crystal particles ranged between ± 6 – ± 12 µm, whereas at 80°C, the crystal particles were slightly smaller, varying from ± 4 – ±10 µm. Feng et al., (156) also noticed the significant influence of temperature on the average particles size. However, they reported that their results were different from those in the literature, because of the use of additives in their study, and therefore, the effect of temperature could be different in the presence of additives.

Feng et al. (156) have also observed that as temperature increases, the crystallization process gets faster, emphasising the role of temperature during calcium carbonate crystallization kinetics in solution. Amor et al. (157) showed that

low temperature promotes heterogeneous nucleation whereas high temperature supports homogeneous nucleation.

Lastly, the effect of temperature has also been proved via $CaCO_3$ prediction models. Dyer and Graham (158) used a model to predict supersaturation and confirmed it by experimentation. They showed that the tendency to produce deposit increases with the temperature. It was also noticed that under the conditions applied and at 50°C, no calcium carbonate was formed. The possible explanation for this was that at low temperature, the kinetics is also slow. Additionally, Rukuni et al., (159) have concluded that calcium carbonate solubility increases with decrease in temperature and in pressure.

3.6.3 Partial CO₂ Pressure

During oil and gas extraction processes, pressure varies considerably in the system and could reach up to 100 MPa. Partial CO_2 pressure is intrinsically related to pH environment, and by controlling one the other can be monitored for the process of scaling formation. Studies by Dyer et al., (158) have shown that the effect of pressure for $CaCO_3$ deposition using dynamic tube blocking tests is more relevant at high temperatures. At fixed high temperature (i.e. ≥100°C), it has been observed that scaling tendency increases with decrease in pressure (i.e. from 2000psi to 200psi). This can be related to $CaCO_3$ faster kinetics at high temperature and low pressure leading to quick deposition in the tubing. Figure 3.12 shows different scenarios for $CaCO_3$ deposition at different pressure and temperature regimes
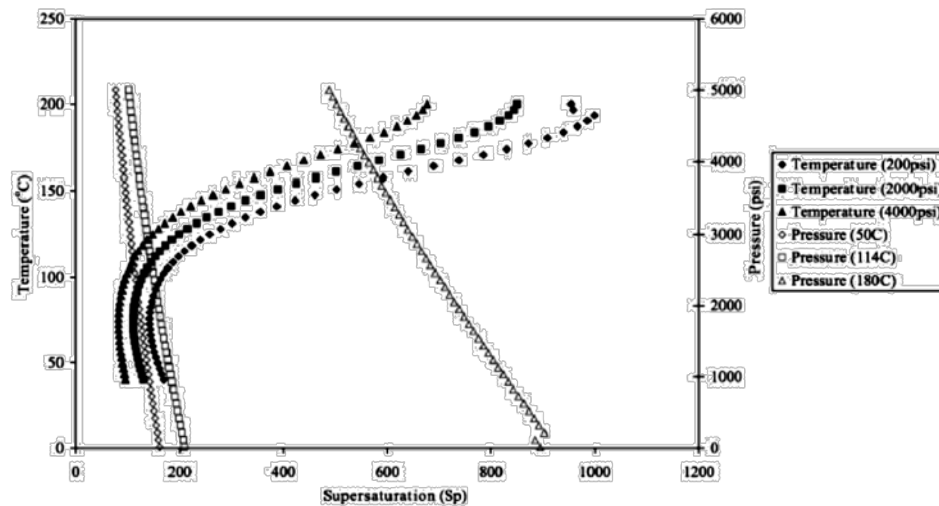
Figure 3.12: Predicted calcium carbonate supersaturation. Open symbols represent the variation in supersaturation with changing pressure at the fixed temperatures (158)

It can be observed that supersaturation levels were similar at 50ºC and 114ºC. Conversely, at 180ºC, supersaturation values decreased with increase in absolute pressure. Another explanation for this can be related to the brine vapour pressure changes with temperature.

3.6.4 pH

The formation of calcium carbonate is controlled by the calco-carbonic equilibrium, which is ruled by the dissolution of carbon dioxide in water, as shown from Equations (3.1) to (3.4) (160). Figure 3.13 illustrates the repartition diagram of the different C-species according to pH in solution (161).
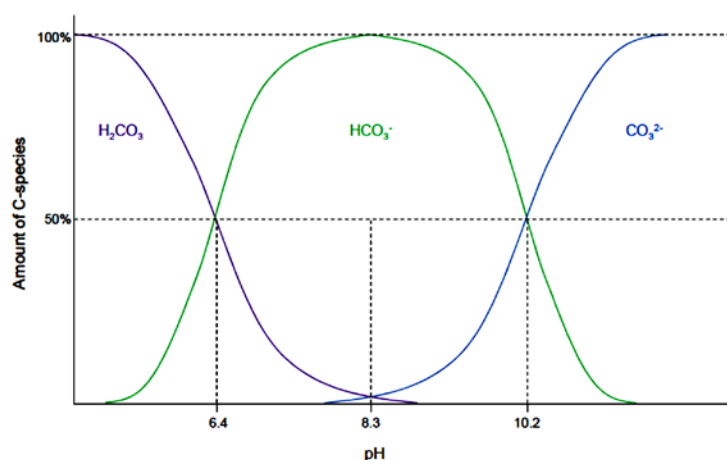
Figure 3.13: Dissolution of carbonic ions as a function of pH

The formation of $CaCO_3$ is favoured at high pH due to the hydrocarbonate – carbonate buffer equilibrium. pH measurements are of extreme importance to understand and follow the crystallization kinetics (162). During crystallization a local accumulation of protons near the crystal surface takes place, and this can be reflected in pH values. This high concentration of protons can produce a proton attack to sites at crystal surface, leading to facial growth. Thus, calcium carbonate precipitation at free pH drift is a result of both crystallization and dissolution processes (75).

Controlling and keeping the pH at low values is one of the methods used in industry for managing $CaCO_3$ scale formation. The pH can also affect the morphology of the $CaCO_3$ crystal as found by Chen et al. (75), the morphology of crystals in presence of polyacrylic acid was affected at pH value of 12 (the same was not observed at pH=9). The particle size seems to be in correlation with the pH: a high pH means a small average size of the particles. At high pH the nucleation rate is increased as the supersaturation increases leading to a change in the morphology of the crystals.

Moreover, the induction time decreases with the increase of the pH as seen with the increase of the supersaturation.

3.6.5 Presence of Impurities or Foreign Ions

The presence of impurities or foreign ions has been broadly investigated (163) (164) (165). Among all ions affecting calcium carbonate formation, magnesium seems to have a great impact on induction times and morphologies (166) (167). It was found that the inhibiting effect of magnesium ions influences the bulk precipitation more than the surface crystallization process (167). Devos et al., (168) also studied calcium carbonate electrodeposition in the presence of magnesium and noticed changes in the crystal morphology, with an increase in magnesium concentration which promoted aragonite. Moreover, at sufficient concentration, magnesium ions seem to inhibit nucleation and growth.

Wada et al., (169) studied the effect of seven divalent cations upon calcium carbonate morphology and kinetics. Most of the ions showed the same influences as those of magnesium, as described previously. According to their results, most of the tested cationic impurities, such as Fe^{2+}, Mg^{2+}, Ni^{2+}, Co^{2+}, Zn^{2+} and Cu^{2+}, promoted aragonite formation whereas Cd^{2+} seems to have no effect. This lead to a hypothetical mechanism which could explain the influence of these ions to $CaCO_3$:

- The incorporation of impurities within $CaCO_3$ crystal lattices would enable morphological changes from early stages of crystallization process (i.e., nucleation). This explains how aragonite precipitated spontaneously in presence of cationic impurities from the bulk solution.

- The adsorption of impurities onto the metastable phase (aragonite) would conversely inhibit its growth. Hence, ions such as Ag^+, Al^{3+} and Cr^{3+} would similarly favour aragonite formation and reduced the crystal growth rate due to adsorption of impurities.

By forming a neutral complex inhibiting the growth of the crystals, it was also recently shown that trace amounts of copper and zinc, when properly applied, could actively inhibit the formation of calcium carbonate. The efficiency of copper was found to be higher than that of zinc.

3.6.6 Effect of Flow Hydrodynamics

Hasson et al., (170) tested the effect of two different flow systems on calcium carbonate formation and its inhibition by additives. One method consisted of a flowing

supersaturated solution dropping as a film on a pipe wall, whereas in the other one, the supersaturated solution was flowing completely through the pipe. Results have shown that both deposition and inhibition mechanisms were different in those two systems and the deposition rate was larger in the film falling system. A possible given explanation suggests that the supersaturation profile in the pipe flow system was uniform whereas in the falling film the profile was sharp. This sharp profile could lead to a very high degree of supersaturation, creating colloids by spontaneous nucleation and then starting to grow by diffusion once reaching the surfaces. Furthermore, Hasson et al., (101), Koutsoukos (171) and Quddus (172) have also investigated the relationship between scale deposition and increase in Reynolds number. For different types of mineral scale it was found that scale deposition rate is linearly dependent on Reynolds number (Figure 3.14), making the whole process diffusion controlled.
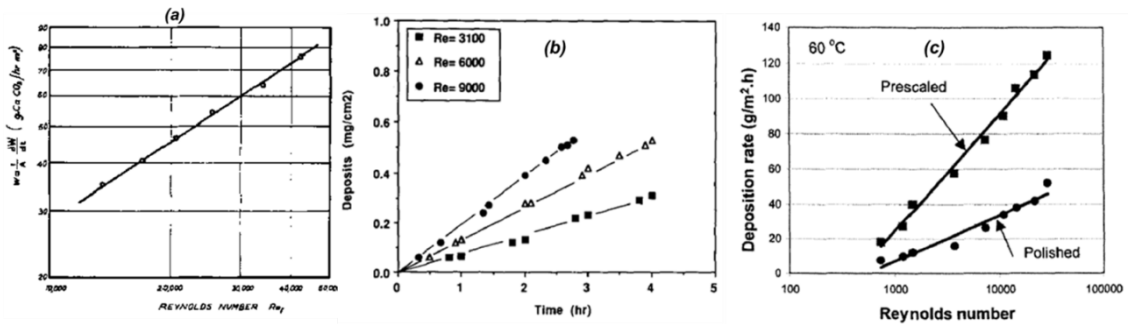
Figure 3.14: Effect of Reynolds number in deposition rates: (a) $CaCO_3$ deposits on heat exchanger (101); (b) PbS deposition rate changes with Re (171); (c) $CaSO_4$ deposition rate in pre-scaled and polished surfaces (172)

Another investigation done by Trippa and Jachuck (173) showed results obtained on $CaCO_3$ crystallization in narrow channel reactors. These studies observed an influence of the flow rate on the precipitating particle's size. Thus, as the flow rate increased, the particle size distribution would decrease and better mixing profiles were attained.

The effect of the flow rate on the morphology and structure of the deposit was analysed by Karabelas (174) whose studies showed that for a fixed temperature and saturation level, a low velocity seemed to promote a non-compact scale deposit. An effect of the flow rate on the morphology of the crystals formed was also observed by Andritsos et al., (175); they observed elongated prismatic calcite due to the flow for a given supersaturation degree.

Regarding fouling rates, it has been found that increasing the flow velocity results in a decrease in induction time and increase in growth rate (176). However, Helalizadeh

et al., (131) noticed contradictions regarding the effect of flow velocities on the fouling rates in heat exchangers for calcium sulphate. They therefore conducted a study to assess the effect of the Reynolds number on the scaling tendency and better understand the mechanism and origin of the contradiction. It appears that crystallization fouling is either reaction-controlled or mass-transfer controlled. These different mechanisms of deposition (reaction-controlled and/or mass-transfer controlled) varied according to the flow velocity (177). Another aspect regarding surface fouling and the effect of flow and hydrodynamic conditions was upon the adhesion of the scale. However, it was the type of the substrates that influenced the adhesion rather than the velocity or shear stresses themselves (178) (179).

3.6.7 Wettability and Contact Angle

Nancollas et al., (180) compared the use of contact angle and wettability measurements for solid-liquid systems, with those typically used during crystallization involving solubility and particle size. Results for the interfacial tension during nucleation stage were of the same order of magnitude, giving reproducibility in values attained from different techniques. Furthermore Bargir et al., (181) have also tested a theoretical approach for determining the interfacial tension and compared it to experimental values from contact angle measurements in stainless steel, gold, aluminium and PTFE (Polytetrafluoroethylene) substrates. The results obtained indicated that adhesion tests can complement the scaling deposition process.

3.6.8 Nature of Crystallising Substrate Material

The nature of the substrates has been shown to influence the amount and kinetics of scale formed on a surface. Lédion et al., (182) tested various types of copper for comparison with polyethylene, stainless steel and tin plated steel. The degrees of supersaturation of the waters used were 1.16 and 1.32 and it was found that the tendency of copper to scale was lower than the others materials studied. The fact that copper ions from the surface are emitted in the water inhibited scale deposition. Indeed, they showed that the concentration of copper ions dissolved in the water has an inhibition effect on calcium carbonate crystallization. However, under different conditions, MacAdam and Parsons (183), who studied the effect of stainless steel, copper and aluminium, found the opposite, as copper scaled the most.

Jahouari et al., (184) used an electrochemical technique based on oxygen reduction to deposit calcium carbonate onto different surfaces: stainless steel, bronze and gold. It was observed that the nature and state of the substrate influenced the deposition

kinetics and therefore the morphology of crystal, as some polymorphs are more stable and need more time to form. Gold appeared to be the fastest to scale followed by bronze and finally stainless steel. According to the authors, oxygen reduction slows down due to a presence of oxides on the surface, leading to scale precipitation blockade. They concluded that the substrate influenced the nucleation rate, gold being the less oxidizable, and consequently the polymorphs formed on it.

Crystallization kinetics is not always affected by the nature of the substrate. According to Ben Amor et al., (185) the influence of the substrate depends on conditions such as water hardness, substrate nature and temperature. It appears that the nature of the surface for hard water and high temperature, does not act on the kinetics itself, but on the type of nucleation. An opposite behaviour has been observed for weak water. They have also noticed that scale is more likely to deposit on a plastic surface rather than on a metallic surface.

3.6.8.1 Effect of surface roughness

As well as the nature of the substrate, its state (i.e., roughness) could also have an effect on scale formation (186). Rankin and Adamson (187) studied the effect of surface types (metallic and organic) and roughness: their influence on crystallization rate, scale characteristics and adhesion strength was assessed. It appears in their study that the adhesion strength was largely influenced by the factors cited above. The explanation given by the authors was related to the surface energy. Scale adhesion occurs on materials with high surface energy. However, the surface energy of a material can vary with the presence of impurities. The actual surface area is larger than the apparent surface area due to roughness. Consequently, according to Rankin and Adamson (187) the adherence was greater on rough material with a high surface energy due to the reasons stated above. A similar conclusion regarding the influence of the substrate state was reached by Keysar et al., (170). Besides the fact that roughness affects the adhesion strength, they noticed that it also affected the deposit porosity. Calcite formed on rough surfaces was significantly less porous than those formed on smooth surfaces. A recent study on roughness was performed by Herz et al., (186) on stainless steel, they also showed that a larger amount and stronger adhesion of the scale were obtained for rough stainless steel. They also noticed shorter induction times for rougher substrates. As surface energy often seems to influence scale deposition, many authors have attempted to modify the surface energy of different types of substrate by using coatings.

3.6.9 Use of Templates

The impact of the surface chemistry and the nano-scale topology on the heterogeneous crystallization has become a matter of great interest (178) because of the behaviour of molecules at the surface, which is crucial for understanding mechanisms involved during nucleation, as well as for prediction of the crystallization outcomes.

Recent studies show that the crystal polymorph or the morphology of the crystal could be changed by modifying the properties of the surface where the process of nucleation begins. For example various ordered surfaces have been examined using a single crystal of gold, or the organic crystal planes (137) (188) (189), polymers (190) (191), Langmuir monolayers (192) (193), as well as SAM (surface assembled monolayers) of the thiol-base molecules (194).

Popescu et al., (195) examined the adaptability of templates for the oriented crystallization of $CaCO_3$. Systems of bis-urea- based surfactants containing amino head group, were used for the preparation of the SAM. It has been shown that the amino acid groups within the SAM can by choice alter the density of the surfactant molecules in the monolayer, influencing the interaction with calcium ions. The control of calcite growth was also well-achieved by the specific growth of crystals through the template and growth-modifying additives (166) (196). The first approach involved the crystallization of calcite on various templates, such as the Langmuir monolayers, the functionalised polymers, the inorganic substrates, the biological macromolecules and the self-assembled monolayers.

Surfaces have also been modified by treatment such as ion implantation or ion sputtering. Zettler et al., (197) changed the surface properties of stainless steel substrates by ion implantation, ion sputtering, carbo-nitrating and coating.

In general, it has been confirmed that modified surfaces having low surface energy can lead to the reduction in scale formation. However, reported studies showed that the scaling behaviour cannot be simply explained by the surface energy, as there are other factors acting simultaneously and results showed inconsistency.

Finally, recent research on the use of biomimetic surfaces (198) has shown the influence of nanostructured surfaces and their potential benefits to reduce scaling. In addition, it was also shown that low roughness, low surface energy surfaces usually perform better in terms of scaling. Research in biofouling appears to have made clear the influence of surface properties for this type of fouling. However, it is still not well

understood what properties of surfaces are dominant in the process of scale formation and adhesion to substrates.

3.6.10 Summary of Factors Influencing CaCO₃ Crystallization

Literature reviewed in this section has shown a vast number of parameters that influence the process of calcium carbonate crystallization either in bulk or on surfaces. By monitoring the temperature, flow hydrodynamics, contact angle, foreign ions and templates, the kinetics involved in scaling crystallization can be accurately predicted and monitored.

Given all concerns and regulations, the petroleum industry has to follow regarding use of chemical inhibitors; template of scale-free surface with a material that can be used in the oilfield can be the next advance in this area. Nonetheless, more research work is needed to ensure the use of similar cost effective metals (i.e. steel) with the advantage of being a scale free surface. Previous work (197) (198) has shown a straightforward response of scale adhesion to substrates, however, the real mechanism behind it still needs to be further understood in order to achieve better control of scale deposition.

3.7 Thermodynamic and Kinetic Scale Prediction Models

There is a strong need for oil and gas industries to have predicting tools for the environment conditions where exploration takes place. So, computer software for simulation approaches have been developed in the past decades in order to give accurate predictions of supersaturation behaviour under certain conditions. Currently, there are three commercially available scale prediction software used by the oil and gas industry: the ScaleSoftPitzer^{TM} (199), the MultiScale^{TM} (147) and OLI ScaleChem© (200). The MultiScale^{TM} has been used as a tool to support this PhD research on CaCO₃ precipitation modelling from producing oilfield wells. In this section, previous and current models are described and reviewed.

Modelling the precipitation of CaCO₃ from an aqueous solution constitutes a complex issue, because of the numerous parameters that must be taken into account for that system in study.

3.7.1 Empirical Saturation Indices Models

The Langelier saturation index was the first built in an attempt to empirically characterize the water chemistry (201) (202). This scale index model was based purely in the difference between the theoretical water pH and the measured pH-value (202). The main drawback of this model consisted of using the same arithmetic value (LSI=2) for both low and high hardness waters, which led to the creation of another empirical model by Ryznar, known as the Ryznar Stability Index (RSI). This new model could merely distinguish the waters with same LSI by using the equilibrium calculated pH (from the alkalinity) instead of the measured pH. It could also consider the buffer capacity of water, which led to better results specifically at higher water harnesses. However, both LSI and RSI were quite simple empirical approaches and can give relatively reliable results of scaling tendency for fairly clean waters.

3.7.2 MultiScale^{TM} – A Scale Tendency Simulator

Recently, much more advanced scale prediction models have been created and are currently commercialised. These models consider a much broader range of parameters that can influence the scale formation tendency. The simulations are able to replicate field conditions for pressure and temperature variances, hydrodynamics, and apply thermodynamic equations for assessing the behaviour of brine solution. Although, mechanisms of scale formation and respective kinetics are not yet considered in those packages, giving uncertainties about the scale prediction kinetics and potential sites to form.

The MultiScale^{TM} prediction tool (Figure 3.14) considers parameters such as pH, fugacity factors, ionic strength, pressure, temperature, flow rate, brine, oil and gas water composition, whilst using thermodynamic and mathematical models with equations such as Henry's law, Pitzer, Debye-Huckel and Soave-Redlich-Kwong (SRK) equations of state (EOS) model (147), in order to determine the scale tendency (ST) of a specific field brine. MultiScale^{TM} generates output calculations in which the thermodynamic driving force for scale precipitation (i.e. supersaturation) is quantified as either a Saturation Ratio (SR) or a Saturation Index (SI). Once determined, these parameters can be analysed to derive an overall estimation of the scaling risk in a particular system. Hence, the amount of scale that can be physically formed is estimated in terms of SR or SI or concentration (mass/volume). Supersaturation values greater than 1 indicate scaling is possible while values smaller than 1 indicate the system is under-saturated. A value of 1 indicates that the brine in study is at

equilibrium. Figure 3.15 illustrates the key parameters included during scale prediction simulations using the MultiScale™ software.
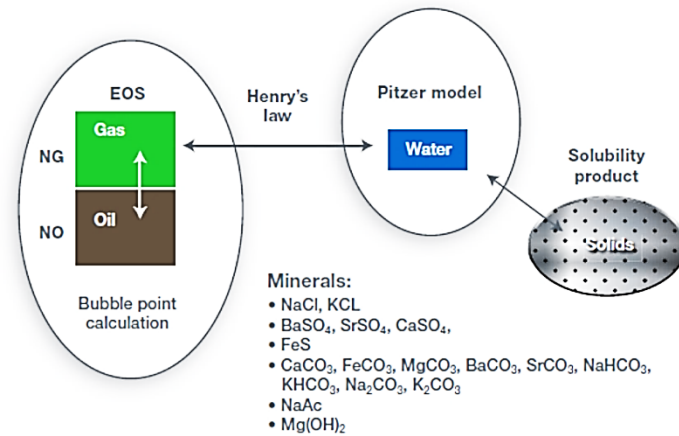
Figure 3.15: MultiScale™ simulation key parameters (147)

During scale prediction modelling, the MultiScale simulator predicts the scaling tendency based on solving a nonlinear system of equations such as:

- Acid equilibrium reactions;
- Mineral precipitation reactions;
- Mass balance equations;
- Charge balance equations

Furthermore, this scale prediction model considers parameters such the system pH, pressure, temperature, alkalinity and salinity which may significantly impact on predictions for $CaCO_3$ scale formation and co-precipitation with other scale types (e.g., $FeCO_3$, $BaSO_4$, FeS, etc) from an aqueous solution.

3.7.3 Review of Experimental Scale Kinetic Models

Current research (203) (204) (205) (206) is still being developed to address uncertainties in creating a universal kinetic model for calcium carbonate. It is strongly believed that a synergetic approach between molecular modelling and experimental work will improve the current knowledge in nucleation kinetics.

$CaCO_3$ crystallization assessment for down-hole scale predictions has been done by Zhang et al., (207) via tube-blocking tests. In this study the deposition kinetics were done ex-situ and the scale film thickness was then correlated to the amount of bulk precipitation. It could be observed that mechanisms and kinetics of scale formation in bulk and surface were different. This model developed by Zhang (207) has also shown similarities with scaling profile measured in the oilfield. Similarly, Morizot et al., (178) (208) showed that precipitation and deposition mechanisms can be

correlated to each other. Results of this study suggested that surface crystals were mainly driven by heterogeneous nucleation at the surface of the metal, leading to smaller particles in surface than in bulk solution. Surface deposition kinetics can subsequently increase if agglomeration from bulk particles takes place by secondary nucleation mechanisms.

Al Nasser et al., (179) noticed this lack of real-time measurements for understanding kinetics and developed a method for assessing crystallization using in-line techniques. They studied $CaCO_3$ kinetics though glass micro models, assessing the changes in particle size as a function of time under several temperatures and ionic strength conditions. The only constrain of this work was that it did not assess the particle size distribution (PSD) in-situ but changes in deposition enabled clarifying the prediction of induction time measurements.

Given the broadness of factors and parameters that can affect nucleation, there is still a lot of research to be done in order to improve current kinetic models. This is where the scope of this study fits in, to add further value for understanding the link between thermodynamics and kinetics and mechanisms of $CaCO_3$ formation in a flowing system within the oil and gas industry.

3.8 Closing Remarks

This chapter started by giving an overview of mineral scale with focus on its deleterious effects on different industrial sectors (e.g., from water treatment to oilfield industries). This PhD research is focused on investigating oilfield $CaCO_3$ scale precipitation and deposition mechanisms and kinetics. Therefore, a detailed literature search has been done covering the fundamentals on calcium carbonate crystallization, including scientific theories on mechanisms of formation, transformation and stability when these crystals precipitate spontaneously in bulk of solutions. Furthermore, the influence of parameters such as the nature of substrates, hydrodynamics, surface roughness and wettability, effect of temperature and pressure, etc has also been investigated, in order to enhance the understanding on $CaCO_3$ kinetic factors and polymorphisms/solubility. The reviewed scientific background was crucial for planning the experimental methodology to be presented in Chapter 5. Lastly, a review of former and current thermodynamic scale prediction models has been done with the ultimate aim of cross relating thermodynamic models with kinetic data on $CaCO_3$ scale. Several thermodynamic models exist based on semi-empirical equation of state models such as the Pitzer, Debye-Huckel and

Soave-Redlich-Kwong. However, these models need to have a link to kinetics and so the MultiScale^{TM} will be used to validate and cross-relate the data gathered from this study. Like many simulation models, assumptions can be made, and it is crucial to understand the basic theory behind the equations applied on MultiScale^{TM}, so the equilibrium state conditions are well interpreted from theory to reality. The use MultiScale^{TM} was relevant to support and assess field case studies for $CaCO_3$ crystallization processes, from experimental and simulation perspectives.

Chapter 4 - Oilfield Corrosion Fundamentals & Literature Review

Summary

This chapter provides relevant theory and a literature review of corrosion processes with particular focus on the oilfield sour corrosion process. It presents aspects of electrochemistry, corrosion mechanisms, types of corrosion products and factors affecting corrosion processes.

4.1 Introduction

Oilfield corrosion poses many consequences such as loss in production time, excessive repair and replacement of equipment costs (e.g., pumps, heat exchangers, valves, etc), environmental damage, health and safety risks, etc, (209). The U.S. oil and gas production industry reported an estimated total annual cost of corrosion of $1.4 billion annually (210). Scale and corrosion are often investigated separately, despite the apparent relationship between their formation mechanisms and kinetic, as often these two phenomena appear in the same field locations.

This chapter (Figure 4.1) provides the basic background on corrosion science, emphasizing the theories behind electrochemical processes and mechanisms, corrosion rate measurements and characterisation of corrosion films. The reviewed fundamentals and synopsis of the relevant literature are going to be useful for the selection of robust methodology and data interpretation when investigating $CaCO_3$ scale and corrosion processes simultaneously. Ultimately, the literature review and theory behind corrosion processes will support the generic goal from section 1.2 of exploring the relationship between the corrosion and scale formation mechanisms and kinetic.
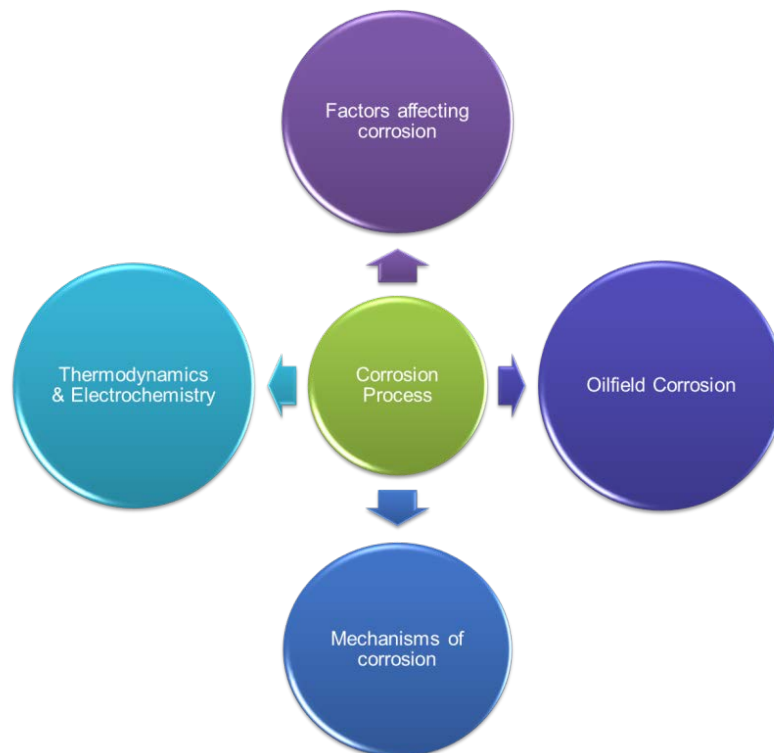
Figure 4.1: Key corrosion process fundamentals and literature review topics to be described in Chapter 4.

4.2 Corrosion Processes

Corrosion is defined as the degradation of materials, usually metals, due to chemical or electrochemical reactions with its environment (211). Deterioration is usually driven by the mechanisms of corrosion which involve the transport of atoms, molecules and ions to the material interface (211). This process cannot be observed on an atomic scale, hence the necessity of applying indirect measurements (e.g., weight loss, corrosion rate) and surface characterisation techniques (product characterisation, identification of pits) in order to understand possible controlling mechanisms to the overall process (212). Electrochemical based corrosion is typically identifiable through the implementation of electrical potential or current measurements, in which simultaneous reduction (cathode) and oxidation (anode) reactions (redox) take place (212) (213). The anode reaction of a corroding metal 'M' can be represented as:

$$M \rightarrow M^{n+} + ne^- \qquad\qquad (4.1)$$

where n is the number of electrons (e⁻) released by the metal. The electrons produced will not flow into the solution but remain on the corroding metal and migrate through the electrolyte solution to the cathode (211) (214). In turn, the cathodic reaction will consume species produced by the anode through absorption to the metal surface.

The equilibrium achieved by these typical redox reactions can be measured by electrical potentials and current flow and will provide the relationship between Gibbs free energy and the corrosion process.

4.2.1 Corrosion on a Steel Surface

Considering a carbon steel or metal surface, there are different regions within the same metal surface that can represent the anodes and cathodes of the electrochemical cell. The iron (Fe) present in the metal surface has a tendency to dissolve into the electrolyte solution as Fe^{2+} ions leaving two electrons behind and giving that area of the metal a small negative charge. This tendency to dissolve Fe^{2+} ions will diminish if nothing happens to remove Fe^{2+} ions around the anodic site. However, in the oilfield facilities, the Fe^{2+} ions are commonly removed by reacting with oxygen (O_2), carbon dioxide (CO_2) or hydrogen sulphide (H_2S). Subsequently, the metal ions combine with other species in the solution forming compounds such as rust (Fe_2O_3), iron carbonate ($FeCO_3$) or iron sulphide (FeS) (188) (215), as illustrated in the diagram from Figure 4.2.
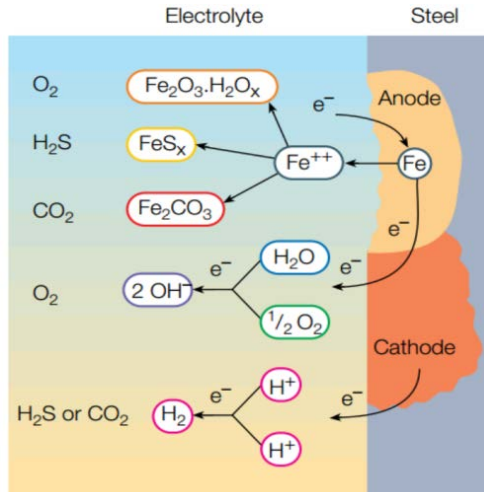
Figure 4.2: Schematic diagram of the corrosion mechanisms on a steel surface
(188)

4.3 Oilfield Corrosion

The problem with oilfield corrosion is predominantly associated with the presence of dissolved acidic gases in the reservoir, CO_2 (sweet corrosion), H_2S (sour corrosion), other associated reservoir constituents and the type of metals selected for the facilities (216) (217).

According to different possible environments encountered within oilfield production facilities, corrosion can occur naturally and be classified as:

- **CO_2 Corrosion** – commonly labelled as *sweet corrosion* this refers to the process manifested in terms of general and/ or localized corrosion (e.g.: pitting corrosion, mesa attack and flow induced corrosion). This kind of destruction is usually related to a wide range of environmental parameters such as temperature, CO_2 partial pressure, fluid hydrodynamics and nature of metallic surfaces, etc (218).

- **H_2S Corrosion** – typically known as *sour corrosion* and refers to the damaging process caused by an enhancement of adsorption of hydrogen atoms into steel pipelines. This creates a strong tendency for sudden local failure due to the formation of pits which then become expansive cracks (localized corrosion) (219) (220). This usually occurs if the piping system is exposed to wet hydrogen sulphide (H_2S) (221).

The consequences of electrochemical corrosion can be severe and vary from a generic loss of metal (i.e. general corrosion) to an embrittlement of the metal and surface cracking. General corrosion is typically the most acceptable among all, as it can be predicted and controlled through use of chemicals or optimum materials selection. When this form takes place the anodic and cathodic areas are continuously changing, which causes all areas to be evenly corroded (211).

Localized corrosion is more serious than the generic one and can lead to early failure. Pitting corrosion can be compared with localized corrosion as it usually occurs as a consequence of a non-homogeneous surface becoming exposed under layers of foreign matter or at breaks within surface coatings. Crevice corrosion is a form of pitting which is typically induced by contact between nuts, bolts or rivets and the normal metal surface (211).

Stress related or cracking corrosion is typically caused by sulphides and can take place in acidic waters with a high content of dissolved CO_2. The dissolved sulphide induces the corrosion cell formation and subsequent production of FeS and hydrogen. Once the hydrogen penetrates the metal surface (i.e. reduction of metal ductility), it creates a high internal pressure at the metal imperfection. Then, hydrogen embrittlement takes place and the metal surface becomes glass-like (brittle) and more vulnerable to cracking (211). Ultimately, there is also corrosion caused by microbial actions but these will not be addressed within this review.

Typically, for a process plant, general corrosion is the main problem (with approximately 25% of the cases), then localised corrosion with approximately 22% of the cases followed by stress corrosion cracking which is often started by pitting and other types (222), as shown in Figure 4.3.
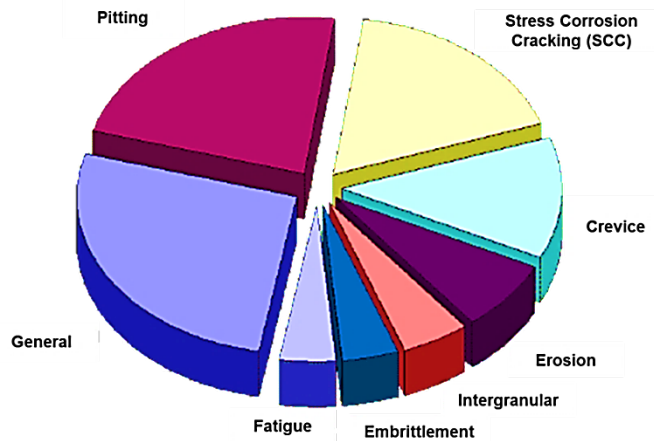
Figure 4.3: Typical distribution of corrosion types for a chemical processing company (222)

General corrosion is often measured by weight loss, electrochemical or non-electrochemical methods. The severity and extent of localised corrosion requires specific tools such as microscopic techniques (223).

4.4 Thermodynamics of Corrosion

4.4.1 Free Energy

Thermodynamics dictates the tendency of a given metal or alloy to corrode in a known environment without giving any information on its rate. Hence, for corrosion to take place spontaneously, the species involved in the reactions must transfer from a high energy state to a lower one (i.e. thermodynamically more stable and favourable) (162).

The Gibbs free energy (ΔG), is the driving force for metallic corrosion and it explains the change in free energy of the metal within its environment (211). If ΔG is negative, it means that there is a greater tendency for the electrochemical reaction to occur, i.e. to corrode spontaneously (162). It has been found that materials with large negative ΔG values are sometimes not accompanied by a large corrosion rate. This is mainly due to the reaction kinetics involved in the corrosion process which will depend on environmental conditions (224). The term ΔG corresponds to the difference between the Gibbs free energies of the final and initial states of the reaction process, disregarding the intermediate stages of the reaction (225).

4.4.2 The Electrochemical Corrosion Cell

Corrosion is an electrochemical process involving the interaction of ions that leads to metal dissolution or surface destruction. Hence, the theory of electrochemistry and electrochemical events needs to be understood to prevent it from happening.

Generally, every electrochemical corrosion cell will have four basic components (211):

- The electrolyte which consists of an electrical conductive fluid in aqueous corrosion.

- The anode electrode, which is the corroding metal (oxidation reaction).

- The cathode electrode, which is the metal in contact with the electrolyte enabling the reduction reaction to take place on the surface.

- The power supply which corresponds to the electrical connection between the anode and cathode, allowing the potential to the electrochemical system for reduction reactions or flow between them.

If any of these components are missing in the cell, electrochemical corrosion will not occur.

There are three main types of electrochemical cells: galvanic, electrolytic and concentration (Figure 4.4).
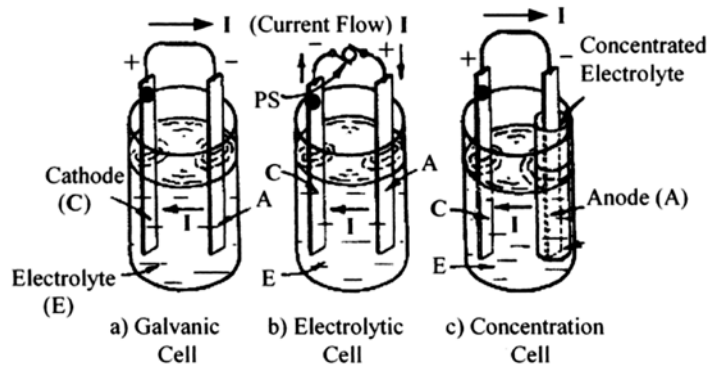
Figure 4.4: Classification of electrochemical cells. PS corresponds to power supply (211)

4.4.3 The Nernst Equation and Cell Potential

In the 19th century, Faraday derived an Equation which shows the relationship between Gibbs free energy change with potential difference and charge transport during the corrosion process:

$$\Delta G = (-nF)E \qquad (4.2)$$

where ΔG is the free energy change for the corrosion reaction in kJmol[-1], *n* is the number of electrons exchanged in the corrosion reaction, F is Faraday's constant (96,494 Coulombs/mole) and E is the potential difference at non-standard conditions in volts.

At ambient conditions of temperature 273.15 K and 1 bar pressure, Equation (4.2) can be rearranged into:

$$\Delta G^o = (-nF)E^o \qquad (4.3)$$

Where ΔG^o is the Gibbs free energy for a range of metals listed on standard half redox reaction tables, E^o is the standard electrochemical potential, F is Faraday's constant (96,494 Coulombs/mole) and *n* the valence number. The addition of (^{o})

guarantees the estimation of values of E° for a range of metals and many other half-cell redox reactions which can be found in electrochemical standard lists (Table 4.1).

Table 4.1: Examples of standard potential for metal reduction (211)

Electrode	Standard Electrode Potential E° (V) (SHE)
$Au^{3+} + 3e^- = Au$	+1.498
$\frac{1}{2}O_2 + 2H^+ + 2e^- = H_2O$	+1.229
$Cu^{2+} + 2e^- = Cu$	+0.337
$2H^+ + 2e^- = H_2$	**0.000 (by definition)**
$Ni^{2+} + 2e^- = Ni$	-0.250
$Fe^{2+} + 2e^- = Fe$	-0.440
$Cr^{3+} + 3e^- = Cr$	-0.744
$Zn^{2+} + 2e^- = Zn$	-0.763

Since corrosion reactions are temperature dependent, the Nernst Equation was derived through combination of Equation (4.3) with Faraday's Law. Thus, under equilibrium conditions the electrical energy and chemical energy are equal and can be summarised by:

$$E = E° - \frac{RT}{nF} \ln \frac{[a_{products}]}{[a_{reactants}]} \qquad (4.4)$$

where E is the potential difference between two half-cells; E° is the standard potential difference across a cell; R is the ideal gas constant (8.134 J.mol^{-1}.K^{-1}), T is temperature (K), F is Faraday's constant and [$a_{products}$], [$a_{reactants}$] are the activity (or concentrations) of all the products and reactants species.

Any electrode potential can provide the difference in potential of a cathodic and anodic cell:

$$E_{cell} = E_{cathodic} - E_{anodic} \qquad (4.5)$$

where E_{cell} is the cell potential in volts, $E_{cathodic}$ is the reduction potential of the cathodic reaction and E_{anodic} is the reduction potential of the anodic reaction.

4.5 Mechanisms of CO$_2$ Corrosion

This research focuses on the CO$_2$ corrosion process. Therefore, understanding the mechanisms involved during the electrochemical interactions with the metal surface is very important.

4.5.1 Cathodic Reactions

The equilibrium between CO_2 molecules in an aqueous environment can be given by:

$$CO_{2(g)} \leftrightarrow CO_{2(aq)} \qquad (4.6)$$

Since CO_2 is soluble in water, its presence in aqueous solution will enhance the electrochemical reaction, therefore increasing the corrosion rate of iron. This occurs because dissolved CO_2 in water, promotes the formation of a weak acid, the carbonic acid (H_2CO_3):

$$CO_{2(g)} + H_2O_{(l)} \leftrightarrow H_2CO_{3(aq)} \qquad (4.7)$$
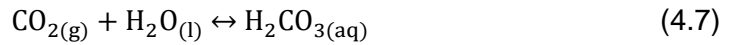
Then, H_2CO_3 partially dissociates in two reaction steps forming bicarbonate and carbonate ions respectively:

$$H_2CO_3 \leftrightarrow H^+ + HCO_3^- \qquad (4.8)$$

$$HCO_3^- \leftrightarrow H^+ + CO_3^{2-} \qquad (4.9)$$

This process is then followed by hydrogen evolution:

$$2H^+ + 2e^- \leftrightarrow H_2 \qquad (4.10)$$
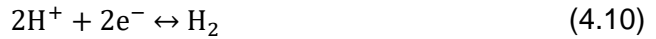
Both homogenous dissociation reactions (4.8) and (4.9) are much faster than other reactions (4.6) and (4.7) for carbonic acid formation. Thus, the hydrogen evolution reaction (4.10) is believed to be the main cathodic reaction, whose rate is dependent on the H^+ concentration transported from the bulk to the metal surface (216).

It is worth noting that the pH environment will have an influence on the kinetics of CO_2 corrosion. At low pH (< 4), the dominant process is the cathodic reduction of H^+ due to the increase in H^+ concentrations. In solution with pH (> 4), the mass transfer of carbonic acid allows hydrogen evolution at a high rate, creating a much more corrosive environment than that found in a solution with a strong acid at the same pH.

4.5.2 Anodic Reactions

The anodic dissolution of iron in acid solutions is given by:

$$Fe \rightarrow Fe^{2+} + 2e^- \tag{4.11}$$

The De Waard and Milliams (226) model for aqueous corrosion undertakes the same mechanism as Bockris (227) (165) and suggests that the cathodic reduction of carbonic acid is directly dependent on the hydrogen evolution at the steel surface, whilst the anodic dissolution of iron is limited by the CO_2 environment and respective kinetics. This has also been agreed by Nešić (228) in more recent studies in which carbonic species are believed to act as chemical ligands which catalyse the dissolution of iron. This has been found to be a pH-dependent phenomenon.

These models led to an overall corrosion reaction given by the combination of (4.9) cathodic and (4.11) anodic reactions:

$$Fe + H_2CO_3 \leftrightarrow FeCO_3 + H_2 \tag{4.12}$$
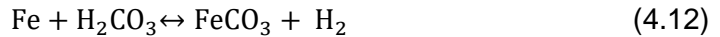
Depending on supersaturation and partial CO_2 pressure (p_{CO2}), then iron carbonate ($FeCO_3$) can be formed as a corrosion product. The formation of iron carbonate at the surface of the metal can reduce the corrosion process by presenting a diffusion barrier, effectively blocking the surface active sites as shown by Equation (4.13):

$$CO_2 + H_2O + Fe \leftrightarrow FeCO_3 + H_2 \tag{4.13}$$
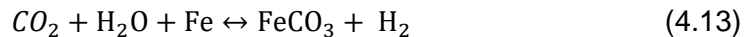
Summarising, CO_2 corrosion is an electrochemical process which involves a corrosion cell with four different components: an anode (where corrosion takes place), cathode (which provides sites for the environment to react), an electrolyte (path for the ionic species) and electrical connection between the anode and cathode. Lastly, it is known that at 25°C and 1 bar the solubility product (in mol/L)^2 of $CaCO_3$ ($K_{spCaCO3}$ = 3.4 x 10^{-9}) is higher than the solubility product of $FeCO_3$ ($K_{spFeCO3}$ = 3.11 x 10^{-11}) (229), suggesting that under specific conditions $CaCO_3$ is more soluble than $FeCO_3$. However, there are other factors such as pH and concentration of ions (230) such as bicarbonate and calcium ions which may affect the scaling tendency for either scale product.

4.6 Electrochemical Characterization

4.6.1 Electrical Double Layer (EDL)

During the corrosion process there are two main reactions taking place (anodic and cathodic) which indicate the ion exchange from the bulk electrolyte to the steel surface as a result of differences in free energy states and concentrations between those two reacting sites.

Therefore, upon corrosion of a metal, its ions depart from their lattice, leaving behind their electrons. Then, the water molecules tend to surround these metal ions as they escape the lattice, hydrating them. The hydrated ions are then free to diffuse away from the metal. This leads to a more negatively charged metal surface given the excess electrons, and consequently tends to attract positively charged ions freely available in the bulk. This means some ions will remain near the surface, instead of diffusing into the bulk electrolyte, forming a layer of charged particles. Thus, the electrolyte layer adjacent to the electrode surface will retain both water molecules and ions from both the metal and bulk electrolyte. Both layers formed at the metal surface and bulk interface are referred to as the electrical double layer (EDL) (211), as shown in Figure 4.5.
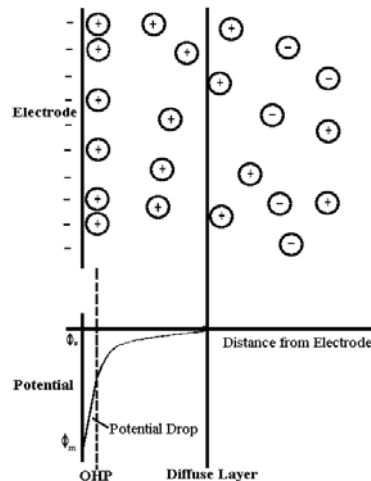
Figure 4.5: Schematic representation of the electrical double layer (EDL) according to the Gouy-Chapman-Stern model (231)

The Stern model illustrated in Figure 4.5 suggests that the interfacial layer could be divided into two parts. In the first layer the ions are strongly bound and can be closely adsorbed at the surface in which the potential decreases rapidly (outer Helmholtz layer – OHP by Gouy-Chapman). Then, in the second part, a diffuse layer of counter ions exists and the potential gradually decreases, possibly affecting the potential resulting from a charged surface (231).

The physical charge separation in an EDL promotes creation of an electrical potential. Hence, a relationship between the EDL composition with voltage and electric current can be established by the Butler-Volmer Equation (211):

$$i_o = i_{corr}\left[e^{\left(\frac{(1-\alpha)nF(E-E_{corr})}{RT}\right)} - e^{\left(\frac{-\alpha nF(E-E_{corr})}{RT}\right)}\right] \qquad (4.14)$$

where E_{corr} is the free corrosion potential in Volts, i_o is the external current in Amps/cm^2 flowing from or to the electrode because of the applied potential, i_{corr} is the corrosion current density in Amps/cm^2 that occurs when the electrode is at E_{corr}, E is the applied potential in Volts, α is a coefficient ranging from 0 to 1 and R, T, n and F have been defined previously.

Furthermore, Equation (4.14) can be converted into an expression based on Tafel slopes (β_a and β_c) in which the gradients of polarisation curves in anodic and cathodic regions for a plot of E vs log(i) can be given as (211):

$$i_o = i_{corr}\left[e^{\left(\frac{2.303(E-E_{corr})}{\beta_a}\right)} - e^{\left(\frac{-2.303(E-E_{corr})}{\beta_c}\right)}\right] \qquad (4.15)$$

This expression in (4.15) is typically used to understand the basics of electrochemical characterization using polarisation techniques.

4.6.2 Open Circuit Potential (OCP) Measurements

The OCP is defined as the measured natural electrode potential difference between two electrode half-cells of an electrochemical cell system. This potential is relative to a standard reference electrode when no current flows to the cell. Hence, it defines the state of redox reaction in equilibrium (211) (232).

4.6.3 Direct Current (DC) Measurements: Linear Polarization Resistance and Tafel Plots

The relationship between voltage and current within a few millivolts of polarisation from E_{corr} has been established as linear by many researchers. Stern and Geary (233) (169) have simplified the kinetic Equation, providing an approximation to the charge-transfer-controlled reaction kinetics given in Equation (4.15) for the case of small over potentials with respect to E_{corr}:

$$R_p = \left[\frac{\Delta E}{\Delta i}\right]_{(E-E_{corr}) \to 0} = \frac{1}{2.303 i_{corr}}\left[\frac{\beta_a \beta_c}{\beta_a + \beta_c}\right] \qquad (4.16)$$

Rearranging Equation (4.16), the following can be obtained:

$$i_{corr} = \frac{1}{2.303R_p}\left[\frac{\beta_a\beta_c}{\beta_a + \beta_c}\right] = \frac{B}{R_p} \qquad (4.17)$$

where R_p is the polarisation resistance (Ohm·cm²) given by the gradient of the polarisation plot at small overpotentials (dE/di) for a plot of E vs i (Figure 4.6). Due to the assumption of a charge-transfer in Equation (4.17), the R_p becomes equivalent to the charge-transfer resistance (R_{ct}). Therefore, the B factor will be dominated by the smaller anodic and cathodic Tafel slopes, i.e. if β_a and β_c are uneven (216). This expression provides the overall corrosion rate at any time for LPR measurements, in which current is almost linear within ± 5 – 20 mV potential range of E_{corr}.
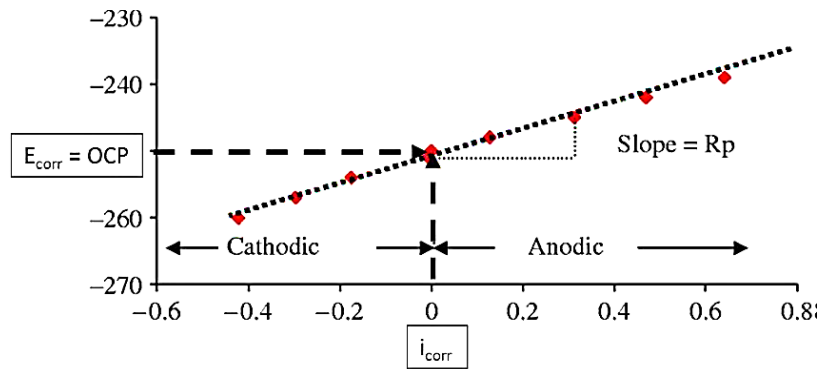
Figure 4.6: Linear polarisation plot illustrating the relationship between potential and current density at low applied potential (234)

Figure 4.6 shows an example in which the OCP was determined at the beginning of the experiment. The potentiostat applies a scanning potential from – 20 mV (negative) to 20 mV (positive), at a typical scanning speed of 0.25 mV.s⁻¹. It can be seen that as the applied potential increases, the measured current density also increases, suggesting a linear relationship, whose slope of the curve (R_p) corresponds to the polarisation resistance ($R_p=\Delta E/\Delta i$). Lastly, it can also be observed that R_p is inversely proportional to the corrosion rate (i_{corr}.)

LPR measurements are a good approach for prediction of long-term general corrosion. However, corrosion rates are only precisely estimated when the Tafel slopes (β_a and β_c) are determined experimentally for each metal under specific environmental conditions. These slopes can be determined through use of a larger DC potential range (200 – 500 mV) and by using the Stern-Geary Equation (4.17).

Alternatively, the corrosion rate of a specific material can also be determined by use of Faraday's Law which states that the mass of a material at an electrode during electrolysis is directly proportional to the amount of electricity transferred at that

electrode. Thus, the mass loss of an elemental material is directly proportional to the equivalent weight of lost elements (211):

$$m = \frac{QM}{nF} \tag{4.18}$$

where m is the mass of the substance liberated at an electrode in grams, Q is the total electric charge passed through the substance in Coulombs and M is the molar mass.

Hence, the corrosion rate expression in terms of Faraday's Law can be reduced to:

$$\text{Corrosion Rate } (\text{moles} \cdot m^{-2}s^{-1}) = \frac{i_{corr}}{nF} \tag{4.19}$$

Using this expression along with conversion factors, the corrosion rate can be expressed in mm/year:

$$\text{Corrosion Rate } (mm/y) = \frac{3.27 \times 10^3 (i_{corr})M}{n\rho} \tag{4.20}$$

where 3.27×10^3 is a combination of several conversion terms, i_{corr} is the corrosion current density in amps/m^2 and ρ is the metal density in g/cm^3 (equal to 7.85 g/cm^3 for carbon steel).

This expression (4.20) has been applied for determining corrosion rates during corrosion analysis by LPR measurements. Although, the LPR method is widely used to monitor corrosion rates, some limitations can be attributed, as it requires sufficient time to stabilise the OCP readings between two consecutive rate measurements and this method is mainly suitable for general corrosion rate control; so further investigation (e.g., pitting microscopic analysis) is needed to characterise localised corrosion.

4.6.4 Alternating Current (AC) Methods

The AC impedance method differentiates from DC measurements as it considers ions moving back and forward between counter and test electrodes over AC cycles during polarisation. This method is usually conducted over a low magnitude polarisation voltage and a small sinusoidal potential perturbation is applied to the working electrode at several distinct frequencies (ω). Therefore, the resulting sinusoidal current will provide further insight into corrosion processes over time for specific materials.

4.7 Factors Affecting Corrosion

The rate at which carbon steel corrodes in a CO_2 environment is affected by a number of different factors and the most common variables are reviewed within this section. These factors are (211): water solution chemistry, CO_2 corrosion products ($FeCO_3$, $CaCO_3$, $CaSO_4$, $BaSO_4$), pH, temperature, partial CO_2 pressure, wettability, corrosion inhibition, fluid hydrodynamics and material selection.

Each of these factors will have a tremendous influence on both kinetics and mechanisms in oilfield corrosion. However, in this work the major focus has been drawn towards the solution chemistry, temperature effect, pH and solubility of possible corrosion products.

4.7.1 Water chemistry

Water solution chemistry is undoubtedly one of the key factors affecting CO_2 corrosion. The solution chemistry can vary from simple to very complex ionic mixtures between the solid-fluid interface in water, the water-oil interface and within the gas condensate systems. Typical water compositions contain ions such as carbonic, bicarbonate, hydrogen, hydroxide, iron, chloride, sodium, potassium, calcium, magnesium, barium, strontium, acetate, sulphate and dissolved gases such as CO_2 and H_2S (228). Pitting and other localized corrosion can be strongly enhanced by high chloride content (i.e. high salinity) under the assumption that some oxygen is also present. Sometimes, the concentration of dissolved salts can be extremely high making the solution non-ideal. In addition, some organic acids (e.g.: acetic acid) can also be present which can strongly influence the corrosion rate (235) (236) (237) (238).

4.7.2 Corrosion Products (Protective Film Formation)

Sweet corrosion of carbon and low alloys is dependent on the surface films deposited during the corrosion process. The protectiveness of the metal surface will depend on the rate of precipitation and stability of the products forming a film as a result of the rate of corrosion within that specific environment (239).

A protective film will be formed when the supersaturation of any of the ions near-surface exceeds its equilibrium limits, resulting in film formation on the steel surface (240). The type of film will depend mostly on the solubility of the salts present in water and the conditions for it to form (i.e. temperature and pressure). However, typical

precipitates formed are iron scales such as $FeCO_3$ and other types of carbonates ($CaCO_3$, $CaSO_4$) and sulphate scales ($BaSO_4$) (241).

Iron carbonate crystals can precipitate at the surface if iron (II) ions (Fe^{2+}) react with carbonate ions (CO_3^{2-}) present in the electrolyte solution:

$$Fe^{2+} + CO_3^{2-} \rightarrow FeCO_{3(s)} \qquad (4.21)$$

Hence, a high supersaturation of Fe^{2+} and CO_3^{2-}/HCO_3^- is needed for the formation of $FeCO_3$ protective films (242). This type of scale, once formed, can inhibit the corrosion kinetics either by creating a diffusion barrier of species participating in the corrosion process or by covering the steel surface region (243) (244).

The integrity of the $FeCO_3$ film deposited depends on parameters such as porosity and thickness. However, the saturation ratio (SR) and the scaling tendency (ST) are two non-dimensional parameters commonly used to identify the level of film protectiveness during corrosion processes, and can be defined by the following equations:

$$SR_{FeCO_3} = \frac{[Fe^{2+}][CO_3^{2-}]}{K_{sp(FeCO_3)}} \qquad (4.22)$$

$$ST = \frac{FeCO_3\ Precipitation\ Rate}{Corrosion\ Rate} \qquad (4.23)$$

Localized corrosion can take place if the film is not uniformly covering the whole surface due to the fact that scale breaks down when interacting with other scale particles in bulk solution, leaving the metal surface in direct contact with the electrolyte solution (245) .

4.7.3 Temperature

An increase in the operating temperature will accelerate all processes taking place during corrosion: electrochemical, chemical and mass transport. The rate of corrosion tends to increase with an increase in temperature at low pH, when specific types of protective scales do not form (246). However, this situation changes significantly when the solubility of iron/calcium carbonate scales is exceeded, usually at higher pH values (247). The increase in temperature will accelerate the crystallization kinetics, resulting in the formation of a protective film at the surface of the metal and subsequently reducing the corrosion rate. Studies have also shown that at higher temperatures, the protective film becomes different in texture, more crystalline and generally more protective, but this will again depend on the water

composition (247). Additionally, at lower temperatures (< 60 ^{o}C), the corrosion products can generally be more easily removed by the flowing fluid and have a smudge-like texture (246) (247).

4.7.4 pH

pH has an indirect effect on corrosion rates as it is critical to the formation of scales, specifically $FeCO_3$ scales (248). Studies have revealed that increasing the pH of a solution from 4 to 5 can reduce the solubility of Fe^{2+} ions by a factor of approximately 5. Further increase in the solution pH from 5 to 6 can reduce $FeCO_3$ solubility by approximately 100 times (249). Additionally, both the CO_2 partial pressure and pH can influence the level of $FeCO_3$ saturation in solution. Hence, for solutions with pH > 5 the probability of $FeCO_3$ film formation can be increased as low solubility products can correspond to higher supersaturation and this will subsequently lead to a decrease in corrosion rates (247).

4.7.5 Flow Hydrodynamics

The relationship between fluid flow velocity and corrosion kinetics is still quite debatable (228). When flow conditions do not result in the formation of a protective inorganic scale film, then the main role of the flow velocity is to enhance the transport of species towards and away from the surface of the metal, subsequently causing an increase in corrosion rates. At high turbulent flow, the protective film formed by either scale deposits (such as $CaCO_3$ or $FeCO_3$), or chemical inhibitor layers, will be partially removed, triggering an increase in the corrosion rates (228) (250). In that case, the accelerated corrosion can also be due to erosion, as solid particles are removed from the substrate. The operating conditions in the oilfield are such that two or more phases can flow simultaneously, i.e. exhibit multi-phase flow. In such environments, a series of flow patterns can be displayed, varying from a single flow to slug, froth and annular flow behaviour (250).

4.8 Corrosion Products Characterisation

Some authors (251) (252) (253) have demonstrated that CO_2 corrosion rates and their characteristics strongly depend on the type of corrosion products formed and on the environment and metal surface where the process takes place. De Waard et al., (247) have shown that the presence of corrosion products in a CO_2 saturated solution

can reduce significantly the overall corrosion rates. On the other hand, the formation of corrosion products is affected by factors such as pH, flow rate and temperature.

There are four main types of corrosion films which can be found when working with carbon steel (254): transparent film, iron carbide (Fe_3C) film, iron carbonate ($FeCO_3$) film and a combination of iron carbonate and iron carbide ($FeCO_3 + Fe_3C$) film.
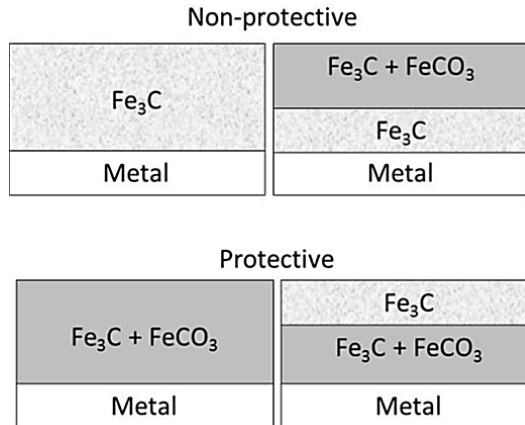
Figure 4.7: Different morphologies for non-protective and protective corrosion films (254)

Figure 4.7 displays a schematic diagram in which different corrosion products can be formed with the ability of protecting, or not, the surface of the metal. The protective layer formation will strongly depend on environment conditions such pH, temperature, solution supersaturation, fluid hydrodynamics and precipitation kinetics.

4.9 Review of CO₂ Corrosion Prediction Models

Over the past decades, several papers have been published to describe an integrated approach for corrosion modelling based on laboratory testing, with the aim of optimising the use of carbon steel in corrosive systems. Different models have been developed for CO_2 corrosion to provide essential information on material degradation in the oil and gas pipelines, under several conditions of temperature and pressure. Typically, these corrosion models are based on different theories, assumptions, and strategies, which allowed classifying them as: empirical, semi-empirical and mechanistic models (255) (256) (228).

Empirical corrosion models are purely based on generic corrosion data, that is either obtained from actual operations or from laboratory experiments. These predictions provide a reasonable approach however the drawbacks of this are that they require a large set of field or experimental data and may not fit well outside the database

conditions (228) (257). Some of the most known empirical models were introduced by Dugstad (258) (259) (260), Mishra (261) and Nesic (262) (263). All of these models estimate the corrosion rates based on different correlation which express the reaction kinetic principles as a function of CO_2 partial pressure, pH and temperature.

The semi-empirical corrosion models apply empirical correlations to determine the corrosion rate and correction factors which are based on theoretical hypothesis. The correction factors are typically represented by parameters such as the $FeCO_3$ film formation, flow velocity, pH and presence of inhibitors. These types of model can be used to predict the general corrosion rate outside the variable ranges tested in experiments, providing higher confidence than the empirical model (228) (257). Furthermore, this type of models tends to be less time consuming and simpler than mechanistic (theory based) models.

The most commonly used semi-empirical models for CO_2 corrosion are by De Waard and collaborators (247) (264). Their first model was based on the assumption of direct reduction of H_2CO_3, assuming a charge-transfer-controlled reaction between carbon steel and carbonic acid. Then, over the years, the De Waard and Milliams models (247) have been extensively revised and now considers factors such as protective scales, changes in brine's pH, water wetting and flow rates. These models are still used in the oil and gas industry, however, the corrosion rates estimation is only valid if the material properties and conditions are very similar to those in their database.

Lastly, the mechanistic corrosion models differ from empirical and semi-empirical as these are purely focused on predictive calculations and do not require any corrosion data for the developing the model. These models have a good extrapolation capacity within the limitations of the theory and can be modified to simulate different systems. However, the implementation of mechanistic models requires an understanding of corrosion science fundamentals related to thermodynamics, kinetics, heat transfer, mass transfer and other fields within science and engineering. These are time consuming models typically developed and validated by research groups.
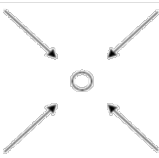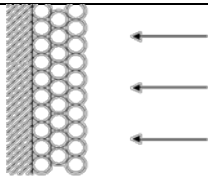
Nesic et al., (257) (248) (265) developed the first mechanistic CO_2 corrosion model which incorporates electrochemical reactions at the metal surface, diffusion of the chemical species between bulk and metal, diffusion of chemical species across $FeCO_3$ films, electro-migration of ions under influence of potential gradients and the chemical reactions taking place in bulk of solution. This model allowed users to predict the film thickness of $FeCO_3$ scale during corrosion processes (266). However, a key limitation of this CO_2 corrosion mechanistic model is that it does not account

the effects of pitting corrosion, mesa attack, flow induced corrosion, thus, all models is based on general or uniform corrosion process under aqueous CO_2 environment (267) (268).

4.9.1 Summary of FeCO₃ Precipitation Models

In order to further understand the CO_2 corrosion of mild steel, it is crucial to correlate the formation of $FeCO_3$ protective film, its kinetics and stability. There are four key $FeCO_3$ precipitation models: Greenberg and Tomson (G&T) (269) (270), Johnson and Tomson (J&T) (271) (272) , Van Hunnik et al. (VP&H) (273) and Sun and Nesic (S&N) (274) (275) (276). A comparative study done by Woollam et al. (277), showed that the main distinction made for these models was that one side of the rate equation considered seeded crystallisation (G&T and J&T model) whilst on the other side, the rate equation was determined by precipitation on an actively corroding metal substrate (S&N model). The VP&H model is assumed to be very similar to the S&N. Thus, the differences in the precipitation rates are attributed to the rate determining step reaction, being the surface reaction kinetics dominant for seed crystal models (G&T and J&T) and diffusion kinetics dominant for the corrosion surface model (S&N), as shown in Table 4.2.

Table 4.2: Comparison between the different mechanistic models for $FeCO_3$ precipitation (277)

G&T and J&T Model	S&N Model
Based on precipitation via seed crystals	Based on precipitation on actively corroding substrate
Single crystal deposit	Uniform film of crystal deposits
Seed crystal ≈ 1µm	Corroding surface film ≈ 0.01m
Diffusion rate >> Surface rate	Surface rate >> Diffusion rate
Surface dominant	**Mass transfer dominant**

Based on Sun and Nesic model (278), the scale growth will depend primarily on the following semi-empirical growth equation:

$$\text{PR} = k_r \times \left(\frac{A}{V}\right) \sigma^r \tag{4.24}$$

Where PR is the precipitation rate for $FeCO_3$, K_r is the kinetic rate constant, A/V is the surface area to volume ratio, σ is the supersaturation and r is the growth order. Taking into account experiments done for direct measurement of $FeCO_3$ amount which precipitates in a corroding steel, the precipitation rate equation can be rearranged as:

$$PR_{FeCO_3} = A_p e^{-\left(\frac{E_A}{RTk}\right)} \left(\frac{A}{V}\right) K_{sp_{FeCO_3}}(S-1) \tag{4.25}$$

Where A_p is the pre-exponential constant, E_A is the activation energy. The S&N model considers lnA_p=28.2 and E_A=64.9 kJmol for a precipitation rate (PR) in mol/m²s.

Lastly Sun et al. (278), proposed a mass change measurement for corrosion rates. This technique enabled to experimentally infer the weight loss of carbon steel sample due to corrosion and the weight gain due to $FeCO_3$ precipitation during the samples exposure in CO_2 environment. Therefore, both corrosion rate equation and precipitation rate equations have been rearranged in terms of change in mass and are expressed as follows:

$$CR(mol/m^2s) = \frac{m_1(g) - m_3(g)}{MW_{Fe}(\frac{g}{mol}) \times t(hr) \times S(m^2) \times 3600(\frac{s}{hr})} \tag{4.26}$$

$$CR\left(\frac{mm}{yr}\right) = CR\left(\frac{mol}{m^2s}\right) \times \frac{365\left(\frac{days}{yr}\right) \times 86400\left(\frac{s}{days}\right) \times MW_{Fe}\left(\frac{g}{mol}\right)}{\rho\left(\frac{kg}{m^3}\right)} \tag{4.27}$$

$$PR(mol/m^2s) = \frac{m_2(g) - m_3(g)}{MW_{Fe}(\frac{g}{mol}) \times t(hr) \times S(m^2) \times 3600(\frac{s}{hr})} \tag{4.28}$$

Where CR is the corrosion rate (mm/year), PR is the precipitation rate of corrosion products (mol/m²s), m_1 is the weight of the metal coupon prior to the start of the experiment (g), m_2 is the weight of the metal sample containing scale/corrosion products at the end of the experiment (g), m_3 is the weight of the sample after scale/corrosion products removal (g), MW_{Fe} is the molecular weight of iron (g/mol), MW_{FeCO3} is the molecular weight of iron carbonate (g/mol), t is the exposed time (hours), S is the exposed surface area of the metal (m²) and ρ is the density of the sample (kg/m³).

4.10 Closing Remarks

Overall, this chapter presented a full review of corrosion fundamentals, elucidating the principles behind this process and the basis for corrosion data analysis. The chapter started with a brief theoretical description and definition of the oilfield corrosion (e.g., sweet and sour corrosion processes). Then, the key fundamentals, literature theories and prediction models were investigated and reviewed with a particular focus on CO_2 corrosion, mechanisms of corrosion reactions and the several factors which strongly influence the corrosion process such as pH, temperature, presence of gases such as H_2S and CO_2, flow rate and mineral scale deposition, such as $FeCO_3$ and $CaCO_3$ deposits. Lastly, a number of techniques previously developed to monitor and understand the processes of corrosion were also briefly summarised, and the understanding of these methods reviewed will contribute to the selection of adequate corrosion tests (e.g., linear polarisation techniques, open circuit potential, etc).

Chapter 5 - Methodology

Summary

This chapter provides a description of the materials; instrumentation and methodologies used during bulk and surface crystallization studies. In addition, a wide range of data analysis approaches used to evaluate the crystallisation stages of nucleation and crystal growth is also presented.

5.1 Introduction

The aim of this chapter is to provide a detailed experimental methodology with effective tools and techniques used to explore the crystallization process of $CaCO_3$ in bulk of solutions and at surfaces, in presence and absence of corrosion process. In order to successfully answer the thesis research question and meet the key objectives described in section 1.2, a robust experimental melthodology has been developed using both computational and analytical approaches.

The chapter starts with an introduction of MultiScale™, a scale simulation software used to calculate the scaling tendency of North Sea brines under different testing conditions. The experiments are categorised into bulk and surface crystallisation tests in which robust methods and process analytical tools have been applied to monitor the crystallization processes in-situ. Crystals were characterised with respect to size and shape using several robust ex-situ techniques. Furthermore, several equations and data interpretation methods were developed and are explained in order to better extract the nucleation and crystal growth kinetic data and mechanisms. Finally, the chapter also presents all testing procedures, conditions, method development for assessing the crystallisation/corrosion and a summary list of the experimental limitations encountered with selected techniques. Figure 5.1 shows a route map of this chapter:
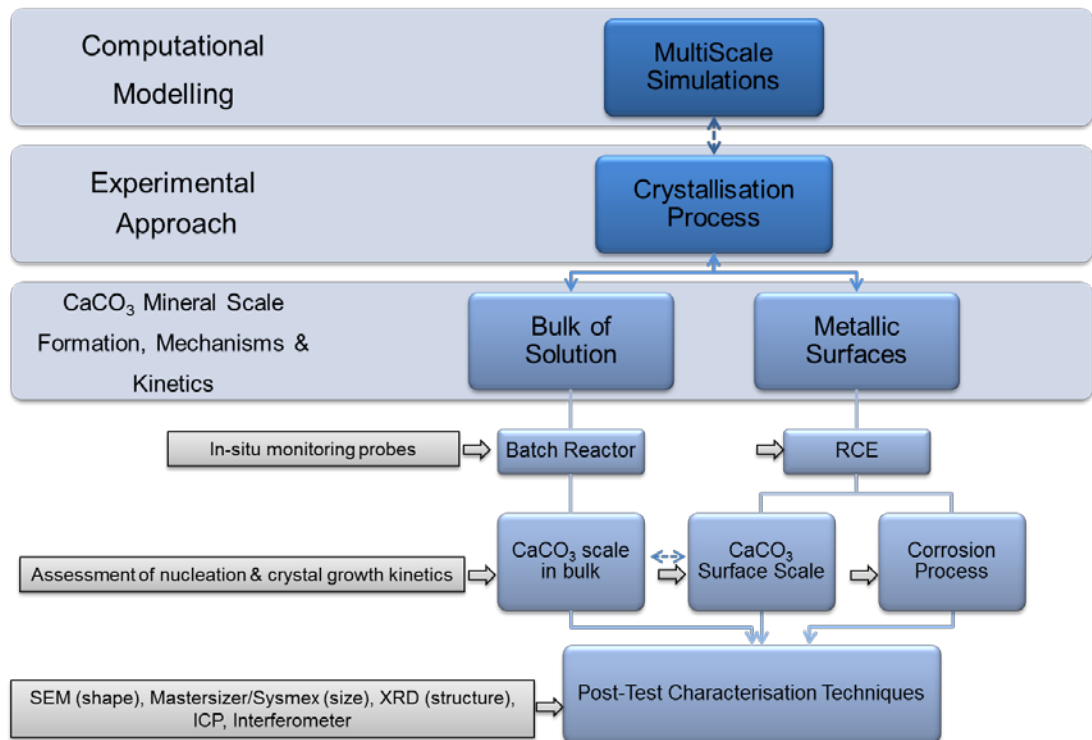
Figure 5.1: Route map of the materials and methodology chapter

5.2 Materials

Distilled water and three main salts were used to prepare synthetic brines: calcium chloride hexahydrate ($CaCl_2.6H_2O$), sodium bicarbonate ($NaHCO_3$) and sodium chloride ($NaCl$), all with purity grade > 98% (i.e. Analar grade).

5.2.1 Synthetic Brine Composition and Preparation

Five different brine chemistries, shown in Table 5.1 were provided as part of a joint collaboration project between the University of Leeds, BP© and the Technology Strategy Board (TSB) UK. These water compositions were representative of North Sea oilfield facilities. The originally given water chemistries were assessed for their $CaCO_3$ scaling tendencies at 80°C using the thermodynamic commercial software, MultiScale™.

For each case study, a two-part synthetic brine of a 50%:50% mixture was prepared with required volumes of anions water (AW) and cations water (CW), by adding the necessary amount of weights of the composite Analar reagent salts into distilled water and stirring it thoroughly. The anionic synthetic brine contained an excess of carbonate scaling ions (CO_3^{2-}), whilst the cationic synthetic brine contained an excess of calcium ions (Ca^{2+}). Those individual brines were well stirred for a maximum period of 30 minutes to ensure all salts were evenly dissolved into a homogeneous solution. The pH was measured at room temperature without any adjustments with buffers.

Table 5.1 illustrates the North Sea brine composition provided by industry as representative case studies. The supersaturation levels were determined using MultiScale™ software.

Table 5.1: Synthetic Brine Compositions (80°C)

Case Studies	Saturation Ratio	Cations	Anions
		[Ca^{2+}] mmol/l	[HCO_3^-] mmol/l
1	**1.52**	5.00	5.00
2	**2.55**	6.50	6.50
3	**4.77**	9.00	9.00
4	**11.00**	12.35	12.20
5	**55.00**	35.94	30.48

5.3 Bulk Crystallisation Tests

A batch crystalliser has been used to monitor the crystallisation stages involved during calcium carbonate formation in the bulk solution. The main principles of this experiment are detailed, as well as the specifics of the device with its in-situ monitoring tools and the established procedures used for each test.

5.3.1 Basic Principles

The aim of this experiment is to monitor spontaneous bulk crystallization over different ranges of temperature (i.e. 25°C, 40°C and 80°C) with time. Any changes in solution during the reactive crystallisation process (i.e. bulk precipitation) are recorded via in-situ probes which tracked pH, turbidity, calcium ions concentration and the solution's temperature. At the end of each experiment, calcium carbonate crystals were collected via vacuum filtration and then evaluated with respect to their size (via Mastersizer and Sysmex), shape (via SEM) and crystals internal structure (via XRD).

5.3.2 Experimental Set – up

The experimental equipment used for the bulk crystallization studies consisted of a jacketed glass 300 mL batch reactor, agitated by Teflon coated retractable curved three blade impeller at 180rpm and equipped with a programmable thermostatically-controlled oil bath (Julabo F25), which was used for monitoring the vessel inner solution temperature. In addition, a combined pH, ion selection electrode and conductivity meter (S70-SevenMulti^{TM} – *version 2.0*) with data interface board (A/D) was connected to a computer unit running LabX® for online data collection through insertion of these probes in bulk solution. The experimental facility is shown schematically in Figure 5.2.

As shown in Figure 5.2, several probes (i.e. pH, turbidity, calcium ion detector and conductivity) were used to control bulk precipitation in-situ.
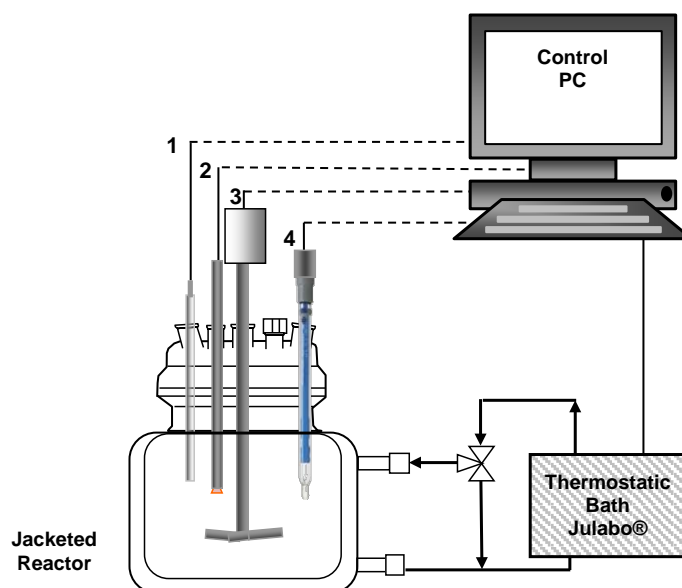
Figure 5.2: Schematic bulk crystallization facility with main in-situ process analytical tools: (1) Temperature probe, (2) Calcium ion selective electrode, (3) Three blade impeller with motor shaft, (4) pH probe

5.3.3 In-situ Control of CaCO$_3$ Bulk Crystallisation

Calcium carbonate crystallization experiments took place in a sealed batch reactor and the entire process has been monitored with help of the following in-situ analytical probes: thermometer, pH, turbidity and calcium ions selection electrode. Each of these instruments is briefly described below.

5.3.3.1 Platinum resistance thermometer

The platinum resistance thermometer (PT100) was used to measure and control the crystallization temperature.

5.3.3.2 Combined glass pH electrode and conductivity probe

A combined glass pH electrode from Mettler Toledo™ (InPro® 4260) was used to monitor the pH and conductivity of bulk solution. In this combined electrode the pH-sensitive glass probe is concentrically surrounded by the reference electrode filled with reference electrolyte solution. The pH electrode responds to single charged ions of hydrogen (H$^+$) as: pH = - log [H$^+$]. It can work within pH ranges from 0 to 14 and temperature range from 0ºC to 130ºC with ± 0.05 pH units of measurement accuracy (279).

5.3.3.3 Calcium ion selective electrode (ISE)

A combined body ion selective electrode from Mettler Toledo^{TM} (Perfect-Ion Calcium) was used to detect and monitor the freely calcium ions in solution. This probe is temperature limited to 40°C and a 1°C difference temperature was expected for 10^{-3} mol/L calcium solution, giving rise to 1.2% error. Calibration can conducted using different methods and including the addition of a calcium ionic strength adjuster (ISA). This ISA solution must be added in order to minimize the interference of other ions present in the crystallizing solution (279).

5.3.3.4 Light transmittance turbidity probe

Turbidity measurements of bulk crystallising solutions were done using a stainless steel laser reflectance and transmittance fibre optic probe. This probe detects the crystallization onset via light transmittance level, when the light is reduced in a range from 0 to 100% due to the interruption of light reflectance caused by the nuclei formed in crystallising solution. The light transmittance readings are not fixed to the number of particles present in the bulk; but still provide a qualitative measurement resultant from the calibration.

5.3.3.5 Lasentec Focused Beam Reflectance

The FBRM provides chord length distributions over time, relating the crystal growth as a function of time. This technique has been successfully applied in different areas of crystallization.

5.3.4 Experimental Procedure

Prior to the start of bulk crystallization experiments, the batch reactor and all probes were cleaned and washed thoroughly with distilled water, then dried with acetone, in order to ensure no residues were left in the equipment from previous experiments. This is very crucial to prevent contamination and changes in the reactive crystallization solution.

Brine solutions were freshly prepared via a simple dissolution method as explained in section 5.2.1, and a two-part homogeneous solution was created, one containing the anions, and the other part, the cations. These brine solutions of equal volume were pre-heated to the desired testing temperatures (i.e. 25°C, 40°C or 80°C) and then mixed up in a batch reactor.

The mixing time to feed the batch reactor was determined with aid of a 250 mL glass burette, a dye solution and a stopwatch. This procedure ensured that both anionic and cationic brines were fed smoothly into the batch reactor. By definition, the mixing time, θ_m is the time required to mix an added dye solution to the contents of the reactor until a certain degree of homogeneity is achieved. The tracer solution consisted of 4mg/mL of potassium permanganate, $KMnO_4$ (purple colour dye) and took exactly 15 seconds to fully achieve a homogeneous looking solution (Figure 5.3). This procedure has been repeated three times, ensuring the mixing time driven by gravity has been kept the same for the same amount of feed solutions.
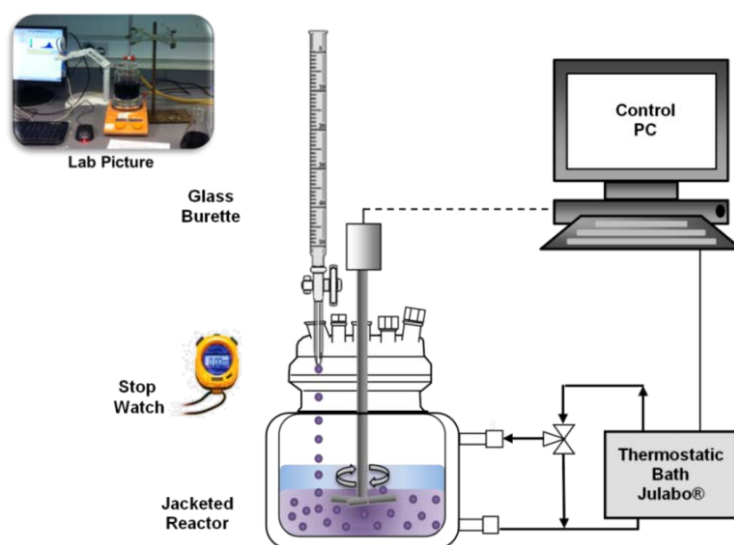
Figure 5.3: Schematic illustration for determination of mixing time with a coloured dye solution and burette.

5.3.5 Data Analyses Methods

Bulk crystallisation studies focused on both nucleation and crystal growth stages. To assess nucleation kinetics, in-situ techniques have been used and the induction time method developed through the analysis of in-situ data (i.e. pH, calcium concentration and turbidity). These in-situ methods have been previously established in the literature (167) (280) for determining the induction period of $CaCO_3$ in bulk systems (seeded and non-seeded). Other nucleation kinetic parameters such as the interfacial tension, critical nuclei size and nucleation rate were subsequently determined using equations from the classical nucleation theory. The interfacial energy was determined using equation (2.13), in which the interfacial energy was determined from the slope of the straight line of $\ln(\tau)$ vs $1/T^3$ $(\ln\sigma)^2$. The critical nuclei size was determined by equation (2.14) and the nucleation rate was determined by equation (2.17).

Furthermore, the bulk crystals growth kinetics was determined ex-situ with assistance of size measurement techniques, which enabled calculating the particle size distribution (PSD) over time, and as a function of supersaturation and temperature. Lastly, the growth rate equations (2.23) and (2.25) have been used to express the overall growth of $CaCO_3$ (calcite) in bulk solution. Subsequent analyses of crystal growth mechanisms were based on theories described in chapter 2 (section 2.5.4).

5.3.5.1 Induction time method development

   a. In-situ pH graphical method

The crystallisation stages of $CaCO_3$ nucleation and growth are strongly dependent on pH conditions, so changes in the solution pH throughout the reaction precipitation are useful to fully understand the progress of the crystallisation reaction (281) (282). Considering an ideal steady state scenario, the induction time for $CaCO_3$ crystallisation can be considered as the period taken for the appearance of first stable nuclei in solution which will depend on the time taken for the solution to reach an optimum pH for the solution supersaturation.

Graphically, the induction period (τ) is typically noticeable by the drop in pH readings towards a more negative slope, due to the bicarbonate ion dissociation (Equations (3.3) – (3.4)), which then reacts with calcium ions also present in solution (equation (3.5) to form $CaCO_3$ crystals. Therefore, the induction time is estimated to be the time in which the pH drops significantly due to nucleation onset. The induction times via pH will be assumed to be the point where the peak of change is observed, i.e., an inflection point. Induction times are very challenging to quantify or measure experimentally. However, previous studies have shown that induction times measured via a pH-method can be reliable to determine the nucleation onset of $CaCO_3$ crystals precipitating in bulk solutions (283) (284) (285).

   b. Calcium-ion concentration graphical method

The calcium ion selective probe was used and in-situ data of the changes in calcium concentrations were recorded as a mean of determining the induction period or the nucleation on-set. This probe indicated the amount of calcium ions available to react in solution and form $CaCO_3$. Since there is a balance between carbonate ions and calcium ions during the reaction crystallization process, the induction time can be estimated by the moment where a sharp drop in concentration is observed before reaching a plateau where the solution either reaches the equilibrium or reaction ends. This "inflection peak" will be expected and taken as the solution's induction time.

Previous literature (286) (287) (288) has confirmed that initial calcium concentration should decrease in order to form $CaCO_3$ (calcite). A very sharp decrease straight after mixing may suggest that instantaneous nucleation takes place (i.e. all nuclei are formed at the same time before growing into bigger crystals), whilst a gradual decreasing curve would suggest that progressive nucleation (i.e. nuclei are formed as the reaction proceeds) is the dominant nucleation type. An understanding of the type of nucleation is also relevant to characterise $CaCO_3$ crystallization process.

c. *Light transmittance turbidity method*

Similar to the previous in-situ techniques, the induction time will be considered as the time elapsed between the achievement of supersaturation and appearance of the first crystal. The light transmittance turbidity probe illustrates this process by sharply reducing the light intensity from 100% (clear solution) to 0% (crystals), providing reproducible results for highly saturated systems. Figure 5.4 shows a schematic illustration of the expected profile using this light transmittance probe.
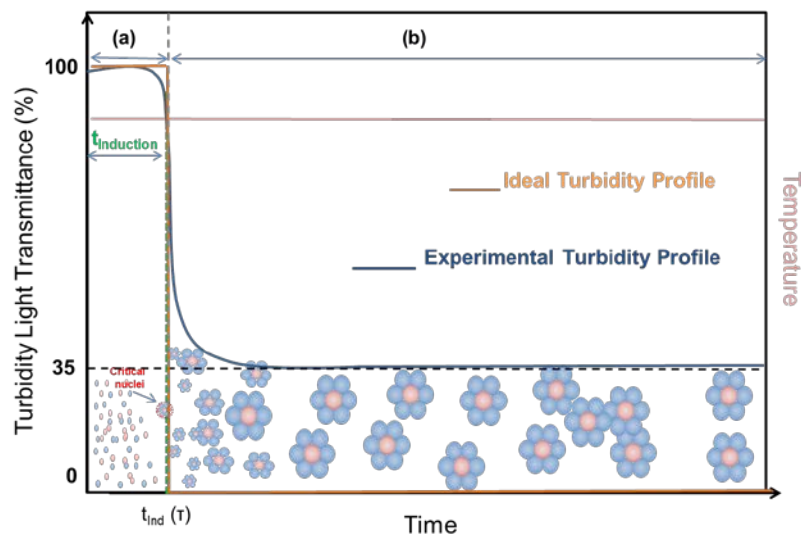
Figure 5.4: Representative illustration of turbidity measurements via laser fibre optic transmittance and reflectance probe during isothermal crystallisation tests. The induction time is given by the drop in light transmittance indicating the (a) nucleation onset and (b) subsequent crystal growth.

5.4 Surface Crystallisation Tests

The rotating cylinder electrode (RCE) device was used for studying the surface crystallisation process happening simultaneously in bulk and in presence/absence of corrosion. The main principles of this experiment are detailed, as well as the specifics

of the device with its in-situ monitoring tools and the established procedures used for each test.

5.4.1 Basic Principles

The aim of this experiment is to monitor surface scale crystallization and any potential corrosion process taking place simultaneously. Two different metal substrates were used: stainless 316L and carbon steel X-65 and tests were done at two different temperatures: 25°C and 80°C. In-situ probes enabled tracking the surface scale deposition rate and pH probes enabled measuring changes in the pH bulk solution. The surface deposition was monitored via in-situ electrochemical LPR measurements and mass gain measurements. Crystals were characterised for shape, size and structure. Lastly, experiments assessed the effect of hydrodynamics during the surface scale deposition.

5.4.2 Equipment Set-up

The experimental equipment used for $CaCO_3$ surface kinetics studies consisted of a rotating cylinder electrode (RCE) immersed in a 1 L double glazed vessel, agitated by magnetic stirrer at 250 rpm speed. A hot plate with incorporated thermometer ensured that the crystallising solution temperature remained constant as these are also isothermal tests. In-situ electrochemical measurements were followed with electrodes connected to a computer unit with data interface board (A/D) for linear polarisation resistance (LPR) measurements using a potentiostat device called ACM® (version 5.5.0). In addition, pH readings were taken to extract kinetic details on simultaneous bulk precipitation and surface deposition processes. The schematic equipment set-up and respective pictorial parts are shown in Figure 5.5 and Figure 5.6.
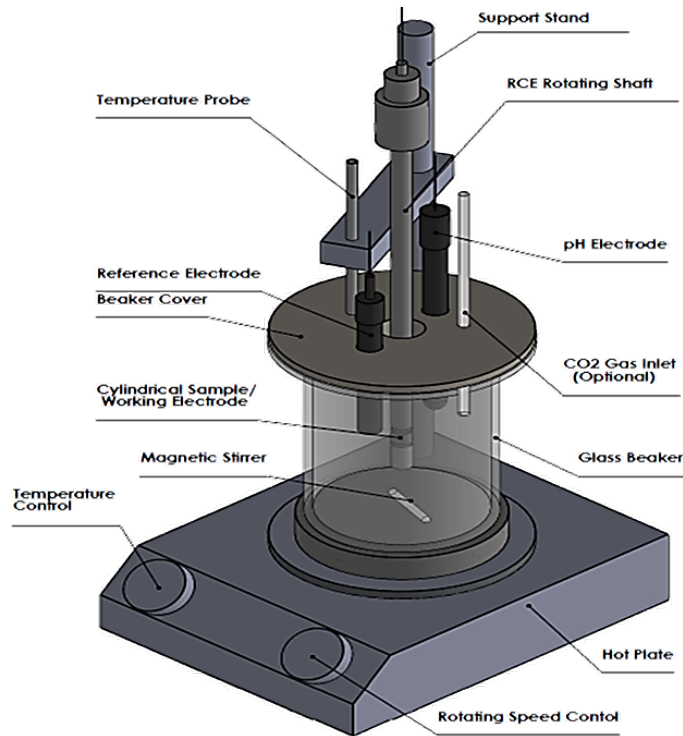
Figure 5.5: Schematic surface crystallization facility with main parts. This is a semi-batch process with rotating cylinder electrode (RCE) device

The RCE is a convenient apparatus used for scale and corrosion tests. It consists of an electrode rotator and is controlled by a main unit that can replicate real field hydrodynamic conditions in a controlled manner (speed varies from 0 rpm – 10,000 rpm). It is made of an insulating material with the metallic cylinder samples which revolve within the vertical shaft (289).
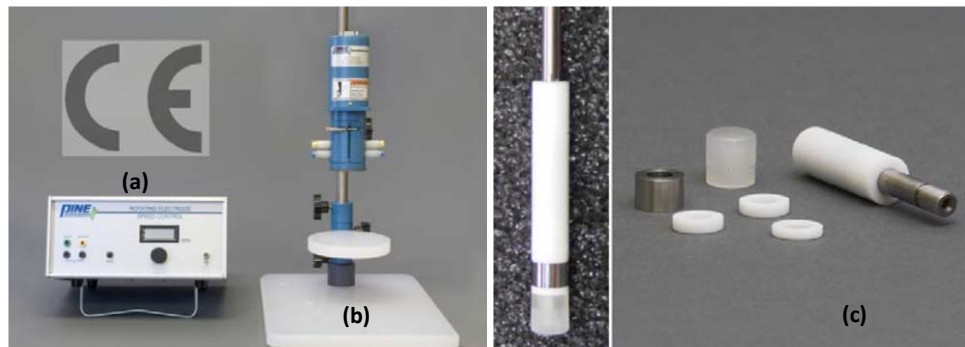
Figure 5.6: Picture of RCE device and respective parts: a) RCE speed control unit; b) electrode rotator unit; c) RCE mounted tip with metallic cylinder (sample) and respective washers and nut keeper (289)

This electrochemical set up is typically used for both scale and corrosion studies and comprises a three electrode cell with a working electrode (i.e. carbon steel X-65 and stainless steel 316L), a reference electrode and a counter electrode.

95

The working electrodes were degreased with acetone, rinsed with deionised water and dried with compressed air to provide a uniform contaminant-free surface prior to immersion into the test solution. These electrodes were immersed in the reactor before the saturated brine solutions are fed in and mixed together to allow a permanent contact with the mixing solution.

No work has been previously published using the RCE for assessing both $CaCO_3$ surface scale and corrosion processes. This methodology has been selected as the set up provides several tools to control and mimic field conditions. However, Neville et al. (290) have previously developed a similar method to use the three-electrode-cell with a rotating disc electrode (RDE). This set up was then later combined with bulk chemistry to study both precipitation and deposition processes (291) (208). In this current work, a similar but different approach has been made using the rotating cylinder electrode which gives a better surface configuration to the pipes in the oilfield industry.

5.4.3 Monitoring of $CaCO_3$ Surface Scale and Corrosion

5.4.3.1 LPR measurements via three-electrode-cell

Linear polarisation resistance (LPR) measurements were performed by polarising the working electrode from – 15 mV below the open circuit potential (OCP) to 15 mV, at 0.25 mV/s scan rate to obtain the polarisation resistance (R_p). The duration of the test was 24 hours, with OCP readings taken each 1 hour. This test used a three electrode cell comprised of a working electrode (metallic cylinder), a platinum-rod redox electrode used as the auxiliary electrode (AE) and a KCl saturated silver chloride electrode (Ag/AgCl) acting as the reference electrode. An assumption of $\beta a=\beta c=0.12V/decade$ has been made during the set-up for LPR corrosion measurements.

5.4.3.2 Selection of metallic working cylinders

Carbon steel X-65 (UNS K03014) and stainless steel 316-L (UNS S31603) are two common metals used within the oil and gas industry, due to their suitable properties and economical value (291) (292). Each of these working electrodes was polished by the manufacturer and showed an exposed surface area of 3.77 cm^2, with an outside diameter of 1.2 cm and cylinder height of 1 cm (Figure 5.7).

Prior to the start of the experiments, these materials were characterised using EDX-S to further understand their chemical composition as shown in Table 5.2.

Table 5.2: Assessment of element composition (weight %) for the metallic substrate

	Fe	C	Mn	Si	Cr	Cu	Ni	Mo	P	Al	S	O
X-65	98	0.05	1.32	0.31	0.04	0.02	0.04	0.31	0.02	0.03	0.002	-
316-L	66	0.4	1.7	0.5	17.6	-	10.3	2.2	-	-	-	1.6

It can be observed that carbon steel X-65 has higher iron (Fe) content and more ion species than stainless steel 316L. On the other hand, stainless steel 316L displays higher contents of chromium (Cr), nickel (Ni) and manganese (Mn) where these species are known as austenite stabilizers which will contribute to the passivity of the metal. Moreover, it is also identified high levels of molybdenum (Mo) which is commonly known as a potent alloying addition to improve general corrosion resistance, and can contribute to the stability of the film formation (225) (293).

Figure 5.7 illustrates the difference in scale deposition when using the carbon steel X-65 (UNS K03014) and stainless steel 316L (UNS S31603) under the same conditions.
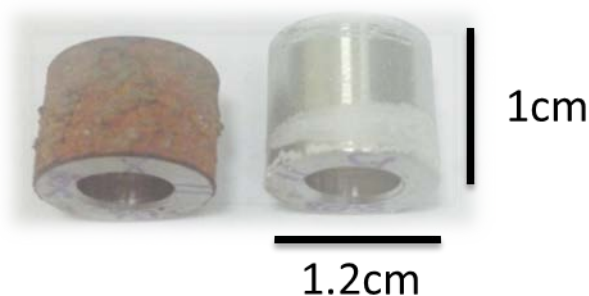
Figure 5.7: Mass deposition rate measurements on carbon steel – CSX65 (left) and stainless steel – SS316L (right). Both samples showed surface deposition and CSX65 had clearly been affected by corrosion and scale

5.4.3.3 Influence of hydrodynamics

The hydrodynamics can affect the scale deposition and corrosion at the surface of the RCE working electrode. Several rotational speeds were selected to assess both scaling (i.e. mass gain) and corrosion (mass loss) effects under low to high rotational speeds. A varied range of speeds between 300rpm and 3000rpm have been selected, representing the turbulent flow to mimic the field flow conditions, as shown in Table 5.3.

Table 5.3: RCE hydrodynamic parameters in this study

Rotation rate, F (rpm)	Rotation rate, w (rad/s)	Surface Velocity, $U_{cyl.}$ (cm/s)	Wall Shear Stress, $\tau_{cyl.}$ (g/cms^2)	Reynolds Number, Re
300	31.41	18.86	2.67	**1269**
500	52.36	31.44	6.37	**2115**
800	83.77	50.30	14.16	**3385**
1000	104.71	62.88	20.70	**4231**
3000	314.14	188.64	133.98	**12692**

The calculated hydrodynamic parameters were based on assumptions of water properties at 25 °C, such as density of 0.997 g cm^{-3}, absolute viscosity of 0.009 g cm^{-1} s^{-1}.

The transition from laminar to turbulent flow is typically characterized by Reynolds number (Re) to quantify the ratio between inertial forces and viscous forces in the solution. Values of Re < 50 are characteristic of laminar flow, whilst values Rec > 300 are characteristic of turbulent flow (294) . The key advantage of using the RCE is that it can actually provide the relevant information about scale and corrosion kinetics if its operating conditions produce similar mass transport to those conditions found in the field. The RCE parameters shown in Table 5.3 were determined using the following expressions:

- Reynolds number (Re):

$$Re_{RCE} = \left(\frac{\omega \times r_{RCE}{}^2}{\mu} \right)$$ (5.1)

Where, Re represents the Reynolds number value, w. (rad s^{-1}) is the rotational rate of the RCE, r_{RCE} is the outside radius of the RCE cylinder, and µ (g cm^{-1} s^{-1}) is the absolute viscosity of the bulk solution, assumed to be the same as seawater.

- Eisenberg's wall shear stress ($\tau_{cyl.}$):

$$\tau_{cyl.} = 0.0791 \times \rho \times Re^{-0.3} \times U_{cyl.}^2$$ (5.2)

Where, $\tau_{cyl.}$ (g cm^{-1} s^{-2}) represents the RCE wall shear stress, ρ (g cm^{-3}) is the density of the solution, Re is the Reynolds number at a specific rotational speed and $U_{cyl.}$ (cm s^{-1}) is the outer cylinder linear velocity.

Figure 5.8 shows the relationship between the fluid velocity and shear stress at the RCE boundary layer.
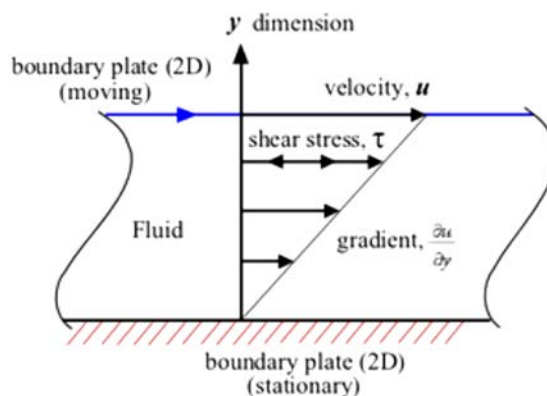
Figure 5.8: An illustration of the wall shear stress at the RCE

Turbulent flow at the RCE will induce shear stress at the surface of the cylinder and this will subsequently affect the mass transfer process within the bulk and RCE vicinities.

5.4.3.4 Influence of the temperature

Further tests have been done to assess the effect of temperature on scaling and corrosion at 25°C and 80°C, and fixed rotational speed of 500rpm (Re=4222). This test provided the mass gain/loss kinetics, $CaCO_3$ phase transformation over time and characterisation of the two metals used for this study with respect to corrosion pits.

5.4.4 Experimental Procedure

The same five brine compositions (Table 5.1) used for bulk crystallisation studies were also used for surface kinetics analysis. Brine solutions mixing time for a 1L vessel was determined via the dye method used in bulk section 5.3.4 and a total mixing time of 35 seconds was obtained. The pH of the mixing solution was controlled throughout the reaction time.

Surface tests were done at two temperatures 25°C and 80°C, using two metals (carbon steel X-65 and stainless steel 316L) and electrochemical LPR readings were taken over 24 hours. Then scale and corrosion deposition kinetics were assessed via weight measurements and surfaces characterised with post-test analyses. For assessing the effect of temperature, a fixed rotational speed of 500rpm was applied. Furthermore, the effect of flow hydrodynamics on scale formation was done using different rotational speeds from 300rpm to 3000rpm as shown in Table 5.3, at a fixed temperature of 80°C. Lastly, crystals were characterised with respect to their shape,

size and structure using SEM, EDXS, XRD and ICP. The white light interferometry was used for characterising the corroded substrates.

5.4.5 RCE Data Analyses

5.4.5.1 Mass deposition measurements

Weight measurements were taken to quantify the amount of scale deposited over time. In theory, the scale deposition rate will follow a profile similar to the one shown in Figure 5.9. This shows a typical representation of the expected behaviour for $CaCO_3$ mass deposition over time under dynamic conditions.
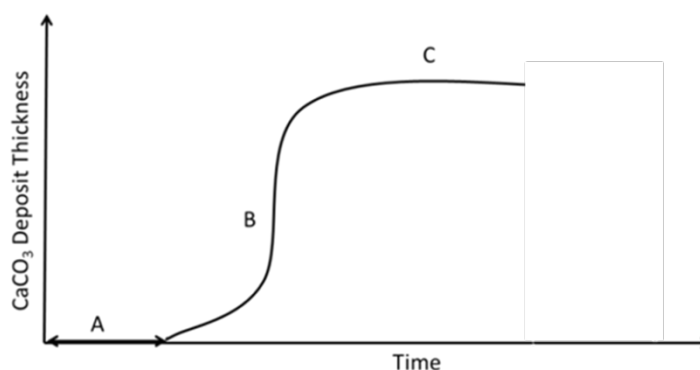
Figure 5.9: Theoretical behaviour of surface scale deposition over time at a fixed flow rate

Four main regions are observed in Figure 5.9, illustrating an overall increase in mass deposition which reaches a plateau after a while. This behaviour has been confirmed in previous studies (101) (295) . Region A can be seen as the induction time and nucleation onset in which very small amounts of scale starts forming at the metal substrate. Region B is demarked by crystal growth as the reaction proceeds. Polymorphic transformation may also take place during the growth stage until it reaches a steady state. Region C indicates that no more scale can be adhered to the metal surface, leading to a constant film thickness up to that point. The surface precipitation rates were determined using Equation (4.28).

5.4.5.2 Corrosion rate measurements

Corrosion rate data was obtained from in-situ LPR measurements and the software considered the surface area of the working electrode and the general corrosion rate expression (4.20). This data was useful to understand the relationship between $CaCO_3$ surface scale deposition and corrosion mechanisms. An assumption has been made to assess the induction time as the time taken for the film to form in the substrate, i.e. period at which the corrosion rate drops.

5.5 Post-Test Characterisation techniques

Post-experiment analyses were supported by ex-situ particle characterization techniques, which helped to further understand $CaCO_3$ bulk and surface crystallization processes, as well as characterize the corroded surfaces after removal of surface scaling.

5.5.1 Mastersizer Hydro – S^{TM} 2000

Mastersizer Hydro-S 2000 (Malvern Instruments Ltd., U.K.) was used to determine the particle size distribution for $CaCO_3$ bulk crystals formed over time. This instrument enabled measuring $CaCO_3$ crystal size particles using a laser diffraction method with a dual wavelength detection system (i.e. from sub-micron to millimetre), single lens system which measured samples from 0.02 µm to 2000µm, ultrasound which ensured no particles agglomeration, agitation which avoided particles sedimentation and software auto align facility which guaranteed precision and optimization of the readings. During the size measurement process (Figure 5.10), a focused laser beam passed through a dispersed solution and the intensity of light diffracted was measured a series of photosensitive detectors. Finally, the particle size distribution was determined according to the measured diffraction pattern as these particles scatter light at an angle that is inversely proportional to their size (296).
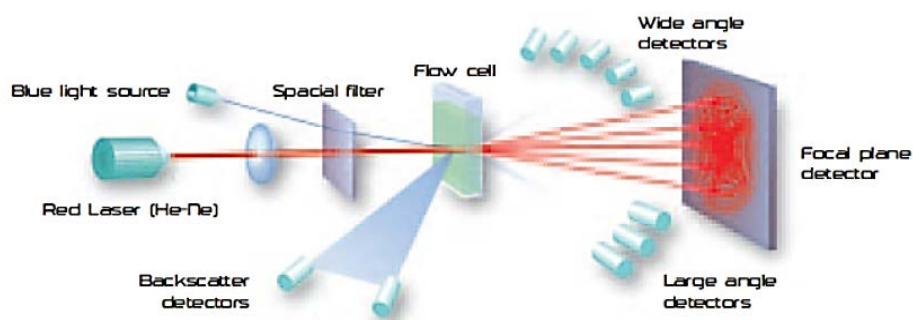
Figure 5.10: Illustration of the laser diffraction components used with Mastersizer particle size measurements (296)

The Mastersizer accuracy for particle size measurements is due to the use of two combined models: Fraunhofer and Mie. The Fraunhofer theory (296) is only suitable for particles with large dimensions and the small scattering angle (< 30º). The Mie light scattering model is more complex but suitable for smaller particles (297) within the sub-micron region and requires the knowledge of optical properties such as the refractive index and the imaginary components of the dispersant and the fluid. The

refractive index was checked with the literature and was taken to be 1.572 for calcite ($CaCO_3$) (296) with an imaginary refractive index of 0.01, and 1.33 as the refractive index for the dispersant (i.e. distilled water).

5.5.2 Sysmex FPIA 2100^{TM}

The operating principle of the Sysmex (Malvern Instruments Ltd., U.K.) device is shown in Figure 5.11 and consists of video imaging analysis that provide a feasible method of determining both size and shape of particles, illustrating whenever agglomerates are present in the solution. The image analysis captures a 2D image of the 3D particle and calculates various sizes and shape parameters from the 2D image (298). The equivalent particle diameter (CE) is determined and assumed to be the diameter of the circle with the same area as the 2D image. Once the distribution is generated all statistical parameters such as mean, median, mode and standard deviation can then be easily calculated. The working size range varies from 0.8 µm to 300 µm, being smaller than Mastersizer size measurement capacity.
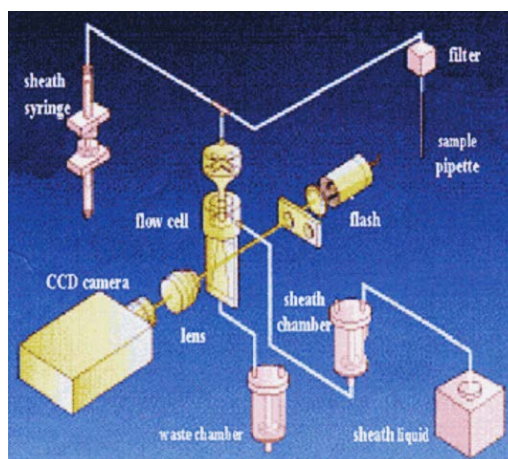
Figure 5.11: Schematic diagram of the main components used during Sysmex FPIA 2100 particle size measurements (298)

5.5.3 Scanning Electron Microscopy (SEM) and Energy Dispersive X-ray Spectroscopy (EDX-S)

The SEM enables observing and characterising materials (organic or inorganic) from a nanometre (nm) to a micrometre (µm) scale. This device works by firing a high energy electron beam onto a specimen. The beam interaction with the sample will cause several subsequent electron emissions/ x-rays to be released from the sample. So, the electron manipulation will control the size, shape and position of electron

beam on the sample (299). The SEM gives the advantage of providing three-dimensional images with a vast range of magnification varying from 10 – 10,000x.

Two different SEM machines were used for characterising $CaCO_3$ crystal particles, namely, the Carl Zeiss Evo MA15® and LEO 1530®. The two SEM machines work in a similar way, with the advantage being that LEO 1530® can provide much higher resolution ranges compared to the Evo MA15®. The working principle consists of irradiating the gold coated samples with a finely focused electron beam which interactes with the $CaCO_3$ crystal surface to provide characteristic features of the sample's surface such as their topographic reflexion, crystallography and chemical composition.

The Phoenix energy dispersive X-ray spectroscopy (EDX-S) was used for elemental analysis or chemical characterisation of the samples, since each of the detected elements would have a specific spectrum. During EDXS analyses, the electron beam intensity was changed to 20 keV and the working distance adjusted accordingly to the sample's height. Finally, the point and ID approach was used during data analyses, providing both qualitative and quantitative analysis for $CaCO_3$ samples.

5.5.4 X-Ray Diffraction

The X-ray diffraction (XRD) is a unique method used for identifying and characterising the chemistry of a crystalline compound. The Philips X'Pert XRD machine was used in this study to aid characterising the crystalline structures of $CaCO_3$. This technique is based on the interaction of an incident x-ray on a targeted sample, which creates a constructive interference and diffracted x-ray when the conditions satisfy the Bragg's law ($n\lambda=2d.\sin\Theta$) (14).

Bragg's law (Figure 5.12) relates the wavelength (λ) of an electromagnetic radiation to the diffraction angle (Θ) (and the lattice spacing) in a crystalline sample. Hence, a characteristic XRD pattern is generated in form of a unique fingerprint of the crystal sample. However, it is important to have an understanding of the chemical components present on the sample for better understand the XRD patterns created.
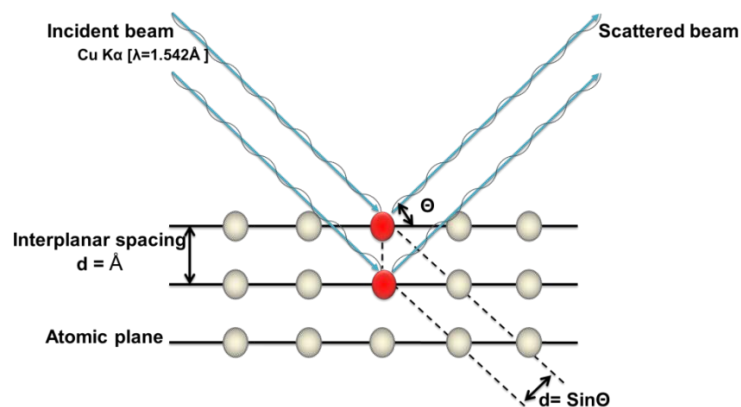
Figure 5.12: Schematic diagram of the constructive interference of an incident beam to a crystal, following Bragg's law principle

For bulk crystals assessment, 1/2g of $CaCO_3$ powder was needed in order to fully cover the round stainless steel disc sample holder. It is very important to use pure powder, tightly packed (i.e. flat) in the sample holder, to avoid poor x-ray intensities with high noise. However, for surface crystals, the sample holder used was a bracket and a cross-sectional area of the RCE working electrode was selected for characterising the film deposits. The metal cylinder was challenging to analyse due to its curvature, which would easily cause background noise when the X-ray reached the surface of the cylinder.

At the start of each test, an X-ray was produced by bombarding the copper metal source (Cu K_α) with a beam of electrons emitted from a Tungsten hot filament. The incident beam of 40keV ionized the electrons from the targeted sample (Cu K_α) and an x-ray resulted for Cu, K_α at 1.542Å wavelength. The Phillips X'Pert HighScore Plus diffractometer software was used during experiments and the scanning time was set to 2 seconds; step length 0.1 ° and the diffractions were run over a 2 Θ – range from 20 °– 60 ° (bulk studies) and from 20° – 40° (surface studies). Lastly, the obtained XRD patterns were analysed using the HighScore Plus database software.

5.5.5 Inductively Coupled Plasma (ICP) Optical Emission Spectroscopy

The ICP is a type of mass spectroscopy technique which is capable of detecting the chemical composition of different samples by quantifying the concentration of specific ions (300). This technique can detect most of the periodic table elements at detection limits within thousands parts per million (ppm). As illustrated in Figure 5.13, the sample is ionised by argon plasma and most of the elements present are excited, emitting a light with a specific wavelength which is characteristic to the detected element. The light intensity will be proportional to the amount of the element present

in the sample. Typically, samples are analysed in liquid form, because solid particles can affect the stability of the readings, and for that reason most solid samples must undergo dilutions.
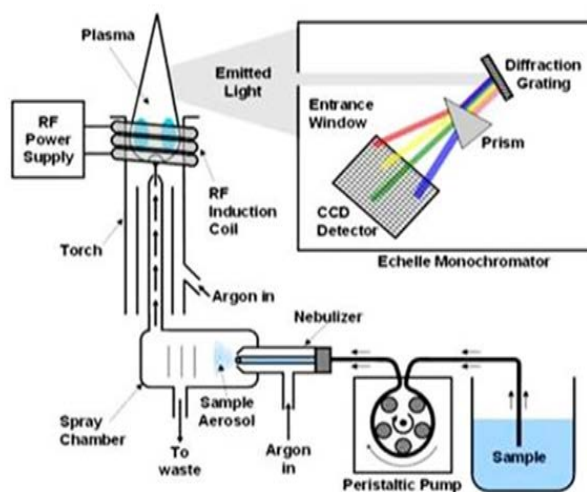
Figure 5.13: Schematic representation of the ICP technique (301)

The use of ICP was crucial for quantifying the amount of calcium and iron species present at the surface of the RCE samples. The solid precipitates deposited at the surface of the RCE were diluted in 20 ml of 10% v/v acetic acid for 48 hours to ensure that all crystals were removed from the sample. Then, 10 ml of the solution containing dissolved $CaCO_3$ scale and any corrosion products were sent for analysis of calcium (Ca^{2+}) and iron (Fe^{2+}) ions. The final results took into account the dilution factor applied during the analysis, and were expressed in milligrams (mg) of calcium (Ca^{2+}) or iron (Fe^{2+}) from the $3.77cm^2$ sample surface area, or converted to mg/cm^2.

5.5.6 White Light Interferometer

The NPFLEX® – 3D interferometer is a non-contact technique which divides a white light beam source (similar to a laser) into two beams and recombines them in order to extract information about the original waves and create an interference pattern of the observed surface (Figure 5.14). The light interference pattern will be crucial to analyse the surface irregularities and aid characterising the RCE steel substrate prior and post testing. This method aimed to identify any damages caused by corrosion at the steel surface. After experiments conducted in carbon steel X-65 samples, the scale was removed from the surface using Clarke's solution. Clarke's solution was prepared by using 20g antimony trioxide and 50g stannous chloride in 1L hydrochloric acid mixed at room temperature for 25 minutes (302).
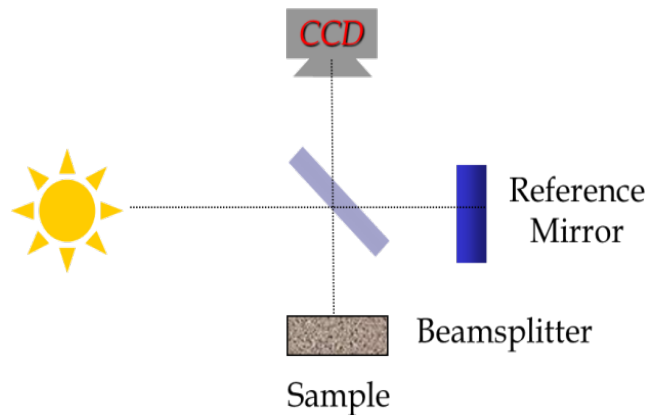
Figure 5.14: Schematic representation of the interferometer apparatus

The key advantage of using the white light interferometer is that it allowed characterising the sample substrate with respect to their surface texture, roughness, depths, peaks, and other characteristics at Angstrom-level of accuracy. Among the different capabilities of this technique, the results were given in terms of identification and quantification of surface irregularities such as pits (i.e. valleys or holes or fractures caused by corrosion) and finally a 3D imaging of the analysed surface. For quantifying the number of deep pits, the NPFLEX® software applied a threshold and would consider pits to have deeper valleys than the set threshold as shown in Figure 5.15. The generated pitting data used two different thresholds depending on the overall surface roughness of the corroded samples. So, the threshold varied from 1μm to 5μm for the least to heavily corroded surfaces. This technique was very important to aid characterising localised corrosion due to the loss of the metal at a specific point of the substrate.
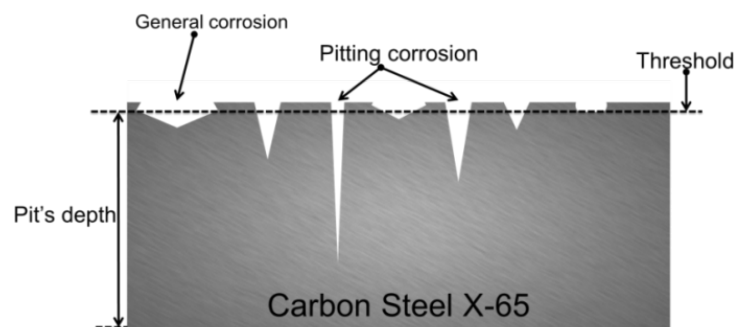
Figure 5.15: Cross-sectional illustration of general and localised corrosion. The pit's depth is taken from the set threshold value.

5.6 Limitations of Selected Techniques

All techniques and methods applied in these studies were selected in order to establish a robust protocol for assessing the crystallization stages (i.e. nucleation and

crystal growth) of $CaCO_3$ in bulk solutions and at metal surfaces. Table 5.4 summarises some of the possible limitations encountered with the techniques used.

Table 5.4: Limitations of techniques used for bulk and surface crystallization studies

Technique	Key Limitations
Brine preparation	Measuring scale calibration and presence of impurity particles in salts
In-situ probes: pH/ISE (Ca^{2+})/light transmittance turbidity	All probes require appropriate calibration prior to use. The ISE (Ca^{2+}) probe could operate only at temperatures below 40°C. Transmittance turbidity probe is only effective for extremely saturated solutions
XRD	XRD readings are not very effective on surfaces that are not flat, causing noisy background and tendency for peaks to shift if the beam hits the curvy RCE edges
Mastersizer	Measurements are volume based and assume that all particles are spherical. Poor size distribution for very low concentrations
Sysmex	Measurements are based on number of particles and it assumes a circumference equivalent diameter based on a 2D pictographic image
RCE Three-electrode-cell set-up	Requires a good contact of the 3 cell electrode to ensure transmittance of conductivity
ICP	Works better for liquids. The dilution from RCE coupons may cause some misleading results
Interferometer	Requires setting of a threshold based on the surface roughness detection

5.7 Closing Remarks

This chapter presented a very detailed description of the materials, experimental set-ups, procedures, testing conditions and several techniques used during the bulk and surface crystallization processes investigation.

The scale simulation software, MultiScale was used for predicting the field's brine saturation ratios at 80°C. These brines have been prepared with Analar Grade salts to avoid contamination during the tests.

The methods developed for bulk and surface crystallization studies have been supported by a literature search in order to understand and select the best approaches to build a kinetic model for $CaCO_3$ mineral scale. The equations used to assess the raw kinetic data are cross-referenced to literature chapters for scale (Chapter 3) and corrosion (Chapter 4).

Lastly, a summary of the key limitations that could be encountered with the selected techniques has been listed and described (Table 5.4) in order to emphasise any experimental errors and assumptions that should be taken into consideration.

Chapter 6 - *In–Situ* Monitoring and Characterization of a Calcium Carbonate Bulk Crystallization Process

Summary

This chapter presents and describes all results obtained for calcium carbonate crystallization experiments from saturated bulk solutions. The crystallization mechanisms and kinetics were assessed for a range of supersaturation at three different temperatures and the key findings are discussed and summarised here.

6.1 Introduction

This chapter presents and discusses all of the results obtained for the bulk crystallisation of $CaCO_3$, taking into account factors such as the supersaturation, temperature, in-situ pH, in-situ calcium-ion concentration and the reaction time. The work presented in this chapter is intended to contribute towards a more comprehensive understanding of the fundamental mechanisms and kinetics involved during $CaCO_3$ crystallization in bulk solutions. The main findings aim to improve the existing understanding of the $CaCO_3$ spontaneous precipitation process and to provide additional knowledge regarding the kinetics and crystal characterization with respect to their morphology and size. The outline of this chapter is given in Figure 6.1:
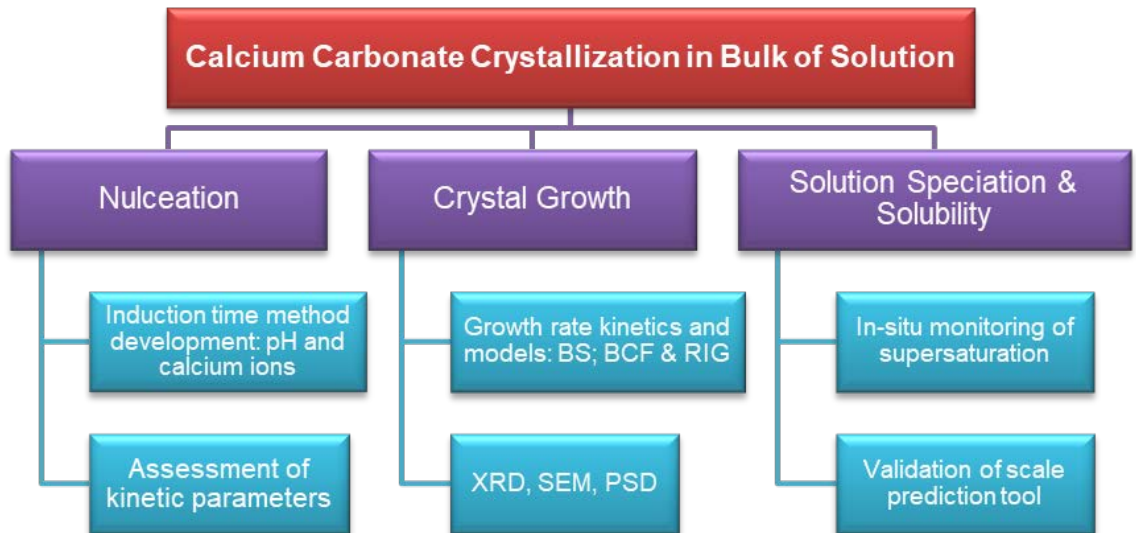
Figure 6.1: Route map for key topics investigated for the results and discussion of calcium carbonate crystallization processes, including methodologies and theories applied for data interpretation

6.2 Calculation of Temperature Dependent Supersaturation from Solution Speciation Data

6.2.1 Scale Prediction Modelling – MultiScale^{TM}

MultiScale^{TM} software (*version 7.1*) was used as a thermodynamic prediction tool to determine the scaling tendency of the original brines at different temperatures. In order to broaden the scope of this research study, further scale tendency predictions have been made at 25°C and 40°C keeping the same initial supersaturation as those given for North Sea field shown in Chapter 5 (Table 5.1). The output obtained from these MultiScale^{TM} simulations provided the brine chemistries to be used in experiments at different temperatures. Furthermore, simulations predicted pH values are also presented.

In these scaling simulations (Table 6.1 – Table 6.5), the original field brine composition (Table 5.1) was used as a baseline to predict identical scaling saturated systems at lower temperatures, so a full study for bulk crystallization could be done considering that same saturated brines can be found at different system temperatures. Therefore, the alkalinity of the system was kept constant (i.e., identical to Table 5.1), but the concentration of calcium species was assumed to change for different parts in the system. The software calculates all parameters as a function of salt composition input. The calcium chloride levels were manipulated in order to achieve the same supersaturation at different temperatures, keeping the alkalinity of the solution constant. In addition, the levels of NaCl had to be adjusted for mass balance purposes. Parameters such as ionic strength and fugacity factors were determined to estimate the supersaturation at different temperatures using thermodynamic and equation of state models (e.g., vapour liquid equilibrium models, Pitzer, Soave-Reddlich-Kwong, Peng-Robinson). To summarize the supersaturation was defined as saturation ratio by Equation (6.1):

$$SR_{CaCO_3} = \sqrt{\frac{\left[(a_{Ca^{2+}})\left(a_{CO_3^{2-}}\right)\right]}{K_{sp,CaCO_3}}} \tag{6.1}$$

It is evident from equation (6.1) that any increase in the concentration of CO_3^{2-} will increase the saturation ratio and vice-versa. This emphasises the effect of CO_2 – equilibrium during $CaCO_3$ crystallization, as the solubility of $CaCO_3$ scale is dependent on species that impact the pH of the system. Therefore, any changes in the system pH can alter the concentration of CO_3^{2-} ions present in the brine. For that reason, the brine composition predictions also calculated the different pH expected

for the fixed saturation ratios. Note that the initial system pH (i.e., pH initial mixture) corresponds to the initial amount of H^+ ions present in the brine in order to induce $CaCO_3$ precipitation. In reality, the system may not be as sensitive to the initial pH value since there is also HCO_3^- in the system which contributes dominantly to the acid equilibrium. On the other hand, the pH equilibrium corresponds to the pH determined after running thermodynamic calculations assuming the equilibrium state has been reached. The synthetic brines were separated into two waters, one containing all anions and the other containing all cations. Therefore, the simulated pH for the water containing anions (i.e., pH_{AW}) and the water containing cations (i.e., pH_{CW}) were also modelled as a function of temperature for each case study. The calculated brine chemical composition as a function of temperature is summarised from Table 6.1 to Table 6.5.

Table 6.1: Brine composition for case 1 of saturation ratio equal to 1.52 (lowest brine case) at 1 bar and three different temperatures

Case 1 (SR=1.52) Temperature (°C)	[Ca^{2+}] mmol/l	[HCO$_3^-$] mmol/l	pH$_{(AW)}$	pH$_{(CW)}$	pH$_{Initial of mixture}$	pH$_{Equilibrium}$
25	12.80	5.00	6.89	7.71	7.71	7.54
40	10.25	5.00	6.69	7.67	7.62	7.45
80	5.00	5.00	6.24	7.55	7.49	7.35

Table 6.2: Brine composition for case 2 of saturation ratio equal to 2.55 at 1 bar and three different temperatures

Case 2 (SR= 2.55) Temperature (°C)	[Ca^{2+}] mmol/l	[HCO$_3^-$] mmol/l	pH$_{(AW)}$	pH$_{(CW)}$	pH$_{Initial of mixture}$	pH$_{Equilibrium}$
25	17.50	6.50	6.89	7.76	7.69	7.31
40	13.70	6.50	6.69	7.67	7.61	7.23
80	6.50	6.50	6.24	7.55	7.49	7.16

Table 6.3: Brine composition for case 3 of saturation ratio equal to 4.77 at 1 bar and three different temperatures

Case 3 (SR= 4.77) Temperature (°C)	[Ca^{2+}] mmol/l	[HCO$_3^-$] mmol/l	pH$_{(AW)}$	pH$_{(CW)}$	pH$_{Initial of mixture}$	pH$_{Equilibrium}$
25	24.30	9.00	6.89	7.76	7.67	7.06
40	19.35	9.00	6.69	7.67	7.59	6.98
80	9.00	9.00	6.24	7.56	7.51	6.94

Table 6.4: Brine composition for case 4 of saturation ratio equal to 11 at 1 bar and three different temperatures

Case 4 (SR= 11) Temperature (°C)	$[Ca^{2+}]$ mmol/l	$[HCO_3^-]$ mmol/l	$pH_{(AW)}$	$pH_{(CW)}$	$pH_{Initial\ of\ mixture}$	$pH_{Equilibrium}$
25	28.95	12.20	6.89	7.98	7.84	6.90
40	24.30	12.20	6.69	7.87	7.73	6.81
80	12.35	12.20	6.24	7.69	7.58	6.75

Table 6.5: Brine composition for case 5 of saturation ratio equal to 55 at 1 bar and three different temperatures

Case 5 (SR= 55) Temperature (°C)	$[Ca^{2+}]$ mmol/l	$[HCO_3^-]$ mmol/l	$pH_{(AW)}$	$pH_{(CW)}$	$pH_{Initial\ of\ mixture}$	$pH_{Equilibrium}$
25	108.00	30.48	6.92	7.88	7.59	6.23
40	87.50	30.48	6.71	7.79	7.49	6.16
80	35.94	30.48	6.26	7.69	7.43	6.19

The predicted pH values for the individual anions (pH_{AW}) and cations water (pH_{CW}) are very important to understand the differences between modelling and experiments and also during data analyses to consider the relationship between thermodynamics and kinetics involved in $CaCO_3$ precipitation.

To summarise, a range of different concentration brines (i.e., saturation ratios of 1.52, 2.55, 4.77, 11 and 55) has been simulated and used for the bulk experimental studies. It is important to emphasise that five saturated brine chemistries were simulated for bulk crystallization studies over a range of temperatures 25°C, 40°C and 80°C.

6.3 Nucleation Study

The nucleation process is the most challenging stage of crystallization as it is hard to identify, analyse and control the formation of nuclei particles, due to their small size. Several approaches (303) (304) (305) have been made to study nucleation phenomena during spontaneous crystallization of $CaCO_3$. One of the reasons none of them have led to a satisfactory quantitative model is due to the fact that the nucleation theory is hard to verify through experimental results. Studies of the $CaCO_3$ nucleation process are sensitive to the techniques and methodology approaches, so

the criteria for judging when the nucleation takes place is not always reliable, usually due to equipment limitations for identifying crystal sizes at such an early stage of crystallization.

The aim of this section is to evaluate a number of process analytical techniques to develop an effective method for bulk induction time measurements and extrapolate the nucleation mechanisms and kinetics from the data acquisition and analysis via the classic nucleation theory.

The following techniques have been selected based on their capabilities to monitor changes in solution in-situ: pH, calcium ions, conductivity, turbidity and FBRM. The most suitable methods will be used to elucidate further knowledge on the nucleation kinetics and mechanisms involved during spontaneous precipitation of $CaCO_3$ under different conditions.

6.3.1 Induction Time Method Development

This part of the study determines the nucleation kinetics and growth mechanisms involved during this reactive crystallization process. The relationship of particle–liquid interactions, crystal size and shape is also recognized and related to the best induction time method selected for the different saturated brines.

6.3.2 *In-situ* pH Measurements

During bulk crystallization process, the pH has been recorded in-situ from the start of each experiment. These tests were done at atmospheric pressure using five saturated brine solutions at three different temperatures, as described in Table 6.1 to Table 6.5. Hence, the relationship between supersaturation, temperature and pH could be elucidated during the spontaneous crystallization process. The measurement of pH in-situ was essential to follow and understand the kinetics involved during $CaCO_3$ precipitation.

6.3.2.1 pH measurements as a function of the initial supersaturation

Two single synthetic brines containing the cations (i.e. calcium ions) and the anions (i.e. bicarbonate ions) were mixed in a batch reactor and the pH mixing of the bulk solution was recorded throughout the experiment. In order to assess the effect of supersaturation on pH, the running temperature was kept constant. The pH measurement results obtained for a range of supersaturated solutions at 25ºC can be seen from Figure 6.2 to Figure 6.6. In addition, the induction time for these

experiments has been estimated using the inflection point method as described in the data analysis section 5.4.2. This approach considers that a drastic change in pH is marked by a peak and that can be taken as the nucleation onset. Typically, during the precipitation of calcium carbonate, an initial drop in pH is expected indicating the ionic dissociation from carbonic acid to form bicarbonate ions which then react with calcium ions to form $CaCO_3$ crystals. However, in an aerated system where there is a continuous vapour liquid interaction from the aqueous solution and air components, the CO_2 may affect the kinetics for the spontaneous precipitation process to take place. These relationships were assessed over a range of saturated brines at different temperatures. So it will be interesting to see how the CO_2 equilibrium may affect the nucleation onset via pH measurements.

Case 1 is the lowest saturated brine solution with a saturation ratio (SR) of 1.52 at 25°C. The induction time has been estimated to be approximately 13 hours and 30 minutes as illustrated in Figure 6.2. This induction time has been estimated based on the fact that the pH trend seems to reach the equilibrium around that time and a maximum peak is registered. In addition, the crystallization kinetics are much slower at such a low concentration (i.e. SR=1.52), being closer to equilibrium condition (i.e. SR = 1). Lastly, the visual observations of the bulk solution remained as a bright clear liquid, with a few crystals visible to the naked eye after 22 hours.
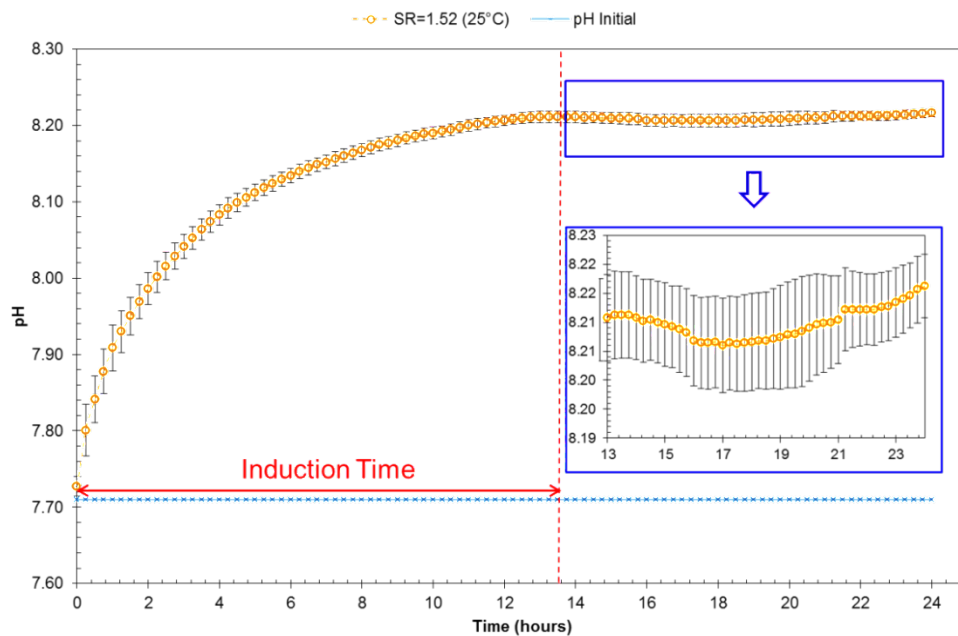
Figure 6.2: Experimental pH profile for Case 1 (SR=1.52) at 25°C.

Case 2 represents the second lowest supersaturated brine studied, whose saturation ratio (SR) corresponded to 2.55 at 25°C. According to the pH profile shown in Figure 6.3, the induction time is estimated to be approximately 11 hours (maximum peak).

This curve does not show the expected drop in pH after mixing both brines. There are a few possibilities that may explain this profile:

- The reaction kinetics for $CaCO_3$ precipitation at low supersaturation and temperature are very slow;
- The mixing pH of the brine needs to increase to an optimum value for the start of nucleation stage;
- The pH electrode cannot detect the precise moment where nucleation starts due to extremely slow kinetics, so no significant drop in pH is observed;
- The supersaturation degree (SR=1.52) is quite close to the equilibrium saturation ratio (SR=1) making it harder to detect the crystallisation onset via pH measurements, as the reaction kinetics are slower and less ions dissolve quickly in solution to form $CaCO_3$ crystals.
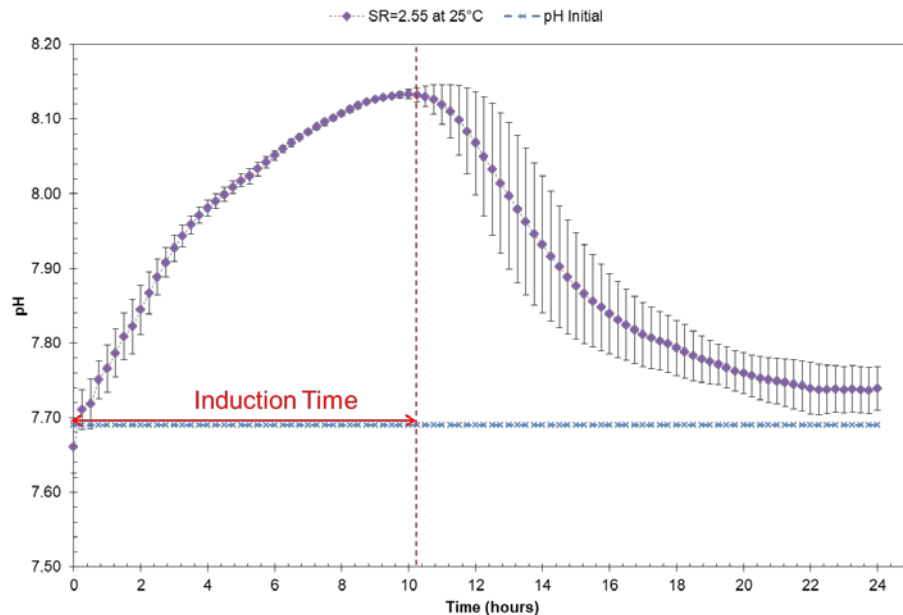
Figure 6.3: Experimental pH profile for Case 2 (SR=2.55) at 25°C.

Case 3 represents the brine with a saturation ratio of 4.77 at 25°C. The pH profile shown in Figure 6.4 illustrates an induction time of approximately 2 hours and 10 minutes.
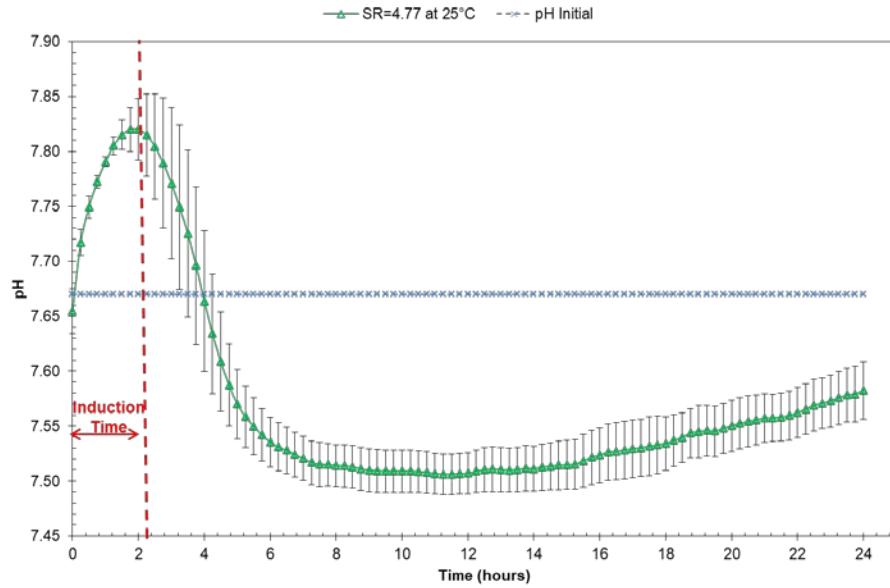
Figure 6.4: Experimental pH profile for Case 3 (SR=4.77) at 25°C.

Case 4 represents the brine with a saturation ratio (SR) of 11 at 25°C. The pH profile differs from the low saturated brine solutions (i.e. Cases 1 to 3) and so the induction time was assessed by the tangent method. The induction time for Case 4 was estimated to be 1 hour and 45 minutes.
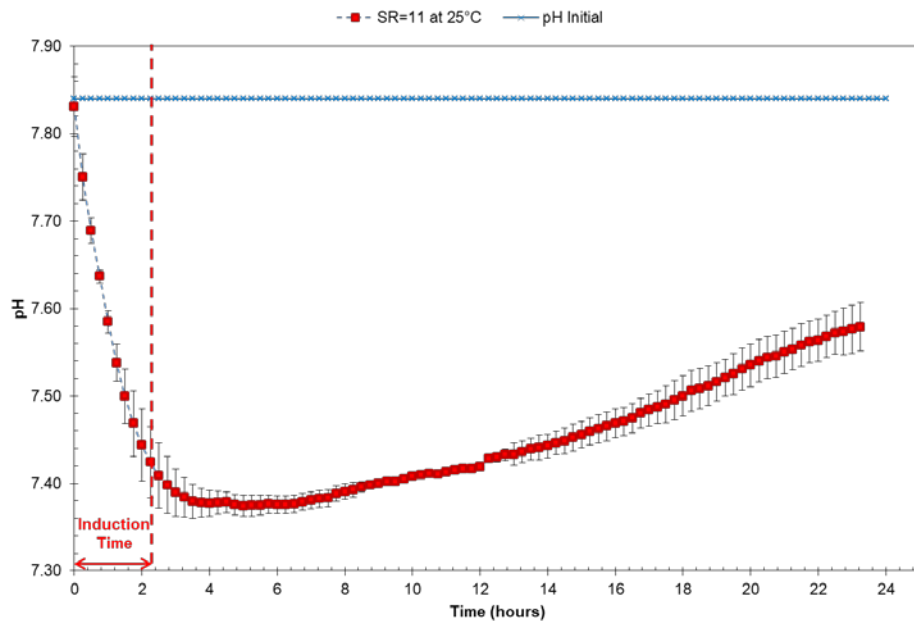
Figure 6.5: Experimental pH profile for Case 4 (SR=11) at 25°C.

Lastly, Case 5 represents the highest saturation case study with a saturation ratio (SR) of 55. The pH profile followed the typical expected curve and the induction estimated as 0.75 hour or simply 45 minutes.
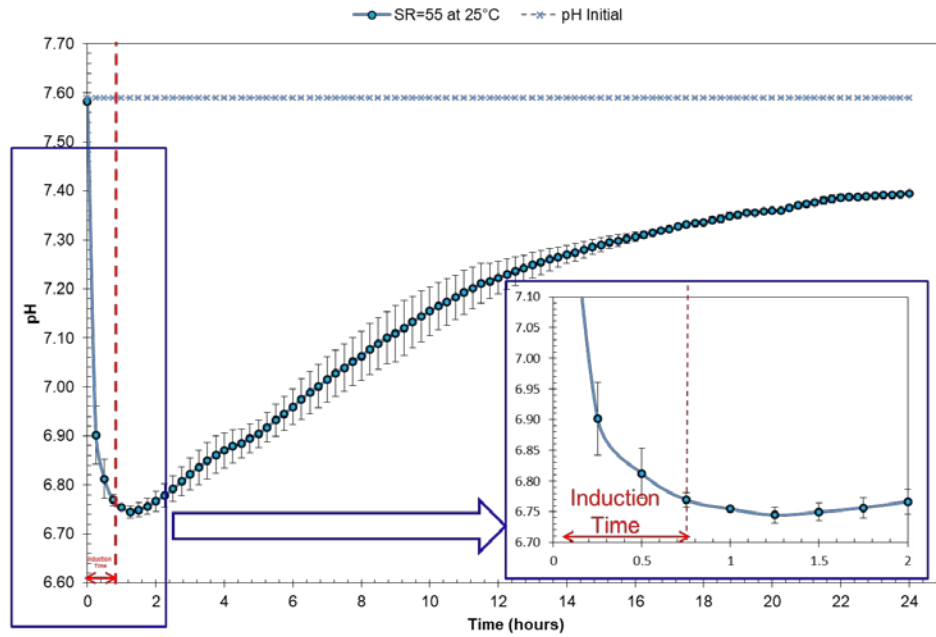
Figure 6.6: Experimental pH profile for Case 5 (SR=55) at 25°C.

It can be observed that the pH profile curves for the low saturation brines (i.e. Figure 6.2 to Figure 6.4) differ from highly saturated ones (i.e. Figure 6.5 and Figure 6.6). This suggests that crystallization kinetics is dependent on supersaturation, as this is the main driving force. Hence, at high supersaturation, the pH curve follows the expected initial decrease during the dissociation of bicarbonate ions from the solution, increasing the amount of hydrogen ions and free carbonate ions. Once the available carbonate ions react with the available calcium ions, the chemical reaction takes place and $CaCO_3$ crystals are formed in the bulk solution. As a result of this reaction shown in Equation (2.13), the pH starts to increase because of the high amount of carbonate ions reacting with calcium to produce more $CaCO_3$ crystals. In addition, the $CaCO_3$ crystals formed in solution are insoluble in water at 25°C and the system tries to get to equilibrium conditions.

As the reaction crystallization proceeds, the initially saturated solution adopts a lower saturation ratio value and more crystals are formed until the equilibrium state is reached and no more bulk crystals can be formed. Therefore, the pH readings can be useful to estimate the time taken for the appearance of the first crystal nuclei, i.e. the induction time. The overall pH profiles at 25°C for all supersaturation case studies are shown in Figure 6.7.
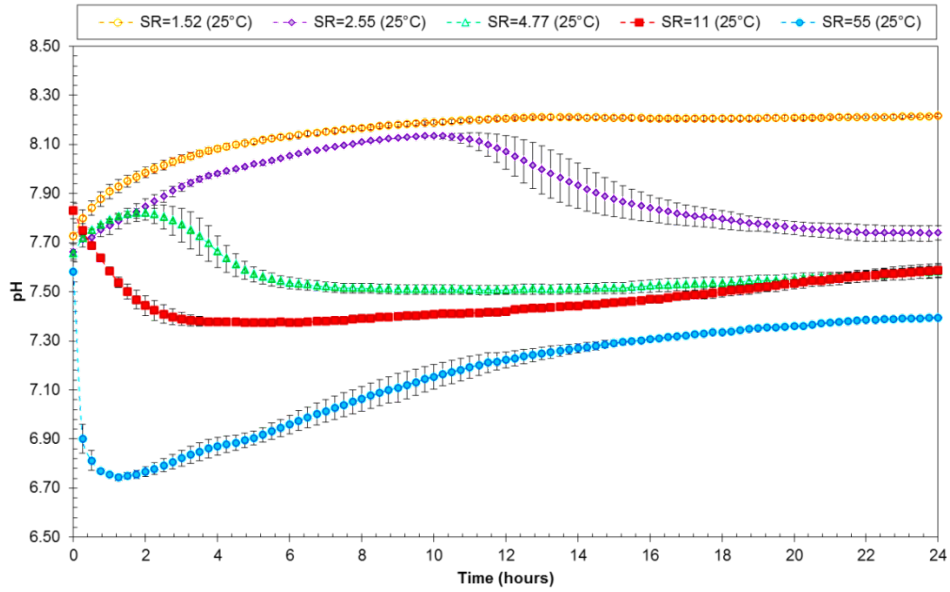
Figure 6.7: pH profile behaviour at 25°C with increased in supersaturation

Peaks falling out of the ideal peak profile earlier described have also been observed in other studies (306) for bulk crystallization of $CaCO_3$ and $CaSO_4$ and the method used to determine the induction time which they called "germination of crystals" is also identical to the proposed "inflection point peak".

6.3.2.2 pH measurements as a function of temperature

The assessment of temperature on $CaCO_3$ crystallization was also monitored through pH measurements to further understand the kinetics involved in this process. Hence, the same five saturated bulk solutions have been left to crystallize for 24 hours at 25°C, 40°C and 80°C, as shown in Figure 6.8 to Figure 6.12.

Each of the in-situ pH measurement tests provided in Figure 6.8 to Figure 6.12, were repeated at least three times under the same testing conditions to ensure reliability of the data collected for accurate estimation of the induction time. The induction time was estimated at 40°C and 80°C and followed the same graphical principles used in section 6.3.2.1 for 25°C. The use of pH profiles for estimating the induction time was critical to understand the kinetics of nucleation and crystal growth stages, in-situ.
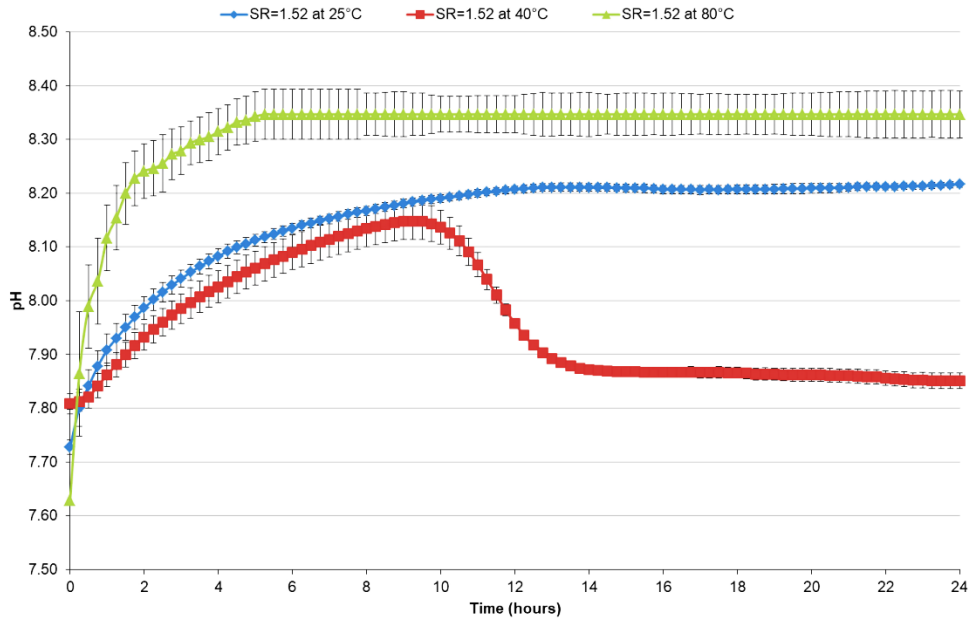
Figure 6.8: Case 1 (SR=1.52) pH changes with increase in bulk temperature

For Case 1, the increase in temperature shows an impact on the crystallization kinetics which is remarked by the different pH curves at 25°C, 40°C and 80°C. These three curves showed a similar initial mixing pH, which started from 7.50 to 7.80. The overall trend did not show an initial pH drop as expected, but in contrast the pH curve increased until a steady pH-value was reached. The pH trends at 25°C and 40°C have shown very similar behaviour from the start of the experiment until approximately 10 hours, where the pH at 40°C shows a decline until reaching a plateau line.
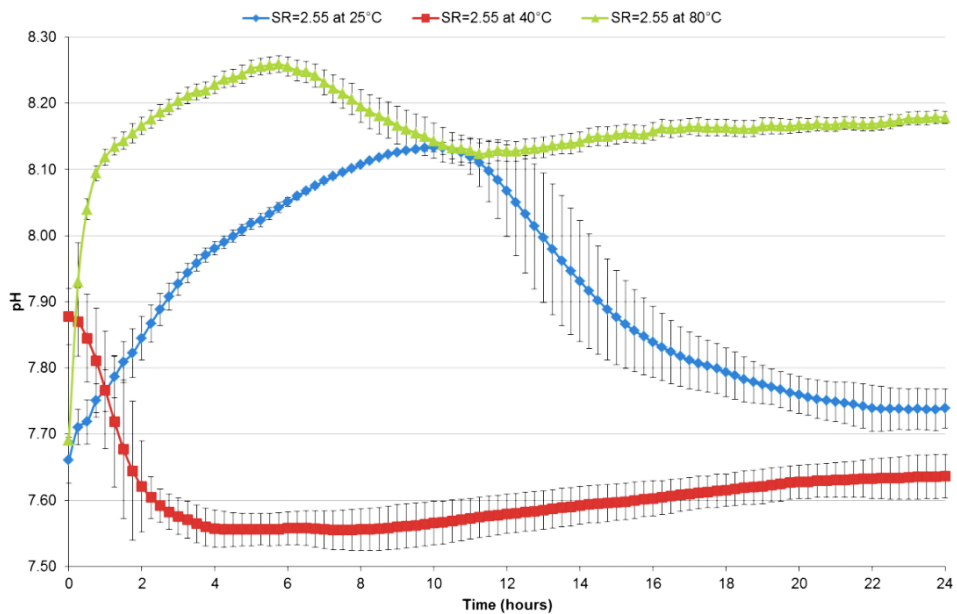
Figure 6.9: Case 2 (SR=2.55) pH changes with increase in bulk temperature

Results shown on pH curves for Case 2 (SR=2.55) were similar to those obtained for Case 1 (SR=1.52). The initial pH of the solution varied from 8.69 to 7.88 and the pH trend at 25°C is similar to 80°C. Similarly to SR=1.52, the pH trend at 40°C showed the lowest pH-value towards the end of the experiment.
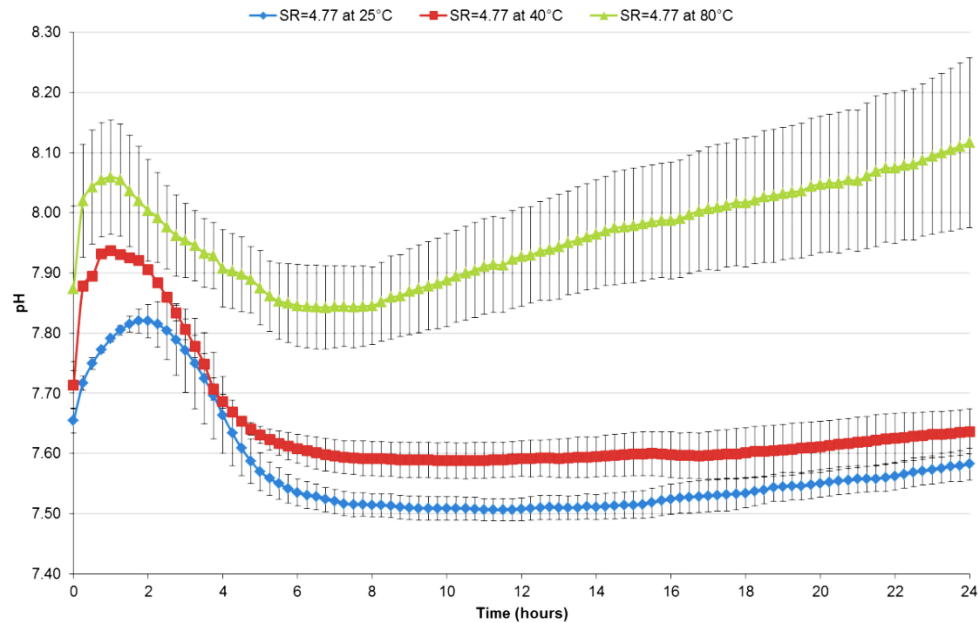
Figure 6.10: Case 3 (SR=4.77) pH changes with increase in bulk temperature.

Case 3 (SR=4.77) showed a very consistent trend for all three temperatures. The trends started from a pH range of 7.50 to 7.88, with a slight increase in pH up to 2 hours and then a decrease and another mild increase until a plateau was observed until the end of the experiment. The increase in temperature showed an effect on increasing the measured pH, so the pH trend at 25°C had the lowest values, followed by the trend at 40°C and lastly at 80°C. However, both plots at 25°C and 40°C showed a similar range of readings, suggesting that the kinetics were similar at those two temperatures for SR=2.55.
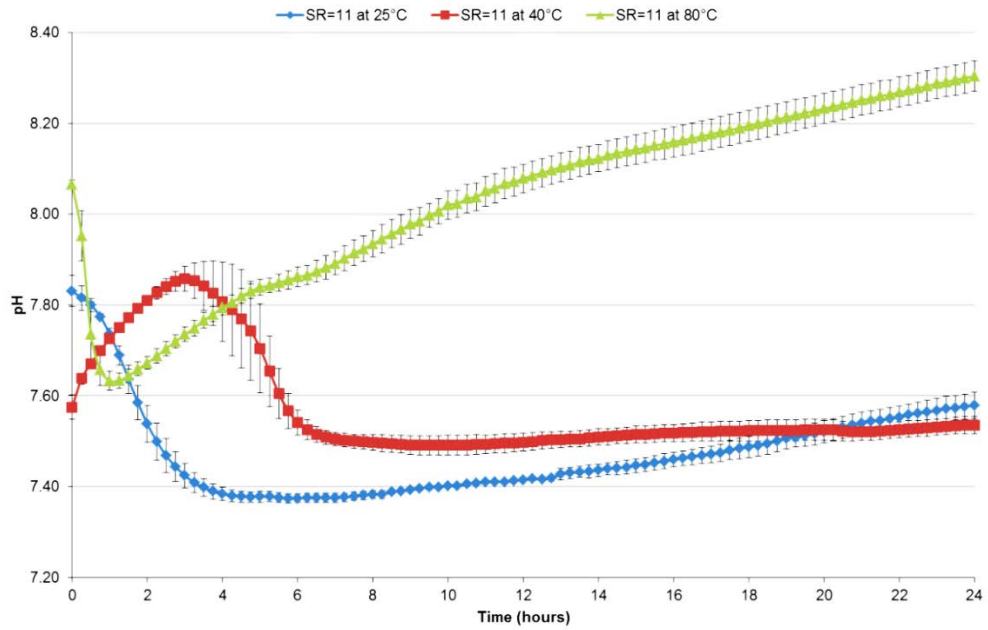
Figure 6.11: Case 4 (SR=11) pH changes with increase in bulk temperature.

Case 4 showed that the higher the temperature the higher the pH of the crystallization solution. The initial pH varied from 7.58 to 8.1 and the curves at 25°C and 40°C were quite similar. At 80°C, it could be observed that there was an initial drop in pH followed by a gradual increase until the end of the experiment.

Similarly to all previous case studies, it was expected that kinetics for SR=11 at 25°C and 40°C are much more similar than the one at 80°C, because the pH trend is completely different. However, this can only be confirmed upon detailed assessment of nucleation and crystal growth kinetics for the same range of temperatures.
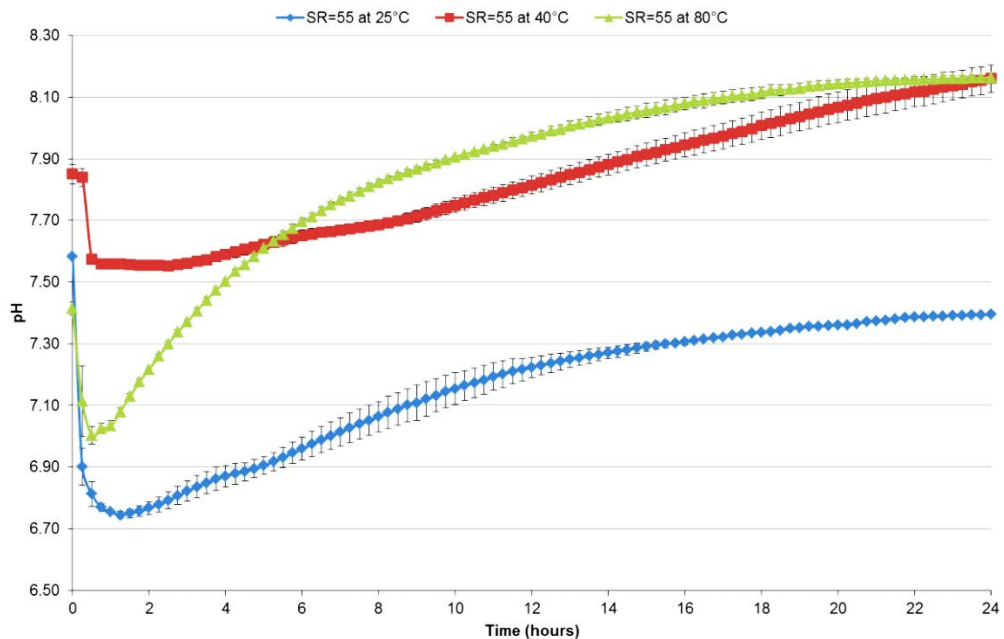
Figure 6.12: Case 5 (SR=55) pH changes with increase in bulk temperature.

Case 5 represents the highest supersaturation brine with initial an SR of 55. In Figure 6.6, it can be observed that the higher the temperature the higher the pH gets. The initial mixing pH varied from 7.45 to 7.88. All three curves showed an initial drop in pH caused by the dissociation of the bicarbonate ions as explained in equations (3.3) and (3.4), contributing to an increase in hydrogen ions (i.e. protons) which induce the pH to drop until $CaCO_3$ crystals are formed in the solution. At that stage the solution pH rises again due to the formation of stable $CaCO_3$ crystals which implies that less H^+ ions were freely available in the solution. In addition, it is also well documented in the literature that $CaCO_3$ solubility decreases with increase in temperature (307) (308). This can be illustrated by the pH of the solution at 80°C which increases significantly from 7.40 to 8.10 where it seems to stabilize until the end of the experiment.

The induction time (described in section 5.3.5.1) was determined using the pH method, in which the inflection point method was used for all low supersaturation case studies (i.e. 1.52, 2.55 and 4.77) and via the tangent method, that was applied for the two high supersaturation case studies (i.e. 11 and 55). A summary of the induction times estimated through the pH measurements illustrated from Figure 6.8 to Figure 6.12 are illustrated in Table 6.6, Table 6.7 and Table 6.8. In addition, pH is temperature dependant and despite the fact that all initial concentrations are the same, the higher the temperature, the higher mass scaling tendency the solutions have because $CaCO_3$ is less soluble at higher temperatures.

Table 6.6: Induction time estimation via pH measurements at 25°C

Saturation Ratio [-]	Temperature [$^{\circ}$C]	Induction time as a function of pH		
		Mean Induction Time [s]	Standard Error, S.E. [-]	Number of Repetitions, n [-]
1.52	25	4.86E+04	± 0.02	5
2.55	25	4.14E+04	± 0.06	4
4.77	25	1.26E+04	± 0.04	3
11.00	25	6.30E+03	± 0.03	3
55.00	25	2.70E+03	± 0.04	3

Table 6.7: Induction time estimation via pH measurements at 40°C

Saturation Ratio [-]	Temperature [$^{\circ}$C]	Induction time as a function of pH		
		Mean Induction Time [s]	Standard Error, S.E. [-]	Number of Repetitions, n [-]
1.52	40	3.96E+04	± 0.03	3
2.55	40	1.71E+04	± 0.06	4
4.77	40	9.90E+03	± 0.05	3
11.00	40	5.40E+03	± 0.04	3
55.00	40	2.16E+03	± 0.05	3

Table 6.8: Induction time estimation via pH measurements at 80°C

Saturation Ratio [-]	Temperature [$^{\circ}$C]	Induction time as a function of pH		
		Mean Induction Time [s]	Standard Error, S.E. [-]	Number of Repetitions, n [-]
1.52	80	2.88E+04	± 0.08	3
2.55	80	1.62E+04	± 0.03	3
4.77	80	6.30E+03	± 0.16	3
11.00	80	2.70E+03	± 0.05	3
55.00	80	1.26E+03	± 0.01	4

6.3.3 *In-situ* Calcium–Ion Concentration Measurements

The spontaneous reactive crystallization of $CaCO_3$ is an equi-molar process which happens when the freely available calcium ions react with the freely available carbonate ions in bulk solution. So, the in-situ measurement of free calcium ions in bulk solution was used as an approach to determine the bulk induction time for all case studies at 25°C, and this is shown in Figure 6.13.
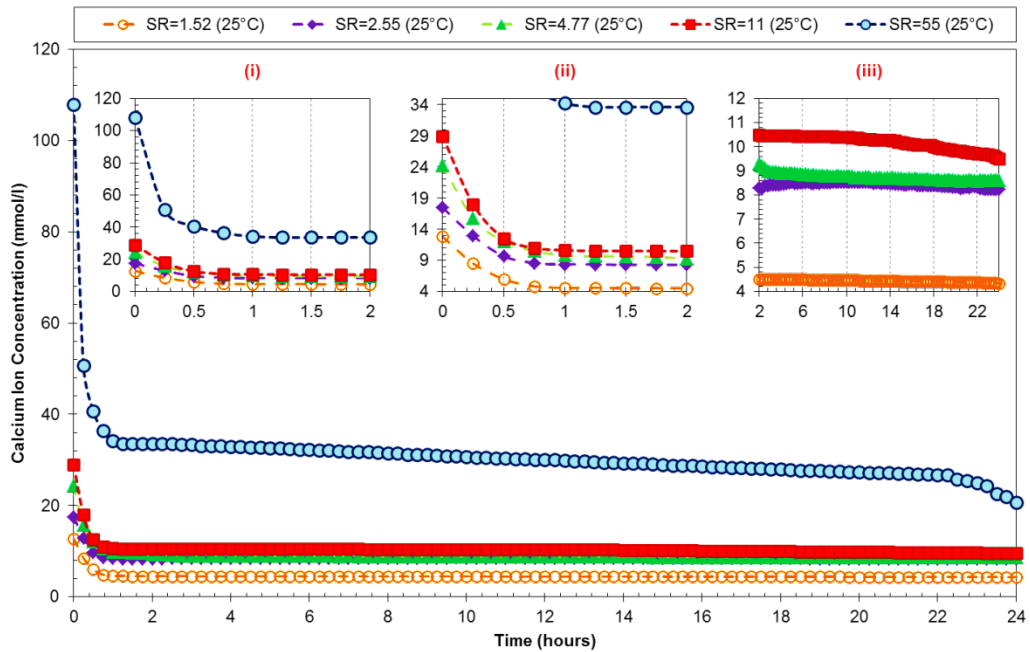
Figure 6.13: Calcium ion concentration changes in-situ during $CaCO_3$ precipitation. Zoomed parts of the overall trend can be seen in plots (i), (ii) and (iii)

Results displayed in Figure 6.13 showed that for each saturated brine solution, the calcium ions concentration decreased sharply in the first moments after mixing both anionic and cationic synthetic brines, this is better illustrated in the amplified part (i) of the graph.

The negative decrease in the slope of the curves is followed by a gradual and slower reduction of ions until a plateau region is achieved for a specific calcium ion concentration, as shown in the enlarged parts (ii) and (iii). The overall profile can provide insights into nucleation onset, as well as support in assessing the mechanisms involved through each stage of the precipitation experiments.

From these calcium concentration trends over time, it can be anticipated that nucleation mechanism occurs instantaneously after the brine's mix, because most calcium consumption takes place at the early stages, indicating that nuclei must have all been formed at the same time, prior to crystal's growth. Once particles were

completely grown, there is possibly a depletion of calcium ions leading to the plateau region observed in part (iii) of the graph for most concentrations. This last stable region in concentration can hypothetically be referred to as either equilibrium or end of the reaction as no more calcium ions are available to react with carbonate species in the solution. Interestingly, the sharp decrease in calcium ions concentration was also observed for the lower supersaturation case, in which the induction time was expected to be quite prolonged as discussed in section 6.3.2. This reinforces the idea that for low saturation ratios, the pH method may not be as effective to detect changes in ionic concentration as the nucleation and crystal growth start. Figure 6.14 displays the hypothetical relationship between supersaturation with pH and calcium ion concentration in a spontaneous $CaCO_3$ crystallization process.
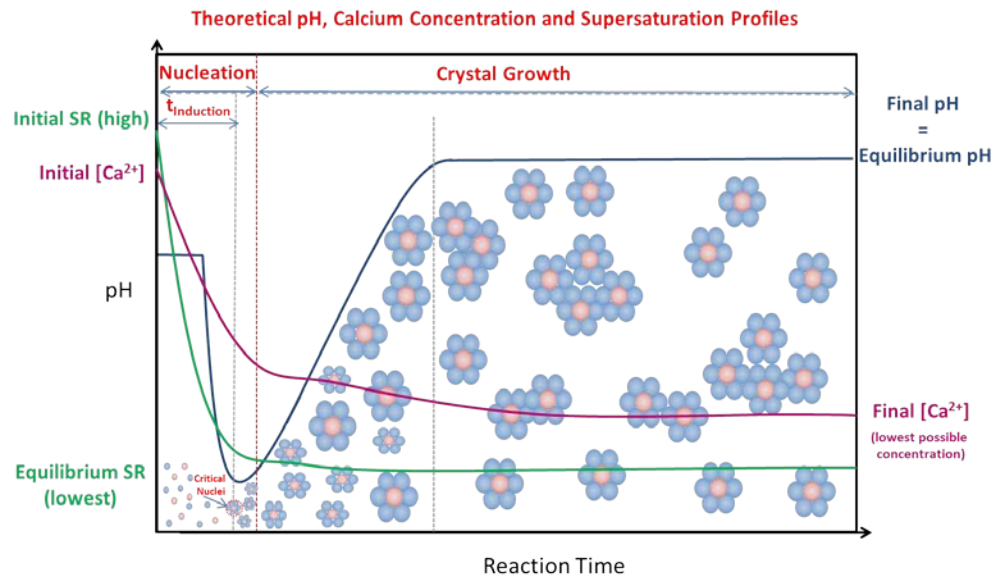
Figure 6.14: Hypothetical picture displaying calcium ion concentration, pH and supersaturation changes during the spontaneous bulk crystallization process.

The re-examination of the basic theoretical kinetic models for solid state reaction systems has led to several discussions (309) (310) to define the nucleation kinetics based on individual crystals in a bulk solution. Hence, several attempts have been made during bulk crystallization studies to ensure that the best possible approach had been used for determining the induction times experimentally.

A robust estimation of the induction times would enable accurate calculations of the nucleation and growth rates. Hence, Table 6.9 provides a summary of the induction time calculated via calcium concentration in-situ measurements.

Table 6.9: Induction time estimation via calcium-ions measurements at 25°C

Saturation Ratio [-]	Temperature [$^{\circ}$C]	Induction time as a function of Calcium Concentrations		
		Mean Induction Time [s]	Standard Error, S.E. [-]	Number of Repetitions, n [-]
1.52	25	4.32E+03	± 0.08	3
2.55	25	3.60E+03	± 0.90	3
4.77	25	3.24E+03	± 0.27	3
11.00	25	2.52E+03	± 0.24	3
55.00	25	1.80E+03	± 0.75	3

The listed induction times were obtained via the slope of each calcium-ion concentration profile shown in Figure 6.13. Experiments at higher temperatures such as 40°C and 80°C could not be assessed in-situ due to the ion selective probe temperature sensitivity. So, the results obtained can only be used for assessing the crystallization kinetics at 25°C.

6.3.4 Relationship between Induction Times via pH and Calcium Ions Measurements and Supersaturation

6.3.4.1 *In-situ* pH as a function of supersaturation

For CaCO$_3$ systems the induction time estimation via pH measurements is one of the most common techniques given that CaCO$_3$ crystallization is dependent on the solution's pH. The pH has been monitored in-situ for all experiments as shown in section 6.3.2. According to the classical nucleation theory, the induction time is inversely proportional to the nucleation rate, and therefore it is also inversely proportional to the supersaturation, as explained in equation (2.12).

Figure 6.15 illustrates the interdependency of the induction time (via pH) with supersaturation and temperature, considering the CNT and experimentally collated data. It can be observed that the higher the supersaturation and temperature, the shorter the induction time becomes. Thus, an inversely proportional relationship is illustrated by the curves as expected from CNT studies (311) (312).
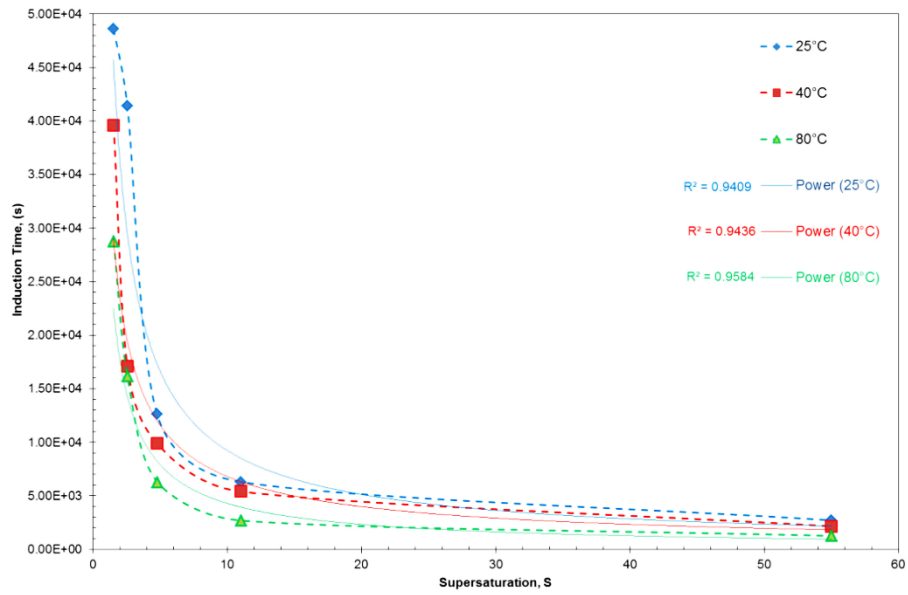
Figure 6.15: Induction times estimated experimentally via in-situ pH readings, for a range of supersaturation at 25°C, 40°C and 80°C.

6.3.4.2 *In-situ* calcium free ions as a function of supersaturation

The induction time measured via calcium ions concentration, freely available in the saturated brine solutions, was summarised in Table 6.9. These results provide an insight into the chemical reaction happening in-situ, as less calcium ions can be detected as the chemical reaction progresses to form $CaCO_3$ in bulk solution. Figure 6.16 displays the relationship between induction time and supersaturation at 25°C.
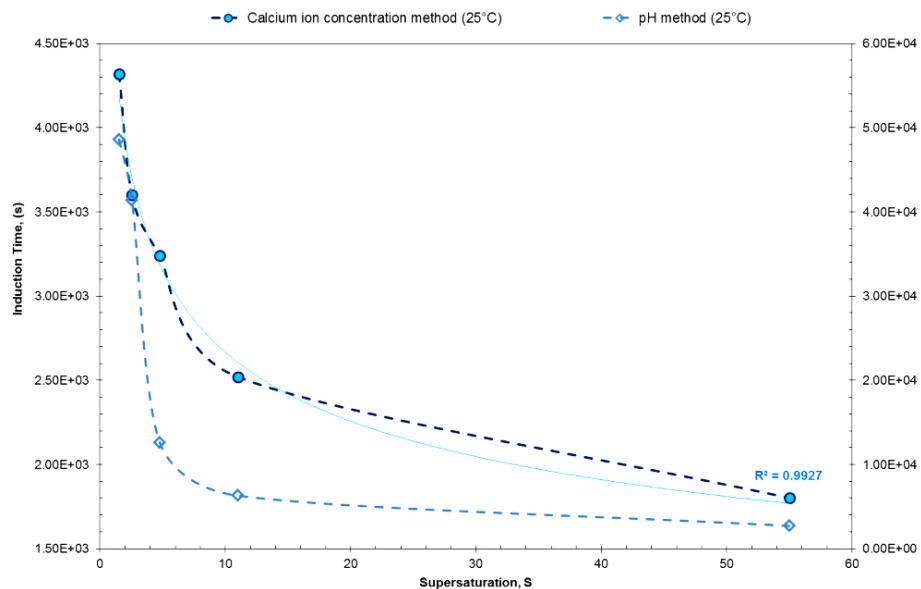
Figure 6.16: Comparison of induction times estimated experimentally via in-situ calcium ions concentrations and in-situ pH for a range of supersaturation at 25°C.

It is noticeable from Figure 6.16 that both measurement methods exhibit a similar shape, but the induction times measured via the trace of free calcium ions are much shorter especially for the lower concentration case studies (i.e. SR=1.52 to SR=4.77). However, the induction times estimated via the calcium ions trace method at highest supersaturation (i.e. SR=55) is extremely similar to that period determined via pH measurements.

6.3.4.3 Link between pH and calcium ions methods

The differences observed in induction time predictions will have an impact on the kinetic analysis for the nucleation process. So, it is worth noting that the impact of experimental errors and in data processing through graphical methods has been taken into account when analysing the experimental results.

Nevertheless, Figure 6.17 illustrates that at high saturation brines, both pH and calcium-ion trace in solution provided a robust means of estimating the induction times, as the differences between the data analysis is relatively small. The induction time estimated for Case 5 (SR=55) at 25°C was approximately 45 minutes via pH method and approximately 30 minutes via the calcium-ion tracing method.
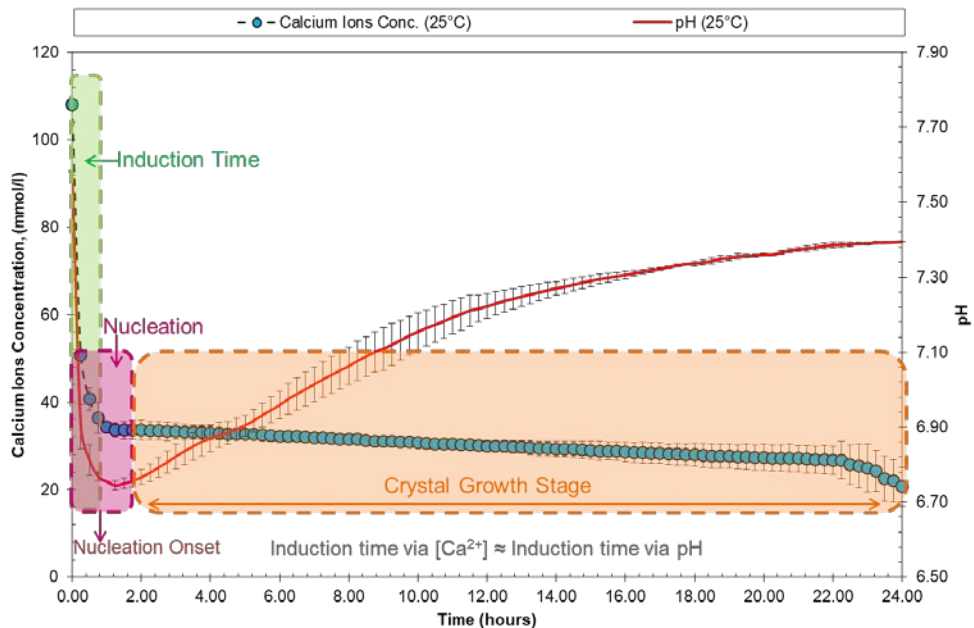
Figure 6.17: Induction times comparison using both pH and calcium ions concentrations for supersaturation 55 at 25°C.

In theory, the pH and calcium plots should provide exactly the same trends because for each mole of calcium, another mole of carbonate should also react with calcium to form calcium carbonate. However, the pH technique is quite sensitive and strongly

governed by the CO_2/ total alkalinity equilibrium and temperature of the bulk solution. In addition, it is more challenging to monitor kinetics at very low concentrations such as those found for Case 1 (SR=1.52), Case 2 (SR=2.55) and Case 3 (SR=4.77).

Overall, the induction times (τ) determined via pH or calcium concentration represented a measure for the appearance of the first crystals following attainment of supersaturation. Hence, the onset of crystallization was marked by either a sharp decrease in pH of mixing solution or by a sharp decay in calcium ions due to the chemical reaction to precipitate $CaCO_3$. At low saturation ratios, the pH is harder to monitor as kinetics are much slower and the supersaturation is closer to a metastable zone. At high saturation ratios, the induction times estimated through those two methods were very close to each other, emphasising the reproducibility of these two different methods.

6.3.5 Conductivity Measurements

Conductivity measurements were done in-situ as an alternative means of determining the induction time of $CaCO_3$ bulk crystallization. From this approach, a decrease is expected in the conductivity readings, after a period of steadiness, which marks the onset of crystallization. The basic principle is to track the solution conductivity through the ions available in the electrolyte solution. Once the ions present in the electrolyte solution react to form $CaCO_3$, the conductivity reduces and stabilizes to an equilibrium value. Previous authors (126) (313) (314) have assessed induction times using the conductance method by in-situ tracking of conductivity, so this hypothetical relationship has been proven to work for $CaCO_3$ spontaneous precipitation systems. Conductivity experiments have been carried out for all saturation ratios at 25°C and 80°C as illustrated in Figure 6.18.

Results shown in Figure 6.18 illustrate that both supersaturation and temperature have an effect on the initial conductivity readings. For each of the saturated brines the higher their saturation ratio, the more total dissolved species (TDS) can be detected from the bulk solution. In addition, temperature seems to facilitate the conductivity of the species and fasten kinetics which can be related to the increase in the conductivity values with increase in temperature. However, for both low (25°C) and high (80°C) temperatures there was no variance in the turbidity values over 24 hours. Hence, the induction times could not be estimated from conductivity measurements. Similarly to the pH-method, the conductivity readings were expected to drop once the $CaCO_3$ crystallization process started in solution, as less ions would be available in solution.
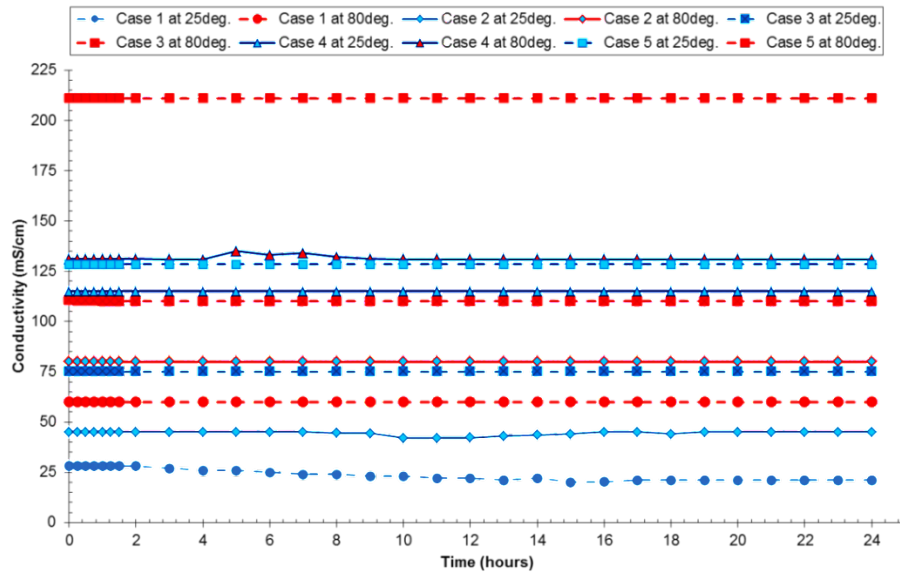
Figure 6.18: Summary of in-situ conductivity measurements at 25°C and 80°C

Experimental results shown in Figure 6.18 were repeated three times, giving an experimental error of approximately 5% when repeated for each case study. Furthermore, other constraints related to this method may be due to the type of the turbidity probe and its sensitivity range, which could not monitor significant changes in solution throughout the crystallization process.

Lastly, experiments at 40°C were no longer performed as the results from the lowest and highest temperatures showed no significant changes in the conductivity throughout the precipitation process.

6.3.6 Light Transmittance Turbidity Measurements

Turbidity measurements of bulk crystallising solutions were assessed using a stainless steel laser reflectance and transmittance fibre optic probe. In order to assess this method, two saturation ratio (SR=4.77 and SR=55) were tested at 25°C, as shown in Figure 6.19.

The results shown in Figure 6.19 revealed that for the highest supersaturation (SR=55) there is a moderate decrease in light transmittance which indicates that crystallization has started. However, a sharp decrease with 0% light transmittance was expected when nucleation started. Nevertheless, the induction time for SR=55 was extrapolated to be around 1 to 5 hours, as the light transmittance decreased from 100% to (i) 90% and then to (ii) 80%. During this experiment it could also be observed that crystals were depositing at the surface of the stainless steel optical probe making it even harder to establish an induction time. Towards the end of the

experiment, the turbidity light transmittance reached 60% and never got to 0% to indicate that precipitation had occurred in the saturated solution, as it could be easily verified by visual observations of $CaCO_3$ crystals suspended in the bulk solution.
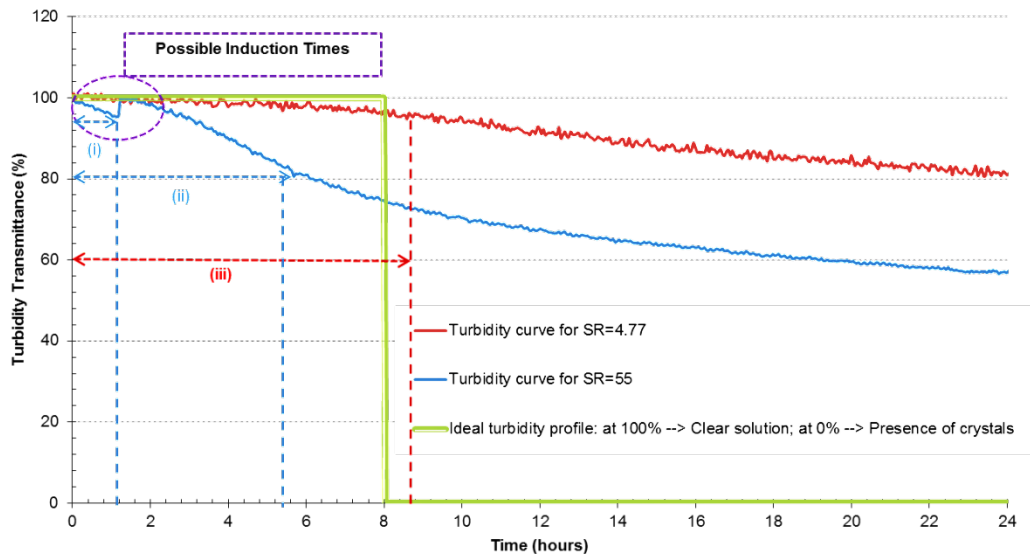
Figure 6.19: Induction time measurement at 25°C using the fibre optic probe for turbidity quantification.

A similar behaviour of this turbidity light transmittance probe was observed for the SR=4.77 at 25°C. For this case, the light transmittance reduced only to 95% after 8½ hours, and then continued to decrease to 80% until the end of the experiment. Likewise, it is very difficult to rely on these experiments as the probe was not detecting all the crystals in the solution. Nevertheless, this method could show that at higher supersaturation more crystals are formed much more quickly than at lower supersaturation.

The fact that both slopes are not as sharp as expected raises uncertainties about the actual induction period. The light transmittance depends on the mass per volume produced, but even for the highest SR case study, the density of crystals per unit volume did not satisfy the conditions to achieve better results with this light transmittance probe. For that reason, this method was shown to be poor for the supersaturation ranges studied and no further analysis was done.

6.3.7 Lasentec© Focused Beam Reflectance Measurement (FBRM)

The Lasentec FBRM has been reportedly to be successful for determining crystal growth over time. Therefore, it has been also used to get in-situ information about the bulk crystallization induction time. However, results have shown that for low SR=1.52 at 40°C, the measurement chords were high from the beginning, so it could

not be distinguished when the nucleation started. Alternatively, this may also support the results from calcium probe, suggesting that nucleation is instantaneous at such low supersaturation. Results at higher supersaturation were inconclusive as many chords continued to change over time suggesting continuous crystal growth.
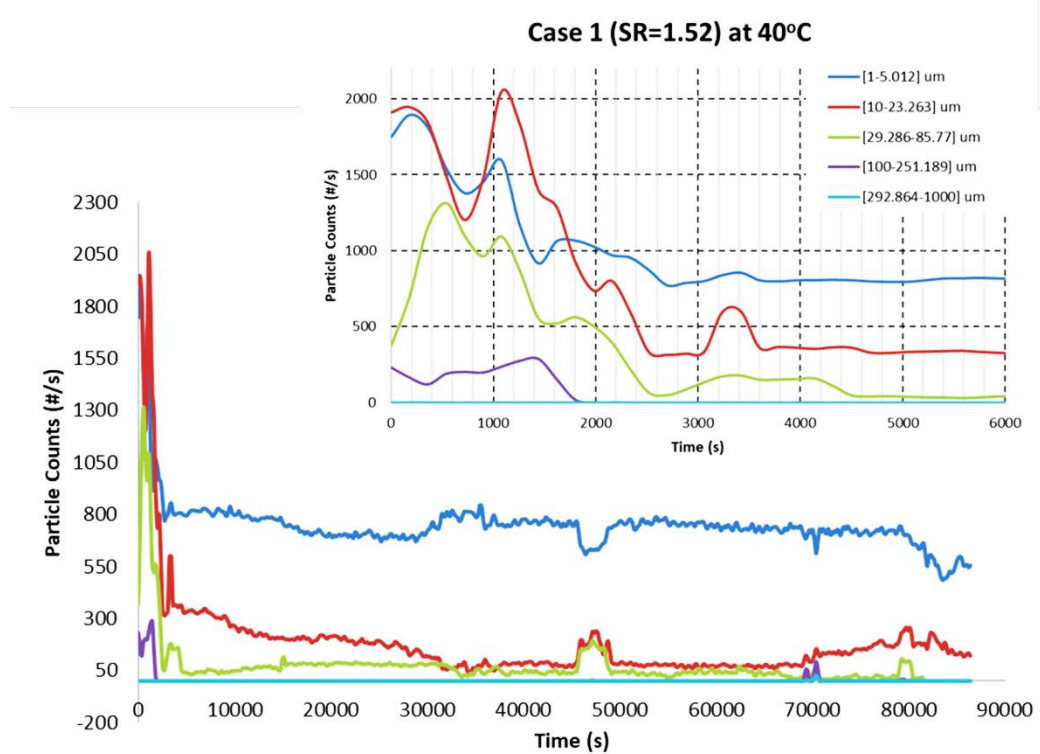
Figure 6.20: FBRM readings for SR=1.52 at 40ºC

A key constraint with in-situ probes is that crystals may deposit at the surface of the probe providing misleading values. It is believed that this has happened for both laser transmittance probes applied to access nucleation.

6.3.8 Bulk Crystals Interfacial Tension and Critical Nuclei Size

Based on the estimated induction time values for a range of supersaturation and temperature (see Figure 6.15), other important nucleation parameters such as the interfacial energy and the critical nuclei size were determined using equations the following equations explained in Chapter 2:

$$\ln(\tau) \propto \left[\frac{\gamma^3}{T^3 (\ln S)^2} \right] \tag{6.2}$$

$$\ln J = \ln\left(\frac{1}{\tau}\right) = \ln(A) - \left[-\frac{16\pi\gamma^3 V_m^2}{3k^3} \right] \left[\frac{1}{T^3 (\ln S)^2} \right] \tag{6.3}$$

133

Rearranging Equation (6.3), it becomes:

$$\ln \tau_{ind} = \ln A + \frac{16\pi\gamma^3 v_m^2}{3k^3\left[T^3(\ln S)^2\right]} \tag{6.4}$$

$$r_c = \frac{2\gamma v}{kT \ln S} \tag{6.5}$$

Taking into account the inversely proportional relationship established by Equation (6.2), plots of log (τ) vs. (logS)$^{-2}$ were constructed (Figure 6.21) and the values of interfacial tension, γ, were calculated from the slope of these plots of and by applying Equation (6.3) parameters. A molecular volume of 6.13 x10^{-29} m^3 was used considering that all crystals were calcite. The interfacial tension (γ) values obtained from the slope of the regression lines used to fit data points for solutions with initial saturation ratio from 1.52 to 55 over a range of temperature. These interfacial tension values varied according to the supersaturation and temperature, overall ranging from 1.41 mJ/m^2 to 25.46 mJ/m^2.

In addition, the interfacial tension at 25°C has also been re-calculated (Figure 6.22) considering the induction time predicted through the temporal evolution of calcium ions in the saturated bulk solutions (Table 6.9). The slope obtained from the linear fit of log (τ) vs. T^{-3} (logS)$^{-2}$ was used in Equation (6.2) and the interfacial tension (γ) values were reassessed and compared with those obtained via pH method 25°C. The high sensitivity of the calcium-ion selective electrode provided readings which gave lower interfacial tension values varying from 0.92 mJ/m^2 to 16.37 mJ/m^2, as detailed in Table 6.10.

The calculated interfacial tension values (Table 6.10 – Table 6.13) for CaCO$_3$ (calcite) in the present work are similar to the values of interfacial tension, previously reported in the literature for calcite by Söhnel and Mullin (313) and Verdoes et al. (280), who reported 40 mJ/m^2 and 37.3 mJ/m^2.

Remarkably, the correlation between the interfacial tension and nucleation rate given in Equation (6.2) could not fully be validated with this study, since the smaller induction times resulted in bigger interfacial tension values. This can be explained by the fact that nucleation time here determined considers only the time required for the nucleus to form in bulk, neglecting the time taken for nuclei crystals to grow into a detectable size. Hence, the expression in Equation (6.2) is only valid when the induction time is mainly dominated by the nucleation time and growth time can be neglected.
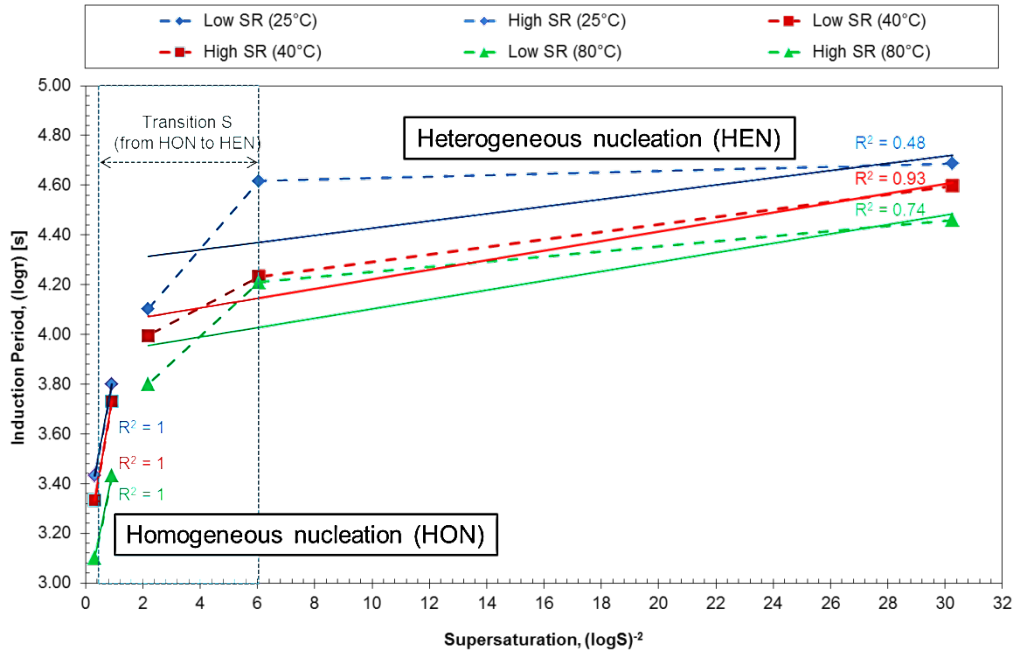
Figure 6.21: Dependence of induction time on the solution supersaturation for calculating the interfacial surface energy.

Figure 6.21 displays a break in the lines suggesting a transition from homogeneous nucleation (HON) to heterogeneous (HEN) nucleation. Within the range of saturation ratio 4.77 and 11 there are changes in the nucleation kinetics which divided the homogeneous and heterogeneous nucleation from a high to a low supersaturation level. The evidence of HEN for the low saturation brines is also marked by the lower linear fits with relative regression fit at 25°C. Typically, when the relationship between $\log (\tau)$ and T^{-3} $(\log S)^{-2}$ is not linear, it provides strong evidence that either heterogeneous nucleation (HEN) or secondary nucleation are taking place at that supersaturation range. Lastly, the temperature showed an effect on the interfacial tension calculations, giving higher values for higher temperatures. This impact was more noticeable at higher saturation ratios as illustrated in Figure 6.22.
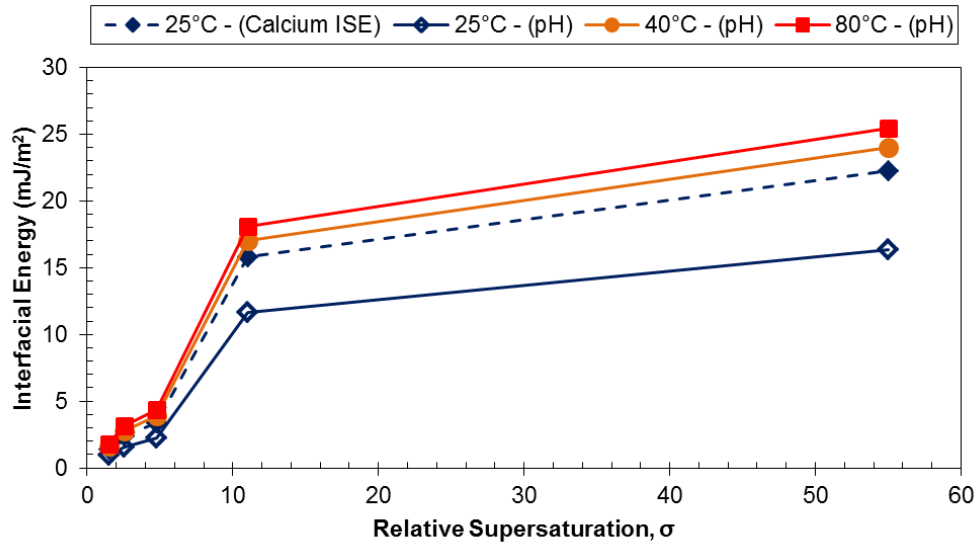
Figure 6.22: Dependence of calculated interfacial energies on temperature and supersaturation.

A summary of the calculated parameters for the interfacial tension values is described from Table 6.10 to Table 6.12.

Table 6.10: Interfacial tension determined for all saturation ratios at 25°C via both pH and Calcium ion induction time methods

SR	T(°C)	Slope		Intercept		γ (mJ/m^2)	
		т (pH)	т ([Ca^{2+}])	т (pH)	т ([Ca^{2+}])	т (pH)	т ([Ca^{2+}])
1.52	25	0.01	0.004	4.28	3.52	1.41 ± 0.8	0.92 ± 0.9
2.55	25	0.01	0.004	4.28	3.52	2.41 ± 0.7	1.57 ± 0.8
4.77	25	0.01	0.004	4.28	3.52	3.40 ± 0.5	2.21 ± 0.3
11	25	0.62	0.25	3.23	3.17	15.82 ± 0.3	11.63 ± 0.8
55	25	0.62	0.25	3.23	3.17	22.27 ± 0.3	16.37 ± 0.8

Table 6.11: Interfacial tension determined at 40°C for all saturation ratios

SR	T(°C)	Slope	Intercept	γ (mJ/m^2)
1.52	40	0.02	4.03	1.63 ± 0.3
2.55	40	0.02	4.03	2.78 ± 0.3
4.77	40	0.02	4.03	3.92 ± 0.3
11	40	0.67	3.11	17.05 ± 0.3
55	40	0.67	3.11	24.01 ± 0.3

Table 6.12: Interfacial tension determined at 80°C for all saturation ratios

SR	T(°C)	Slope	Intercept	γ (mJ/m^2)
1.52	80	0.02	3.91	1.82 ± 0.3
2.55	80	0.02	3.91	3.12 ± 0.3
4.77	80	0.02	3.91	4.39 ± 0.3
11	80	0.56	2.92	18.08 ± 0.3
55	80	0.56	2.92	25.46 ± 0.3

These interfacial values listed in Table 6.10 to Table 6.12 were then used to evaluate the critical radius (r_c) of the nucleus using equations (6.5).

The dependence of the radius of the critical nuclei on supersaturation and crystallization temperature is shown in Figure 6.23. Consistent with nucleation theory, these figures show that larger critical nuclei are formed at higher crystallization temperatures and lower supersaturation levels. The critical nucleus size calculations were based on spherical cluster shape, and overall results varied from 0.64 Å to 2 Å (Angstroms). The overall number of particles for each cluster increased with supersaturation and temperature, as expected from Equation (6.5).

As the critical cluster size is a function of inverse of supersaturation squared, the critical cluster radius is expected to become progressively larger as the supersaturation decreases. However, this behaviour is only noticed from supersaturation range 1.52 to 4.77. Then, at saturation ratio 11 there is a sudden increase in the cluster size which then decreases as the saturation increases to 55. These maximum critical nuclei observed at a transient supersaturation levels can be related to the non-homogeneous nucleation behaviour at such supersaturation. Lastly, at supersaturation 55, the temperature plays a very small impact as the critical nuclei size is quite similar varying from 1.56 Å at 25°C and 40°C to 1.60 Å at 80°C.
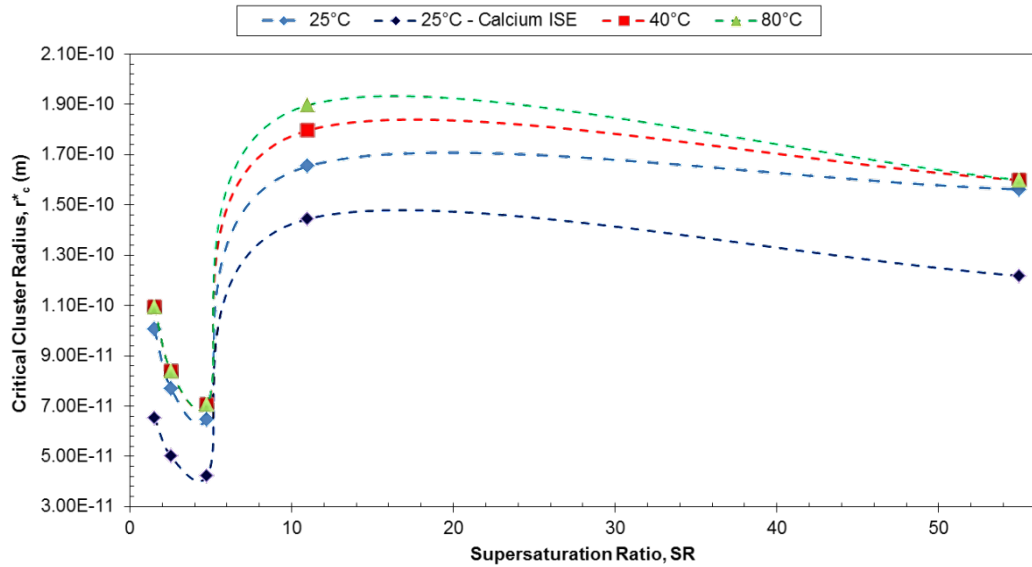
Figure 6.23: Dependence of the radius of the critical nucleus size, r_c* on the temperature and supersaturation

Considering the lower saturated brines (1.52 ≤ SR ≤4.77), it can be seen from Figure 6.23 that an inversely proportional dependency in the radius of the critical nuclei to supersaturation is clearly observed. Then a decrease in the cluster size is also observed when supersaturation and temperature increases for the highest saturated brines (11 ≤ SR ≤ 55). However, unexpectedly there is a significant increase in the crystal size from supersaturation 4.77 to 11 which opposes the established principle by Equation (6.5) from the CNT and the reasons behind this behaviour are unclear.

Lastly, the r_c determined based on calcium ions induction time showed even lower r_c, varying from 0.4 Å to 1.2 Å and still followed the same overall trend as the other profiles obtained via pH induction time measurements.

The existence of a critical nuclei size implies that during nucleation onset, a number of molecules gather together to form a critical stable nucleus. Hence, nucleation can be controlled to some extent by modulating the critical crystal size which is a function of the interfacial energy. The smaller the interfacial energy, the smaller the critical size and more likely nucleation can occur at any given supersaturation.

6.3.9 Nucleation Rates during Spontaneous Precipitation

Nucleation rates (J_N) were determined using equation (2.17) under the assumption that during the induction period, the number of crystals formed are a result of a steady state nucleation as explained by Equation (2.11) ($J_N \sim N/t_{ind}$). In addition, both growth and nucleation rates are inversely proportional to the induction time and this

expression can solely be used when growth rates (G) are obtained via experimental techniques. The nucleation rate constant, K_J was determined from the power law expression shown in Equation (2.27), as illustrated by the plot in Figure 6.24. The α-value was assumed to be 10^{-8} as per previous literature studies (14) . However, the estimation of this α-parameter may influence the nucleation kinetics significantly, especially if it was as low as 10^{-5}. This assumption was taken based on studies done by Verdoes (1992) over similar supersaturation ranges for $CaCO_3$ spontaneous crystallization studies. However, this study also includes higher supersaturation ranges (S >11) than the ones reported by Verdoes. Despite the influence of α-parameter in determining the nucleation rate constant, it is important to stress that its uncertainty can be neglected as the nucleation rates are compared to each other for the range of supersaturation in study. On the other hand, factors such as the induction time and growth rate were determined experimentally and will strongly affect the calculation of the nucleation rates. So, an assumption of 10% standard error deviation (maximum determined for the induction time measurements) has been considered for each calculated nucleation rate over time.
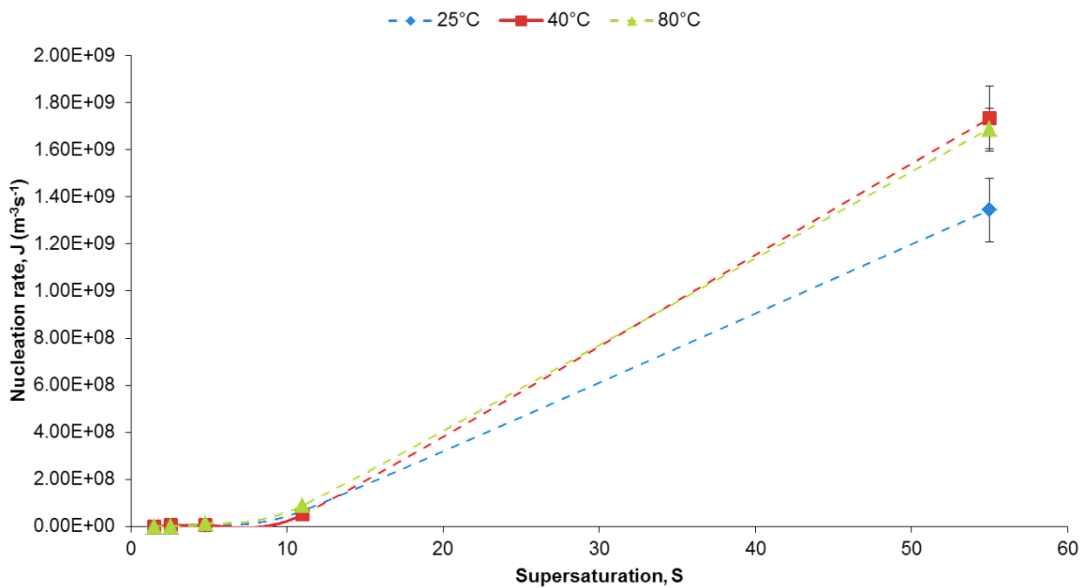
Figure 6.24: Dependence of the nucleation rate (J) on the supersaturation (S) during nucleation of $CaCO_3$ crystals at 25°C, 40°C and 80°C

Figure 6.24 displays an expected increase in nucleation rates with the increase in supersaturation and similarly, an expected higher nucleation rate at higher temperatures (40°C and 80°C). However, for higher temperatures, the nucleation rate values at S > 11 were shown to be very close to each other, suggesting that for very high supersaturation ranges, temperature does not have a huge impact on nucleation kinetics.

Table 6.13 and Table 6.14 provide a summary of the results obtained for the calculated nucleation rates and respective rate constants using the Kashchiev and Rosmalen method (315).

Table 6.13: Nucleation rates as a function of supersaturation and temperature

SR	T (°C)			S.E.	# Rep, n
	25 $J\,(m^{-3}s^{-1})$	40 $J\,(m^{-3}s^{-1})$	80 $J\,(m^{-3}s^{-1})$		
1.52	8.58E+05	4.02E+05	4.70E+05	± 0.10	3
2.55	6.57E+05	5.11E+06	6.74E+05	± 0.10	3
4.77	4.92E+06	7.95E+06	1.21E+07	± 0.10	3
11	6.69E+07	5.11E+07	8.95E+07	± 0.10	3
55	1.34E+09	1.73E+09	1.69E+09	± 0.10	3

Table 6.14: Nucleation rate parameters as a function of temperature determined using Kashchiev and Rosmalen approach

T(°C)	$K_J\,(m^{-3}s^{-1})$	#Exp	S.E.	R^2
25	3.10^7	3	± 0.10	0.99
40	3.10^7	3	± 0.10	0.98
80	3.10^7	3	± 0.10	0.99

The nucleation rate values from this study varied from 4.02E5 to 1.73E9 $m^{-3}s^{-1}$, showing an increase at higher supersaturation and at higher temperatures. On the other hand, the nucleation rate constant obtained for the supersaturation and temperature ranges studied was 3.10^7 $m^{-3}s^{-1}$. This nucleation rate constant value is closer to the values obtained from the Spanos and Koutsoukos (287) studies in which the K_J was 3.10^9 $m^{-3}s^{-1}$ at 25°C and pH=10. Based on these results, it can be concluded that heterogeneous nucleation is dominant as the K_J values are much lower than the theoretical values expected for homogeneous nucleation in bulk solutions (i.e. 10^{31} to 10^{36} $m^{-3}s^{-1}$) (287).

6.4 Crystal Characterization with respect to Size, Shape and Structure

Bulk crystals were collected at the end of each batch crystallization experiment for five saturated brines at 25°C, 40°C and 80°C. In order to understand the kinetics and thermodynamic changes in the bulk solution, these crystals were characterized with

respect to their shape and size using adequate techniques as described in section 5.5.

6.4.1 Crystal Particle Size

Several crystal particles are produced with a particular size and shape during the calcium carbonate bulk precipitation process. Challenges of particle size analysis are typically encountered when crystals are non-spherical, form agglomerates and the bulk solution is polydisperse in shape and size. However, the laser techniques used do take into consideration these variances in shape and size of particles and a few assumptions are made to obtain more accurate readings: all particles are spherical and homogeneous, the real and imaginary components of the refractive index must be known and there are no errors in the intensity distribution.

This study explores particle size characterisation using two different laser diffraction techniques: the Mastersizer and the Sysmex. Assumptions are made during size measurement using these two models. For non-spherical particles, a size distribution is reported considering the predicted scattering pattern for the volumetric sum of spherical particles that would match the measured scattering pattern. This is because the Mastersizer technique assumes a spherical particle shape in its optical model. Thus, the refractive index for $CaCO_3$ has been inserted into the software prior to the start of the tests. Generally, calcite was the dominant polymorph formed in bulk solutions and its refractive index varies from 1.49 – 1.79 which corresponds to a wavelength in air from 589 – 643 nm.

In general, the particle size average at low saturated brines, i.e. 1.52, 2.55 and 4.77 was determined by Sysmex readings and the equivalent circular mean diameter was used for each particulate system, with at least 3 repeats for each sample. The low saturated brines at all temperatures showed a smaller number of crystal particles per batch volume (i.e. lower mass density). Hence, when these bulk particles were placed for measurements into the Mastersizer, there were errors due to the poor obscuration level in the instrument's light transmittance. For that reason, the Sysmex has been used instead of the Mastersizer providing good results for particle sizing based on mass volume and circularity (Figure 6.25).

SR=1.52 at 25°C, after 24 hours
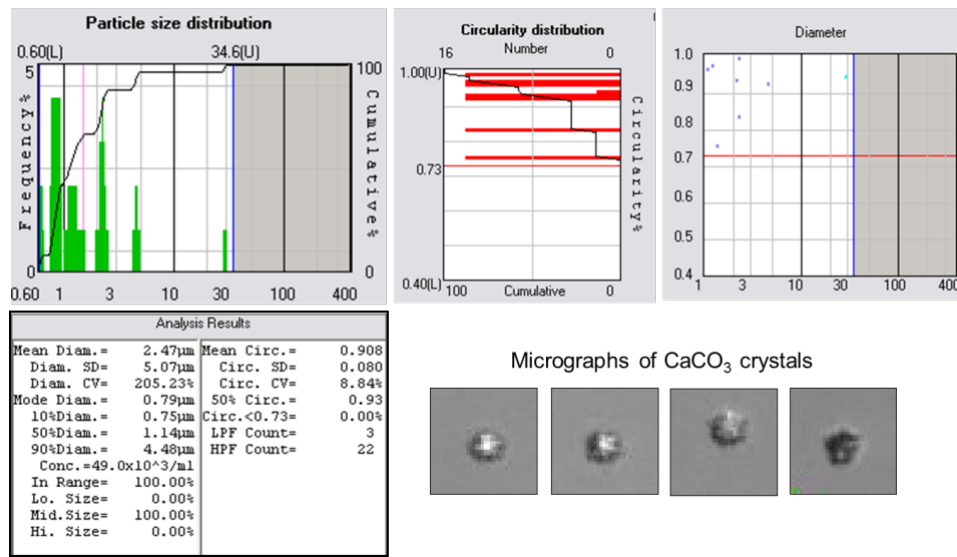
Figure 6.25: Typical data file collected from Sysmex experiments: particle size distribution, circularity distribution, diameter and micrographs. This example shows a run for SR=1.52 at 25°C after 24h, with a mean particle diameter of 2.47µm.

On the other hand, the Mastersizer was mainly used for the higher supersaturation brines, i.e. at SR=11 and SR=55, as sufficient particles could be crystallized per batch volume, fulfilling all criteria for attaining accurate readings.

The Mastersizer data presented in Figure 6.26 and Figure 6.27 is based on the average of 10 consecutive repeated measurements for each particulate case study. At the end of each measurement, a standard deviation or coefficient of variation (C.V.) was calculated considering the normal Gaussian size distribution.

For particles above 1µm, the standard C.V. for each $d_{0.1}$, $d_{0.5}$ and $d_{0.9}$ should be ≤ ± 2%, whilst for particles lower than 1µm the C.V. ≤ ± 4% as shown in the example from Table 6.15. The averages of each equivalent volume mean ($d_{[4, 3]}$) were taken as the mean size for each case study under specific conditions.
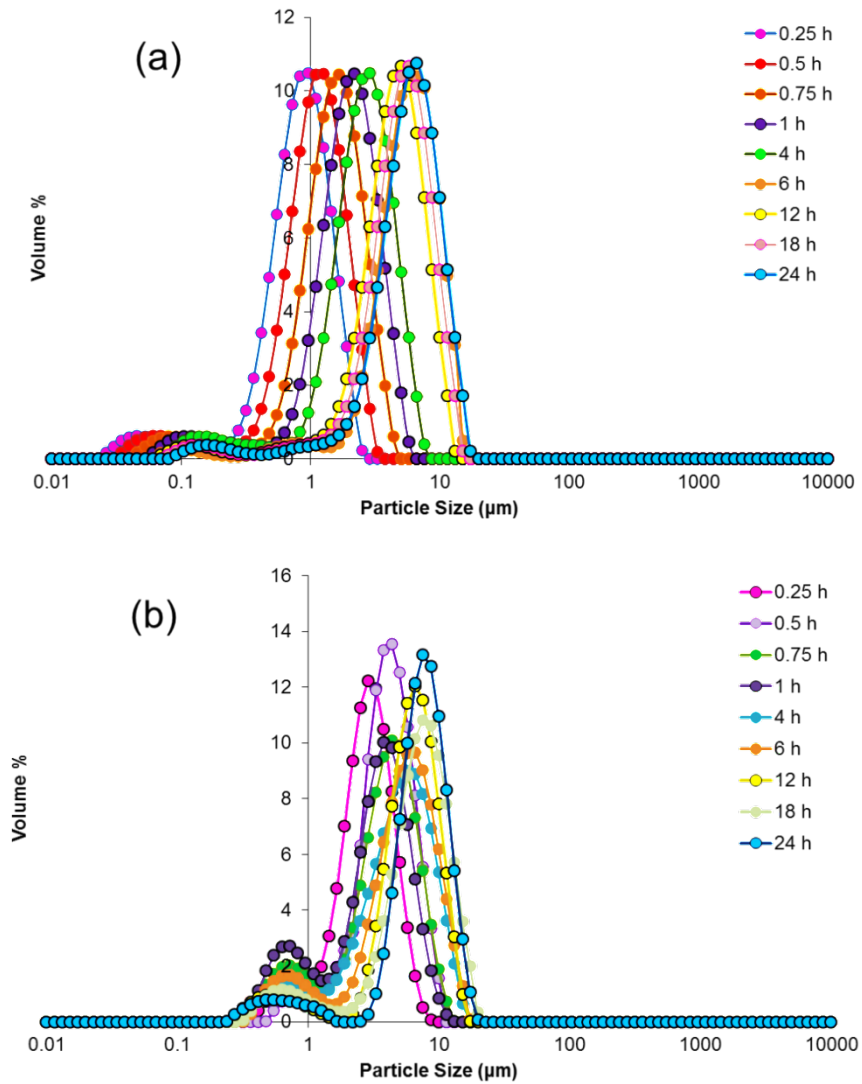
Figure 6.26: Time evolution of the $CaCO_3$ crystal's size distribution at fixed supersaturation and temperature: (a) SR=11 (25°C) and (b) SR=55 (25°C).

In addition the effect of temperature, on particle size distribution has also been assessed as summarised in Figure 6.27.

143
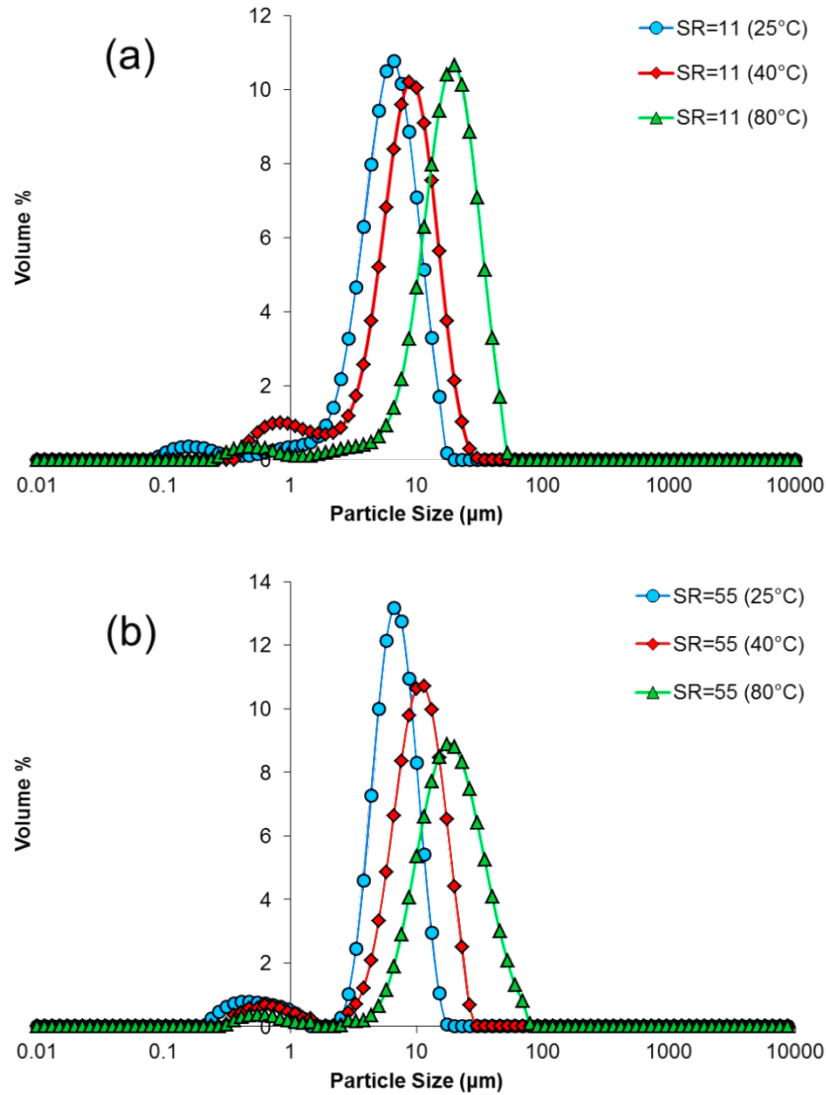
Figure 6.27: CaCO$_3$ particle size distribution as a function of temperature at 24 hours running time: (a) SR=11 and (b) SR=55.

The size distribution data in Figure 6.26 and Figure 6.27 clearly shows that CaCO$_3$ (calcite) particles in bulk display a bi-modal peak at all three temperatures (25°C, 40°C and 80°C), and the respective mean values of size distribution, gradually increased over time for a supersaturation range between 11 and 55.

As an example of the data analysis for each case study, Table 6.15 displays the main particle size distribution parameters obtained for supersaturation 55 at 25°C after 24 hours.

Table 6.15: Particle size distribution mean, standard deviation and coefficient of variation calculations based on 10 repeated measurements for CaCO$_3$ samples at SR=55 (25°C, 24 hours)

Record Number	d(0.1)	d(0.5)	d(0.9)	d(4,3)	Obscuration
1	1.54	8.48	18.77	9.46	6.26
2	1.53	8.42	18.63	9.39	6.26
3	1.53	8.40	18.64	9.39	6.26
4	1.52	8.36	18.58	9.35	6.24
5	1.52	8.33	18.52	9.32	6.24
6	1.52	8.28	18.48	9.29	6.24
7	1.51	8.24	18.37	9.23	6.24
8	1.51	8.22	18.36	9.23	6.23
9	1.50	8.17	18.28	9.18	6.23
10	1.50	8.14	18.25	9.16	6.23
Average (µm)	1.52	8.30	18.49	9.30	
Standard deviation	0.01	0.11	0.17	0.10	
%CV	**0.78**	**1.37**	**0.93**	**1.09**	

Table 6.15 represents a single run for SR=55 at 25°C after 24 hours, with 10 subsequent measurements using the Mastersizer. The results obtained for these runs showed that the diameter of 10% of bulk samples was approximately 1.52µm, for 50% of the crystals the diameter was approximately 8.30µm, for 90% of the particles the diameter was approximately 18.49µm and lastly the mean volume based diameter of the particles in bulk for that test were approximately 9.30µm. The mean diameter over volume (D$_{[4,3]}$) is also known as the DeBroukere mean and provides the mean value of the particle size histogram, following the equation:

$$D_{[4,3]} = \frac{\sum_{i=1}^{n} D_{ivi}^4}{\sum_{i=1}^{n} D_{ivi}^3} \qquad (6.6)$$

where D$_{[4,3]}$ is the mean volume diameter, D$_i$ is the diameter of the ith particle and n represents the number of crystals sampled per measurement.

To summarise, all crystal's size distribution data gathered through both Sysmex and Mastersizer is given in

Table **6.19** and Figure 6.28. It is important to note that, the same procedure was followed for each temperature over time and the mean particle size for all the repeats was taken as the representative crystal size at a specific time and temperature as illustrated in Figure 6.25 to Figure 6.27.

Table 6.16: Particle size for all saturation ratios, at all temperatures after 24 hours

	Mean particle diameter, $D_{[4,3]}$ (µm)		
SR	25°C	40°C	80°C
1.52	2.18 + 0.01	3.68 + 0.03	5.34 + 0.18
2.55	2.95 + 0.04	4.83 + 0.02	10.20 + 0.33
4.77	7.35 +0.01	8.64 + 0.02	13.74 + 0.06
11	7.76 + 0.11	10.43 +0.08	21.80 + 0.12
55	8.84 +0.03	10.93 + 0.12	22.62 + 0.08
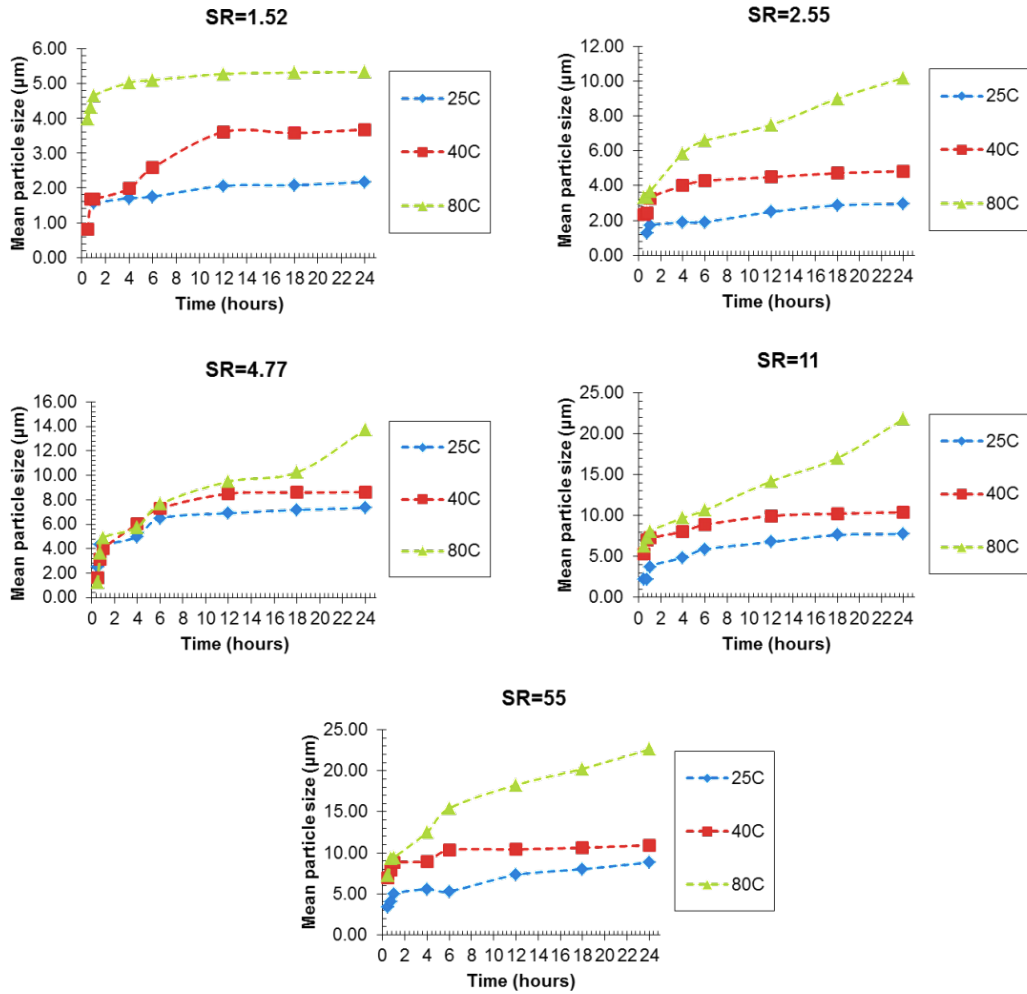
Figure 6.28: Summary of CaCO$_3$ average crystal size for all saturation ratios and temperatures (25°C, 40°C and 80°C) over time.

Overall, it can be observed from Figure 6.28, that particle size is affected by factors such as the initial supersaturation, temperature and experimental time. Furthermore, a decrease in primary crystal size due to an increase in the nucleation rate at higher supersaturation levels or with increase in temperature was noticed. This observation supports studies done by Söhnel and Garside (316) on classical nucleation and growth mechanisms for CaCO$_3$ precipitation in bulk.

Lastly, it is crucial to recall that crystal size is intrinsically related to crystal shape, as one factor depends on the other. The size measurement techniques used considered the assumption of spherical CaCO$_3$ crystals spontaneously growing in bulk solution. Hence, approximations and shape factors were taken into account to determine the size of particles more accurately.

6.4.2 Crystal Particle Shape

Bulk crystal particles were characterised with respect to their shape using microscopic techniques. Initially, some bulk particles were observed in-situ using an optical microscope (Figure 6.29) to get an awareness of their growth at real time. However, as more particles were being formed there was a need to understand the level of transformation these crystals went through during the crystallization experiments. Therefore, bulk crystal samples were collected and filtered over time to be analysed in greater detail using the scanning electronic microscope (SEM). This technique combined with the EDX-S enabled further insights on the morphologies acquired for each batch crystallization experiment.
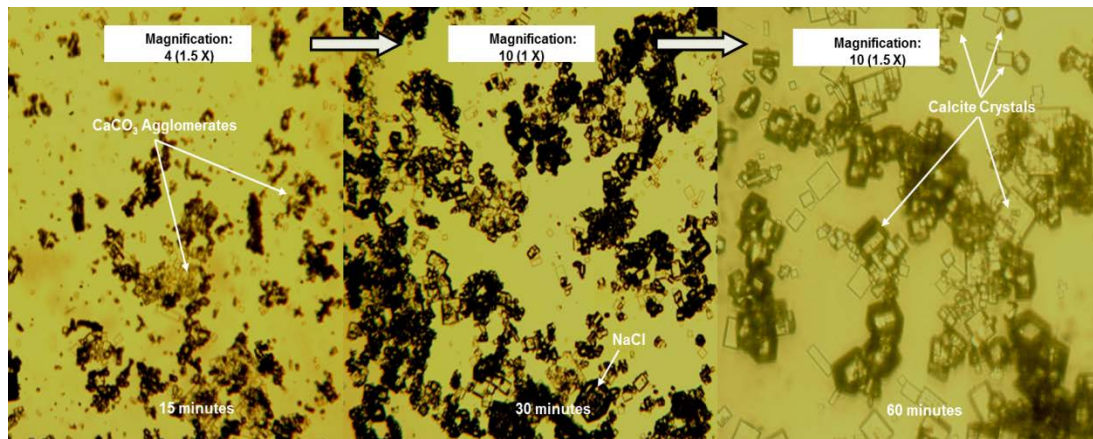
Figure 6.29: In-situ optical observations for SR=4.77 at 80°C over time

The micrograph illustrated in Figure 6.29 shows the overall crystal growth with time, however, it was very difficult to measure the crystal sizes, describe their shape and control agglomeration. Hence, the SEM technique was preferred as it could give higher quality and magnification of each individual crystal in the bulk solution. Particle shape and its time evolution were monitored via SEM and Sysmex considering factors such as supersaturation, time and temperature. In addition to that some SEM/EDX-S measurements were also done to help in identifying the different components present in each $CaCO_3$ polymorph. The Sysmex micrographs enabled observing the crystals in the solution from a 2D perspective which was also interesting since the SEM is more accurate and captures 3D images.

6.4.2.1 Morphologies via Sysmex®

In-situ images were taken as 2D photographs whilst tracking the size of $CaCO_3$ particles in solution using Sysmex FPIA 2100. The software separated the different

pictures according to different size ranges and the selected examples illustrated in Table 6.17 to

Table **6.19** consider observations over time and at different temperatures (25°C, 40°C and 80°C). These selected images could also be compared with the ex-situ measurements done using the SEM. This was especially important to verify any similarities in shape and size using two different techniques.

Table 6.17: Optical micrographs obtained over time via Sysmex for five saturated brines at 25°C
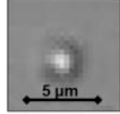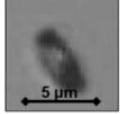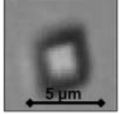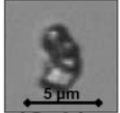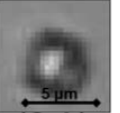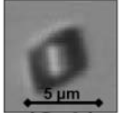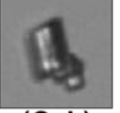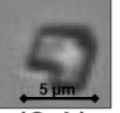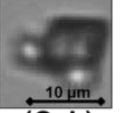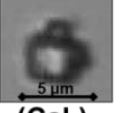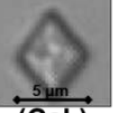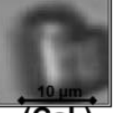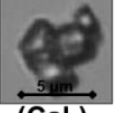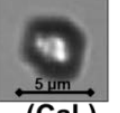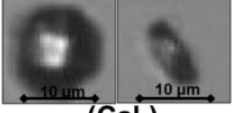
It can be observed from the images in Table 6.17, Table 6.18 and Table 6.19, that vaterite crystals quite commonly appear in the first stages of crystallization (approximately up to 1 hour), especially at saturation ratios below 11 at 25°C and 40°C. Then, for each supersaturation there is a transformation of vaterite into calcite crystals which become more dominant particularly after 12 hours of reaction for experiments done at 25°C and 40°C. Temperature does show an effect on the shape of the crystals at 80°C, as calcite appears as the stable form that grows over time consistently for all supersaturation levels with the exception of supersaturation 1.52 at 1 hour. For SR=1.52 at 80°C, after 1 hour, a circular blurry image was taken and it

is assumed to be vaterite instead of calcite, however after 6 hours of reaction all vaterite crystals seemed to have converted into calcite.

Table 6.18: Optical micrographs obtained over time via Sysmex for five saturated brines at 40°C

Table 6.19: Optical micrographs obtained over time via Sysmex for five saturated brines at 80°C

The main disadvantage of this Sysmex imaging technique relies on the fact that for some particles it is not very clear what their actual shape is. This was observed when two particles overlapped each other in bulk, as an example calcite and vaterite, giving a very unclear pictorial image. In addition to that, the angles at which the software took these images for size measurement is so fast that some images are quite unclear and blurry. So, SEM is definitely the best approach when it comes to particle size characterisation. However, the Sysmex gave a good idea of what kind of polymorphs could be expected for each of the supersaturation as a function of time and temperature.

6.4.2.2 Morphologies via SEM

The key aim of SEM observations is to detect the different morphologies and respective sizes of $CaCO_3$ crystals precipitated spontaneously in bulk solutions. In addition, it is also part of this study to investigate how the growth of $CaCO_3$ particles is influenced by the initial supersaturation and temperature (25°C, 40°C and 80°C). These analyses will elucidate information about the crystallization kinetics for each of the five saturated brine systems.

Observations at 25°C (Figure 6.30 to Figure 6.34) focused on assessing the crystals' morphology over a 24 hour period, for a range of supersaturation levels. The effect of temperature in the morphology was investigated after a 24 hour reaction period, as shown in Figure 6.35 and Figure 6.36.
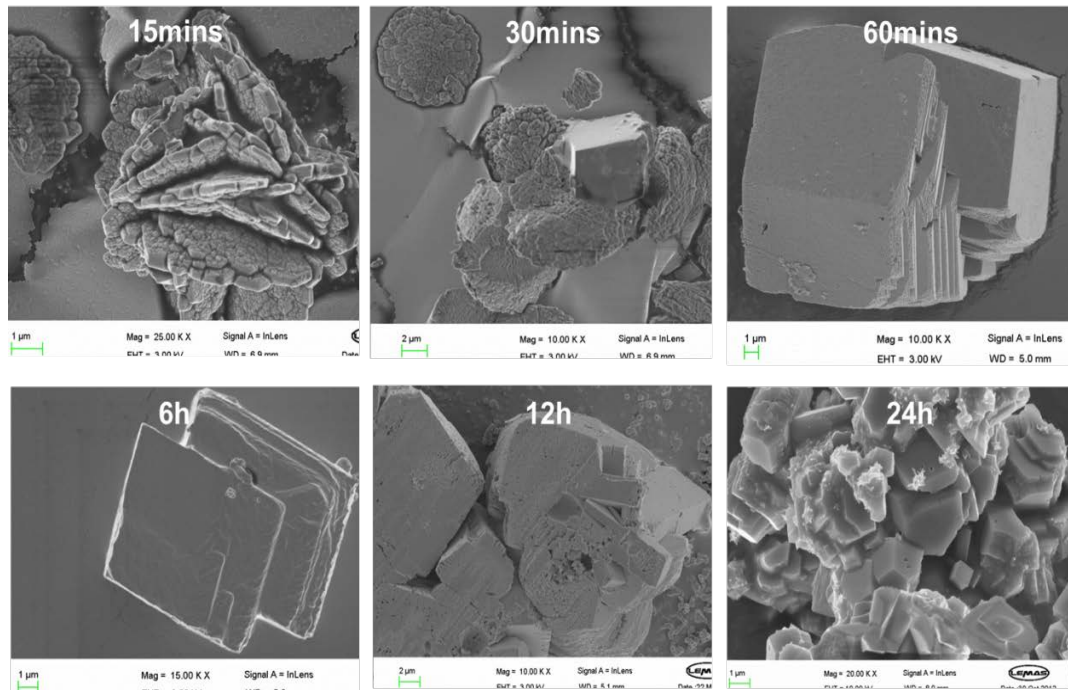
Figure 6.30: Morphology of crystals precipitated from SR=1.52 at 25°C over 24 hours

The SEM images in Figure 6.30 show calcium carbonate particles formed at an initial supersaturation of 1.52 at 25°C, over a 24 hour experiment. There is a notable growth of these crystals over time and their morphology also changed from the very start to the end of the experiment. After 15 minutes from the reaction start, very few particles where observed in solution, and primary spherulite particles aggregated forming vaterite crystals. As the reaction time proceeded, at 30 minutes, more vaterite crystals were observed and some calcite crystals also started to appear in the solution. Then, between 1 to 6 hours, only calcite crystals were observed and some relatively larger crystals were growing through the screw and drive dislocation mechanism. Towards the end of the experiment, plenty of agglomerated calcite crystals were recorded with sizes ranging from ± 2 µm – ± 5 µm.
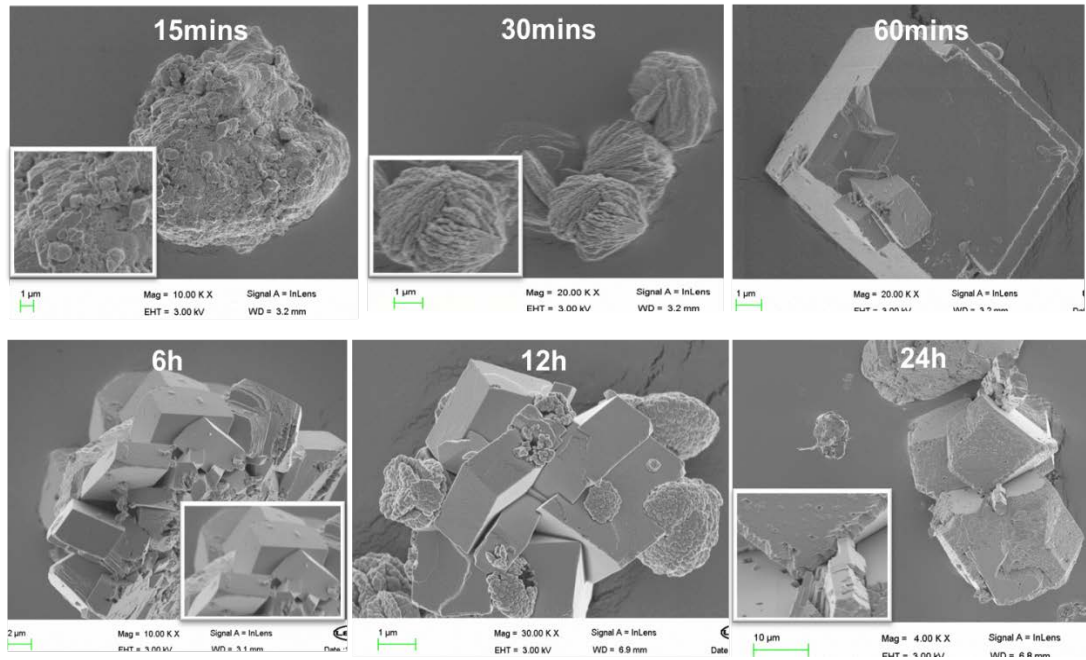
Figure 6.31: Morphology of crystals precipitated from SR=2.55 at 25°C over 24 hours

Figure 6.31 illustrates the polymorphic changes over time when the initial supersaturation was 2.55 at 25°C. Similar to the previous case (SR=1.52) in Figure 6.30, the first stages of crystallization (between 15 minutes and 30 minutes) are marked by the agglomeration of some nano rod particles approximately ± 0.5 μm in size, which then assemble forming spherulitic vaterite crystals. The vaterite crystals will keep growing and some will transform into calcite in up to 12 hours. Then, at 24 hours, only calcite crystals were observed in the solution. This suggests that there was a phase conversion from the metastable form (vaterite) to the most stable one (calcite), as shown in Figure 6.31 for a 12 hour experiment. The final grown calcite crystals obtained after a 24 hour experiment displayed different size ranges (± 2 μm – ± 8 μm) and some, as seen in the image (Figure 6.31), were as big as ± 10 μm. However, it is hard to describe the overall crystal size through SEM given the presence of agglomerated particles. Lastly, it was also noticeable that during calcite crystal growth, the spiral mechanism was predominant, as illustrated in Figure 6.31 after a 1 hour run.
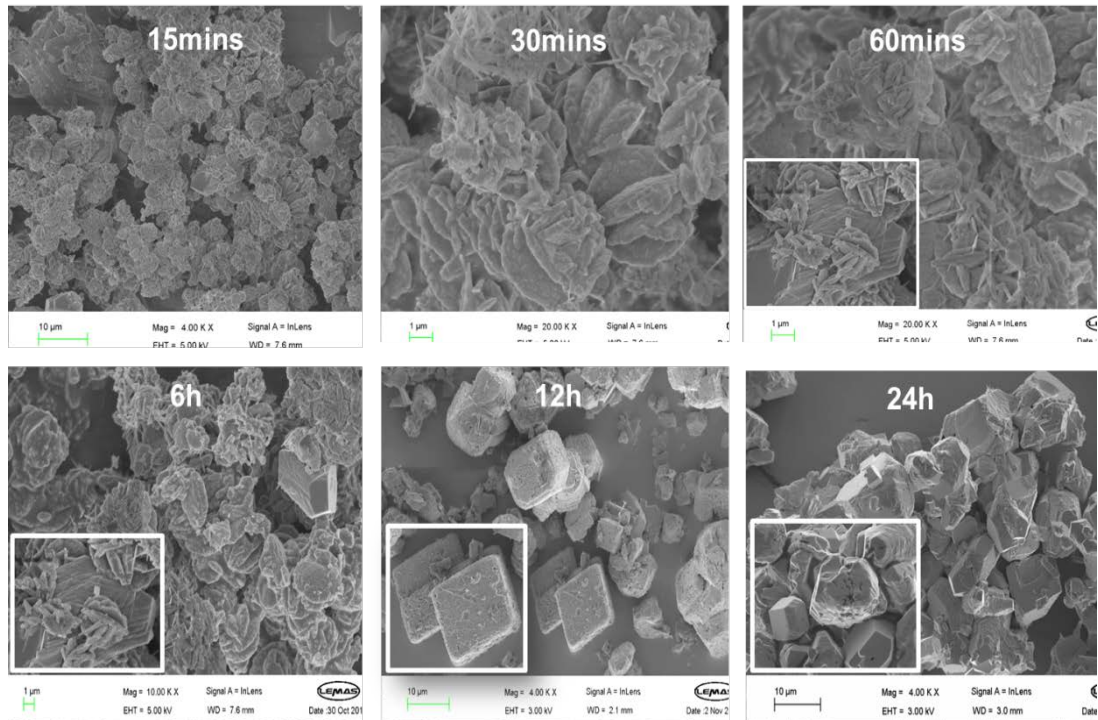
Figure 6.32: Morphology of crystals precipitated from SR=4.77 at 25°C over 24 hours

Figure 6.32 displays the SEM images for supersaturation 4.77 at 25°C throughout a 24 hour period. It is clear that for this initial saturation ratio, more crystals are formed and plenty of vaterite spherulitic crystals are observed from 15 minutes to 1 hour. Then some rhombohedral calcite crystals start appearing at 6 hours and continue to grow up to 24 hours, suggesting these calcite crystals become the main and most stable polymorph of $CaCO_3$ in the solution. Agglomerated crystals are observed and some calcite crystals show a few signs of non-uniformity or breakage at the edges because these were also placed into sonication baths for size analysis. The overall crystal size observed varied from ± 3 µm to ± 10 µm.
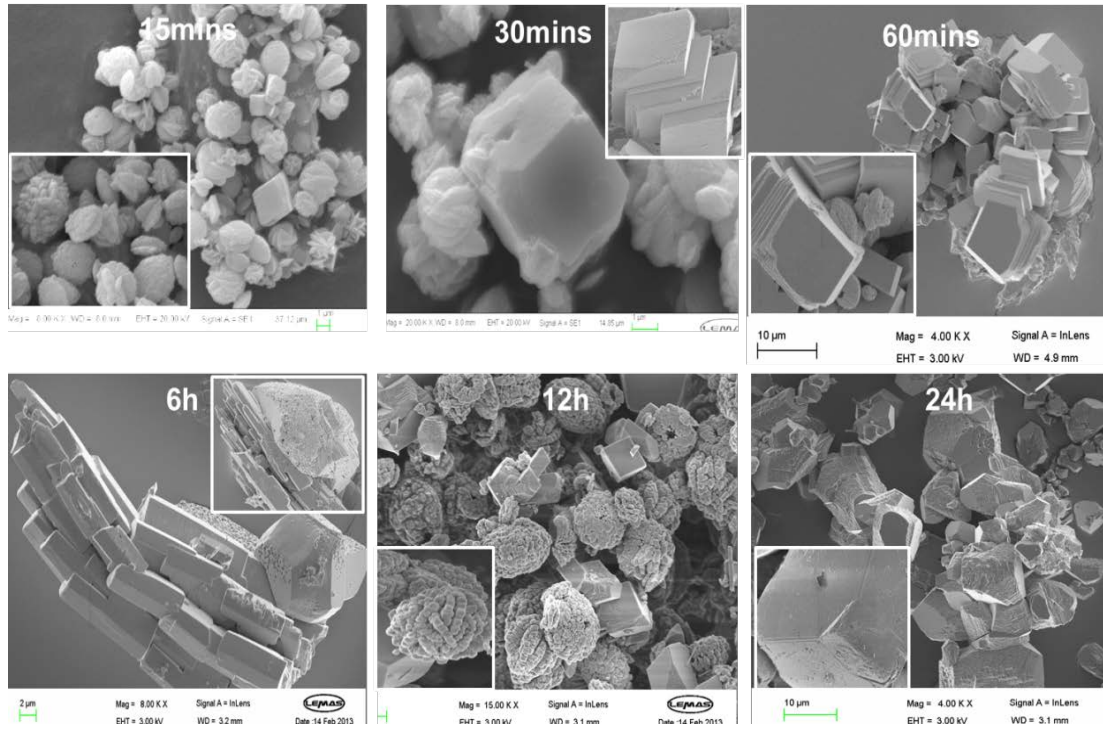
Figure 6.33: Morphology of crystals precipitated from SR=11 at 25°C over 24 hours

Figure 6.33 illustrates the SEM images for initial supersaturation 11 at 25°C, over a 24 hour experiment. Like all previous case studies, during the first stages of crystallization, vaterite is the most dominant anhydrous polymorph of CaCO$_3$ to appear in the bulk solution. However, in this case study, some calcite crystals were also observed 15 minutes from the start of the experiment. Initially, all crystal sizes varied from ± 1 µm to ± 2 µm. Then at 30 minutes of reaction, calcite crystals got bigger (± 4 µm) in comparison to vaterite (± 2 µm). From 1 hour to 6 hours there was a significant growth of calcite marked by the formation of some tabular calcite crystals after 6 hours. The well-defined spherulitic vaterite crystals started disappearing after 12 hours and at 24 hours, only calcite crystals were left in the supernatant liquid solution. It is also interesting to observe the differences in shape for vaterite, which was initially (at 15 minutes) very spherulitic with plates and then when aged or overgrown (at 12 hours), they are reduced to hexagonal discs, some of them hollow in the middle.

Considering that calcite crystal growth is due to vaterite transformations in bulk, then, Ostwald's principle must be taken into account during this crystallization process. During this growth stage, dissolution of smaller particles takes place to form new and bigger calcite crystals. So, this whole phenomenon can explain the variances in the appearance of vaterite over time. Note that a similar mechanism was observed in Figure 6.31 for SR=1.52 at 25°C. Overall, crystal sizes ranged from ± 5 µm to 10 µm.
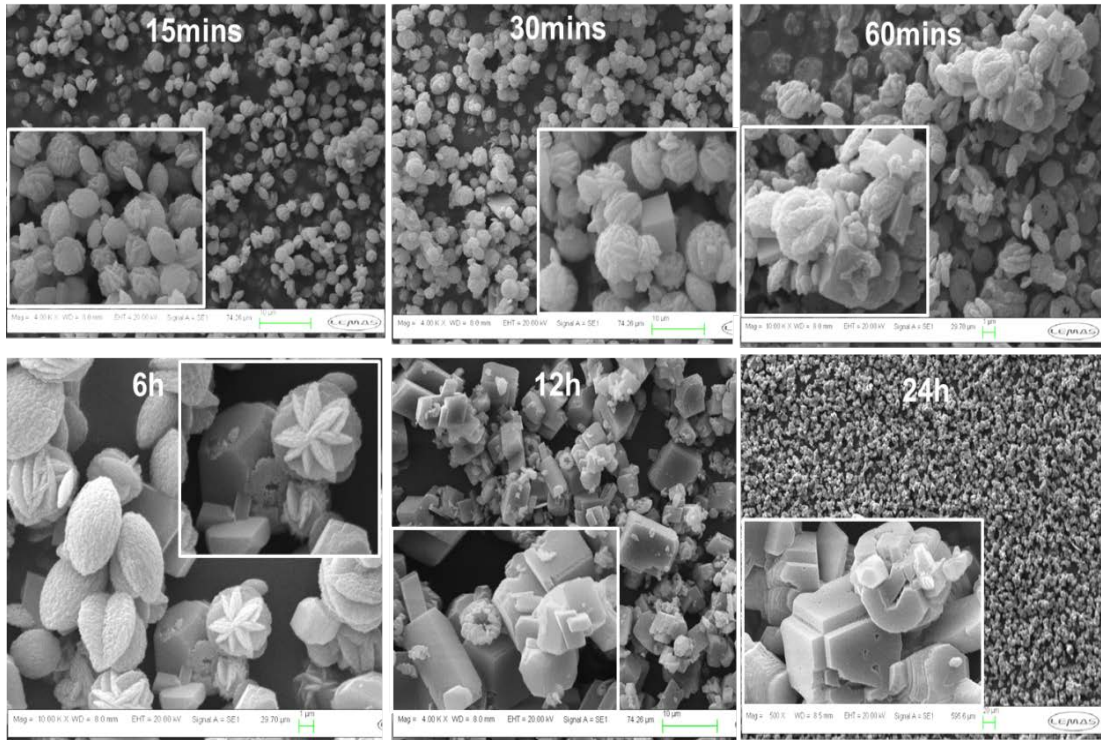
Figure 6.34: Morphology of crystals precipitated from SR=55 at 25°C over 24 hours

Figure 6.34 represents the highest supersaturation case study with SR of 55 at 25°C. As expected, the kinetics should be faster in a higher supersaturation level and therefore a lot of vaterite crystals were formed after 15 minutes with sizes ranging between ± 1 μm to ± 3 μm. From 30 minutes to 1 hour, a few large calcite crystals (± 5 μm) were observed and still plenty of spherulitic vaterite crystals were crystallised in the bulk solution. As the reaction proceeds, well defined rhombohedral calcite crystals were seen in the solution at 6 hours and then, at 12 hours, there were more calcite than vaterite crystals. At the end of the experiment (24 hours), all crystals were converted into calcite, agglomerates were also observed and the overall size varied between ± 5 – 12 μm.

Observations done at 25°C over time, for each initial supersaturation revealed the synergy between thermodynamics and kinetics because the most stable form is not always the first crystal form to appear in solution during $CaCO_3$ precipitation. There is a clear transition of polymorphs driven by its kinetics (i.e. supersaturation) and following mechanisms in which a less stable polymorph gradually converts into a more stable one. It should also be noted that at higher supersaturation more crystals are formed faster in solution, however these appeared to be smaller than those formed slowly at lower supersaturation levels.

Temperature is another critical factor for investigating the $CaCO_3$ crystallization in bulk. So, SEM analyses have been done for the same five saturation ratio brines at 40°C and 80°C, as shown in Figure 6.35 and Figure 6.36.
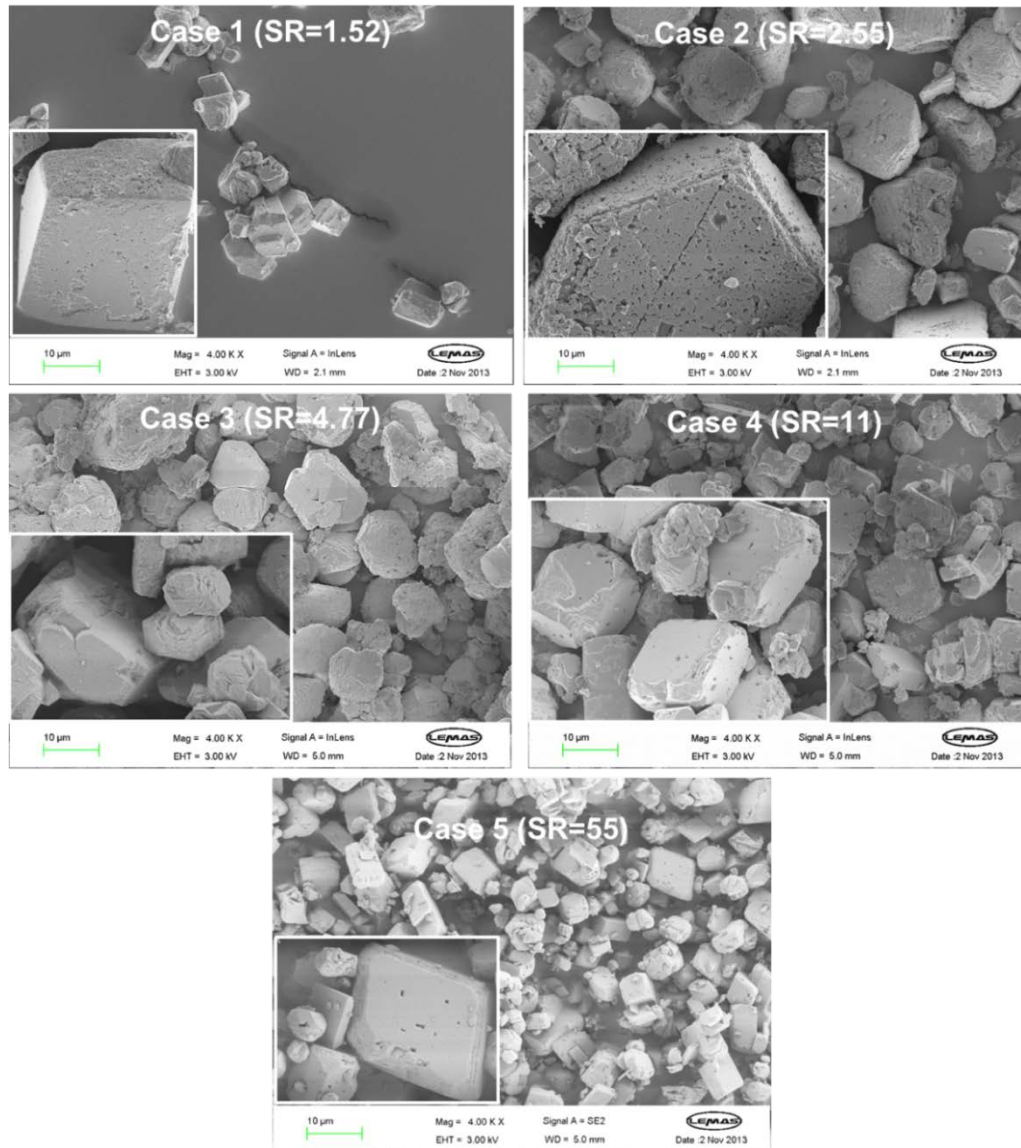
Figure 6.35: Morphology of crystals at 24 hours for a range of supersaturation at 40°C

Figure 6.35 displays the images of $CaCO_3$ crystals formed at 40°C after a 24 hour experiment over a range of saturation ratios. It is noticeable that for all different saturation ratios, it was calcite crystals which were predominantly formed. However, there are a few differences with respect to the amount of crystals observed and their size ranges which varied for each of the different five concentrations studied.

For the lowest saturation ratio, SR=1.52, a few calcite crystals were precipitated and their size ranged from ±1 µm to ±6 µm. For supersaturation 2.55, calcite crystals size

varied from ± 3 μm to ±10 μm, whilst supersaturation 4.77 showed even more calcite crystals with some kinks and steps typical of a spiral growth mechanism and sizes ranged from ±4 μm to ±11 μm. Similarly, both high supersaturation brines (11 ≤ SR ≤ 55) displayed a lot of calcite crystals, most of them with an even size ranging from ± 5 μm to 12 μm for SR=11 and for SR=55 sizes were between ± 5 μm to 15 μm. Overall, there were more crystals precipitated at the same initial saturation ratio, but higher temperature because $CaCO_3$ is less soluble at higher temperatures, increasing the mass scaling tendency in bulk.
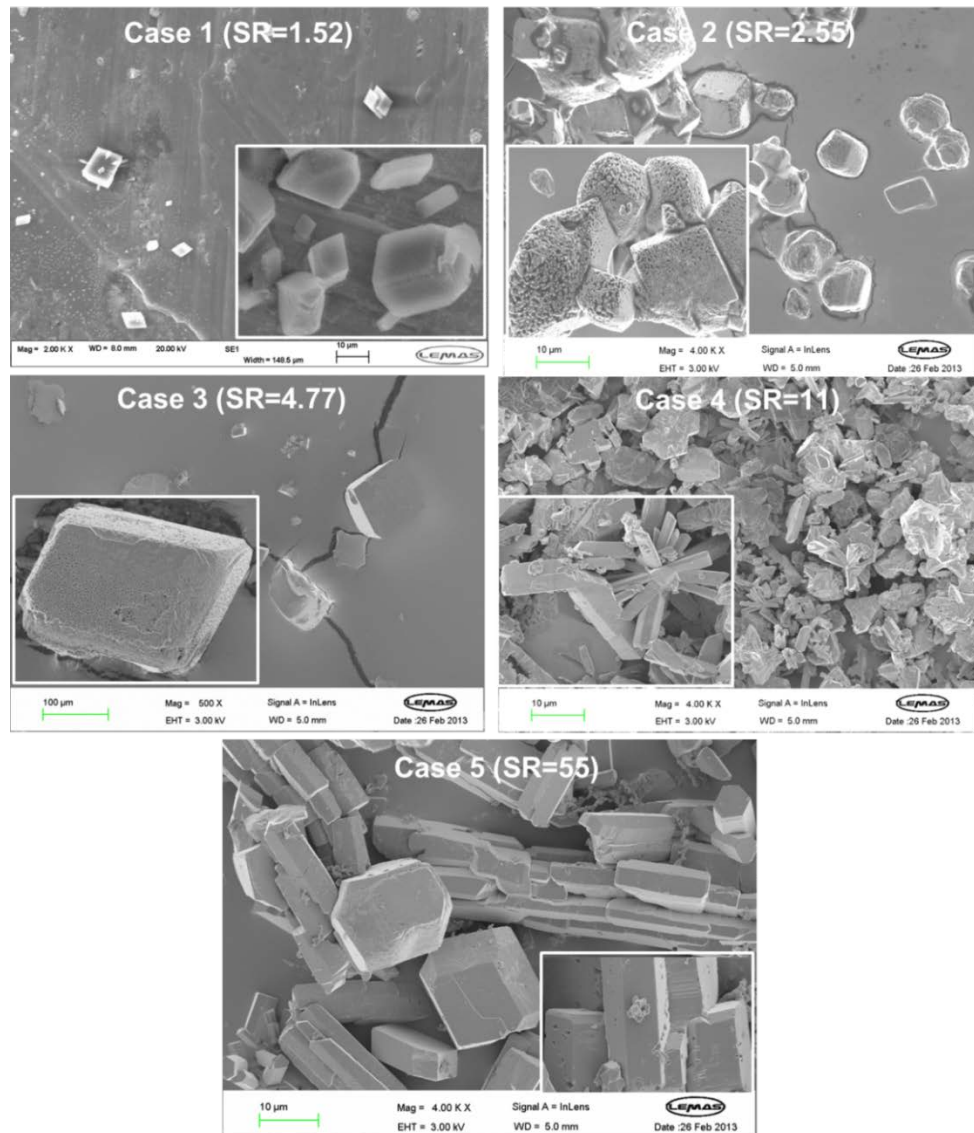
Figure 6.36: Morphology of crystals at 24 hours for a range of supersaturation at 80°C

Results obtained for bulk $CaCO_3$ precipitation at 80°C (at 24 hours) are displayed in Figure 6.36. Overall, it can be seen that the higher the supersaturation, the faster are the kinetics and more crystals are obtained. Nevertheless, comparing the amount of

crystals formed in Figure 6.36 to those formed at 24 hours for 25°C and 40°C, it is even more noticeable that there are significantly more crystal particles at 80°C. Each case studied at 80ºC, after 24 hours showed calcite as the most dominant and main polymorph for $CaCO_3$. The lowest saturation ratio of 1.52 displayed some rhombohedral-shaped calcite crystals with shiny flat surfaces, whose size varied from ± 2 μm to ± 5 μm. At saturation ratio of 2.55 it was observed that calcite crystal size varied from ± 5 μm to ± 10 μm. Then for saturation ratio of 4.77, several calcite crystals with size ranging from ± 7 μm to ± 10 μm were observed. At saturation ratio 11, the SEM showed a huge amount of calcite crystals, most of them agglomerated with sizes ranging from ± 8 μm to ± 15 μm. In addition, some aragonite crystals (pellet like) were also noticeable in a small amount showing evidence of twinning, where crystals are formed by intergrowth, passing through each other with the incorporation of twin planes. Finally, at the highest supersaturation (SR=55), mostly calcite crystals and some aragonite crystals were observed with an overall size ranging from ± 8 μm to ± 20 μm. The aragonite crystals displayed unidirectional growth of their elongated orthorhombic face.

It is worth noting that the size ranges observed are based on samples taken from the bulk solution, so they may not be showing exactly the same values as the size measurement techniques calculated but they are within the ranges determined. It can also be noted that these calcite particles displayed some sort of porosity due to the CO_2 interactions in bulk solution when these were heated up.

6.4.2.3 EDX-S analyses

The presence of $CaCO_3$ polymorphs was confirmed from a combination of techniques which included the SEM (described in section 6.4.2.2), the EDX-S and the XRD (described in section 6.4.3.1). EDX spectroscopy helped in characterising $CaCO_3$ crystals during SEM analyses, providing the elemental analysis of a particular region from the sample.

It can be seen in Figure 6.37, that a region is selected from the SEM sample representing the location point where the electron dispersive spectroscopy analysis took place. The resultant EDX spectrum displays the number of x-rays and energy emitted from the sample (y-axis) to the atoms (x-axis). Hence, all atoms present in the sample are scanned and identified through the x-ray detector. For these analyses, $CaCO_3$ particles are assessed and thus its atoms are to be expected, specifically calcium, carbon and oxygen. Other atoms which may also be present are: Au, because all samples are gold coated; Al, Cu, Cr, Fe because the crystals are on a

metal stud which contains those elements and can be easily detected by the x-ray beam. Lastly some Na and Cl could also be detected in some cases, since sodium chloride salt may show up as a residual from the bulk solution.
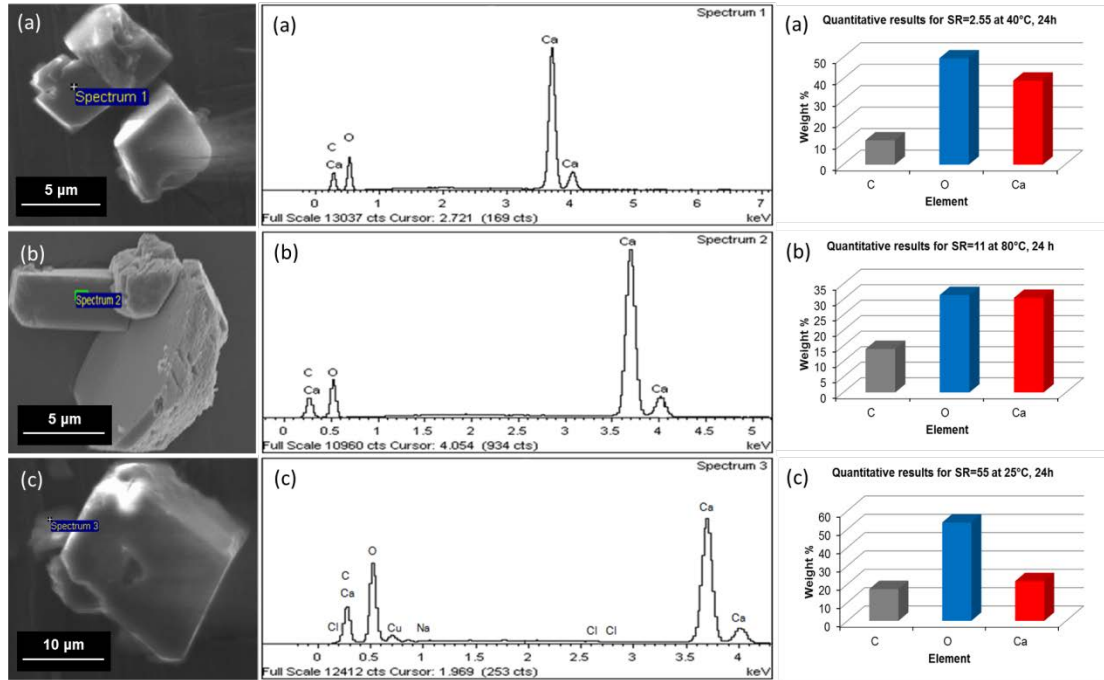
Figure 6.37: Examples of electron dispersive spectroscopy point and identification method for different CaCO$_3$ crystals after 24 hours: (a) Sample from solution with SR=2.55 at 40°C; (b) Sample from bulk solution with SR=11 at 80°C and (c) Sample from bulk solution with SR=55 at 25°C. Images display the SEM region of observation, with its respective spectrum and quantitative analysis via weight percentage.

EDX was mainly used when oddly shaped crystals were observed to ensure these had CaCO$_3$ elements and could be a polymorph in a different angle or with unusual features caused by breakage of the crystals, for instance.

It can be seen from Figure 6.37 that the x-ray penetration varied from sample to sample as the beam penetrates at different depths depending on the porosity and amount of the crystal on the selected region. Hence, from the example in Figure 6.37 (a), the spectrum 1 shows a higher weight percentage of calcium compared to the one in Figure 6.37 (c) (39% against 21%) but both carbon and oxygen levels are very close to each other.

EDX helped quantifying the crystals being pictured via SEM but a more accurate confirmation of CaCO$_3$ polymorphs was acquired through XRD analyses.

6.4.3 Crystal Particle Internal Structure

6.4.3.1 XRD measurements

The final $CaCO_3$ crystals obtained from 24–hour experiments at 80°C have been filtered and analysed using the powder XRD technique. The internal structure of the three crystalline anhydrous forms of $CaCO_3$ (i.e. calcite, aragonite and vaterite) obtained from the literature is shown in Figure 6.38. These peak patterns are unique fingerprint characteristic of each $CaCO_3$ polymorph.
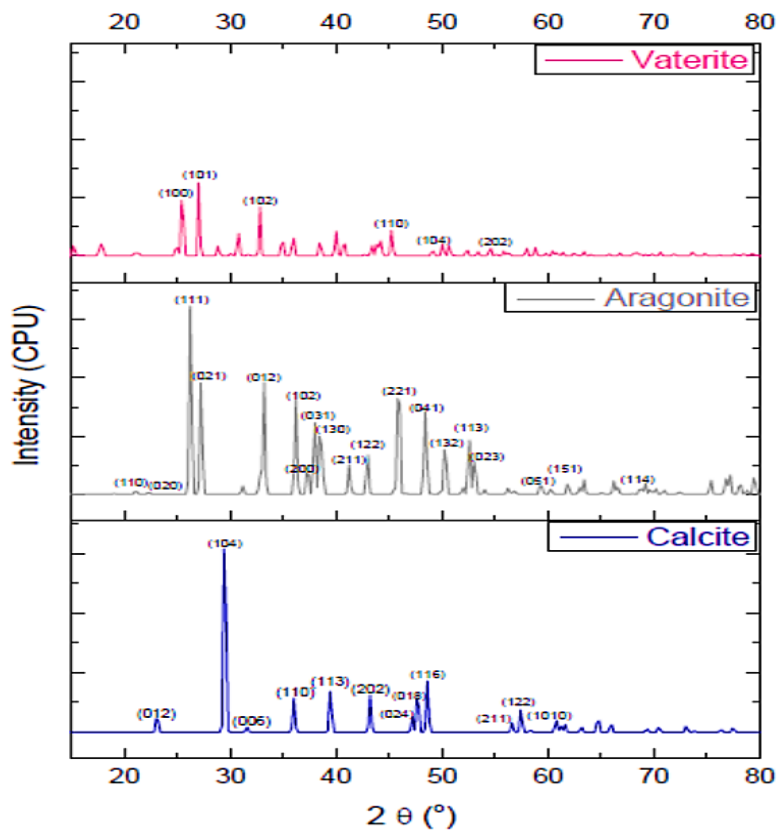
Figure 6.38: Standard PXRD patterns for three main $CaCO_3$ polymorphs: calcite (317), vaterite (318), aragonite (319)

The crystallographic structure of these three main polymorphs is readily available in the literature and several identical PXRD patterns can be extracted from the standard crystallographic database, as the ones presented in Figure 6.38. It can be observed that for all polymorphs, there is a peak index identifying the most characteristic peaks encountered for each of these forms of $CaCO_3$. Typically, the peak indexing can be determined using Bragg's law and Miller Indices (hkl) for a specific crystal system.

Calcium carbonate bulk samples only were collected at 80°C after 24 hour-experiments, as only these experiments could produce a sufficient amount ($\pm1/2$ g)

of powder to be placed in sample holder for PXRD analyses. Hence, the internal structure of the crystals for each saturation ratio was only investigated at the end of the experiments, at 80°C. The peak patterns obtained were recorded by the XRD instrument, and then treated to match each diffraction angle detected to a corresponding reference database from the literature. The peak relative intensities were analysed to match the 2Θ angles from the generated XRD pattern of the reference sample in the literature. The best fitting match was taken as the final XRD pattern. Results of these studies are summarised in Figure 6.39, including two reference peaks used for data analyses.
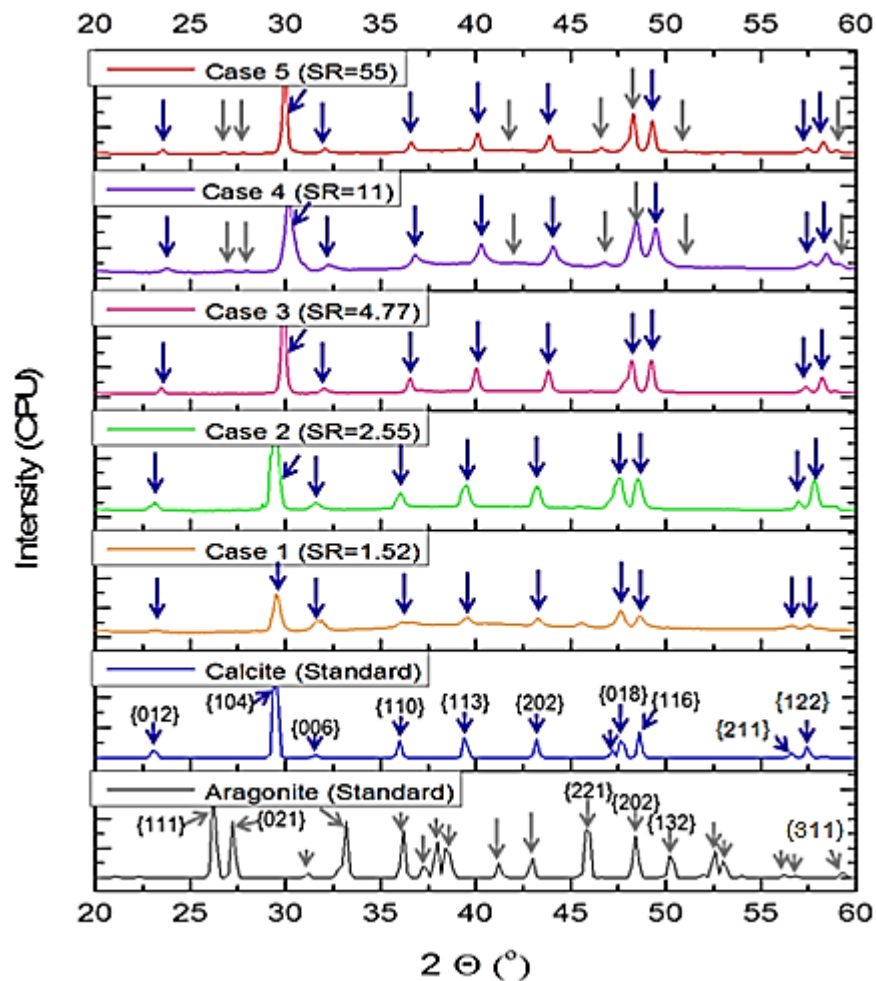
Figure 6.39: X-ray diffraction pattern for samples crystallised in of bulk solutions at different saturation ratios, after 24 hours at 80°C. The standard reference XRD patterns for calcite (317), and aragonite (319) were used for data comparison

Figure 6.39 displays the XRD pattern for the five case studies at 80°C after 24 hours. It is noticeable that calcite is the dominant polymorph crystallised for all saturation ratios, however, some traces of aragonite are present in samples for Case 4 (SR=11) and Case 5 (SR=55). The resultant peaks were analysed through a match with the

reference XRD pattern found from the crystallographic database. Their relative intensities and inter-atomic spacing enabled characterising each of the five case studies. At higher supersaturation (11 ≤ SR ≤ 55) a few traces of aragonite crystals were observed (Figure 6.39.), marked by tiny matching peaks. Overall, peak's indexing was achieved through comparison with reference XRD patterns from the literature, and also through calculations of the interplanar spacing and 2Θ angle through Bragg's law (Figure 6.39).

Calcite is the most thermodynamically stable polymorph of $CaCO_3$ and it crystallises as a trigonal-hexagonal lattice with a space group of $R\overline{3}C$ (126). The lattice parameters determined as the unit cell lengths are a = b = 4.99 ≠ c = 17.06, and the angles between them α = β = 90° ≠ γ = 120°(126). As an example on how to determine the Miller indices of each peak, it is important to calculate the interplanar distance (Equation (6.7) using the cell dimensions and considering the crystal system (for calcite is trigonal-hexagonal) of the specific $CaCO_3$ polymorph. Then, by applying the Bragg's law (Equation (6.9), 2 Θ positions can be determined for a specific {hkl} crystal face. It is known from the literature that the calcite major growth determining plane is {104}, so considering *hkl* = (104), the inter-atomic d – spacing and respective 2Θ angle can be determined as described by Equations (6.7) to (6.9):

$$\frac{1}{d^2_{(hkl)}} = \frac{4}{3}\left(\frac{(h^2 + hk + l^2)}{a^2}\right) + \left(\frac{l^2}{c^2}\right) \qquad (6.7)$$

$$\frac{1}{d^2_{(104)}} = \frac{4}{3}\left(\frac{1^2 + (1 \times 0) + 0^2}{4.99^2}\right) + \left(\frac{4^2}{17.06^2}\right) \rightarrow d_{(104)} = 3.04\ \dot{A} \qquad (6.8)$$

$$n\lambda = 2d\sin\theta \rightarrow \sin\theta = \frac{n\lambda}{2d} \qquad (6.9)$$

$$\sin\theta_{(104)} = \frac{(1 \times 1.54)}{2 \times (3.04)} \rightarrow \theta = 14.67° \rightarrow\therefore 2\theta = 29.34° \qquad (6.10)$$

As it can be seen from the calculations above and Figure 6.39 (blue line), calcite {104} peak is at approximately the 2Θ position of 29.34º, where a distinct peak with high intensity is observed. Subsequently, all other peaks obtained for $CaCO_3$ (calcite) were identified, indexed, their atomic d-spacing were calculated and the Miller indices corresponding to the diffraction angles were established from those recorded in the literature (Figure 6.38) (317). Overall the main calcite peaks found are identical to the literature and correspond to the following positions: {012} at 23.05º, {104} at 29.34º, {110} at 36.01º, {113} at 39.42º, {202} at 43.19º and {116} at 48.46º. Table 6.20

displays the differences between calcite reference peaks and the experimentally measured peaks for each supersaturation case study. The inter-atomic spacing was exactly the same as the one found for calcite crystallographic data literature, subsequently suggesting a good correlation of the Miller indices. However, some of the 2Θ location shifted slightly compared to the reference pattern found in the literature, due to the tendency of calcite powder to form a slight uneven surface layer after grinding. Ideally, the flatter the samples the better is the peak pattern. Both literature and experiments used the same copper radiation source. Details about each individual data are shown in Table 6.20.

Table 6.20: Comparison between XRD data obtained in this study and literature provided for calcite (317)

Main Peak {hkl}	2Θ/° (*literature*)	2Θ/° (experimental)					d-spacing/ Å (*literature = experimental*)
Case study nr.		1	2	3	4	5	1 – 5
{012}	23.06	23.06	23.05	23.05	23.05	23.05	3.85
{104}	29.36	29.34	29.34	29.35	29.36	29.37	3.04
{110}	36.01	36.01	36.01	36.03	36.01	36.01	2.49
{113}	39.42	39.42	39.42	39.42	39.42	39.42	2.28
{202}	43.19	43.18	43.18	43.18	43.18	43.18	2.09
{018}	47.37	47.37	47.37	47.37	47.37	47.37	1.92
{116}	48.46	48.46	48.46	48.46	48.46	48.46	1.88
{122}	57.46	57.46	57.46	57.46	57.46	57.46	1.60

Aragonite is the metastable form of $CaCO_3$ and its reference XRD peak is also found in Figure 6.38 (grey line). The Miller indices for aragonite crystals were confirmed by applying a similar method for XRD peak identification as used for calcite. The main difference is that aragonite crystal system is orthorhombic with a space group of Pmcn and cell dimensions as a =4.96 ≠ b = 7.97 ≠ c = 5.74 and the angles between them α = β = γ = 90°. So, Equation (6.11) can be applied for calculating the inter-atomic spacing and the Bragg's law Equation (6.13), for 2Θ of a specific Miller Index. Now, considering the plane *hkl* = (111) for aragonite, as this is the typical largest growing face:

$$\frac{1}{d^2_{(hkl)}} = \left(\frac{h^2}{a^2}\right) + \left(\frac{k^2}{b^2}\right) + \left(\frac{l^2}{c^2}\right) \tag{6.11}$$

$$\frac{1}{d^2_{(111)}} = \left(\frac{1^2}{4.96^2}\right) + \left(\frac{1^2}{7.97^2}\right) + \left(\frac{1^2}{5.74^2}\right) \rightarrow d_{(104)} = 3.39 \, \dot{A} \qquad (6.12)$$

$$n\lambda = 2d \sin\theta \rightarrow \sin\theta = \frac{n\lambda}{2d} \qquad (6.13)$$

$$\sin\theta_{(104)} = \frac{(1 \times 1.54)}{2 \times (3.39)} \rightarrow \theta = 13.13° \rightarrow \therefore 2\theta = 26.26° \qquad (6.14)$$

Comparing the diffraction patterns of each SR case study, it can be elucidated from the shape and size of the diffraction peaks, the actual size of the crystalline material formed in each sample analysed. Large crystallites tend to form narrow and sharp peaks, whilst smaller crystallites usually give smaller and broader peaks. Hence, the size of crystals in supersaturation 1.52 and 2.55 is notably smaller than those from supersaturation 4.77 to 55. These size variances were also observed through SEM and particle size distribution measurements.

Lastly, the number of peaks is also related to the symmetry of the crystal, so for calcite there is lower number (trigonal – hexagonal) of peaks than for aragonite (orthorhombic). Lastly, aragonite main peaks shown in Figure 6.39 for SR=55 and SR=11 have very small intensities, suggesting very small amount of it present in the sample. The main observed peaks for these two case studies are at 2Θ position 26.27° for peak {111}, then at 27.27° for {021}, at 48.57° for {202} and at 59.38° for {311}.

To conclude no vaterite peaks were observed after 24 hours bulk precipitation under given conditions of pressure and temperature, hence, no peaks were detected via XRD (Figure 6.39).

6.5 Crystal Growth Kinetics and Mechanisms

6.5.1 Crystal Growth Rates and Growth Mechanisms

Particle size measurements detailed in section 6.4.1 showed the relationship between crystal crystal growth as a function of supersaturation, temperature and time. The overall linear growth rate (G=dL/dt) can be converted into an overall mass growth rate (R_G) under the assumption that all crystals formed are calcite and utilising the equation (2.25). Based on those size measurements and on previous studies by Kralj (140) and Verdoes (280) for vaterite and calcite growth in water, it can be expected that there will be a non-linear relationship between the crystal growth rate

and supersaturation. Hence, the relationship between the average growth rates and the relative supersaturation (σ) for CaCO₃ bulk precipitation is shown in Figure 6.40.
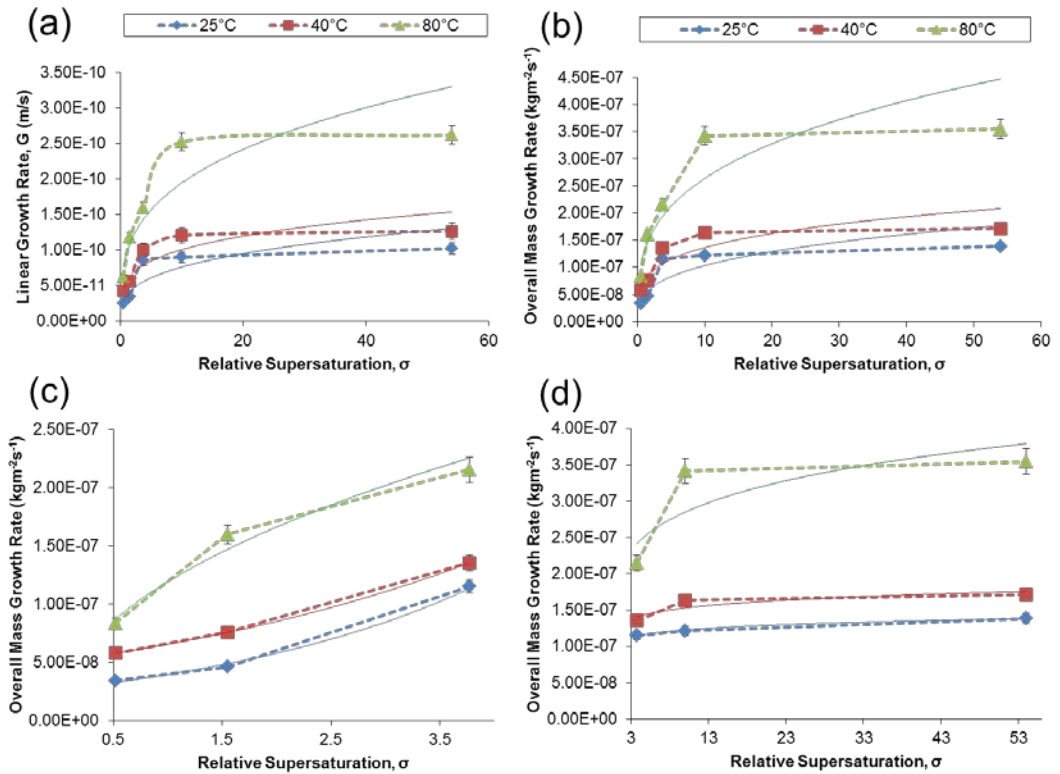
Figure 6.40: Growth rates as a function of relative supersaturation and temperature: a) Overall linear growth rate; b) Overall mass growth rate; (c – d) Differences between the overall mass growth rate at low (c) and high (d) relative supersaturation levels, suggesting different growth mechanisms for σ > 4

Figure 6.40 (a and b) shows that both overall linear and mass crystal growth rates possess similar trends at 25°C, 40°C and 80°C. However, it is noticed that different mechanisms can be expected to dominate as the supersaturation increases. From Figure 6.40 – c, it can be seen that at low supersaturation (σ ≤ 10), a parabolic relationship characteristic of spiral growth mechanism is expected to control the overall rate. However, at the higher supersaturation regime (σ ≥ 10), the overall crystal growth becomes steadier and it is likely to follow either a 2D nucleation or diffusion mechanism, if the best fit curve for Figure 6.40 – d is either exponential (2D nucleation) or linear (diffusion). In order to simplify and obtain more accurate estimations of growth mechanisms and kinetics during spontaneous precipitation of CaCO₃, analysis will be done separately, considering low (0.52 ≤ σ ≤ 3.77) and high (3.77 ≤ σ ≤ 54) supersaturation ranges.

The extraction of the growth rate (G or R_G) is based on the assumption of size independent growth. The growth rate constants (K_G) at 25°C, 40°C and 80°C are going to be determined by plotting the data points extracted from size measurement experiments at varied initial relative supersaturation. Given the differences observed in Figure 6.40 (c – d), the growth rate constant and respective growth mechanisms are going to be investigated considering the BCF model to better explain the mechanisms that control $CaCO_3$ crystal growth in bulk solutions. The relationship between the overall rates for determining a range of superstation at different temperatures is summarised in Table 6.21.

Table 6.21: Growth rates as a function of supersaturation and temperature

SR	T (°C)			Number of repetitions, n
	25 G (m/s)	40 G (m/s)	80 G (m/s)	
1.52	2.52E-11 ± 0.01	4.26E-11 ± 0.03	6.18E-11 ± 0.10	3
2.55	3.41E-11 ± 0.04	5.59E-11 ± 0.02	1.18E-10 ± 0.13	3
4.77	8.51E-11 ± 0.01	1E-10 ± 0.02	1.59E-10 ± 0.05	3
11	8.98E-11 ± 0.11	1.21E-10 ± 0.08	2.52E-10 ± 0.11	3
55	1.02E-10 ± 0.03	1.27E-10 ± 0.12	2.62E-10 ± 0.08	3

Assuming that spiral growth (power law) mechanism is the dominant one for the bulk precipitation experiments done over a range of supersaturation, then a linear relationship is expected when plotting the square root of growth rate (R_G) against the relative supersaturation (S-1), as shown in Figure 6.41. The slope of this plot will provide the growth rate constant (K_G) and the order is assumed to be 2 (g=2).

Results presented in Figure 6.41, show a strong linear relationship at low relative supersaturation ranges (σ ≤ 4) at 25°C, 40°C and 80°C. However, at higher relative supersaturation levels (4 ≤ σ ≤ 54) the strong linear relationship can only be observed at 25°C, as linear fit (R^2) decreased with increase in temperature (i.e. at 40°C and 80°C). The poor linear fit at high supersaturation suggests a different mechanism is dominant.
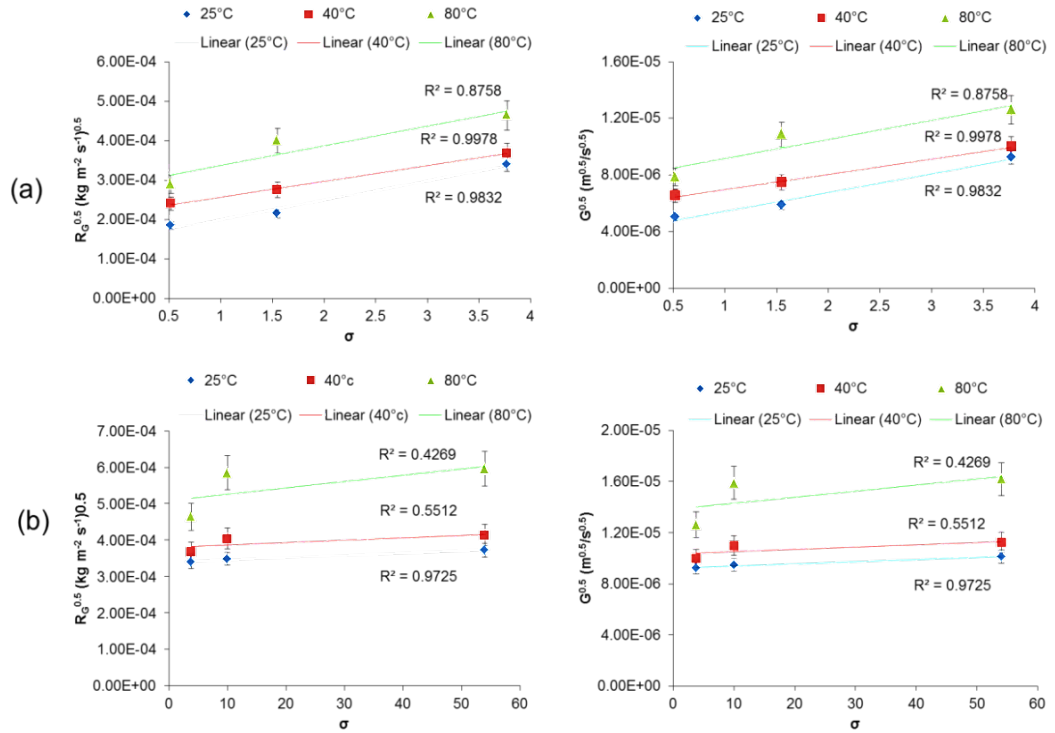
Figure 6.41: Square root of the overall mass growth rate for calcite as a function of relative supersaturation: (a) low and (b) high, at 25°C, 40°C and 80°C

As an example, the best fit line for the low supersaturation ($\sigma \le 4$) range at 25°C is given by Equation (6.15) or by Equation (6.16) which represents the overall mass of calcite in bulk:

$$\sqrt{G}[m.s^{-1}]^{0.5} = (1.00 \pm 0.08) \times 10^{-6}(S-1) \tag{6.15}$$

$$\sqrt{R_G}[kgm^{-2}s^{-1}]^{0.5} = (5.00 \pm 0.08) \times 10^{-5}(S-1) \tag{6.16}$$

Then, the growth rate expression can be re-written as shown in equations (6.17) and (6.18). Since growth rates were based on particle diameter, half of this value is frequently used to express the growth rate in terms of particle radius ($\dot{r}=dr/dt$), as illustrated in Equation (6.18).

$$G[m.s^{-1}] = (1.00 \pm 0.03) \times 10^{-12}(S-1)^2 \tag{6.17}$$

$$\dot{r}[m.s^{-1}] = (0.50 \pm 0.03) \times 10^{-12}(S-1)^2 \tag{6.18}$$

The growth rate constant value (based on particle radius) at 25°C is $k_r=0.0050 \pm 0.03$ nm/s and is relatively lower than values reported by Spanos et al. (287), studies.

According to the classical nucleation theory, both nucleation and crystal growth rates depend on the solution supersaturation. However, the rate constants for nucleation

($k_{J\text{ or }}k_r$) and crystal growth (k_G) are not supersaturation-dependent. These constants are typically calculated according to the analysis of the kinetic data (280). Both growth rate constant and the growth orders were determined from log (S-1) vs. log r plots within the supersaturation range investigated and the results are shown in Table 6.22. At all conditions examined the results are close to the expected second order growth mechanism of surface controlled growth.

Table 6.22: Growth rate constants (k_r) and growth rate order calculated for calcite crystals at 25°C, 40°C and 80°C assuming spiral growth mechanism (g=2).

SR	Temperature (°C)					
	25		40		80	
	k_r(m/s)	g	k_r(m/s)	g	k_r(m/s)	g
1.52	5.00E-13 ± 0.01	1.83	5.00E-13 ± 0.03	1.53	5.00E-13 ± 0.10	1.62
2.55	5.00E-13 ± 0.04	1.83	5.00E-13 ± 0.02	1.53	5.00E-13 ± 0.13	1.62
4.77	5.00E-13 ± 0.01	1.83	5.00E-13 ± 0.02	1.53	5.00E-13 ± 0.05	1.62
11	2.00E-16 ± 0.11	1.08	2.00E-16 ± 0.08	1.03	1.25E-15 ± 0.11	1.02
55	2.00E-16 ± 0.03	1.08	2.00E-16 ± 0.12	1.03	1.25E-15 ± 0.08	1.02

Overall the growth rate constants at 25°C are slightly smaller than values found in the literature for calcite or vaterite. However, according to Kralj et. al., (320) the ionic strength may affect the growth rate, so higher ionic strength usually leads to an increase in the growth rates. In this study, the ionic strength varied from 0.79 – 1.38 mmol/l, values much lower than those reported by Kralj (320) at 25°C (i.e. 15 - 315 mmol/l). This explains why the growth rate constant found from the low saturation range experiments are a bit lower than those determined in spontaneous precipitation of $CaCO_3$ for Krajl (320), Andreassen (321) and Hounslow (322) and Ellen (323) studies. On the other hand, calcite grows slower than vaterite and therefore a lower rate constant than values in the literature is also a result of differences in the polymorph growth mechanisms.

Typical studies on calcite crystallisation in water were done under the low supersaturation range and for that reason; calcite growth order is ca. 2, i.e. a surface controlled growth mechanism. Results for the lower supersaturation range showed the order changing from 1.52 to 1.83, which are fairly close to 2.

For higher supersaturation case studies, it is clear that the growth order exhibits a more complex dependence on temperature, and seems to decrease from 25°C to 80°C. Furthermore, given that the diffusion mechanism seems to control the overall growth of calcite at high supersaturation and when the temperature was increased. According to the BCF theory, under extremely high supersaturation and temperature

conditions, there is a higher diffusion of ions from the bulk solution towards the surface of the crystal, hence a surface growth mechanism is more predominant. This theory was supported by the appearance of some aragonite crystals at 80°C. For more accurate results at higher supersaturation at least another value of high supersaturation should be included, reducing the possibility for error whilst interpreting the kinetics at high supersaturation.

High growth rates at elevated temperatures are difficult to determine using the method applied in this work. The depletion of calcium and carbonate ion activities is very fast, resulting in few uncertainties for the high supersaturation range.

In conclusion, it is probably unusual for the rate of crystal growth be controlled by a single mechanism. Depending on supersaturation and temperature, several mechanisms can take place simultaneously, however the faster growth mechanism controls the overall rate (316). For $CaCO_3$ crystals at low supersaturation, spiral growth and mono-crystalline particles are likely to appear, whereas moving to higher supersaturation regimes, the crystals tend to grow via 2D nucleation, exhibiting rougher surfaces before entering the regime of diffusion control which might produce the final crystal shape.

6.5.2 Growth Kinetics via the Arrhenius Approach

When no pre-assessments are made about the growth rate mechanism, the apparent activation energy (E_A) can be determined from calculated growth rate constants at each temperature. Hence, the relationship between the growth rate constant, k_G or k_r and the absolute crystallising temperature, can be given by the Arrhenius equation, as follows:

$$logR_G = logk_G + g \times log(S - 1) \tag{6.19}$$

A linear regression model from log (R_G) versus log (S-1) was used and the best fit line equation provided the reaction order (g) from the slope of the trend, the growth rate constants (k_G) from the y-intercept.

The Arrhenius activation energy was then determined using Equation (6.20):

$$k = A \times e^{-Ea/RT} \tag{6.20}$$

where k is the rate constant, A is the collisional frequency factor, E_a is the activation energy, R is the gas constant and T is the crystallising temperature. Then, the activation energy is calculated from the slope of the logarithmic of Equation (6.20):

$$logk = logA \times \left(\frac{-E_a}{R}\right)\left(\frac{1}{T}\right)$$ (6.21)

Using the growth data in Equations (6.19) and (6.21), the Arrhenius activation energy of 14.7 ± 0.15 KJ/mol is obtained for the heterogeneous crystallization of calcite in bulk solutions. This result is compared with studies done by Koutsoukos (324) when determining the growth kinetics of $CaCO_3$ precipitation in seawater over a range of temperatures, in which the activation energy of calcite was ±34.20kJ/mol. According to Mullin (14) if the activation energy is between 8kJ/mol – 20kJ/mol, diffusion is the dominant growth mechanism, and if it is between 40kJ/mol – 60kJ/mol, the surface growth mechanism is the most dominant. For this study, there is clearly a transition from the surface spiral growth mechanism at low relative supersaturation values (σ ≤ 4) to surface diffusion controlled mechanism at higher relative supersaturation values (11≤ σ ≤ 54). However, results obtained have shown that the overall dominant mechanism is controlled by diffusion. Results obtained by Koutsoukos (324) have also shown a transition from surface to diffusion growth mechanism; however the activation energy obtained for a higher supersaturation range (i.e. 10≤ σ ≤ 100) was slightly higher.

Typically studies previously done on $CaCO_3$ precipitation have usually focused on either low or high supersaturation ranges. However, in the work presented here, a broader range is investigated and as a result calcite growth is mainly driven by diffusion control rather than spiral growth mechanism. In addition, this justifies the appearance of vaterite and aragonite (at higher temperatures) crystals prior to the formation of calcite (as shown by SEM analysis). The average rate constants determined are slightly higher than those determined from a spiral growth assumption and these are 1.93E-11 ±0.10 m/s (25°C), 2.56E-11 ±0.15 m/s (40°C) and 4.85E-11 ±0.12 m/s (80°C). Lastly, the growth rate orders obtained were 1.38 ± 0.05 (25°C), 1.29 ± 0.05 (40°C) and 1.37 ± 0.05 (80°C), again suggesting a diffusion growth mechanism as the order is closer to 1.

Results shown in Figure 6.42 illustrate the main plots used to extract the data through the Arrhenius equation approach.
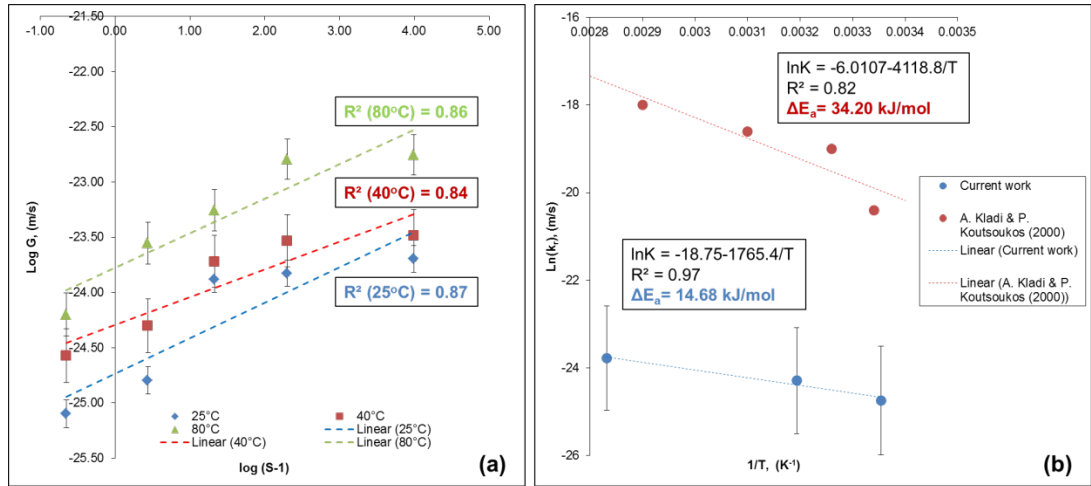
Figure 6.42: Calculation of activation energy (E_a) for $CaCO_3$ bulk crystallization process: (a) provides the growth rate constants and growth orders at each individual temperature; (b) provides the overall activation energy over a range of temperatures (25°C, 40°C and 80°C).

6.6 Validation of MultiScale^TM from *In-Situ* Crystallisation Studies

The in-situ monitoring of calcium ions present in solution throughout bulk crystallisation enabled investigating the kinetics involved for the de-supersaturation process over time. The depleting calcium concentrations measured (Figure 6.13) were used for recalculating the in-situ supersaturation for each case study at 25°C, over time (Figure 6.43).

No nucleation was detectable through batch experiments, as confirmed by the particle size and shape results via the Mastersizer, Sysmex and SEM. Thus, the reduction in supersaturation can only be a result of $CaCO_3$ crystal growth. In addition, changes observed via Sysmex (Table 6.17) and SEM (Figure 6.30 – Figure 6.34) in particle shape and size, reinforce that crystal growth and development took place throughout the depletion of calcium ions in solution, which reacted with carbonate ions to form vaterite initially, and then calcite at 25°C.
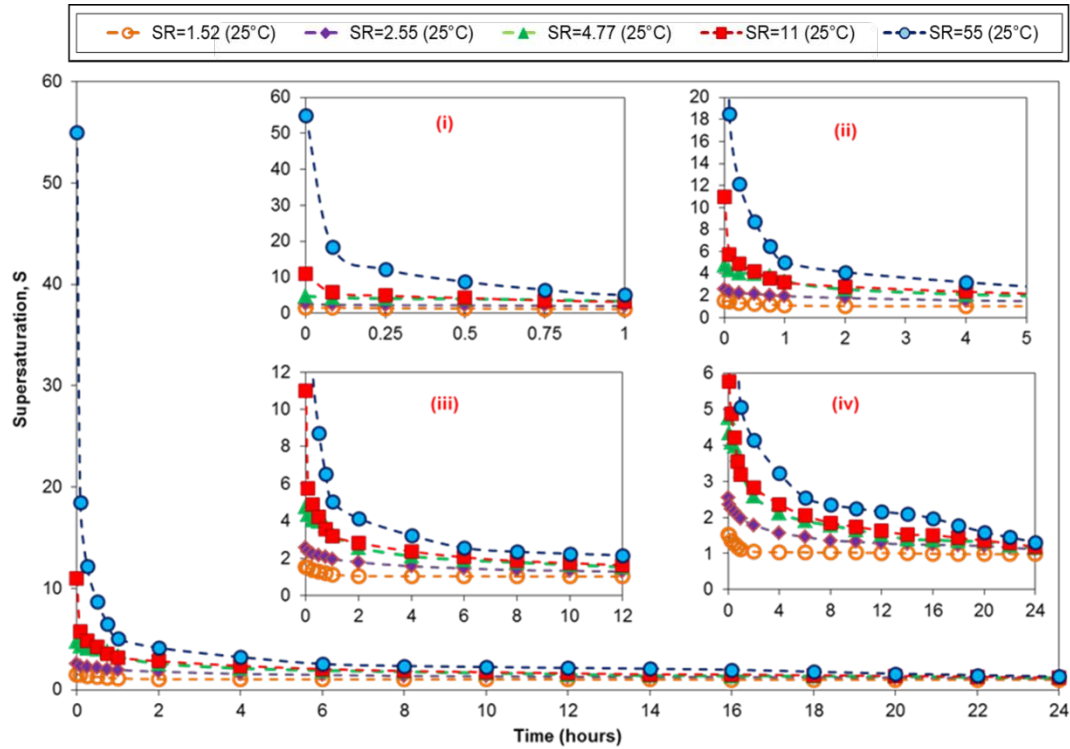
Figure 6.43: De-supersaturation profiles as a function of time and initial calcium concentrations at 25°C

It is clearly noticeable from Figure 6.43, that all five saturated brines showed a sharp decrease in the first instance of the reactive crystallization process. This behaviour suggests an instantaneous nucleation for all cases studied. Even at lower initial supersaturation levels ($1.52 \leq SR \leq 4.77$) there is an instantaneous decrease in calcium concentration and subsequent decrease in supersaturation, suggesting that nuclei may form at the interface between fluid elements of the synthetic brines. Hence, nucleation can take place at a non-stationary supersaturation where a boundary layer exists due to diffusion of ions. After the initial negative slope observed for the five case studies, there is a much more gradual decrease in supersaturation, especially at lower concentrations.

Similar trends to these shown in Figure 6.43, have been observed for both spontaneous and seeded $CaCO_3$ bulk crystallization studies (314) (325). Towards the end of the experiments, the lower saturated brines ($1.52 \leq SR \leq 4.77$) reached equilibrium (SR=1) quicker than the higher saturated brines ($11 \leq SR \leq 55$), which experienced a gradual decrease in supersaturation over time. Furthermore, this indirect measurement of the bulk supersaturation in-situ via monitoring of calcium ion concentrations has supported the use of MultiScale^{TM} software to help with re-calculation of the in-situ supersaturation by inputting in-situ calcium ions experimental data (Table 6.9).

The supersaturation is defined as the square root of the activity product of calcium and carbonate ions, divided by the thermodynamic solubility constant as shown by Equation (2.5).

The activity of calcium and carbonate ions is defined as the product of the mean activity coefficient ($\gamma_\pm$), and the free concentration of the respective species. The concentration of ions is decreased once the chemical crystallisation process starts, because of its association with other constituents in solution. In this work all equilibrium concerning species are: H_2O, $CO_{2(aq.)}$, $CO_{2\ (g)}$, H^+, OH^-, HCO_3^-, Ca^{2+}, Na^+, Cl^- and the aqueous neutral complex $CaCO_3^o$. The MultiScale™ 7.0 helped in determining the measured supersaturation, as well as the free ion concentrations and the activities using the Pitzer model (326), as shown in Table 6.23. Activity based supersaturation values are crucial for validating growth mechanisms of crystals due to the non–ideal behaviour, even at very low thermodynamic driving forces (ionic strength).

Table 6.23: MultiScale™ calculated parameters for the de-supersaturation experiments of spontaneous precipitation at 25°C

$S_{calcite}$	$S_{aragonite}$	$S_{vaterite}$	free $[Ca^{2+}]_i$ mmol/l	$\gamma_\pm$	pH
1.52	1.10	0.43	12.80	0.24	7.70
2.55	1.85	0.71	17.50	0.24	7.69
4.77	3.47	1.32	24.30	0.24	7.67
11.00	8.03	3.07	28.95	0.23	7.84
55.00	40.04	15.32	108.00	0.22	7.59

One of the constraints of thermodynamic models such as MultiScale™ is that all predictions are based on the most stable polymorph of $CaCO_3$, i.e. calcite. Nevertheless, the saturation ratios for aragonite and vaterite have been calculated from the square root of the ratio of calcite and vaterite or aragonite solubility products, multiplied by the saturation ratio of calcite. This is explained in Equation (6.22) for vaterite and in Equation (6.23) for aragonite.

$$S_{Vaterite} = \sqrt{\frac{K_{sp,calcite}}{K_{sp,vaterite}}} \times S_{calcite} \qquad (6.22)$$

$$S_{Aragonite} = \sqrt{\frac{K_{sp,calcite}}{K_{sp,aragonite}}} \times S_{calcite} \qquad (6.23)$$

Scale prediction studies done for aragonite and vaterite at 40°C and 80°C are displayed in Table 6.24. The aim of the experiments was to keep the supersaturation of calcite constant at all temperatures, thus calcite supersaturation remains unchanged, whilst the other two polymorphs supersaturation increased slightly with increase in temperature.

Table 6.24: Predictions of supersaturation for each crystalline CaCO$_3$ polymorph at 40°C and 80°C using MultiScale™

	40°C			80°C	
S$_{calcite}$	S$_{aragonite}$	S$_{vaterite}$	S$_{calcite}$	S$_{aragonite}$	S$_{vaterite}$
1.52	1.13	0.46	**1.52**	1.15	0.66
2.55	1.89	0.77	**2.55**	1.92	0.90
4.77	3.52	1.45	**4.77**	3.62	1.55
11.00	8.09	3.09	**11.00**	8.85	3.13
55.00	40.62	15.42	**55.00**	42.15	15.42

Figure 6.44 displays the initial supersaturation in terms of ionic activity product for all experiments done at moderate pH, five different concentrations and different temperatures. During de-supersaturation process of the crystallising solutions, over a range of temperatures (25°C, 40°C and 80°C), the data points will move down, passing the lines of vaterite and aragonite before ending up at the calcite solubility line, as shown in Figure 6.44 by circle dots in red (vaterite), green (aragonite) and blue (calcite).
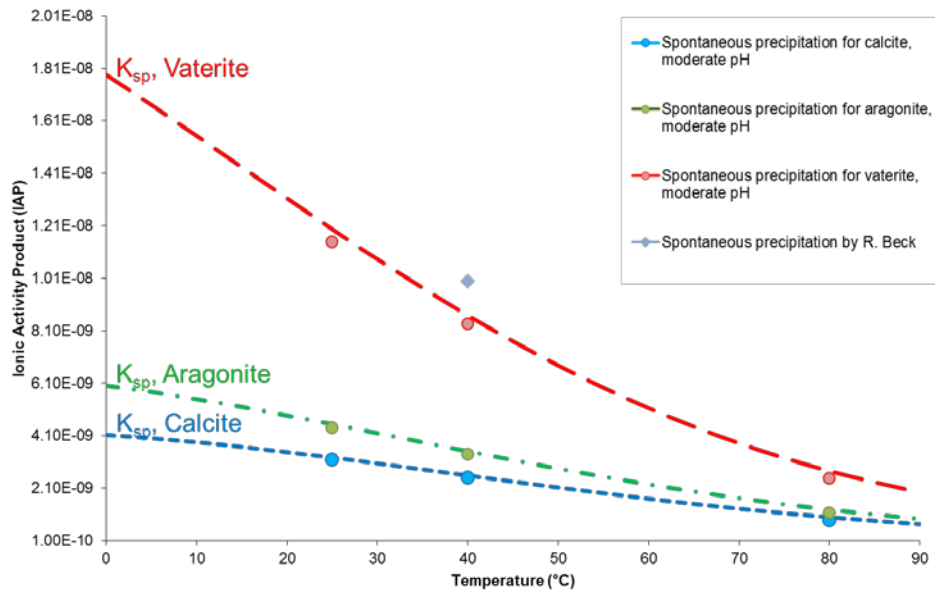
Figure 6.44: The initial ionic activity product (IAP) for all reported experiments on spontaneous precipitation of CaCO$_3$. The solubility product constants for calcite, aragonite and vaterite at a wide range of temperatures were adopted from the work of Plummer and Busenberg (115)

The areas covered in this study are represented by data points of the spontaneous de-supersaturation experiments done at 25°C, 40°C and 80°C. Previous work done by R. Beck et al. (327), for spontaneous crystallisation of vaterite at fixed composition is also marked in the image.

All three polymorphs are expected and were detected in the spontaneous precipitation tests. However, temperature showed a significant role in controlling the kinetics and transformation of each $CaCO_3$ polymorph. Therefore, at the start of each experiment vaterite was identified for all supersaturation levels, despite being slightly below the solubility curve at 25°C in Figure 6.44. The content of calcite increased with time for all case studies, due to the inherent solution assisting transformation by dissolution of other polymorphs. Furthermore, temperature played a significant role in controlling the morphologies and its kinetics especially at 40°C and 80°C, where the solubility lines get very close for these two polymorphs. Results observed from SEM, showed only a very small amount of aragonite at higher supersaturation levels.

Understanding the solution speciation and solubility of experiments done for bulk crystallization studies was crucial to validate the modelling software as well as understand how the saturation changes affect the crystal growth mechanisms in particular relating it to mechanisms of transformation of $CaCO_3$ polymorphs at different supersaturation and temperatures.

6.7 Relationship between Crystallisation Kinetics and Polymorphism

The classic nucleation theory approach supports the formation of nuclei through ion pairing. However, there are more recent studies which oppose the CNT (65) and suggest that $CaCO_3$ crystals are formed through a nano-particle mediated process. Nonetheless, the nature of $CaCO_3$ formation mechanisms of polycrystalline particles is still not firmly established in the literature. Following the CNT approach, it is well understood that a polymorphic transformation can spontaneously occur from the less stable form (i.e. vaterite) to the most stable (i.e. calcite), however, factors such as temperature and the presence of impurities can affect the mechanisms of crystal growth and its transformation process (e.g., Ostwald's principle). Hence, there is a need for complementary investigations to elucidate the relationship between the kinetics and crystal growth mechanisms with the solution's thermodynamics. Figure

6.45 illustrates the differences between the classical and non-classical mechanisms of CaCO$_3$ precipitation in solution.
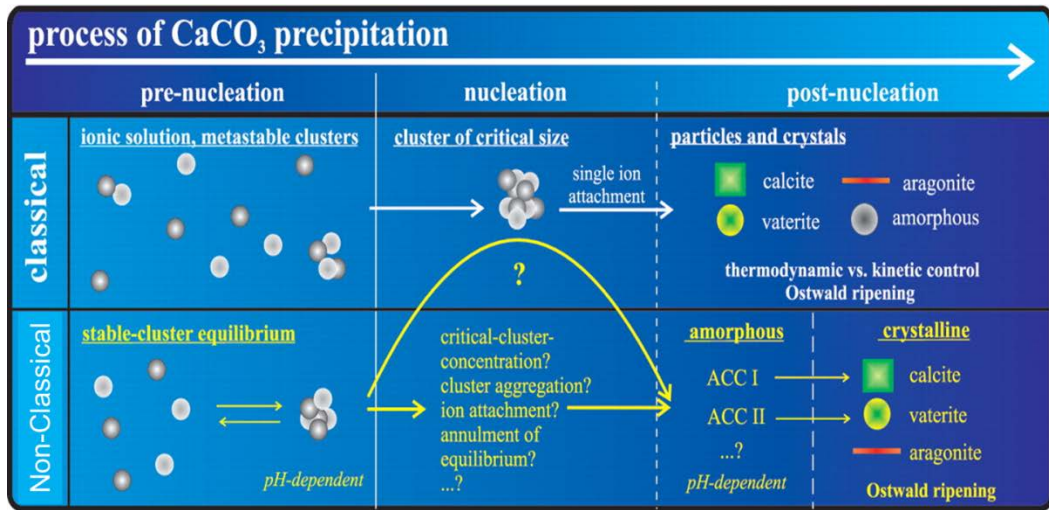
Figure 6.45: Calcium carbonate bulk precipitation via classical and non-classical approaches (65)

A review of the SEM studies (section 6.4.2.2) is done, taking into account both of these mechanistic theories. It was noticed from all Sysmex (section 6.4.2.1) and SEM (section 6.4.2.2) images, that vaterite is the first visible polymorph to crystallise around fifteen minutes from the start of the bulk crystallization study, for a range of supersaturation and temperatures. In addition, analysis done for the solubility of each polymorph (Figure 6.44) and calculations obtained via MultiScale™ and Equations (6.22) and (6.23) indicated that both aragonite and vaterite supersaturation increased, with an increase in temperature, as shown in Table 6.23 and Table 6.24.

Vaterite is the most common crystal observed during the first instances of bulk SEM analysis (i.e. ± 15 minutes of reaction time). Images from Figure 6.30 to Figure 6.34 illustrate the gradual transformation of vaterite into calcite towards the end of the experiments. In Figure 6.46, a proposed mechanism for CaCO$_3$ precipitating spontaneously in bulk solution at constant temperature.
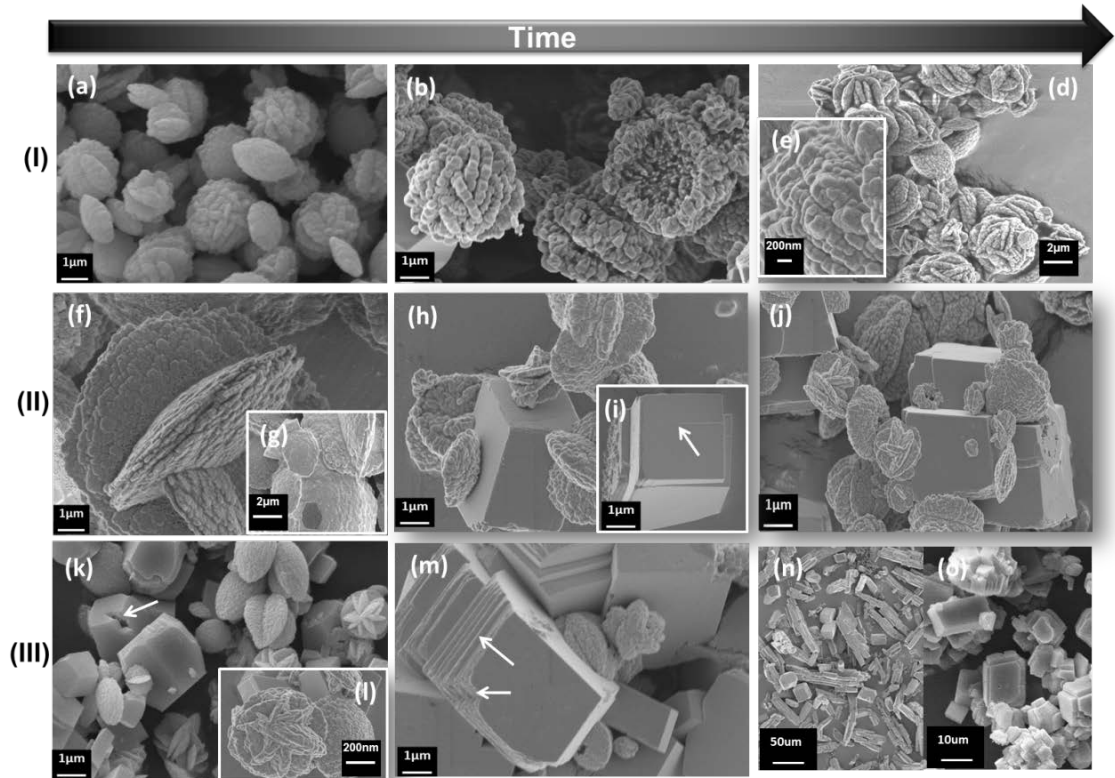
Figure 6.46: SEM images of CaCO$_3$ evolution over time through a three phase growth development. Stage I (a – e) illustrates already formed vaterite spherical crystals; Stage II (f – j) shows the transformation of vaterite into calcite crystals; Stage III (k – o) represents the growth of calcite crystals around vaterite or aragonite, depending on supersaturation and temperature conditions.

The proposed mechanism in Figure 6.46 suggests there are three different stages in the formation of CaCO$_3$ in solution. In stage 1, there is the formation of spherulitic vaterite crystals via ion-pairing mechanisms. In stage 2, spherulitic vaterite crystals grow in solution and start to gradually transform into calcite via dissolution and recrystallization mechanisms with a reaction rate controlled by the surface area of calcite (appearance of screw dislocations). Lastly, in stage 3, most of the vaterite crystals are fully converted into rhombohedral calcite crystals, which will continue to grow until equilibrium state is reached. Note that in this stage, vaterite may also convert into aragonite before fully converting into calcite. This is typical at high supersaturation and high temperature conditions, where growth kinetics are faster and growth tends to become diffusion controlled.

An important result of this study is that the crystals observed do not give any evidence to support the hypothesis of nanoparticle self-assembly (i.e. non-classical approach). Furthermore, despite the several theories on vaterite formation mechanisms, the spherulitic growth gives the simplest explanation for vaterite flower-like crystals and aragonite elongated pellets to be observed under specific conditions of bulk

experiments. Hence, the classical approach best describes the morphological changes of $CaCO_3$ crystals in this study.

To conclude, analysis of these experiments elucidated the fact that when $CaCO_3$ bulk crystallization starts through homogeneous nucleation, the supersaturation decreases over time and subsequently changes are observed in the crystal shapes. Therefore, it was expected from the experiments that at high supersaturation, spherulitic and dendritic growth and some hopper crystals are initially formed, and then as the supersaturation decreases the crystal growth is continued via screw dislocations and fronts (Figure 6.46 k – m), filling the crystal's cavities and generating flat faces. This process describes the evolution of crystal formation and best characterises the approach illustrated in Figure 6.46. Finally, it can also be concluded that changes in the solubility due to crystal transformation to another phase will automatically alter the crystal growth rate due to mechanisms involved during the attachment of molecules from bulk solution to the surfaces of $CaCO_3$ crystals. Therefore, $CaCO_3$ crystal's evolution will strongly depend on the energy barriers seen by molecules from both dissolution and re-crystallization stages as previously shown by Davies et al., (328) and Chernov (329) studies.

6.8 Closing Remarks

This chapter provided a full analysis and review on mechanisms of calcium carbonate crystallization from a bulk of saturated solutions and assessment on the kinetics involved during the nucleation and crystal growth stages.

A commercial thermodynamic software, Multiscale was used to simulate the different scaling scenarios from an original given field brine, over a range of temperatures. These scaling brines ranged from low to high saturation ratios and bulk tests were done at $25^{\circ}C$, $40^{\circ}C$ and $80^{\circ}C$.

Several in-situ analytical tools have been used to develop a suitable approach for taking induction times. Overall, the pH and calcium ion selective probe showed the best results, enabling acquiring in-situ data which was interpreted according to nucleation onset and crystal growth. Therefore, the induction time was estimated using combined pH and calcium ion measurements under the assumption that the system was in a non-equilibrium state and that CO_2 present in air could impact the pH readings. Overall, the induction times increased with decrease in supersaturation and temperature, which are in quite good agreement with the classic nucleation

theory. Results have shown that at lower saturation ratios (1.52 – 4.77) the spiral growth mechanism is dominant whilst at higher supersaturation (11 – 55) the 2D nucleation was the most prominent. The nucleation and crystal growth kinetic parameters are summarised in Table 6.25.

Table 6.25: Nucleation & growth parameters calculated for the range of brine's supersaturation as a function of temperature

Parameters for a range of five supersaturation cases	Temperature		
	25°C	40°C	80°C
Interfacial energy (mJ/m^2)	0.92 – 16.37	1.63 – 24.01	1.82 – 25.46
Growth rate (m/s)	5 x 10^{-13} to 1.25 x 10^{-15}		

Furthermore, the crystal growth data was used to determine the growth kinetics and mechanisms for each case study. It could be concluded that both supersaturation and temperature cause an impact during crystallization process of CaCO$_3$. The kinetics appears to be faster with increase in supersaturation and temperature. Therefore, different morphologies with different sizes were observed in these studies. Overall, temperature played a significant role in increasing the kinetics for the lower saturated brines. For higher saturated brines, the effect of increase in temperature on crystal growth rates was negligible. Therefore, smaller crystal particles precipitated in higher amounts, suggesting that fast growth rates are due to high saturation levels.

The analyses of growth mechanisms and kinetics also suggested that calcite can form from different mechanisms depending on supersaturation and temperature. If completely different supersaturation regimes are being assessed for growth mechanisms, it is important to have a significant amount of growth data to reduce any misleading results following semi-empirical equation models such as the Arrhenius equation, commonly used for determining the activation energy of a reactive crystallising system.

Ultimately, a new growth mechanism based on the classic approach has been reviewed, in which key thermodynamic parameters (i.e. supersaturation and temperature) can determine the final shape of CaCO$_3$ crystals in bulk solution. Vaterite was the first polymorph to precipitate when the supersaturation was high, due to faster growth mechanisms. The spehrulitic growth of vaterite was followed by its fast dissolution and transformation into calcite via spiral growth. At higher temperatures vaterite transformed into aragonite through rough interface growth mechanisms, then aragonite crystals converted into calcite through diffusion,

originating some tabular looking calcite. This proposed mechanism links the thermodynamic factors to the kinetics and growth mechanism.

To sum up, the analysis of nucleation and growth kinetics via nucleation theory enabled establishing semi-empirical derivation of both nucleation and growth of calcite to simulate what would happen in the oilfield under those conditions. Thus, the rate equations determined can easily be implemented in current thermodynamic scale simulators, providing the advantage estimating growth rates and main crystal phases over time. This would be a remarkable advance to improve the current flow assurance tools and optimize the production of oil and gas.

Chapter 7 - *In-Situ* Control and Characterization of Calcium Carbonate *Surface* Crystallization & Corrosion Processes

Summary

This chapter comprises the reporting of the results, analysis of the results and discussion obtained from the experiments conducted for calcium carbonate *surface* crystallisation process. A parametric study of $CaCO_3$ surface growth kinetics and mechanisms is investigated under different conditions, in absence and presence of corrosion process. The surface deposits are characterised with respect to their size and shape over time. Finally, the proposed surface deposition model is compared with bulk precipitation kinetic model.

7.1 Introduction

Calcium carbonate crystallisation experiments have been studied for bulk processes (330), however, the *surface* crystallisation kinetics and mechanisms associated with $CaCO_3$ deposition on metals are less clear. Additionally, it is known that the surface can have a significant influence on $CaCO_3$ deposition mechanisms and subsequently its kinetics (331) (291) (332). Therefore, this chapter addresses the research question in Chapter 2 (section 1.2) to further understand $CaCO_3$ *surface* crystallisation processes in oilfield systems, considering that processes of corrosion and inorganic scale take place simultaneously, under the same environmental conditions.

This chapter presents the experimental results analyses and discussion for the *surface* crystallisation mechanisms and kinetics of $CaCO_3$ scale combined with corrosion process. The experimental analysis is divided into three main sections:

- A parametric evaluation of $CaCO_3$ *surface* crystallisation as a function of supersaturation, flow rate, temperature, exposure time and metal substrate;
- Evaluation of corrosion processes in the presence of $CaCO_3$ scale;
- Inter-relation between a simultaneous $CaCO_3$ bulk precipitation and surface deposition mechanisms and kinetics;

Ultimately, all of the results gathered from this study describe a novel contribution of findings relative to previous research, and for the first time in oilfield research, corrosion and mineral scale processes are addressed simultaneously. Subsequently, the outcomes of studies in oilfield corrosion and $CaCO_3$ *surface* crystallisation mechanisms and kinetics will have a significant contribution to improve the current scale and corrosion management strategies, within the oilfield sector. Figure 7.1 displays an overview of this chapter.
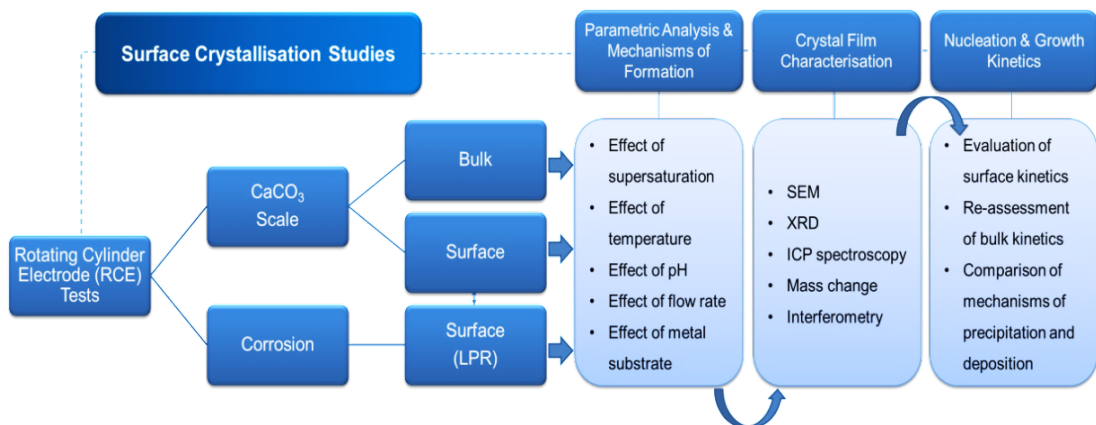
Figure 7.1: Route map of parametric studies for $CaCO_3$ surface crystallisation and corrosion processes with key results and discussions topics

7.2 Parametric Analysis of Oilfield Corrosion in Carbon Steel

In an attempt to understand and simulate oilfield corrosion mechanisms of formation and kinetics, a parametric study has been made using the rotating cylinder electrode (RCE). The effect of varying parameters such as the brine solution composition and chemistry, (i.e., brine supersaturation and total dissolved salts), temperature and pH was assessed during the corrosion process of carbon steel X-65, in a non CO_2 saturated environment (i.e., aerated). Table 7.1 shows the matrix of the tests performed in this stage of the investigation.

Table 7.1: Corrosion experimental matrix

Parameters	Conditions
Material	X-65 Carbon steel
Solution	1L Synthetic brine mixture
Brine Saturation Ratio (SR)	Five SR cases: 1.52, 2.55, 4.77, 11 and 55
Brine TDS (mg/L)	50,000 – 100,000
Temperature (^{o}C)	25 ^{o}C and 80 ^{o}C
pH$_{initial}$	7.5 - 7.7
CO_2 Partial Pressure (bar)	1 bar
Gas Composition	Atmospheric Air (no CO_2 bubbling)
Rotational Speed	*500rpm, 800rpm and 1500rpm – turbulent flow
Surface Roughness	Rotating cylinder electrode (RCE) smoothly polished

The DC linear polarisation resistance technique was applied to monitor the electrochemical responses of carbon steel X-65, such as the corrosion rate and electrical potential when $CaCO_3$ scale and corrosion products (e.g., $FeCO_3$ or Fe_2O_3) were forming a protective layer. On the other hand, the corrosion rate measurements were based on measurements of the polarisation resistance (R_p) of the metal (carbon steel X65) to the electrolyte solution (brine solution), accompanied by changes in the current density (i_{corr}).

Initial tests were performed to evaluate the initial OCP values in carbon steel under given conditions (temperature and solution chemistry) and to verify the relationship between the free corrosion potential and the polarisation resistance.

Assuming no external polarisation, oxidation and reduction reaction took place at the same time as the electrode was immersed in the electrolyte brine solutions, then, the opposing anodic and cathodic current densities are equal in magnitude, giving a zero net current. At this point, the OCP values are measured over time until they became stable, assuming that a steady state has been reached and any changes from that

point can provide information about the surface reactions on the electrode. For example, when OCP shifts to a more negative potential value, this suggests a change in the corrosion kinetics, favouring the anodic reaction (333). Polarization resistance measurements were conducted by polarising the working electrode (WE) at ±15mV at a scanning rate of 0.25mV/s. A typical plot obtained of current density vs. potential is shown in Figure 7.2, illustrating that the measured current density is linearly proportional to the applied potential.
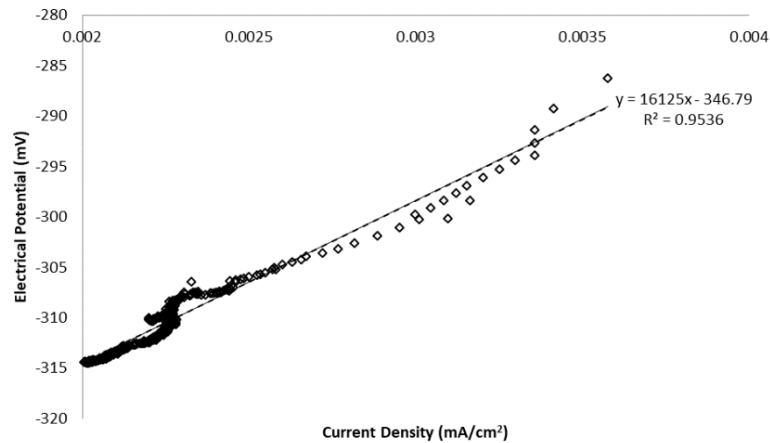
Figure 7.2: Typical Tafel plot showing the linear potential-current relationship at low applied potential. The gradient of this graph is used to obtain the polarisation resistance (R_p) – values.

In this work, the electrodes were left to corrode at their open circuit potential for all periods outside the electrochemical measurements. The resultant OCP for carbon steel X-65 varied around -0.6V vs. Ag/AgCl for a pH of 7.5. Figure 7.3 displays the relationship between the free corrosion potential (E_{corr}) and the polarisation resistance (R_p) on carbon steel X-65.
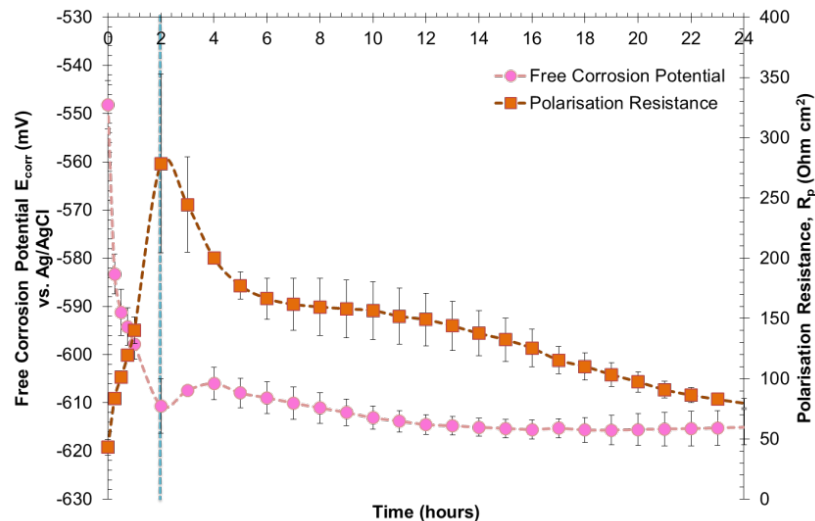
Figure 7.3: Relationship between the free corrosion potential and polarisation resistance for carbon steel X-65 sample in low saturated brine (SR=1.52), 80°C, pH of 7.5, 1 bar, 500rpm and non-CO_2-saturated environment

Regardless of the solution's supersaturation and the metal's nature (e.g., carbon or stainless steel), the free corrosion potential can often mirror the trend in polarisation resistance, as shown in Figure 7.3. The very first decrease in free corrosion potential (E_{corr}) corresponds to a sharp increase of the polarisation resistance (R_p), which then follows a much slower adsorption process (i.e. stable slope of the trend), generally resulting in an increase of the polarisation resistance (R_p). It should be remembered that the free corrosion potential is adopted as a result of the combined anodic and cathodic reactions.

7.2.1 Effect of Temperature

Temperature is one of the key parameters tested to observe its effect on corrosion rates and on $CaCO_3$ *surface* deposition rates. Hence, this initial study focused on the effects of temperature on corrosion and surface crystallisation kinetics.

The corrosion tests were performed for five different saturated brine solutions at initial pH ranging from 7.5 to 7.7. The rotating cylinder working electrode was smoothly polished by its manufacturer, and LPR measurements were taken at 25°C and 80°C to assess the corrosion rate and film precipitation over time.

For the corrosion rate calculations under dynamic conditions, β (i.e., Stern Geary coefficient) was assumed to be maintained at 0.12V/decade (233), so that all presented corrosion rates become comparable with each other as done previously by many research groups (333) (233) (334). It is important to recall that even though the assumption that βa=βc=120mV/decade may not be entirely accurate, it only gives a systematic error (332) and therefore its usage is justifiable as a conversion factor in this work.

Figure 7.4 and Figure 7.5 show the comparative results obtained for experiments performed at 25°C and 80°C for low to high saturated brine solutions (i.e., SR=1.52, 2.55, 4.77, 11 and 55). Furthermore, the generic trend of the corrosion rate curves suggests that corrosion rates increase with an increase in temperature. These result trends are consistent with previous studies (335) (336) (337).
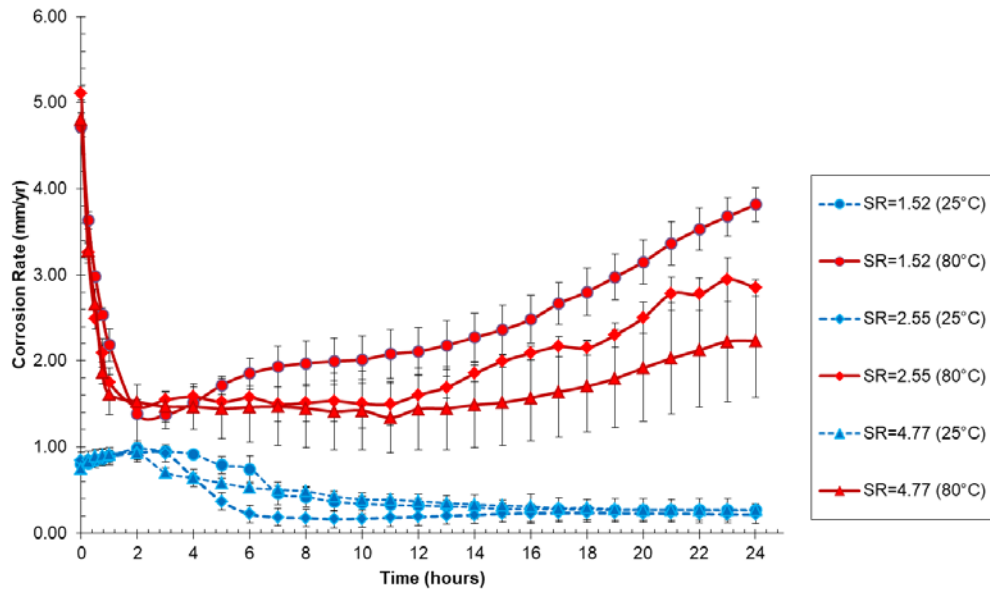
Figure 7.4: Effect of increase in temperature on corrosion rates of carbon steel X-65 (RCE working conditions: 500rpm, 1.52 ≤ SR ≤ 4.77, 1 bar)
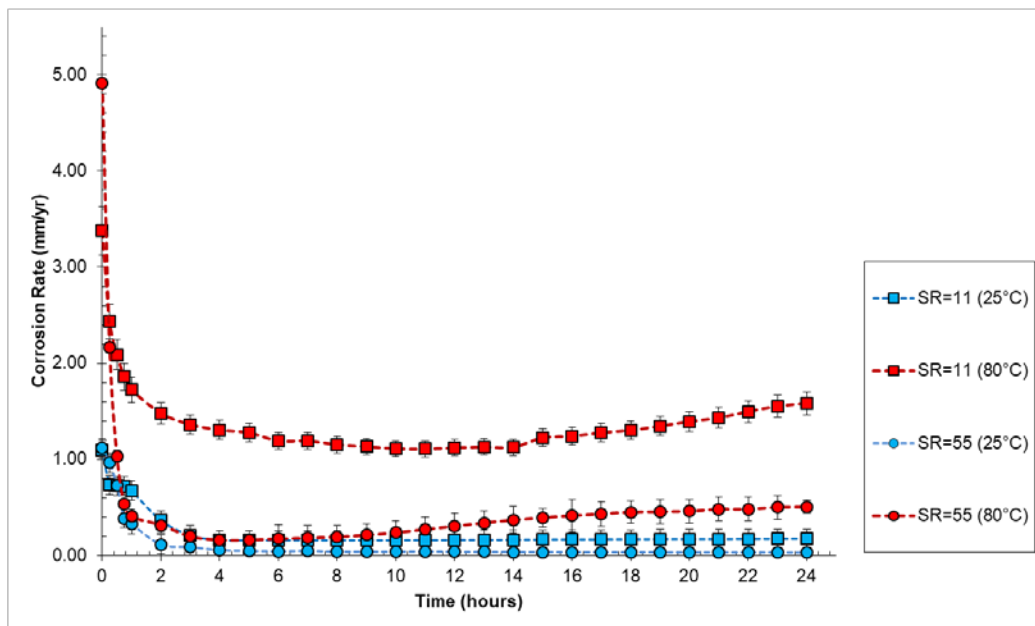
Figure 7.5: Effect of increase in temperature on corrosion rates of carbon steel X-65 (RCE working conditions: 500rpm, 11 ≤ SR ≤ 55, 1 bar)

Considering a constant initial saturation ratio, the low concentration case studies (i.e., SR=1.52, 2.55 and 4.77) display an initial corrosion rate lower than 1mm/year. These corrosion rates follow a similar trend in which the curves show an initial gradual increase in the corrosion rates, followed by a relatively steady drop which stabilises to a value around ±0.2mm/year, over 24 hours period. Similarly, for higher brine concentrations (i.e., SR=11 and 55), the overall corrosion trend is identical, however,

the kinetics appear to be faster as the initial increase in corrosion rates takes place much quickly and is followed by a relatively sharper drop before stabilising at a low corrosion values of ±0.1mm/year. The sudden drop in corrosion rates is associated with the formation of a protective film, whose nature needs to be assessed for the given conditions.

Overall, it is evident that at 80°C, the initial corrosion rates are higher than those values obtained at 25°C, due to increase in corrosion kinetics at higher temperatures. In addition, all high temperature corrosion measurements performed at 80°C display an instantaneous sharp decrease moments after the start of the experiments. This significant drop in corrosion rate at 80°C takes place within the first 2 hours considering an assessment for all saturated brine cases. After reaching the lowest corrosion values, a plateau trend is observed, suggesting that a protective film is stable and protecting the metal surface against corrosion (i.e., blocking active corrosive sites). Nevertheless, after a while, the stabilised low corrosion rates at 80°C started to increase gradually over time and this was mostly observed for the low saturated brine cases ($1.52 \leq SR \leq 4.77$) rather than the high saturated brines ($11 \leq SR \leq 55$). This sudden increase in corrosion after protective film formation indicates that the protective film may be porous or unevenly spread leading to the development localized corrosion and reappearance of active corrosion sites. Hence, the gradual increase in the corrosion rate over time post film formation.

In conclusion, temperature plays an important role in the corrosion kinetics and protective film formation and stability. The corrosion rates are faster at higher temperatures because there is a faster interaction between the cathodic and anodic reactions from the surface-bulk interface.

Furthermore, the type of inorganic scale deposits will depend on brine's composition/chemistry and temperature. The different brines used for these experiments are saturated with respect to calcium carbonate scale. Therefore, a protective scale film containing $CaCO_3$ crystals is expected to form in the solution and at surface of the RCE metal. Since $CaCO_3$ scale becomes less soluble at higher temperatures, at 80°C more crystals can be deposited. However, corrosion products such as $FeCO_3$ and Fe_2O_3 may also be expected under these testing temperatures. A detailed assessment of the protective film is required to understand the kinetics and mechanisms of co-precipitation for the different types of scale.

7.2.2 Effect of Supersaturation

Another critical parameter used to assess the corrosion kinetics was the brine solution chemistry and composition. In general, during corrosion testing the scaling ions (carbonate and sulphate ions) are commonly omitted from the synthetic brines in order to avoid unwanted precipitation and mislead the corrosion rates readings. However, in this research work, one of the aims is to assess the simultaneous corrosion and inorganic scale precipitation. Therefore, five different brine concentrations have been prepared with different TDS (total dissolved salts) concentrations and tested at 25°C and 80°C for their corrosion rates via LPR readings. From literature (338) (339), it is known that high salt (NaCl) content in brines may have a significant impact in carbon steel corrosion, as the increase in salt concentrations increases the solution resistance, thus reducing the solubility of carbon dioxide, which will retard the cathodic and anodic reactions, limiting current density across the surface of the metal.

Figure 7.6 and Figure 7.7 show the corrosion rates obtained for all experiments as a function of supersaturation and temperature. The error bars on the data points plotted are based on the average of the corrosion rate measurements with a minimum of three individual and repeatable experiments over a 24-hour period each.

The high initial corrosion rates observed in Figure 7.6 and Figure 7.7 are related to the release of iron ions near the metal's surface, leading to a local high saturation of the solution. This local saturation combined with a high concentration of carbonates from the bulk solution, may allow the formation of iron carbonate, as a corrosion product. However, as calcium is also present in bulk solution, the surface scale deposition will depend on competition between $CaCO_3$ and $FeCO_3$.

Since the saturation ratio is the driving force for scale precipitation, thus, any increase in the saturation ratio will cause a decrease in the solubility of scale. This emphasises the role of CO_2 equilibrium in sea water systems, as any increase in carbonate ions will increase the saturation ratio (and vice-versa).
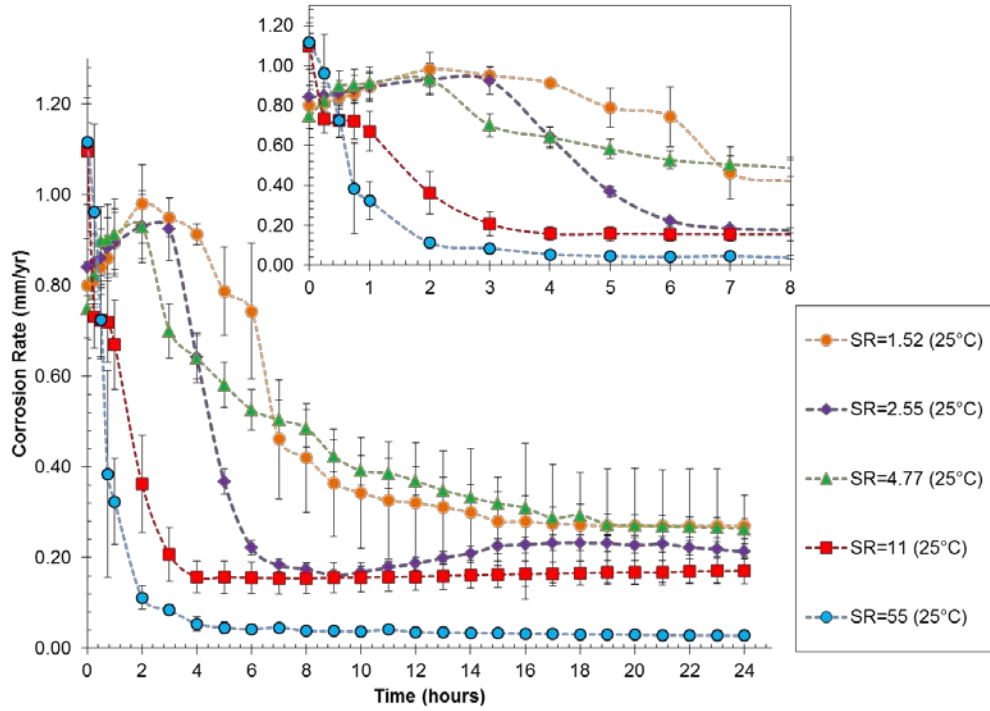
Figure 7.6: Average corrosion rates from linear polarisation resistance measurements for carbon steel X-65 exposed over a range of saturated brines at 25°C, 1 bar, 500rpm and non-CO$_2$-saturated system
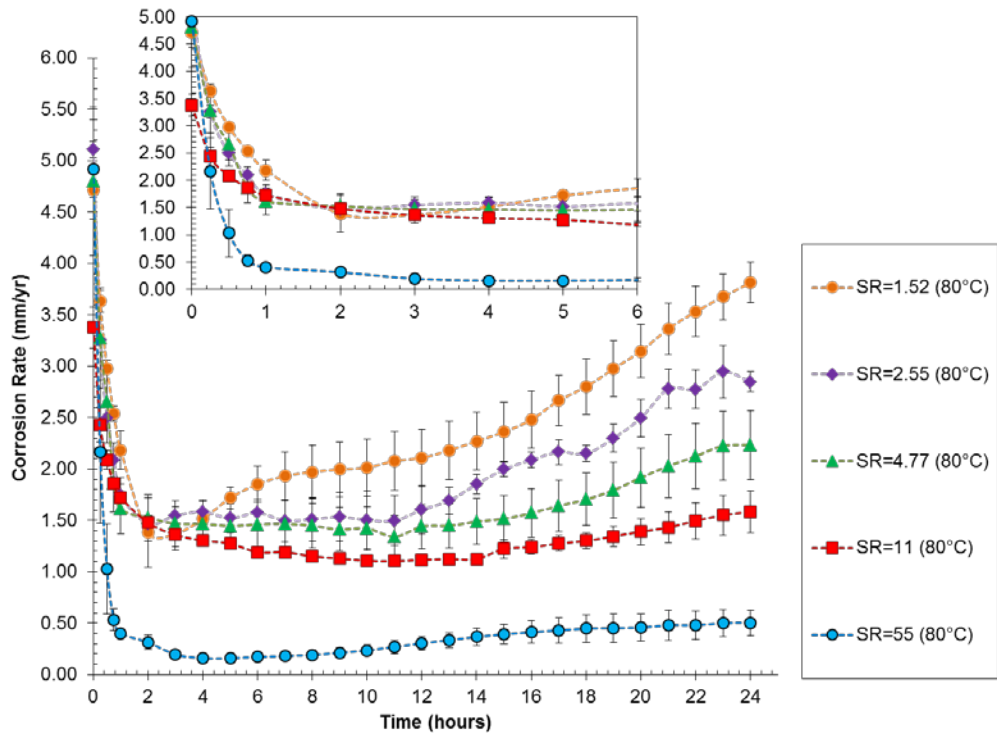
Figure 7.7: Average corrosion rates from linear polarisation resistance measurements for carbon steel X-65 exposed over a range of saturated brines at 80°C, 1 bar, 500rpm and non-CO$_2$-saturated system

In this work, a similar behaviour is observed for the highest TDS brines (i.e., higher concentration) and it can be observed that the higher the supersaturation, the higher are the initial corrosion rates. However, the reaction crystallisation process taking place at the surface of the mild steel will block the active sites for development of general corrosion. This behaviour is observed in particular for higher saturated brines (i.e., $11 \leq SR \leq 55$), at both testing conditions ($25^{\circ}C$ and $80^{\circ}C$).

Supersaturation is the main driving force for precipitation and is affected by temperature. Therefore, regardless the initial concentration values, once precipitation takes place at the surface of mild steel; the corrosion rates will drop, stabilizing to a lower value whilst there are no interactions between the ions at the carbon steel with the electrolyte bulk solution. This behaviour is shown for all five brines investigated at $25^{\circ}C$. A clear identification on how supersaturation affects corrosion is seen by how quickly higher saturated brines tends to have not only initial higher corrosion tendencies, but also tend to form a protective film much quicker. The level of film protectiveness will depend on testing conditions.

At $80^{\circ}C$, Figure 7.6 shows that corrosion rates for all case studies dropped instantaneously after the start of the experiments. However, the protective film formed was not sufficient to keep the corrosion levels down for the duration of the experiment (24 hours). Overall, the corrosion kinetics was enhanced by the increase in temperature and after a few hours, the corrosion rates started to increase again. It was noted that the higher the supersaturation, the smaller was this increase in corrosion rates. This suggests that for lower saturation brines, more porous films are formed and localized corrosion takes place. For the lowest saturation ratio brine (SR=1.52) a steady increase in corrosion was observed after film formation, and the final corrosion value was increased up to 3.5mm/year, which is quite close to the initial corrosion rate value of 4.6mm/year.

Previous studies have demonstrated that calcium ions can be incorporated into surface layer leading to a significant reduction of corrosion (98) (254). Furthermore, calcium ions present in bulk solution can promote the growth of a protective layer once $CaCO_3$ crystals nucleate from the surface or migrate into the metal by adhesion mechanisms (208). However, studies by Tomson and Johnson (270) suggested that a layer containing more than 5% of calcium can lead to the formation of an irregular and non-adherent protective layer. On the other hand, Ueda et al., (340) also observed a reduction of the general corrosion rate in presence of $CaCl_2$, but an increase in the localised corrosion. The brines used in this study contained high

calcium concentrations, thus the surface could have incorporated more than 5% of calcium ions, explaining the partial protection given by the film.

In summary, supersaturation strongly influences the corrosion rates. The higher the supersaturation, the more ions are present in solution to interact with carbon steel surface ions, and so, the higher will be the initial corrosion values. On the other side, the brine supersaturation can induce inorganic scale formation at the surface of the carbon steel which in turn forms a protective film layer that may temporarily minimize the corrosion kinetics. However, localized corrosion can be formed under the scale deposits, causing serious cracks on the metal and piping integrity.

7.2.3 Effect of pH

It is know from literature that pH has an effect on the CO_2 corrosion of carbon steel and its corrosion and scale film deposition kinetics.

In this study, the initial pH for the brines was adjusted with buffer solutions; however, it was not kept constant via CO_2 bubbling, throughout the LPR corrosion tests. This enabled the understanding of surface growth mechanisms taking place simultaneously during scale and corrosion processes at mild steel substrates. Furthermore, the relationship between the surface kinetics and bulk pH was also investigated.

SEM images were taken for samples over time and the solution's pH were measured. Considering the lowest saturated brine case, at SR=1.52 (25°C), a critical drop in corrosion was observed after 2 hours at a critical pH of 7.60. This drop in corrosion accompanied by an increase in pH demonstrates that the development of a protective film is more favourable at pH ≥7.60.

Figure 7.8 illustrates an example of the pH-trend for the lowest saturation case study (SR=1.52) after reaching its highest corrosion peak (at corrosion rate of ±1mm/year). Under the assumption that a protective film is formed during the corrosion drop, it can be observed that the pH increased from ±7.6 to ±7.91. This slight change in pH is not significant however the fact that a protective film is formed can be related to the reduction in carbonate ions (less CO_2 in the bulk solution) due to its reactive crystallisation process to form $CaCO_3$ crystals or deposition of corrosion products such as $FeCO_3$ scale. Furthermore, the types of scale or corrosion film formed will depend on their solubility under given testing conditions. Lastly, any increase of the initial CO_2 concentration would decrease the pH and subsequently increase the $CaCO_3$ solubility. This is the reason why $CaCO_3$ scale solubility is dependent on

species that impact the pH system (H^+ or OH^- ions), thus, a change in the system pH will cause changes in the carbonate (CO_3^{2-}) ions concentration.
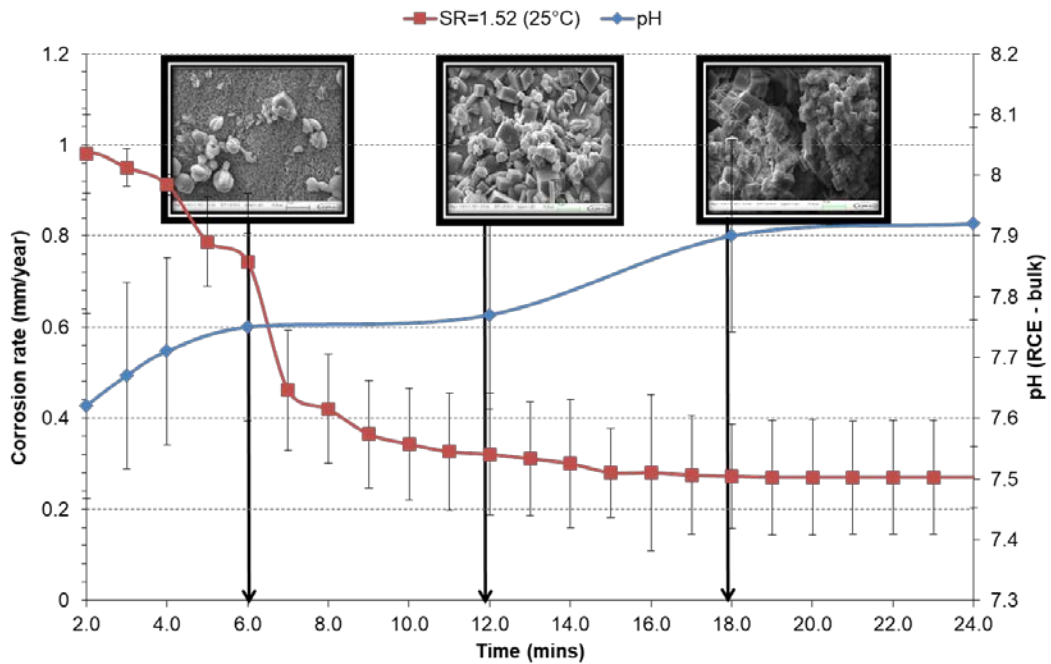
Figure 7.8: Relationship between the corrosion rate and bulk solution pH for RCE with carbon steel X-65, 500rpm, brine at SR=1.52 and 25°C

From SEM observations (Figure 7.8), it is also remarked that once the corrosion rate reaches a steady plateau at lower values, there is even more scale deposits temporarily blocking any active corrosion sites. For this case study, the nucleation on-set happens just before 2 hours followed by crystal growth at the mild steel surface in which the corrosion rate continues to drop whilst the bulk solution pH starts to gradually increase from pH 7.6 to 7.7 (at 6 hours). Then from 6 hours to 12 hours the pH increases from 7.7 to 7.8 whilst the corrosion rate keeps dropping until stabilising to a lower value of ±0.2mm/year from 18 hours till the end of the 24 hour experiment. The amount of crystals deposited on the surface of carbon steel increased over time and with increase in pH by ±0.1 differences. It is evident that different crystal morphologies and sizes were deposited over time under slightly different pH ranges. This is also due to the fact that the supersaturation of the solution decreased once the crystallisation process started in bulk and at surface of the carbon steel metal.

7.2.4 Effect of Flow Hydrodynamic

In order to assess the effect of flow rate in corrosion, the following rotational velocities have been applied to the RCE working electrode: 500rpm, 800rpm and 1500rpm. All of the selected rotational velocities correspond to turbulent to highly turbulent flow

regimes (i.e., $Re_{(RCE)} > 300$). These values have been selected solely for the purpose of assessing the effect of increase in flow rate to corrosion kinetics.
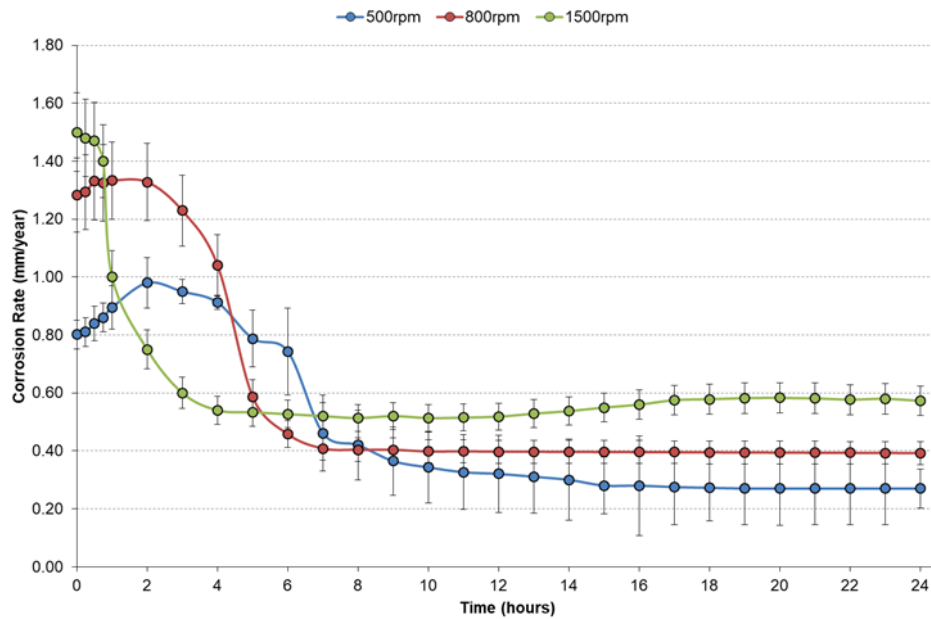
Figure 7.9: Effect of RCE flow velocity on carbon steel corrosion rates for case 1 (SR=1.52, T= 25°C, pH$_i$=7.5)

Figure 7.9 illustrates the results obtained using the low saturated brine (SR=1.52) at 25°C over 24 hours. The results from these experiments showed that a higher initial corrosion rate is observed for the highest flow velocity. This is expected as a higher flow across the RCE surface will contribute to higher mass transport of species away from the surface, lowering the local saturation ratio and hence increasing the corrosion rate from the start of the experiment. Nevertheless, for the higher flow rates, a faster drop in corrosion is observed, suggesting that a protective film is formed at faster rotational speeds.

The rapid drop in corrosion at higher rotational velocities elucidates the effect of flow. The rapid formation of a protective film, suggests that the anodic part of the polarisation shows typical resistivity behaviour, whilst cathodic polarisation becomes more diffusion controlled at higher flow rates.

The kinetics involved during scale and or corrosion products formation at higher flow rates will have a strong impact on the reaction mechanisms and given that at higher velocities more Fe^{2+} are removed from the steel surface, then if conditions are favourable more $FeCO_3$ or combined $FeCO_3$ and $CaCO_3$ scale can be formed. Furthermore, the presence of oxygen in the brines will speed the oxidation reactions

between the carbon steel Fe^{2+} and dissolved O_2 ions, giving a chance of forming Fe_2O_3 rust at higher rotational speeds.

At the end of the experiment, the corrosion rates remained lower for the lower velocity, thus, at RCE velocity of 500rpm, a stable protective film was formed and enabled lower corrosion rate values at the end of the test. In contrast, at higher flow rates, the protectiveness of the corrosion or scale film was unstable, leading to higher corrosion values at the end of the test. Hence, a faster flow rate may imply a lower adherence to the surface, suggesting that in these experiments, a less protective film was formed at 1500rpm. Additionally, it is important to take into account that at higher flow rates, particles adhered at the RCE sample may be mechanically removed by dragging forces and collision with other bulk crystals.

A similar observation on the impact of flow rate to corrosion was reported by Nesic et al. (266) when conducting studies with RCE. On their results, the corrosion rates dropped faster for the highest RCE rotational speed and at the end of the experiment the corrosion rate was lower for the lowest RCE velocity test. At the end, they've concluded that the protective film was re-dissolved or chemically damaged by the higher rotational speeds, which led to higher corrosion rates. These experiments support the results obtained for an aerated RCE test using carbon steel over different ranges of turbulent flow.

7.2.4.1 Weight change measurements on carbon steel X-65

Mass gain measurements were taken at the end of these tests (Figure 7.9), in order to determine the corrosion products precipitation rate using Equation (4.28) from Chapter 4 (section 4.9.). The estimated corrosion rate at the end of the test assumes that corrosion is constant over the total period of the experiment and that mostly $FeCO_3$ scale is formed and deposited at carbon steel surface after 24 hours.

Figure 7.16 shows that the precipitation rate reduces with an increase in flow rate (RCE velocity), which in turn agrees with the LPR measurements shown in Figure 7.9.
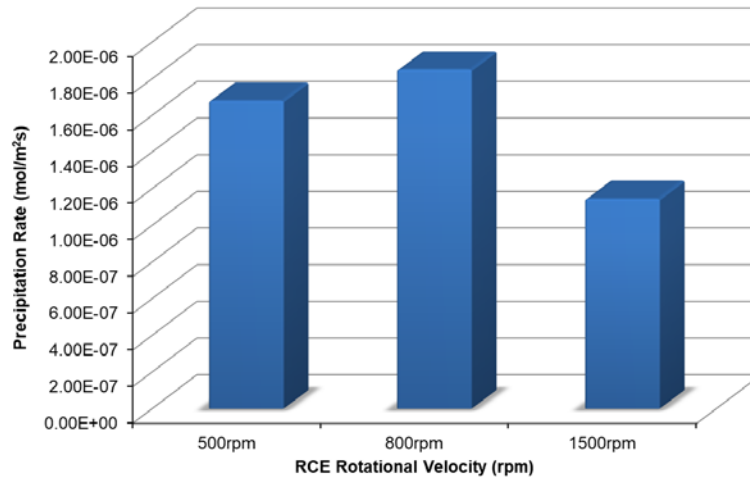
Figure 7.10: Precipitation rate determined from mass gain measurements at the end of 24 hours for variable flow velocities and working conditions of SR=1.52, 25°C, pH$_i$=7.5

7.2.4.2 Characterization of corrosion and scale deposits

Lastly, samples of the corroded cylinder electrodes were analysed via SEM for film characterization with respect to their shape and size after 24 hours reaction.
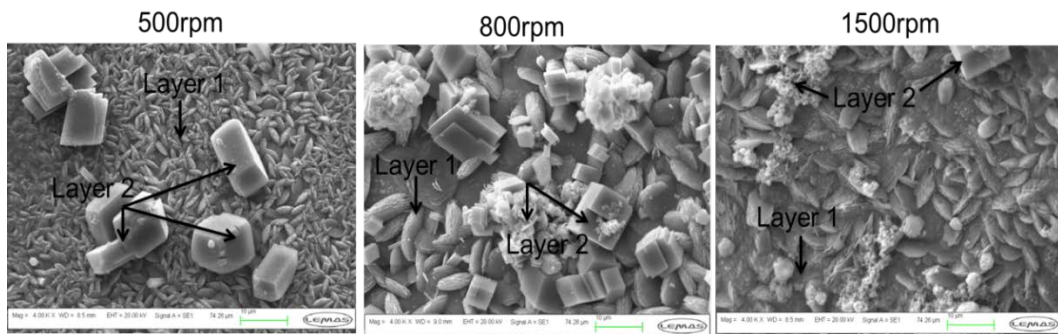
Figure 7.11: SEM images of cross-sectional surface area of RCE tests under different flow regimes for brine at SR=1.52, 25°C

From the SEM images it can be seen that for the highest flow rate, crystals form a non-uniform protective layer, whilst at lower flow rates, the protective film appears to be more uniformly distributed, thus giving higher precipitation rates and lower corrosion readings. The crystals size distribution appears to be affected by the flow turbulence, so slightly smaller and more porous crystals are seen at 1500rpm velocity whilst at 500rpm and 800rpm the protective films are more identical. The 800rpm velocity displayed a couple of agglomerated crystals suggesting that some particles were adhering from bulk to the surface. Overall, for all different flow rates, two main layers of films were noticeable. The first protective film layer contained smaller oval-like crystals attached directly to the surface of carbon steel. It may be argued that for faster velocities, the Fe^{2+} ions concentration across the surface would be higher,

resulting in higher initial corrosion values as seen from the LPR measurements. Additionally, with increase in flow rate, this first protective layer becomes less uniform, as crystals cannot grow in a controlled manner and become less well shaped and may be also removed from the surface due to higher flow turbulences. In fact, if SEM images at 500rpm with 1500rpm are compared, it can be concluded that the dominant crystal growth mechanisms at higher flow rates is caused by the rough interface growth which leads to less defined crystal morphologies (e.g., spherulitic or needle particles). Therefore, the flow velocity may strongly impact on scale morphologies for both $CaCO_3$ and $FeCO_3$.

In the first protective film layer, particles ranged from ±2µm to ±5µm, whilst on the second film layer, bigger spherical and rhombohedral crystals of sizes varying from ±5µm to ±10µm were also observed. The rhomboheadral crystals are potentially $CaCO_3$ crystals, however, the smaller spherical crystals may be either vaterite ($CaCO_3$) or $FeCO_3$. Lastly, samples from the bulk solution showed tiny ferrous rust deposits and these are presumably also present as a corrosion product.

In an attempt to characterize the film composition, EDX analyses were also taken for the corroded surfaces at different flow rates. As displayed in Figure 7.12, the EDX of scanned areas showed a mixture of different elements such as calcium, iron, carbonate and oxygen irons, suggesting that different scale types (i.e., $CaCO_3$, $FeCO_3$ and Fe_2O_3) may co-precipitate in the protective film.
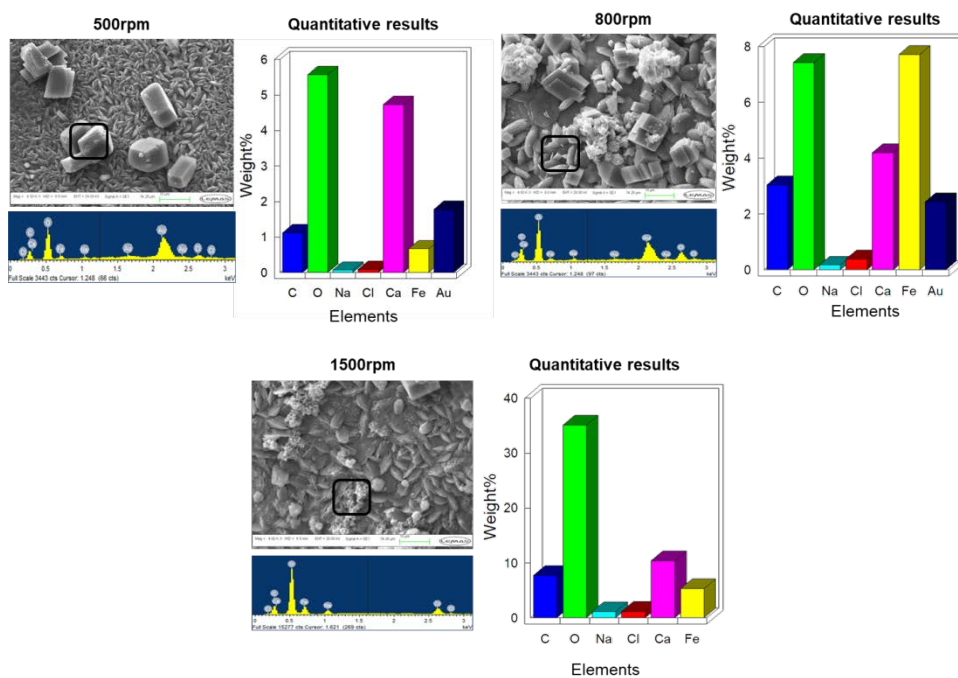
Figure 7.12: SEM/EDX analyses for RCE samples under different flow velocities for brine at SR=1.52, 25°C, 24 hours

An interesting aspect is the variations observed in the calcium and iron content, for different scanned areas of the RCE sample. At 500rpm the rhomboheadral shaped crystals appear to be composed mostly of $CaCO_3$ which may suggest that layer 2 for that sample was purely $CaCO_3$ scale. Furthermore, at 800rpm there is a significant amount of both calcium and iron elements which may suggest that both $CaCO_3$ and $FeCO_3$ films are dominant at this rate. Lastly, at 1500rpm, the protective film appears more uneven and the levels of calcium and iron content for the specific scanned area (layer 1 and 2) appear to have dropped whilst there is a high content of oxygen present in the metal. This last may suggest that more Fe_2O_3 is actually formed when the flow rate is highly turbulent since the environment is aerated and the cathodic reaction is accelerated at the surface of the metal. Note that some traces of sodium, chloride and gold were also identified and this is due to NaCl present in brine solutions which may have re-crystallised after rinsing the samples with distilled water and the gold peaks are present since these samples were gold coated for better visualisation of the crystals.

The EDXS provides only a quantitative evaluation of the contents present in the sample. Therefore, a detailed XRD analysis would be ideal to confirm the characterization of the polymorphs of the scale deposits. A more detailed crystal characterisation will be addressed later in this chapter.

To summarise, there are many other variables which can influence the corrosion and film formation processes. The effects of some of these parameters are well-established in the literature but for others it remains unknown.

This section focused on the analysis of some the key factors which can strongly influence the corrosion kinetics during its formation in presence of scaling saturated brines. All experiments were repeated and error bars were included to express the sensitivity of these results.

7.3 Impact of Inorganic Scale Formation on Corrosion Processes

In the previous section (7.2), several factors were investigated to assess their influence on carbon steel corrosion process. In section (7.2.4), the effect of flow hydrodynamics in corrosion was evaluated, and the protective film briefly characterized for the different flow regimes. Results showed that under a non-saturated CO_2 environment, mineral scale can be formed; however, the level of film

protectiveness tends to change with increase in flow rate. In this section, additional experiments were carried out in order to:

- Investigate the differences in crystallisation mechanisms and kinetics for corrosion and *surface* scale deposition, and bulk precipitation;
- Analytically determine and compare the corrosion rates to precipitation rates via mass measurements as a function of supersaturation, temperature and exposure time;
- Characterize the inorganic protective film using analytical tools such as ICP, SEM, EDXS and XRD;
- Assess the carbon steel surface post corrosion tests via interferometry techniques to identify the possibility of localized corrosion pits under different conditions of temperature and brine composition;

7.3.1 *Surface* **Scale Nucleation Kinetics & Mechanisms**

Surface nucleation is very difficult to measure when using the RCE, because it comprises a dynamic set up in which the working electrode is constantly rotating in order to simulate the flow turbulence of real piping systems. However, the induction time for inorganic scale deposition (i.e., $CaCO_3$ and corrosion products) at the surface of carbon steel can be estimated as the period in which the corrosion rates drop due to the formation of scale deposits. This assumption has been taken into consideration assessing the nucleation time on carbon steel X-65 substrates.

In the previous section (7.2), the relationship between brine supersaturation and testing temperature has been investigated. From results shown in Figure 7.6 and Figure 7.7, it can be extrapolated that the induction time at surface decreases with an increase in supersaturation and temperature. However, the increase in temperature showed a stronger effect for the nucleation onset at the carbon steel surface, giving almost instantaneous drop in corrosion rates for most of the saturated brine case studies (Figure 7.7).

Interestingly, for the highest saturation ratio case (SR=55) the drop in corrosion was monitored at around the same time, this suggests that temperature no longer plays a critical role for accelerating the nucleation kinetics at very high supersaturation levels, thus, there were not big differences for this particular case study.

The *surface* induction times are displayed in Table 7.2 and were determined from corrosion rate tests done on carbon steel X-65 at 500rpm.

Table 7.2: Mean induction time estimated from corrosion rates at carbon steel surface

Supersaturation, σ	Average induction time at carbon steel surface (τ_s), s as a function of temperature	
	$T_1=25°C$	$T_2=80°C$
1.52	2.52E+04 ±0.15	9.00E+03 ±0.15
2.55	2.16E+04 ±0.13	7.20E+03 ±0.15
4.77	1.44E+04 ±0.10	5.40E+03 ±0.13
11	1.08E+04 ±0.12	3.60E+03 ±0.10
55	6.66E+03 ±0.11	2.70E+03 ±0.11

Nancollas (341) had already emphasised that studying these phenomena simultaneously is quite challenging due to the possible interactions between bulk and surface ionic species. To validate this approach for induction times, it is crucial to review and understand the mechanisms of scale formation on the RCE substrate. The mechanisms of corrosion have been extensively studied in the past and several theories were developed to enlighten the processes occurring at the surface of steel during corrosion (342). However, when studying these phenomena it was not considered that these could take place simultaneously. So, in order to better understand the interactions between the bulk and surface kinetic reactions, the schematic diagram in Figure 7.13 must be taken into consideration:
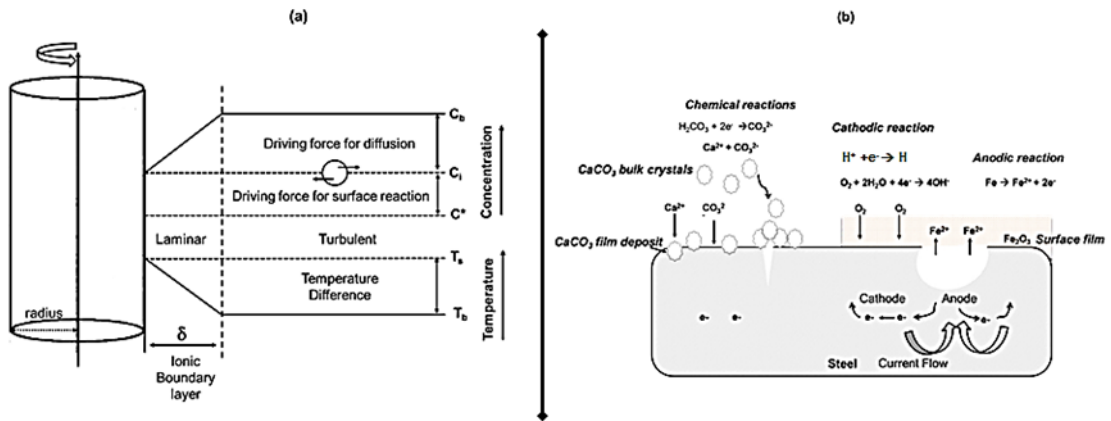
Figure 7.13: Schematic illustration of scale and corrosion processes taking place in the RCE bulk-interface regions. Part (a) shows the radial temperature and concentration profiles and part (b) illustrates the various chemical and electrochemical interactions that contribute for ions transport and formation of protective scale and corrosion films

Figure 7.13 illustrates a schematic representation of key factors which will influence the scale deposition during corrosion in a RCE set up. It is important to understand

that surface and diffusion mechanisms will control the entire process of corrosion and surface crystallization. Therefore, different scenarios relate parameters such as solution's concentration and temperature with the anodic and cathodic reactions taking place at the surface.

The diagram proposes that when scale and corrosion are taking place at the same time, the kinetics involved will strongly depend on system conditions such as concentration of ions, presence of CO_2 or O_2 and temperature. In the proposed mechanism, there is a preferential formation of calcium carbonate at cathodic sites is due to its low solubility and an increase in the local pH value, which induces the formation of a thin $CaCO_3$ film electrochemically formed over carbon steel surface. Additionally, some of the $CaCO_3$ crystals formed in the bulk can also migrate and adhere to the mild steel surface, inducing secondary nucleation and growth of the film deposits. On the other hand, corrosion products may also be expected in particular $FeCO_3$ and Fe_2O_3 due to the continuous supply of O_2 and CO_2 from air. However, there will be a kinetic competition between all ions in solution and the most thermodynamically favoured will stabilise and create the protective film first.

Lastly, some SEM images (Figure 7.14) were taken at the end of the experiments, in order to compare the crystal's appearance and understand the difference in the scale formation in bulk and at steel surface.
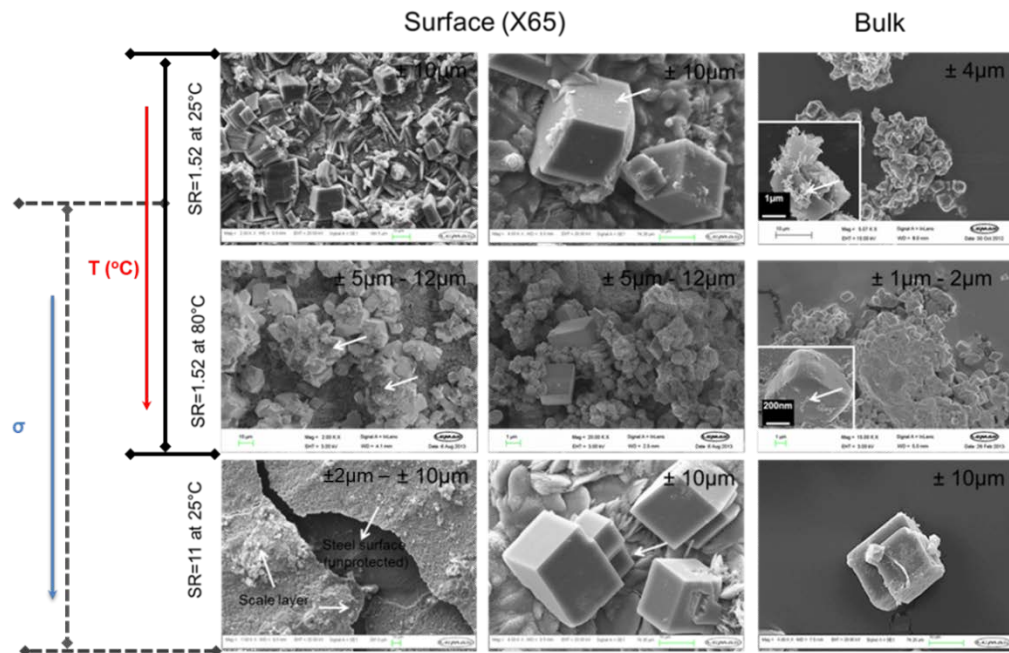
Figure 7.14: SEM images illustrating the mechanistic model for $CaCO_3$ deposition as a function of temperature and supersaturation after 24 hours-tests

Results in Figure 7.14 show that mechanisms of surface scale deposition (i.e., $CaCO_3$, $FeCO_3$ or Fe_2O_3) can be affected by an increase in temperature and increase in supersaturation. It can be inferred from the presented results that at low supersaturation, the surface crystals (calcite) were significantly bigger (±10μm) than those observed from the bulk (±4μm), suggesting that nucleation kinetics at surface of steel is faster than at bulk solution. A similar behaviour has been observed when the low supersaturation brines were tested at higher temperature (80°C). However, at higher temperature (80°C) and supersaturation, the crystal's size ranged more broadly (±2μm – ±12μm), and the scale deposits appear to be slightly smaller particles due to the fast growth mechanisms involved for the scale deposits at higher temperature.

Furthermore, it can be seen that the protective film layer for higher saturated brine is so dense that it cracks, leaving the surface of the carbon steel directly exposed and prone to further corrosion. This is expected as the surface and bulk interactions increase due to increase in concentration. The film layer cracked showing the steel substrate exposed to general corrosion.

Overall, heterogeneous nucleation is expected at low supersaturation whilst homogeneous nucleation is expected at high supersaturation. The results proposed a mechanism which is in agreement with the classical theory of nucleation and also some work previously done by other authors in CO_2 corrosion environments (101) (343) (207).

7.3.2 *Surface* Crystal Growth & Characterization

The inorganic scale crystals formed during corrosion processes in carbon steel X-65 where characterized via SEM/EDXS techniques with respect to their size and shape, as a function of supersaturation and temperature. Furthermore, the protectiveness of scale deposits on carbon steel was assessed using white interferometry techniques, in which the corrosion and scale deposits were removed from the steel surface to identify the possibility of pits due to localized corrosion.

7.3.2.1 Effect of supersaturation on protective film growth

Carbon steel X65 samples were analysed using SEM technique over six-hour intervals from the start of the experiment. These analyses aimed to assess the crystal growth at the surface of steel and evaluate the surface coverage of a cross-sectional region of the RCE coupon. The standard working conditions were at 500rpm for a range of different brine solution saturation ratios. Results shown from Figure 7.15 to

Figure 7.19 illustrate the changes observed for a range of supersaturated brines at 25°C, over 24 hours.
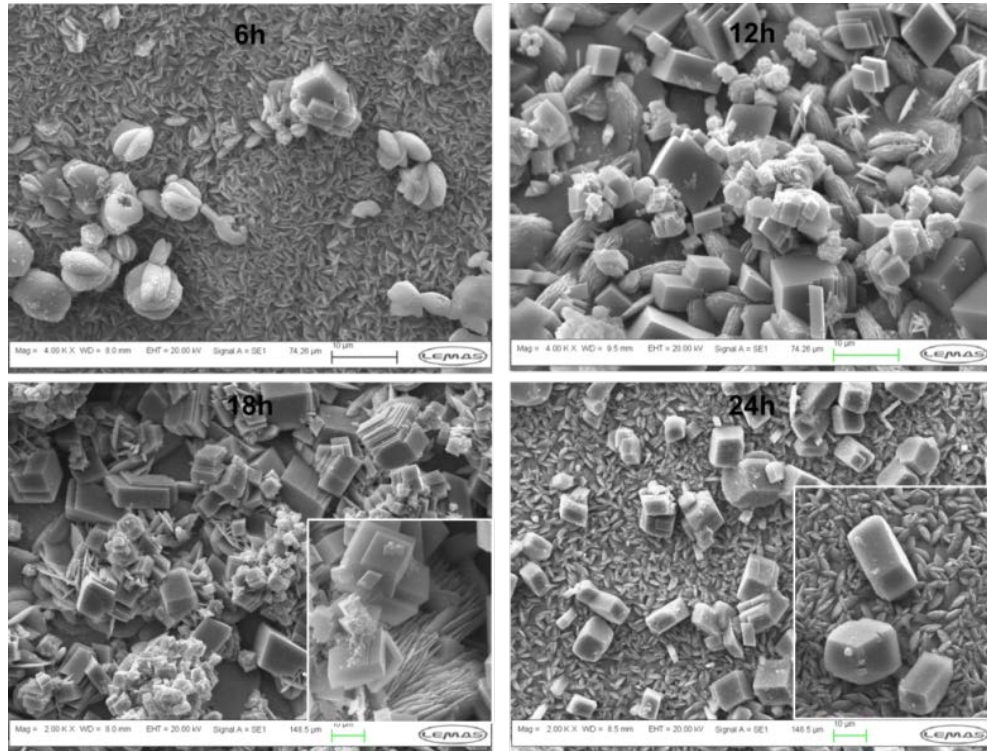
Figure 7.15: Surface crystals deposited on carbon steel over time for SR=1.52 at 25°C
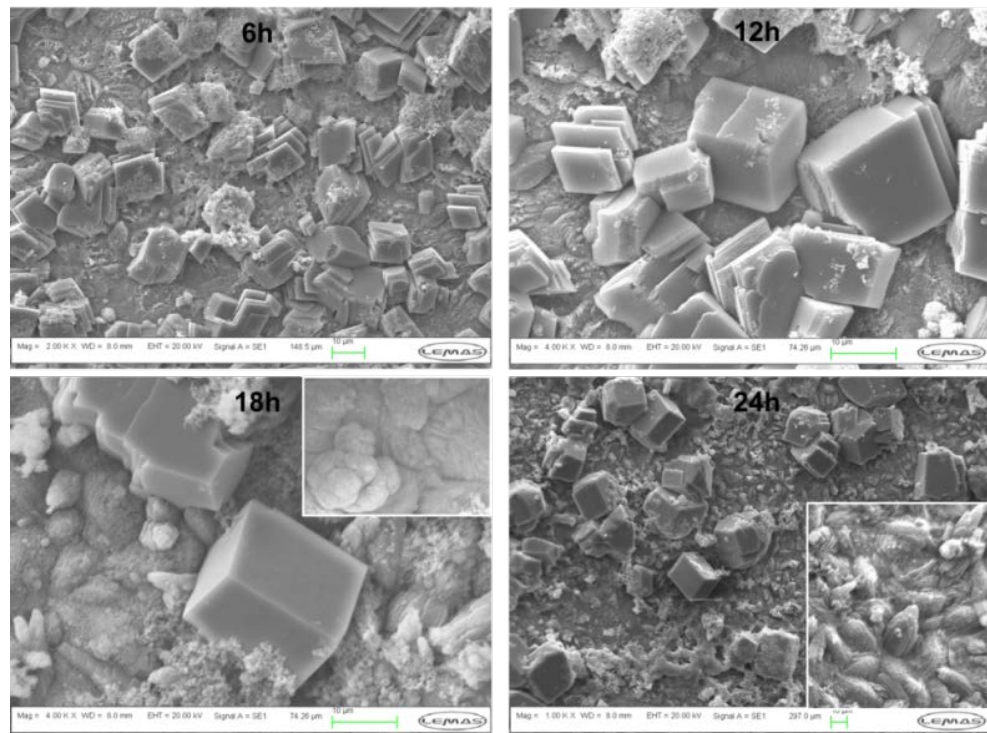
Figure 7.16: Surface crystals deposited on carbon steel over time for SR=2.55 at 25°C
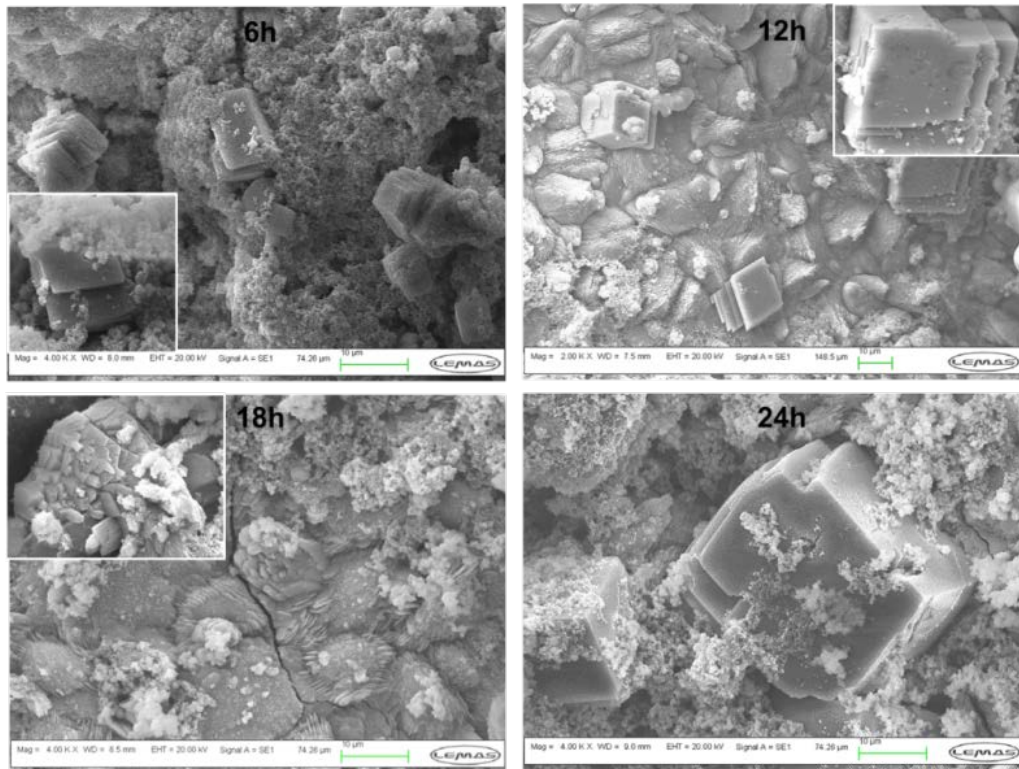
Figure 7.17: Surface crystals deposited on carbon steel over time for SR=4.77 at 25°C
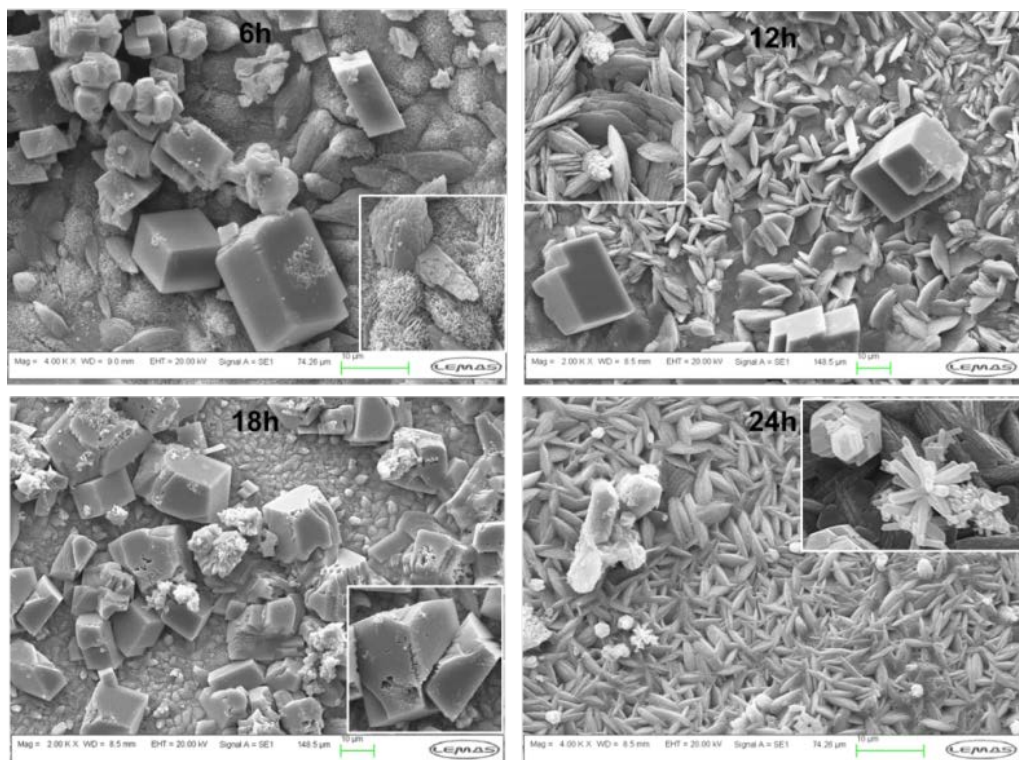
Figure 7.18: Surface crystals deposited on carbon steel over time for SR=11 at 25°C
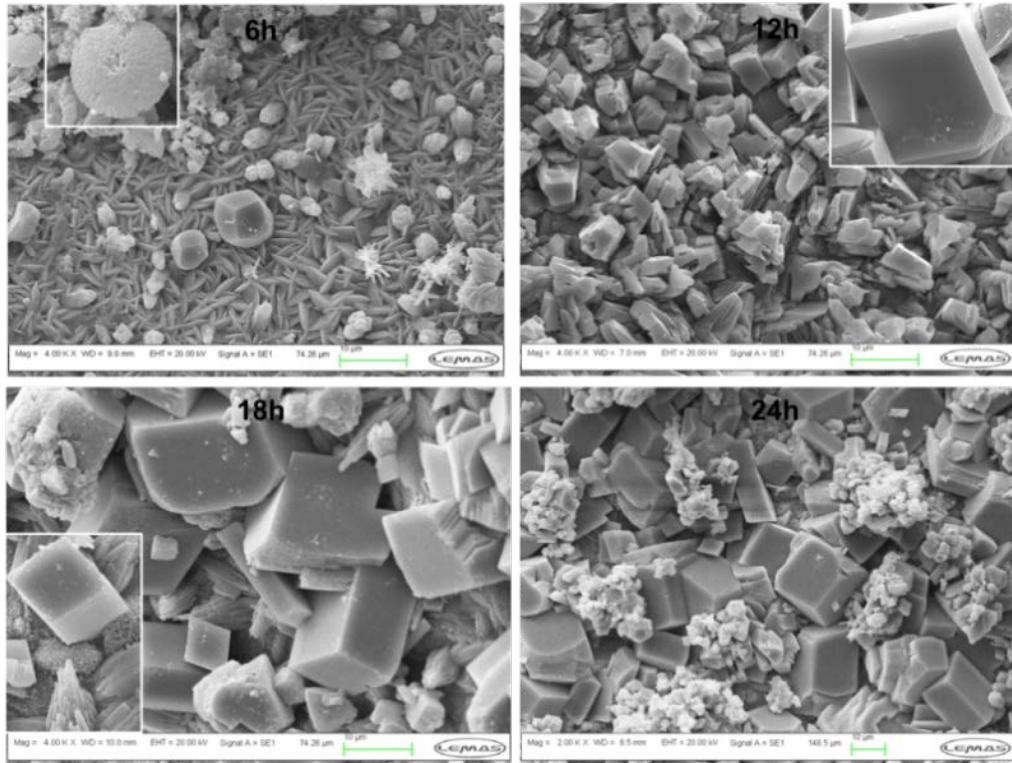
Figure 7.19: Surface crystals deposited on carbon steel over time for SR=55 at 25°C

SEM images from Figure 7.15 to Figure 7.19 showed that for a range of saturated bulk solutions (at 25°C), an inorganic scale protective layer is formed and continuously grows after 6 hours. These observations support the corrosion rate results displayed in Figure 7.6. The SEM analyses were taken every six hours to observe the crystal growth over time at a fixed rotational speed of 500rpm. The differences in polymorphism, crystal size and density across the metal surface was crucial to characterise the protective film.

The stages of crystal growth at surface of carbon steel appeared to be identical, as in general, after six hours there was a layer of smaller stable and homogeneously distributed crystals across the surface of carbon steel, followed by progressive growth and adhesion of bigger particles.

Throughout the growth process of crystals at surface, it is visible that the higher the supersaturation the more crystals deposited at steel surface. In addition, the peak for the crystal growth appeared to be between 12 hours and 18 hours for all case studies. During that stage it could be seen agglomeration of particles which could be transferred from bulk to the surface by flow hydrodynamics. Surprisingly after 24 hours, for all cases with exception of SR=55, the amount of crystals left in the RCE is less dense. This suggests that the protective film may start to deteriorate due to

gravity and dragging forces (associated with the turbulent flow); leading to an uneven film formation and possible exposure of the steel surface. These SEM images are also in agreement to the fact that at 25°C, the corrosion rate starts increasing after a steady drop. This suggested that the scale film was no longer providing sufficient protectiveness against the corrosion reactions. For SR=55 the initial particles formed are smaller and the crystal growth and agglomeration supports a stable film for the duration of the experiment.

Changes observed in crystal size and morphology over time confirmed that the surface saturation ratio with respect to inorganic crystals being formed was decreasing as the crystals grew and agglomerated at the steel substrate.

Considering that most of the scale precipitated is $CaCO_3$, it can be also observed changes in polymorphism over time for a constant rotational speed. The first layer of scale deposits is formed by half-moon crystal shapes which could be an indication of vaterite crystallised directly at the steel surface. However, these morphologies will be confirmed later in the chapter with XRD analyses. The second layer was mostly formed by calcite (rhombohedral crystals) and at higher supersaturation ($11\leq SR\leq$ 55) some aragonite (needle-like crystals) were also observed. Furthermore, for all low saturated brines, corroded particles (i.e., rsust) were visible not only at the RCE coupon but also in the bulk solution. These corroded particles were most visible at RCE's from cases 2 (SR=2.55) and 3 (SR=4.77). SEM of the iron oxide particle showed agglomerates of tiny spherulitic particles.

Under the assumption that the protective film is predominantly formed by $CaCO_3$ crystals, the SEM was used to support the investigation on $CaCO_3$ growth mechanisms on steel surfaces. The growth mechanisms for calcite appear to be by spiral growth given the evidence of kinks and dislocations (e.g., Figure 7.17 at 12 hours – zoomed image). On the other hand, the appearance of vaterite at early stages and growth at steel surface supports the surface diffusion mechanism for spherulitic growth. Lastly, aragonite crystals formed at higher supersaturation ($11\leq SR\leq$ 55) also suggest that rough interface growth is expected under those conditions (e.g., Figure 7.18 at 24 hours – zoomed image and Figure 7.19 at 6 hours).

Lastly, the surface transport of ions between bulk and the metal allowed the formation of spherulitic particles, known as iron oxide (Fe_2O_3) and possibly the precipitation of iron carbonate ($FeCO_3$). The presence of iron oxide particles may be an indication of localised corrosion taking place underneath the $CaCO_3$ scale film, when the solution is exposed to air.

7.3.2.2 Effect of temperature on protective film growth

Further tests were then taken to assess the effect of temperature during $CaCO_3$ *surface* crystallization and corrosion process on carbon steel X-65. Temperature has been shown to have a significant impact on corrosion; hence, it is expected to affect the mechanisms of formation and kinetics of surface scale. Furthermore, for $CaCO_3$ crystallisation, temperature is known to affect the shape and size of crystals shape and size. Results obtained for all supersaturation brine cases at 80°C and after 24 hours are shown in Figure 7.20.
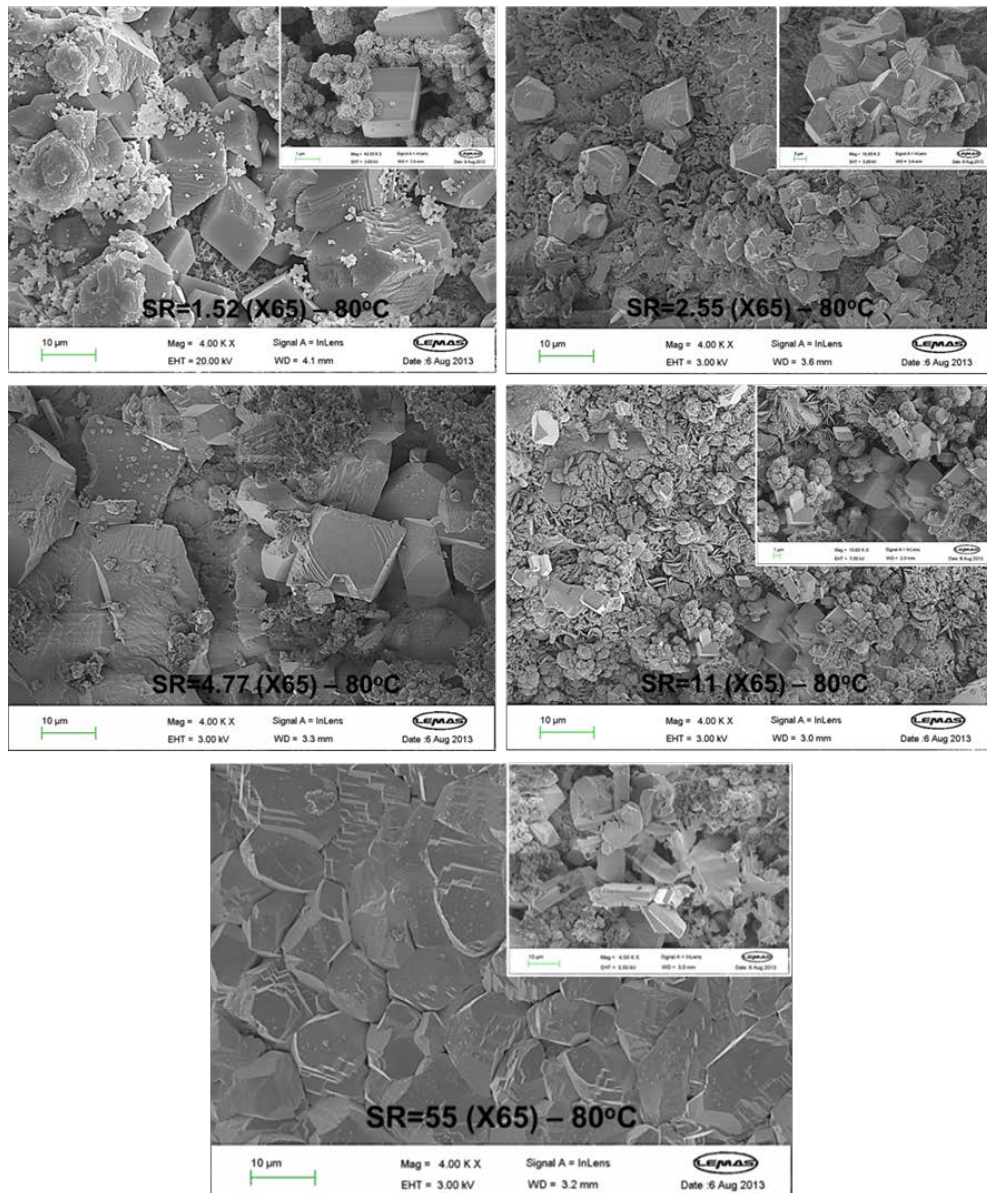
Figure 7.20: Surface crystals deposited on carbon steel X65 for different supersaturation levels at 80°C, after 24 hours

SEM examination of $CaCO_3$ crystals revealed a variety of crystal shapes comprising rhombohedral, half-moon, cauliflower, needles and prismatic rods.

Results shown in Figure 7.20 illustrate that at the end of 24-hours, the inorganic scale ($CaCO_3$ and corrosion products) is more compact, comprising crystals of slightly smaller size than those observed in the 25°C film (Figure 7.15 – Figure 7.19). This also supports the earlier notion that scales formed at higher temperature are more protective than those formed at lower temperatures (344).

Rhombohedral calcite appears to be the most prevalent phase of $CaCO_3$ over the supersaturation range studied. In addition, plenty of grown spherulitic vaterite crystals are particularly observed at supersaturation 11, and few small aragonite crystals are seen at supersaturation 55. Although, it is hard to define the precise size of particles attached to the metal, it can be seen that calcite crystals formed at 25°C (24 hours) were slightly bigger and more defined than those formed at 80°C. This can be explained by the fact that temperature accelerates the deposition kinetics, resulting in slightly smaller crystal deposits. Furthermore, the crystals observed at saturation ratio 55 resemble $FeCO_3$ crystals, however, at this stage with visual analysis it cannot be confirmed if any $FeCO_3$ scale is also present at the surface of carbon steel. For the lower supersaturation, iron oxide (Fe_2O_3) particles were visible on top of calcite crystals. The identification and characterisation of the scale film deposits was based on understanding the possible morphologies of $CaCO_3$ and iron products that may be formed under similar testing conditions. This polymorphic characterisation was aslo supported with EDXS analyses (section 7.3.2.3). However, to be more accurate, XRD results (section 7.3.2.4) will confirm the actual crystals deposited under these testing conditions.

Lastly, studies done by Alsaiari et al., (269) (345) have emphasised the influence of calcium during iron carbonate precipitation, showing that calcium carbonate deposition kinetics are faster than those involved during iron carbonate formation. Thus, it is more likely to form $CaCO_3$, reducing the carbonate ions available for iron carbonate formation. Furthermore, the presence of oxygen in the solution would induce the formation of iron oxide from the reduction of oxygen at the surface of the metal.

7.3.2.3 EDX quantitative analysis on carbon steel scale deposits

During SEM observations, EDX spectrometry was used to analyse the samples for better understanding the morphologies present in each sample. Figure 7.21 shows

an example of the main elements present in those samples. This technique aided differentiating the crystals observed by providing their elemental composition. However, only XRD analysis (section 7.3.2.4) can give further clarification in identifying and characterising the crystals deposited at the metal surface.
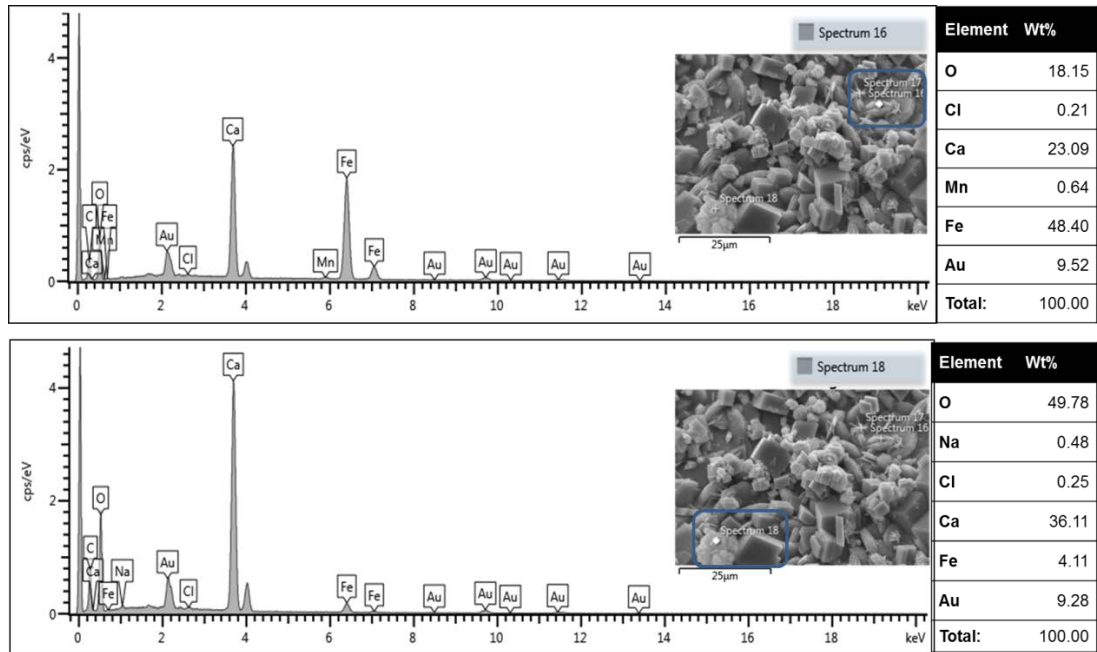
Figure 7.21: Example of EDXS analyses performed on carbon steel X-65 tested for brine at SR=1.52, at 25°C, after 12 hours

A spectrum with results table is given by EDX analyses, in which the X-ray beam penetrates the sample to approximately 2mm and identifies the elements composing the selected scanned area. As EDX is semi quantitative, a weight percentage table is also provided with the quantification of the elements identified. This is clearly illustrated in Figure 7.21, where different areas of the same sample are scanned, resulting in different quantifications of the elements present in the same sample. The main components of interest are calcium, carbon, oxygen and iron, and all of these are included in the results analysis. Furthermore, some traces of sodium, chloride and gold were also identified. NaCl can precipitate out of the solution and some of its residues are detected by the EDX. Gold (Au) is from the coating on the samples prior to analysis.

In spectrum 16, a spherulitic crystal (vaterite) is selected and since this is closer to the substrate, high intensity peaks for calcium and iron are obtained. However, given the presence of carbon and oxygen elements and the visual appearance of the crystal, the selected crystal is considered to be $CaCO_3$ and the iron peak is assumed to be from the substrate (carbon steel). Similarly, in spectrum 18, the selected calcite

crystal is identified as $CaCO_3$ because these elements are present and calcium has higher weight percentage than iron, since this crystal is on top of other $CaCO_3$ agglomerates. This confirmed that iron peaks identified for this sample belonged to steel from the metal substrate and possibly co-precipitates of $FeCO_3$ and Fe_2O_3 deposits.

7.3.2.4 XRD analysis on scale deposits from carbon steel X-65

X-ray diffraction patterns were recorded ex-situ at the end of each experiment for carbon steel samples. This technique enabled identifying and verifying the presence of $CaCO_3$ polymorphs non-identifiable by SEM/EDX. The XRD spectra were done within $20°$ – $40°$ (2Θ) to minimize the effect of iron (Fe^{2+}) peaks from the RCE round edges. Otherwise, when XRD spectra were taken for a broader 2-theta (2Θ) range (up to $50°$), the film deposit peaks were significantly reduced due to the higher intensity from the steel (iron II) peak. Another limitation encountered during these XRD experiments was to do with the fact that RCE samples are cylindrical in shape and therefore peaks could shift slightly when analysing, so some tests had to be repeated to get the correct match whilst identifying the crystal deposits.

Figure 7.22 and Figure 7.23 illustrate several reference peak patterns obtained from the literature to better characterise the inorganic scale and corrosion products from the tested RCE samples.
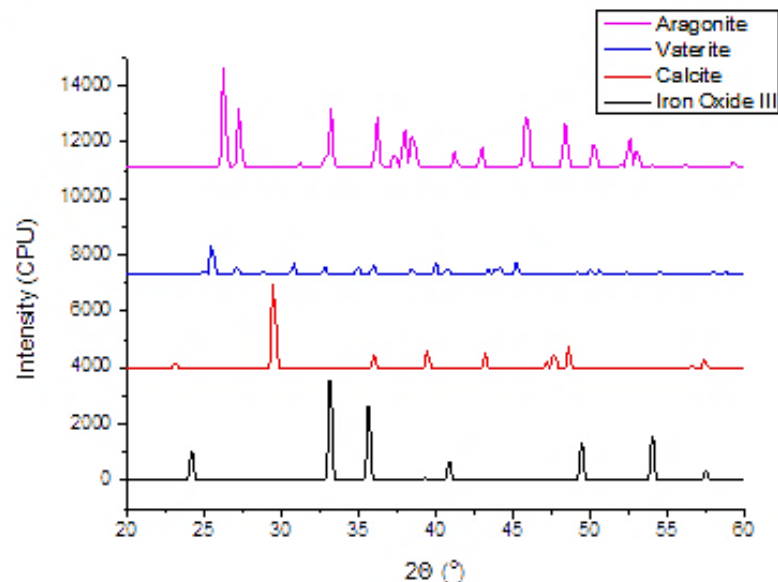
Figure 7.22: Reference XRD for calcite (317), vaterite (318), aragonite (319) and iron (III) oxide (346)
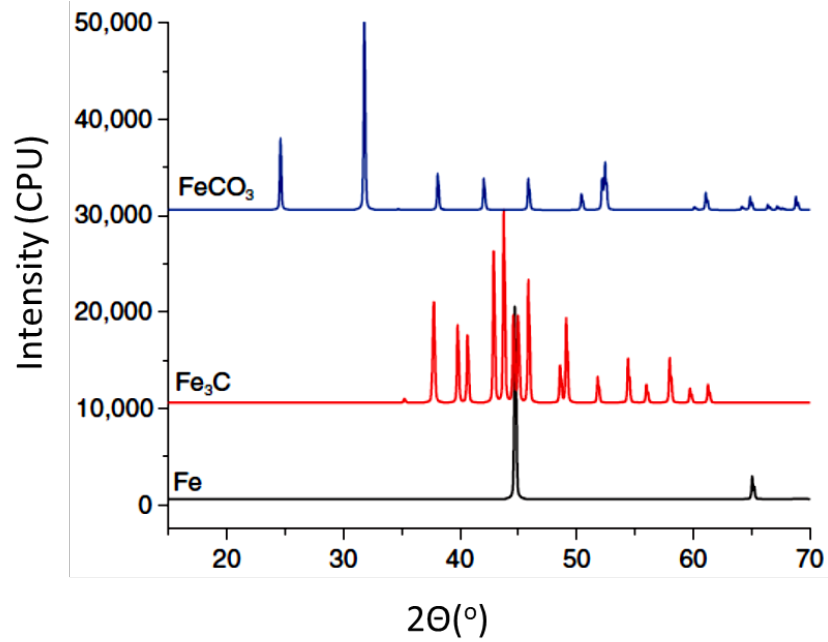
Figure 7.23: Reference XRD patterns for iron carbonate (FeCO₃), iron carbide (Fe₃C) and steel (Fe) (347) (245)

Figure 7.24 and Figure 7.25 display the XRD patterns recorded ex-situ for the RCE carbon steel samples at the end of the experiments done at 25ºC and 80ºC.
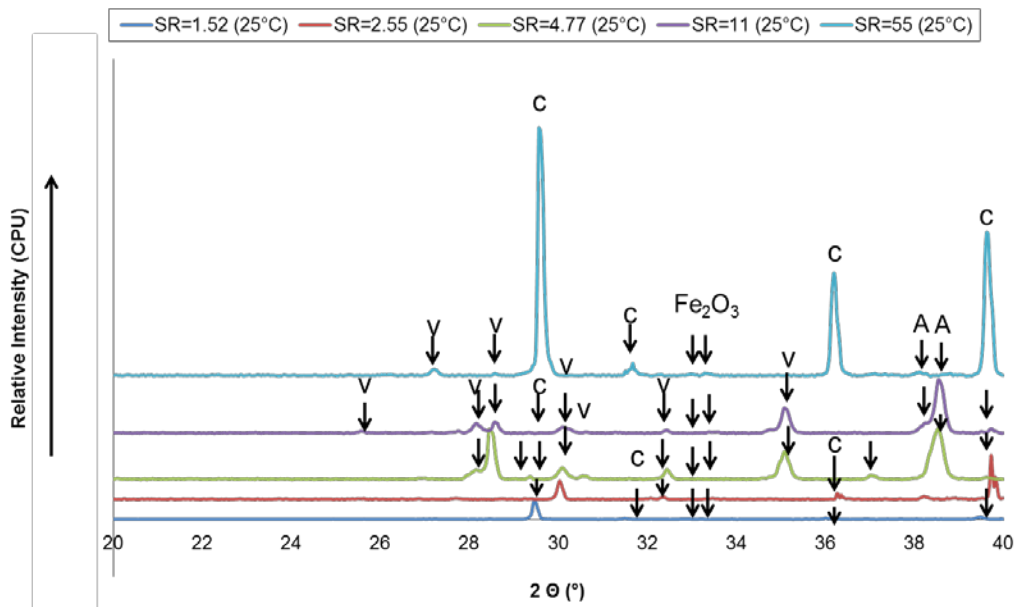
Figure 7.24: XRD patterns obtained ex-situ, for all RCE carbon steel samples at 25°C, after 24 hours. Key: C: calcite, V: vaterite, A: Aragonite. Arrows display some of the minor crystal phases and the relative intensity scale is arbitrary.

Results in Figure 7.24 show that at 25ºC the protective film formed is mostly composed of $CaCO_3$ and Fe_2O_3 crystals. The intensity of each peak's scattering vector revealed that all three polymorphic phases of $CaCO_3$ are encountered in

samples tested at 25°C, but their distribution changed according to the brine's initial's supersaturation. In addition, the XRD peak intensity can be useful to describe polycrystalline samples, and indirectly quantify the most dominant crystal structure present in the area assessed. However, no integration of the area covered by crystals has been done to quantify the amount of scale/polymorphs present in each sample using the Rietveld refinement method. Thus, the fewer the deposits encountered at the surface of the RCE cylinder, the smaller their peak's relative intensity. This constraint was particularly seen for crystals at lower saturation ratio, whose peak intensity was much smaller, making it harder to display when comparing them all together. Nevertheless, these XRD results supported those obtained from SEM/EDXS visualisations at 25°C.

In general, it could be seen that the half-moon shaped/spehrulitic crystals observed in layer 1 corresponded mostly to vaterite, as these peaks were identified for all cases at different intensities. Furthermore, calcite appears to be the most dominant polymorph crystallised at the surface after 24 hours for all saturated brine studied. However, at higher supersaturation (11≤SR≤55), some aragonite and vaterite crystals were also detected. Lastly, Fe_2O_3 crystals were also detected over the different samples.

Results from Figure 7.24 showed a variety of $CaCO_3$ polymorphs being formed as a function of supersaturation. At low supersaturation (1.52 ≤ S ≤ 4.77) less scale was deposited at the surface of the metal. As a result, the XRD peaks illustrate the most prevalent phases encountered at that particular area of the steel surface. Assuming a uniform film is deposited, then it can be concluded that at SR=1.52 mainly calcite deposits were found at the substrate. For SR=2.55 crystals were identified to be mostly vaterite with some traces of calcite, whilst for SR=4.77, all $CaCO_3$ polymorphic phases (calcite, vaterite and aragonite) were identified but vaterite displayed the best match. For SR=11, all phases were similarly identified and vaterite was the most dominant, with some traces of aragonite and calcite. Lastly, at SR=55, calcite was the predominant phase with few traces of vaterite and even fewer of iron oxide (III). Iron oxide scale appeared to have smallest peaks for all case studies at 25°C. These results supplement the analysis done by SEM/EDX.

Further XRD tests were conducted for RCE tests performed at higher temperature, to observe the effect of temperature on the protective film crystal structures. Figure 7.25 illustrates the different crystal structures obtained between 1.52 ≤ SR ≤ 11 at 80°C, after 24 hours. Results obtained for SR=55 at 80°C after 24 hours are to be

displayed separately (Figure 7.26) so the peaks can be more clearly identified. These contained much denser film as per shown SEM and therefore their XRD peaks were a lot higher in intensity.
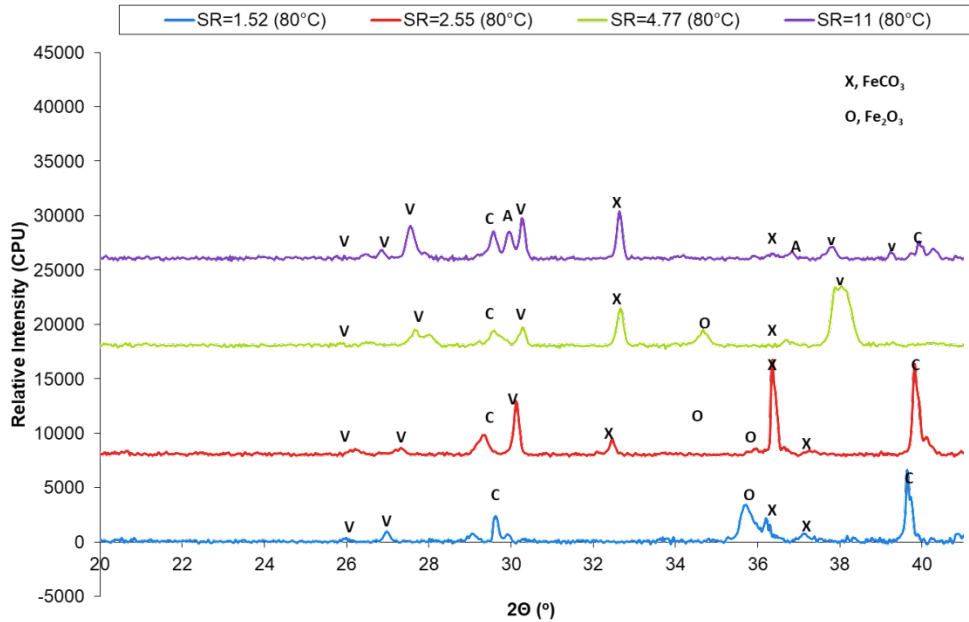
Figure 7.25: XRD patterns obtained ex-situ, for RCE carbon steel samples of 1.52 ≤ SR ≤ 11 at 80°C, after 24 hours. Key: C: calcite, V: vaterite, A: Aragonite. Arrows display some of the minor crystal phases and the relative intensity scale is arbitrary.

In order to compare the effect of temperature, Figure 7.26 summarises the differences observed for tests performed at highest saturation ratio at different temperatures.
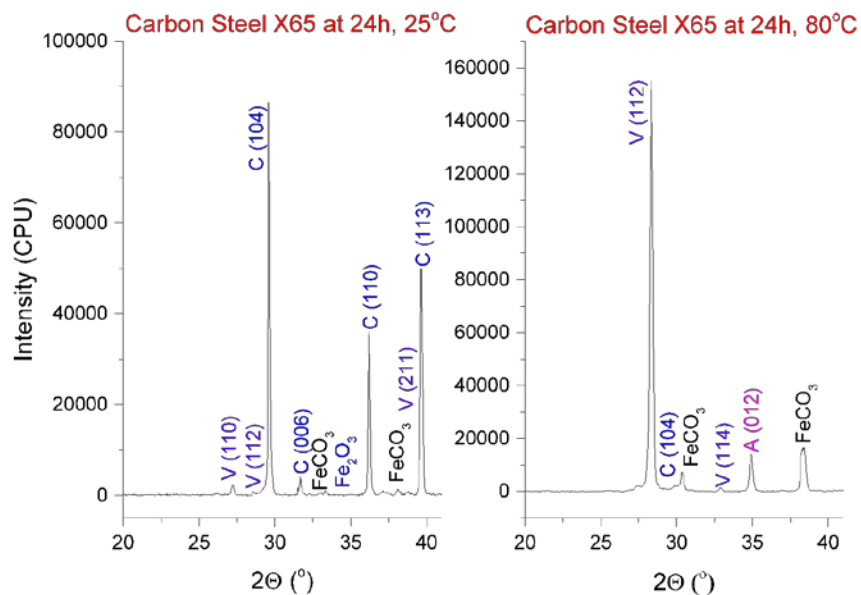
Figure 7.26: XRD pattern comparing crystals formed at same metal and different temperatures (SR=55 after 24 hours)

Results from Figure 7.26 show that at 25°C, calcite (1 0 4) and vaterite (1 1 2) appear to be the most dominant phases, with vaterite forming the first layer of deposition (smaller uniform crystals) and calcite grown on top of vaterite (Figure 7.19). With increase in temperature to 80°C, it is clear that $FeCO_3$ scale is formed and accompanied by calcite, vaterite and aragonite crystals. The formation of $FeCO_3$ scale (Figure 7.20) suggests that a local supersaturation is created at higher temperatures and the reaction kinetics for $FeCO_3$ is faster than $CaCO_3$ at the steel surface. At lower temperature (25°C), no $FeCO_3$ was identified via XRD; however some Fe_2O_3 was formed as a corrosion product. This also suggests that corrosion surface mechanisms are strongly dependent on supersaturation and temperature.

7.3.3 Assessment of carbon steel X-65 surface post simultaneous corrosion and scale deposition processes

From corrosion rate measurements (7.2) and surface deposition characterization (7.3), it could be seen that both $CaCO_3$ crystals and corrosion can form a film which may be beneficial for temporary protection against general corrosion. However, this film protectiveness is likely to change over time and so it is crucial to further investigate the potential of local pits formation during simultaneous corrosion and scale deposition processes. A pit in carbon steel is considered as a specific surface area around a localized cavity that is evidently deeper than the surrounding surface area. Therefore, it is important to emphasize that the pit depths presented in this section are relative to previously corroded surface.

At the end of each corrosion test in carbon steel X-65, the protective film (i.e., scale and corrosion deposits) was removed using Clarke's solution and prepared for white light interferometer analysis (chapter 5.5.6). The pits encountered on the cross-sectional area of carbon steel X65 samples considered shallow pits to have a maximum depth is inferior to ±5μm. These shallow pits would be typically found in general corrosion. The pits wildness is varied and according to the literature there is not an established value for it. On the other hand, localised pits are characterised by its depth > ±10μm, and sometimes these can have a wider appearance from the top of the surface. In this study, pits of minimum penetration depth of ±10μm will be considered as deep or harmful.

In this study, the surfaces of carbon steel X65 have undergone both general and localised corrosion, as shown in the example in Figure 7.27. The colour coding for blue means negative size (in microns) implying that it is a deeper surface, whilst red has a positive size (in microns) implying that it is at the top of the surface.
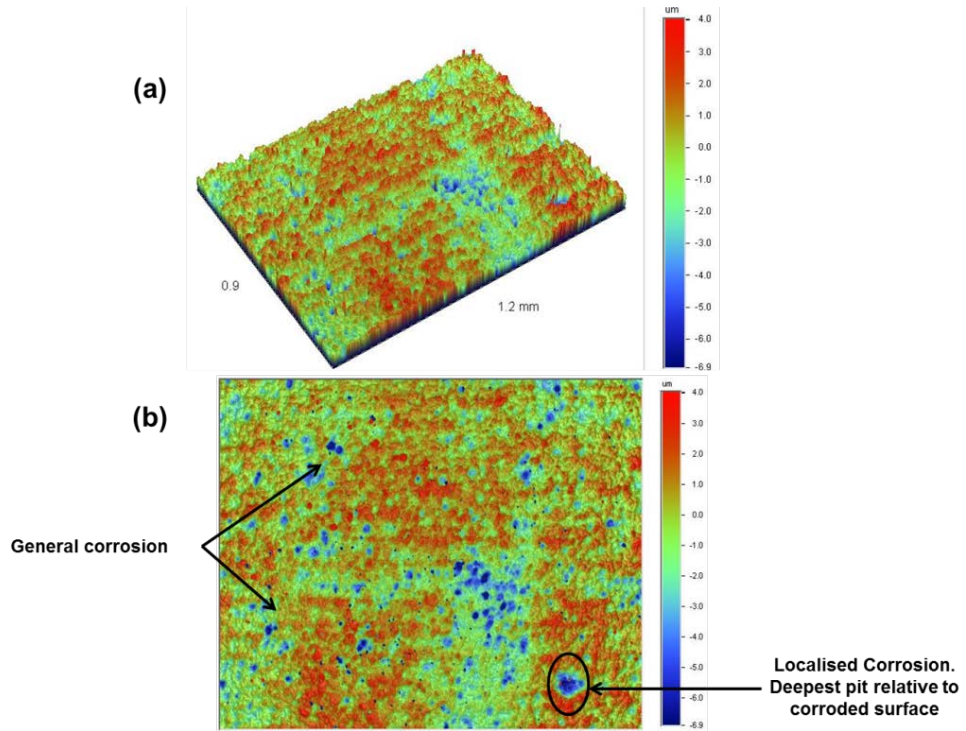
Figure 7.27: Example of a corroded sample analysed via white interferometry. (a) 3D topographic image and (b) 2D topographic image illustrating general corrosion and localised corrosion

Topographical images displaying the aspect of the carbon steel surfaces post corrosion tests and after removal of protective film are shown from Figure 7.28 to Figure 7.32. The deepest pits over the generic corroded surfaces are characterized with respect to their depth as a function of temperature (Table 7.3).
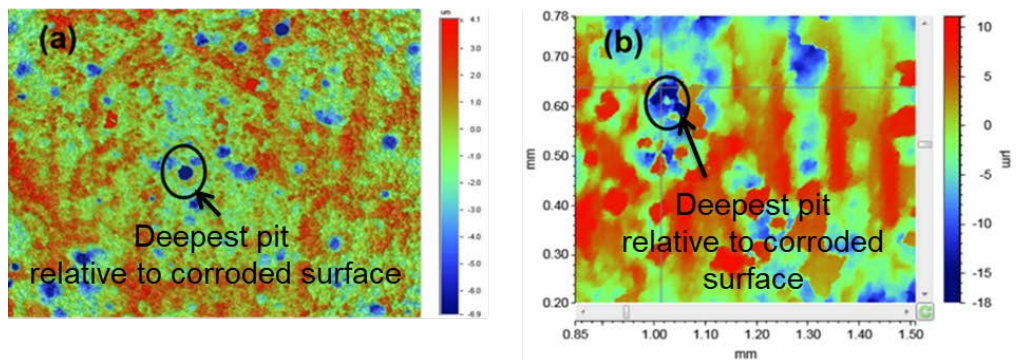
Figure 7.28: Interferometry 2D profiles of measurable maximum pits on carbon steel X 65 surface for SR=1.52, at (a) 25°C and (b) 80°C
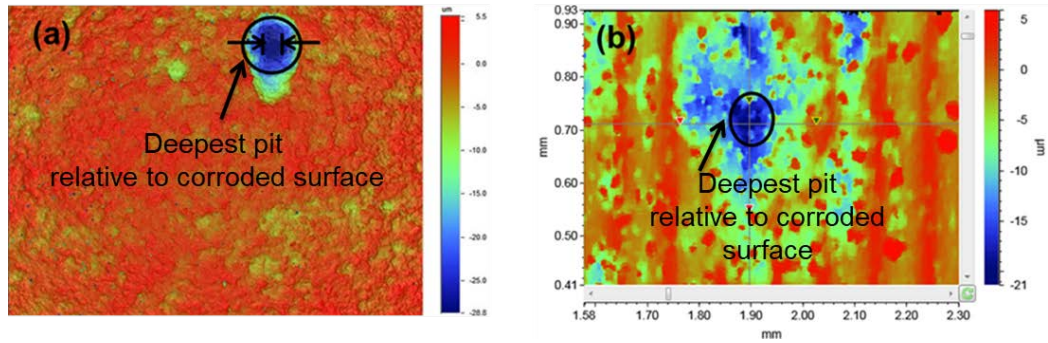
Figure 7.29: Interferometry 2D profiles of measurable maximum pits on carbon steel X 65 surface for SR=2.55, at (a) 25°C and (b) 80°C
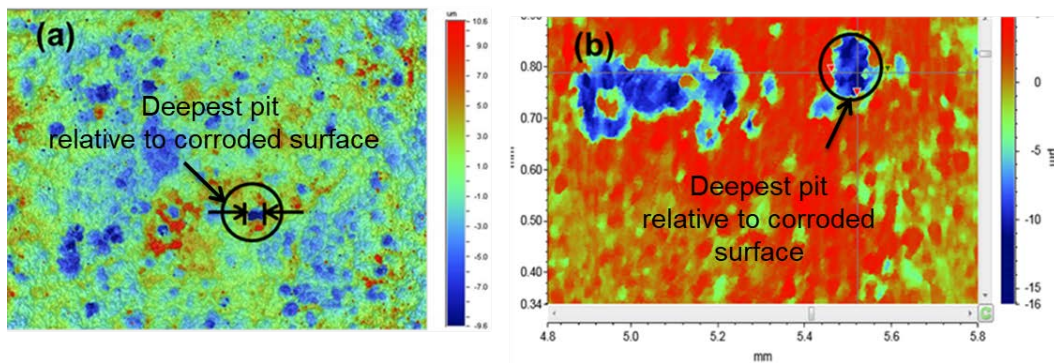
Figure 7.30: Interferometry 2D profiles of measurable maximum pits on carbon steel X 65 surface for SR=4.77, at (a) 25°C and (b) 80°C
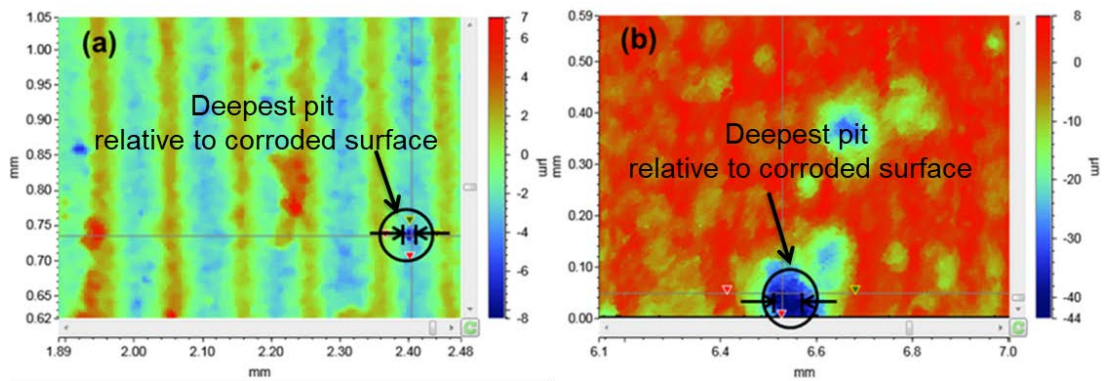
Figure 7.31: Interferometry 2D profiles of measurable maximum pits on carbon steel X 65 surface for SR=11, at (a) 25°C and (b) 80°C
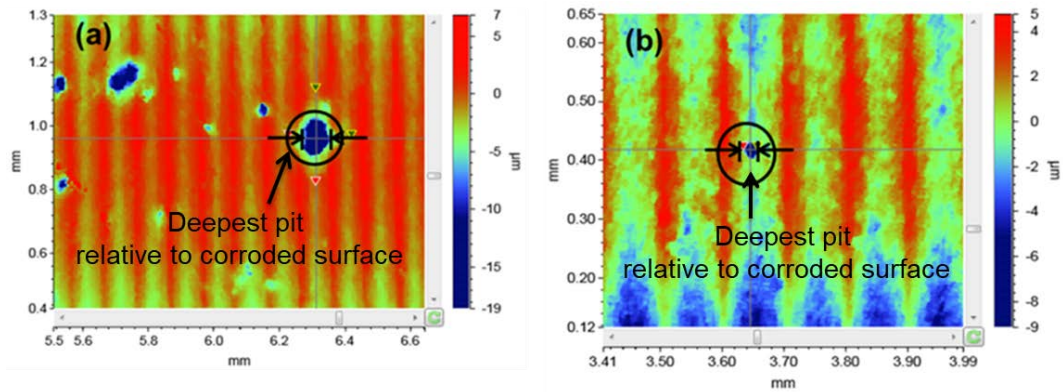
Figure 7.32: Interferometry 2D profiles of measurable maximum pits on carbon steel X 65 surface for SR=55, at (a) 25°C and (b) 80°C

During data analysis a threshold of ± 5µm was applied in order to differentiate the general corrosion pits from the localized pits. Subsequently, results have shown that samples collected at 25°C after 24 hours, showed pits more evenly spread across the surface with a varying depth between ± 3µm to ± 5µm. However, the severity of localised corrosion at 25°C appears to be greater than at 80°C (Figure 7.28 – Figure 7.32). The interferometer data analysis results in Table 7.3 considers the average pit depth for 10 deepest pits to the corroded surface area.

Table 7.3: Depth penetration of local pits post scale and corrosion as a function of temperature.

SR	Pit Depth (µm)	
	25 °C	**80 °C**
1.52	13 ± 0.05	18 ± 0.05
2.55	33 ± 0.08	10± 0.06
4.77	12 ± 0.03	16 ± 0.05
11	25 ± 0.05	19 ± 0.02
55	22 ± 0.07	18 ± 0.10

The results shown in Table 7.3 in have shown that metal penetration rate (i.e., pitting rate) occurs faster than shown by the general corrosion profiles. In particular for the higher saturated brine cases, in which the formation of a passive oxide layer seems to enhance the pits initiation and propagation. However, if already initiated pits are covered by corrosion and scale products, then the pit propagation is likely to be inhibited. This explains why at higher temperatures where more film is deposited at the metal surface the pits encountered are relatively smaller than at lower temperature.

Overall, the differences between pitting size are fairly small and tests were solely done to assess their depth as a function of supersaturation and size. However, the results obtained can give insights for pitting propagation pathways. Lastly, these results are also in agreement to some work previously done for CO_2 saturated corrosion environments (245) (248), in which the pH of bulk solution contributed to form $FeCO_3$ inhibiting the propagation of the pits by pseudo-passivation at the mild steel surface.

7.3.4 Quantitative Analysis of Scale and Corrosion Film

7.3.4.1 Precipitation rate from weight measurements on carbon steel

Total weight measurements are commonly used to characterise the RCE surface kinetics caused by $CaCO_3$ scale (mass gain) or corrosion (mass loss). In this study, the same samples studied for LPR tests (Figure 7.6 and Figure 7.7) have been assessed with respect to their weight changes before and after 24 hours experiments (Figure 7.33). Furthermore, ICP analyses for calcium and iron (II) ions have been taken to quantify the amount of deposits dissolved from the metal substrate after 24

(a)

(b)
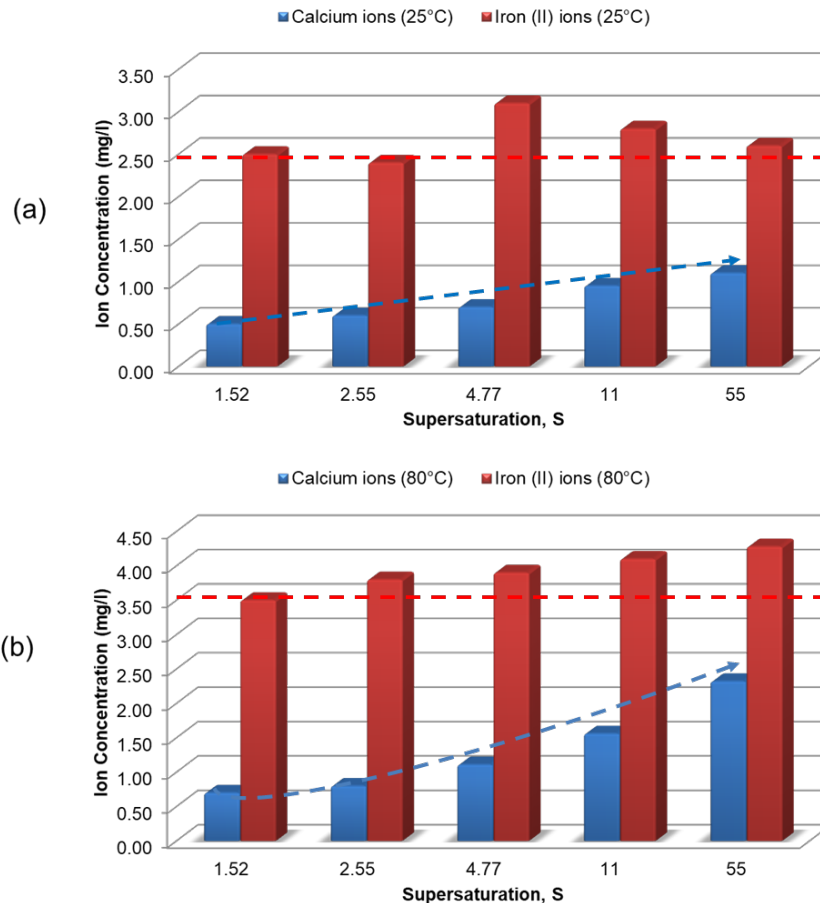
hours (

Figure 7.34). These analyses provide an insight into scale surface crystallization kinetics, complementing the SEM/EDXS and XRD results previously discussed (7.3.2).

Results presented in Figure 7.33 show the changes in mass caused by scale and corrosion taking place simultaneously at the surface of carbon steel X-65, over a range of supersaturated brines and at two different temperatures (25°C and 80°C).

Despite the weight losses observed in particular for supersaturation cases 2.55 and 4.77 at 25°C (Figure 7.33 – a), the overall weight of the RCE samples increased over time. This suggests that there is a significant increase in the amount of $CaCO_3$ scale and corrosion deposits, which protect the metal from further general corrosion (i.e. mass loss). For experiments done at 80°C (Figure 7.33 – b), there was less evidence of mass loss on the RCE and a gradual increase in the weight of the sample could be seen due to scale and corrosion products deposited at the surface over time. This elucidates the fact that $CaCO_3$ kinetics are driven by temperature, so nucleation and crystal growth are faster, ensuring the protection of the metal surface for the duration of the experiments. However, the maximum mass gain was obtained at the highest supersaturation for both temperatures (i.e. 25°C and 80°C).
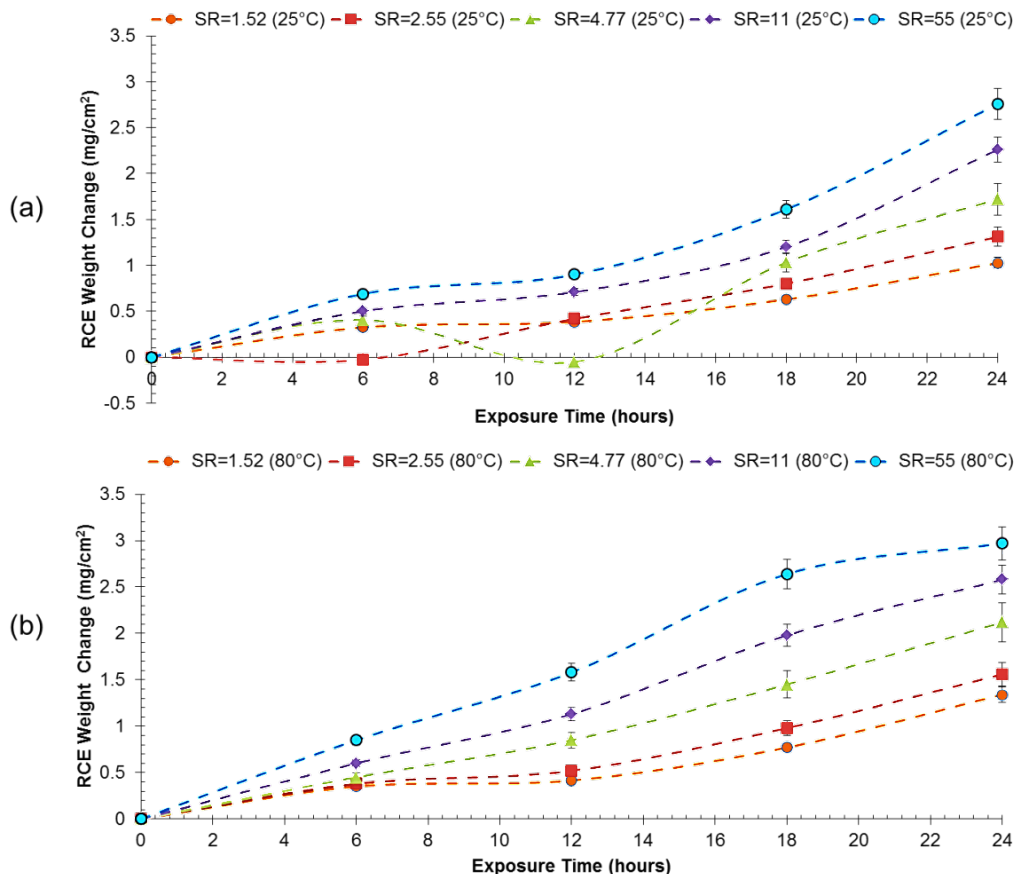
Figure 7.33: RCE weight changes at 500rpm due to CaCO$_3$ deposition and corrosion (mass loss) on carbon steel X65 at: a) 25°C and b) 80°C

Interestingly, there was very little difference between the maximum weight for these samples (Figure 7.33), as 2.8mg/cm^2 were obtained at 25°C and 2.99mg/cm^2 was obtained at 80°C. This may suggest that at lower supersaturation levels, corrosion may have a greater impact in the weight loss measurements under the same testing conditions.

Lastly, in order to quantify the amount calcium and iron (II) ions deposited at the film, the RCE samples were dissolved in Clarke's solution, quenched and taken for ICP analysis at the end of the experiments, as shown in Figure 7.34.

The ICP results helped in quantifying the ions removed from the rotating cylinder metal in order to quantitatively estimate the amount of surface scale (CaCO$_3$ and/or FeCO$_3$ or Fe$_2$O$_3$) were present in the tested samples.
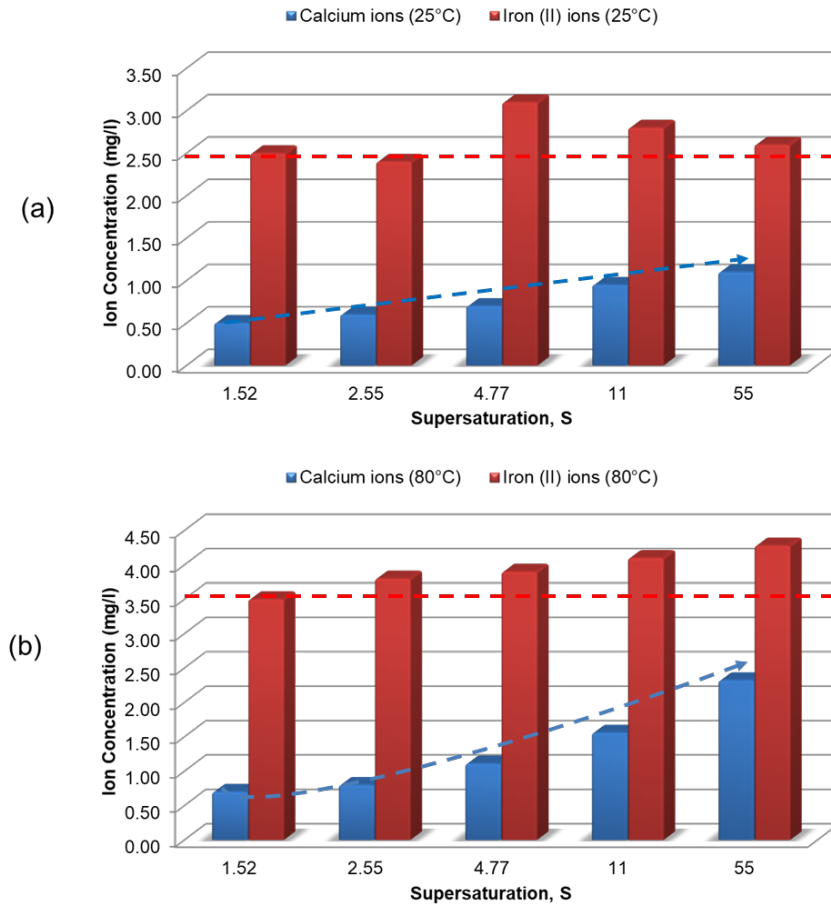
Figure 7.34: Representation of calcium and iron precipitation rates via mass gain at 500rpm: a) 25°C and b) 80°C

Results shown in Figure 7.34 illustrate that at 25°C, the amount of Fe (II) released from the surface to form corrosion products remained almost constant over different saturation ratio tests. On the other hand, the amount of calcium ions deposited increased with increase in brine supersaturation, but remained smaller than the overall content of iron (II) ions. These results elucidate the fact that interactions at surface of the metal are faster to form corrosion products (e.g., Fe_2O_3 scale) at lower temperatures, because a local supersaturation is created. However, $CaCO_3$ crystals deposition kinetics only gets faster with increase in bulk supersaturation. Thus, a more protective film with combined corrosion and $CaCO_3$ scale deposits is expected mostly at higher supersaturation for tests done at 25°C.

On the other hand, tests done at 80°C showed that the protective film contained higher contents of both calcium and iron (II) concentrations, than those measured for corrosion rates at 25°C. A similar precipitation rate trend is observed given that the bulk solution supersaturation controls the deposition of calcium carbonate scale at carbon steel and it is enhanced by the increase in temperature. Furthermore, the

222

amount of iron (II) released was within the same range, increasing slightly at higher bulk concentrations. This is quite interesting because it can be related to the ions competition to precipitate at the carbon steel substrate first. So, it can be concluded that the local surface supersaturation for iron products is accelerated by the increase in temperature. These results can explain the formation of $FeCO_3$ in a non-CO_2 saturated environment, at 80^oC as per SEM (7.3.2.2) and XRD (7.3.2.4) analysis.

7.3.5 Results Overview on Corrosion and Surface Scale Crystallization

In this section (7.3) several factors affecting corrosion and surface scaling mechanism and kinetics have been assessed and the key results can be summarised as follows:

- During corrosion processes in carbon steel, a drop in corrosion rates can be taken as the onset of nucleation and crystal growth;

- Temperature has a huge impact on the surface kinetics creating a local supersaturation for corrosion products to be formed;

- During protective film formation in saturated scaling brines, there is a competition between the iron (II) ions released from the metal with calcium ions present in the bulk. The testing parameters will determine the dominant phase to form;

- At 25^oC corrosion products were mainly Fe_2O_3 whilst at 80^oC $FeCO_3$ deposited due to its low solubility under these conditions.

- Calcium carbonate polymorphs were formed and changed over time according to flow rate, temperature and supersaturation;

- At later stages, surface scale can be removed from the RCE due to flow turbulence; and this may change the film protectiveness and affect the corrosion rates as it can increase again.

- Localized corrosion has been identified over different temperatures and results showed that protective film formation by scale can inhibit pits during general corrosion processes;

- The effect of pH on film precipitation and corrosion rates has been briefly explored;

- XRD confirmed that vaterite is the first layer of scale to form at 25°C and at 80°C more aragonite crystals are deposited elucidating the heterogeneous nucleation mechanisms and rough interface crystal growth for higher saturated brines.

- The estimation corrosion products deposition rate ($FeCO_3$ and Fe_2O_3) needs to be linked to mass changes measurements and interferometry analysis to provide a true representation of the film protectiveness.

7.4 CaCO$_3$ Surface Deposition and Bulk Precipitation

In this section, the surface and bulk crystallization kinetics is going to be assessed using the RCE set-up with stainless steel 316L. The key advantage of using stainless steel 316L for $CaCO_3$ growth kinetics studies is that its passive nature gives the steel a better protection against corrosion onset, hence, it enables better control of the $CaCO_3$ scaling process at steel surface without any interferences from the corrosion mechanistic reactions. Furthermore, bulk kinetic analyses will be presented and compared to those results obtained in Chapter 6.

7.4.1 Mass Deposition Rates on Stainless Steel 316L

Surface growth rate were determined considering the overall mass gain of $CaCO_3$ scale deposits spread around the RCE metallic surface over time.

Figure 7.35 illustrates the changes in mass deposition over time for a stainless steel RCE, at 25°C and 80°C.

It can be observed from the plots in Figure 7.35 that the overall mass deposition at 25°C is slower than at 80°C. Therefore, the amount of calcium carbonate deposits is expected to increase more rapidly over time at 80°C.

Remarkably, at lower supersaturation (1.52 – 4.77) very little difference is observed in the slope of these curves, and these seem to get a steadier growth after 6 hours due to a potential decrease in the local surface supersaturation. Conversely, at 25°C, the higher supersaturation case studies show an increase in mass suggesting that particles continue to grow and adhere to the stainless steel surface. An additional increase in the mass is observed after 12 hours saturation ratios between 4.77 and 55. Tests done at 80°C showed an identical trend, however a more retarded additional growth which happened around 18 hours for 4.77≤SR≤55.
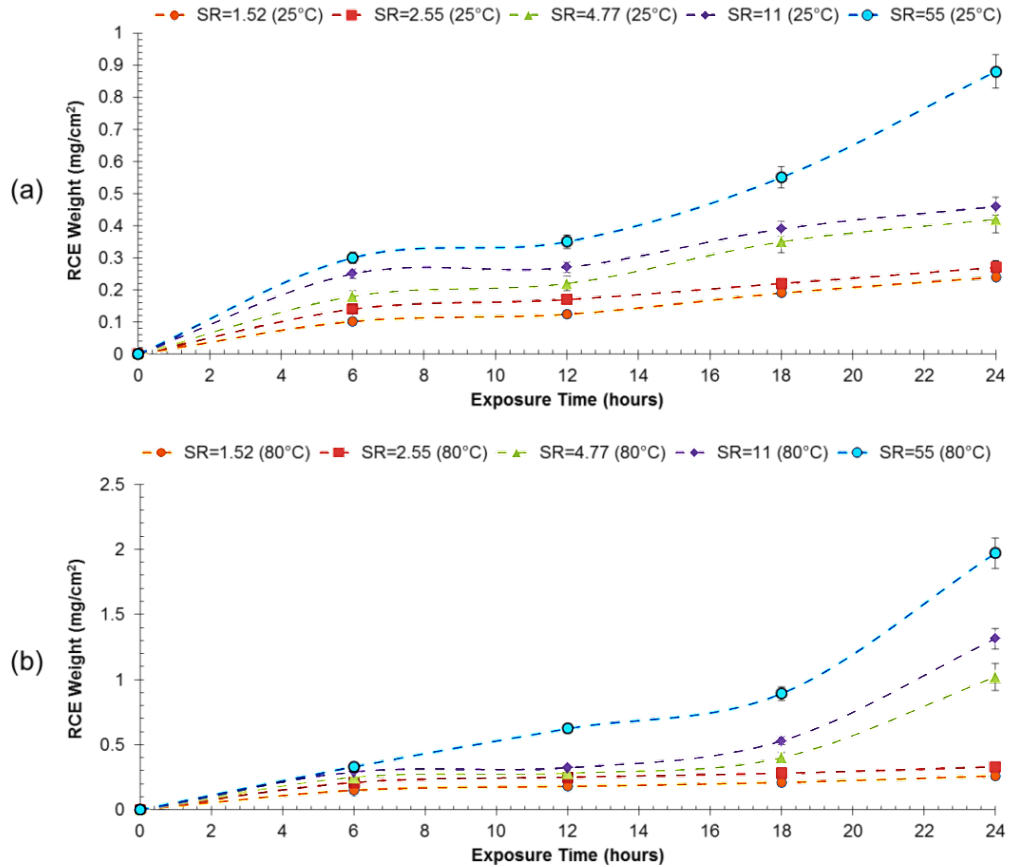
Figure 7.35: CaCO$_3$ deposition rates for a range of supersaturation on stainless steel 316L at: a) 25°C and b) 80°C

The overall surface growth rate (R$_{Gs}$ or G$_s$) was determined from the slope of the mass deposition (Figure 7.35) and results are summarised in Table 7.4.

Table 7.4: Surface mass growth rates as a function of supersaturation and temperature

SR	T (°C)		Number of repetitions, n
	25	80	
	R$_G$ (g/m^{2}s)	R$_G$ (g/m^{2}s)	
1.52	2.6E-09 ± 0.05	2.7E-09 ± 0.05	3
2.55	2.8E-09 ± 0.05	3.3E-09 ± 0.05	3
4.77	4.4E-09 ± 0.05	1.0E-08 ± 0.05	3
11	5.0E-09 ± 0.05	1.3E-08 ± 0.05	3
55	8.3E-09 ± 0.05	2.1E-08 ± 0.05	3

ICP analyses for calcium were taken at the end of the experiment, in order to quantify the scale deposited as a function of temperature and time, as shown in Figure 7.36.
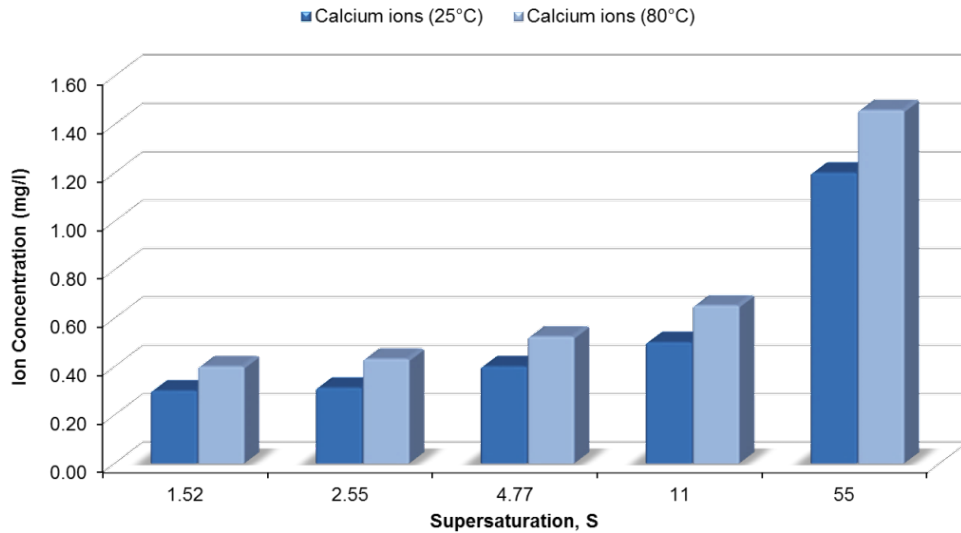
Figure 7.36: Representation of calcium ions concentrations identified via ICP on stainless steel samples tested at 25°C and 80°C

It is evident from Figure 7.36, the small amount of $CaCO_3$ scale formed on the metal surface after 24 hours of experiment. However, these results emphasised that the main difference in calcium content was registered essentially for higher supersaturation levels (i.e. 4.77 – 55) at 80°C, where more calcium ions were identified as a result of precipitation on the metal surface. These results are also in accordance with some previous work done by Morizot et al. (348), in which the heated rotating disc electrode (RDE) surface triggered an increase in the total amount of scale deposits from tap water.

7.4.2 Morphologies on Stainless Steel 316L

$CaCO_3$ crystals deposited at the stainless steel surface were characterized with respect to their shape and size using the SEM. Crystals deposited on the stainless steel formed a very thin and un-even film constituted solely of $CaCO_3$ crystals. Since the surfaces were smooth and no corrosion was happening during the scaling formation, fewer crystals were formed for the same supersaturation ranges in study.

Figure 7.37 shows an example of the crystal evolution throughout 24 hours, 25°C and 500rpm on a stainless steel RCE.
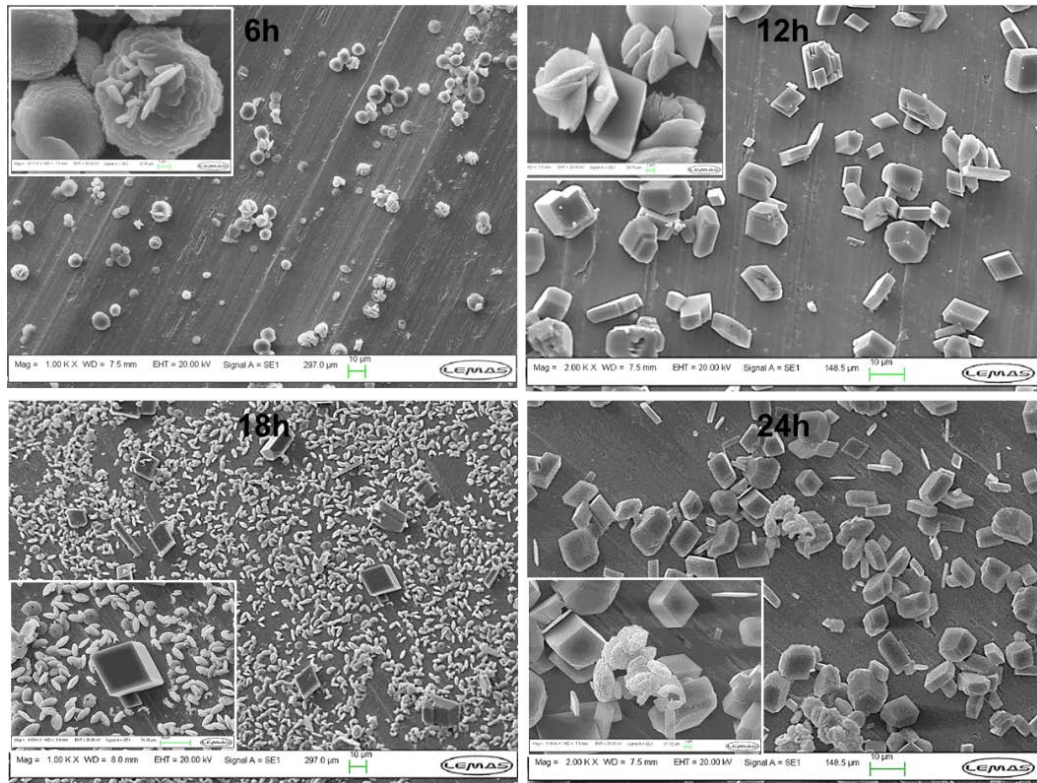
Figure 7.37: Changes in $CaCO_3$ surface crystals deposited on stainless steel over time for RCE at 500rpm, supersaturation 55, at 25°C

As illustrated in Figure 7.37, after 6 hours of reaction, sereal flower-like vaterite crystals of ±10μm size were deposited on the stainless steel substrate. After 12 hours, most of the vaterite seemed to have transformed into calcite (±10μm). Then at, 18 hours more half-moon like vaterite crystals showed up at the surface of the RCE, creating an even film containing small vaterite crystals (±2μm - ± 5μm) and big calcite crystals (±10μm - ± 15μm) and. Finally, after 24 hours, most of the vaterite crystals were fully grown (± 8μm) and redissolved to transform into bigger rhombohedral calcite (±10μm - ± 15μm). These changes in shape and size over time from an unstable to a more stable polymorphic form, suggest that the supersaturation was reaching the equilibrium conditions and subsequently the growth rate of the crystals was slowing reducing.

The general evolution of the polymorphs is quite similar to what has been observed during spontaneous bulk precipitation shown in Figure 6.34. However, particles formed at the surface appear to be slightly bigger than those formed in the bulk as shown by Figure 7.38, emphasising that heterogeneous nucleation took place at the surface. Furthermore, the fact that more vaterite crystals appeared after 12 hours also support the heterogeneous nucleation phenomena.
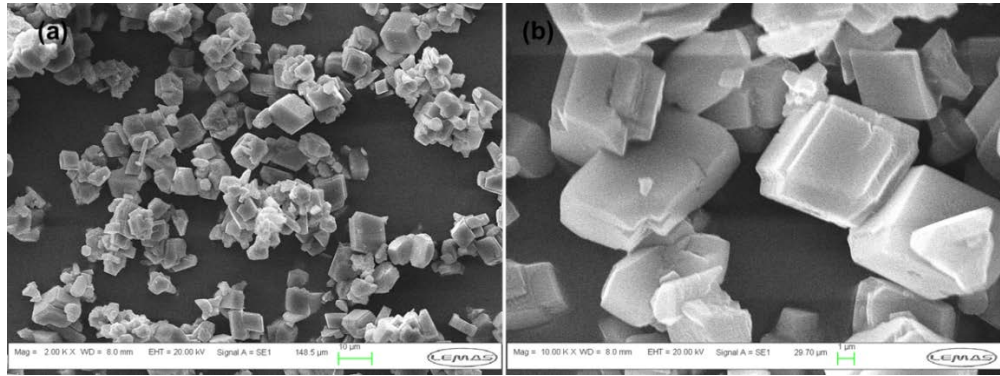
Figure 7.38: CaCO$_3$ bulk crystals collected from simultaneous surface and bulk crystallisation at 24 hours, for RCE at 500rpm, supersaturation 55, at 25°C

7.4.2.1 Effect of temperature and supersaturation

The effect of temperature on surface crystallisation was also investigated for characterising the shape and size of crystals at the end of the experiments (24 hours). These morphological changes at 25°C and 80°C are shown in Figure 7.39 – Figure 7.40.
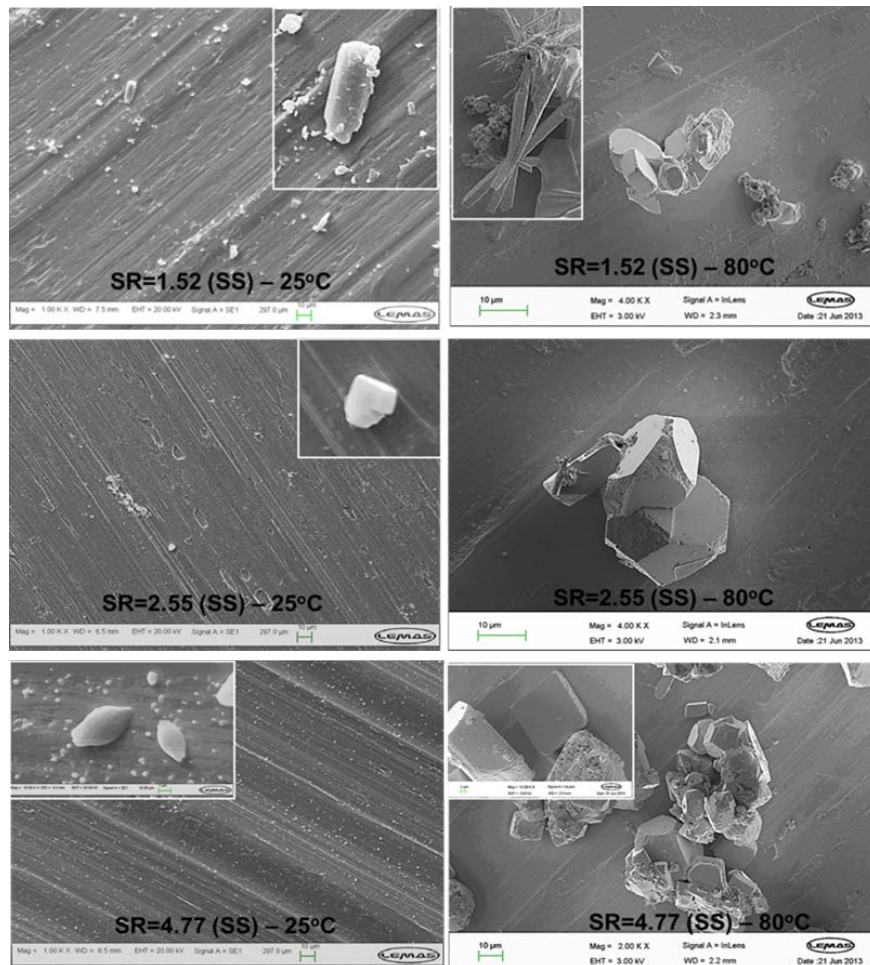
Figure 7.39: CaCO$_3$ surface crystals deposited on stainless steel for low supersaturation cases (1.52 ≤ S ≤ 4.77) after 24 hours and at different temperatures

At low supersaturation ranges (Figure 7.39), the increase in temperature affected not only the size of $CaCO_3$ polymorphs, but also their thermodynamic stability, converting less stable phases into more stable ones, as shown for supersaturation 1.52 and 4.77.

In the first example aragonite crystals transformed into calcite after 24 hours, whilst at supersaturation 4.77, moon-like vaterite crystals have all converted into rhombohedral calcite. Additionally, the increase in temperature affected the amount of $CaCO_3$ crystals deposited across the surface and some agglomeration is evident due to other surface interactions with the bulk crystals. It is worth noting that the flow rate plays a crucial factor during scale deposition and might be also controlling the growth kinetics at the stainless steel surface. Typically, a decrease in primary particle size, due to an increase in temperature, leads to an increase in the nucleation rate. This has been observed in this investigation and it supports the classical nucleation growth mechanisms as a consequence of more effective mixing at higher shear rates (313).

Figure 7.40 illustrates the final morphologies obtained at high supersaturation levels (11 – 55) at 25°C and 80°C, respectively. It can be observed that calcite remained the main crystal depositing at both temperatures. In addition, at SR=55 few vaterite crystals can be also observed at 25°C, however, as the temperature increased to 80°C, the stainless steel surface became more covered with calcite crystals and few traces of needle-like aragonite crystals were also observed.

In terms of particle size changes after 24 hours, there was not a significant variation. The overall crystal size ranged between ± 5µm and ±10µm. However, with increase in temperature more calcite crystals formed at the surface of stainless steel, providing more surface coverage. For SR=55, there was a slight reduction on the crystals size at 80°C (± 5µm - ±10µm) in comparison to those obtained at 25° (± 5µm - ±15µm). This is due to the high supersaturation in bulk solution and at the RCE surface at 80°C, leading to the formation of smaller particles which ten to agglomerate due to the kinetics under these conditions. Calcite crystals adhered to the surface displayed broken edges due to agglomerates formed in the bulk.
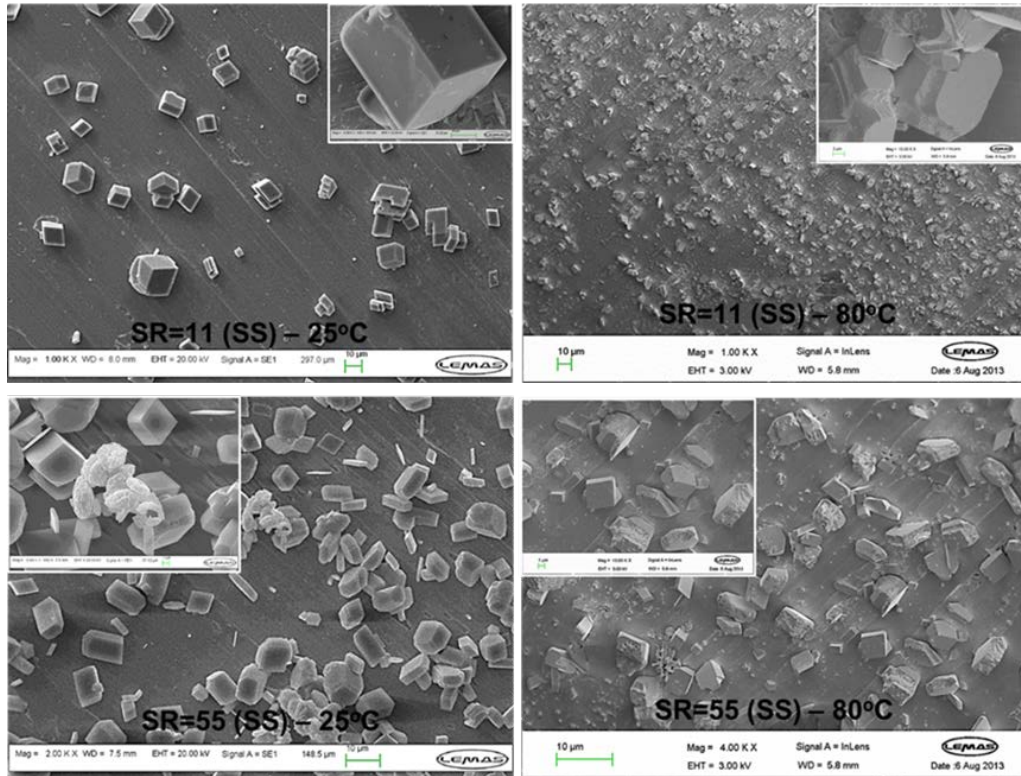
Figure 7.40: $CaCO_3$ surface crystals deposited on stainless steel for high supersaturation cases (11 ≤ S ≤ 55) after 24 hours and at different temperatures

7.4.3 XRD Analysis on Stainless Steel 316L

XRD technique was useful to help characterising the surface film deposit at the end of 24 hours-tests, for each supersaturation, (Figure 7.41 and Figure 7.42).
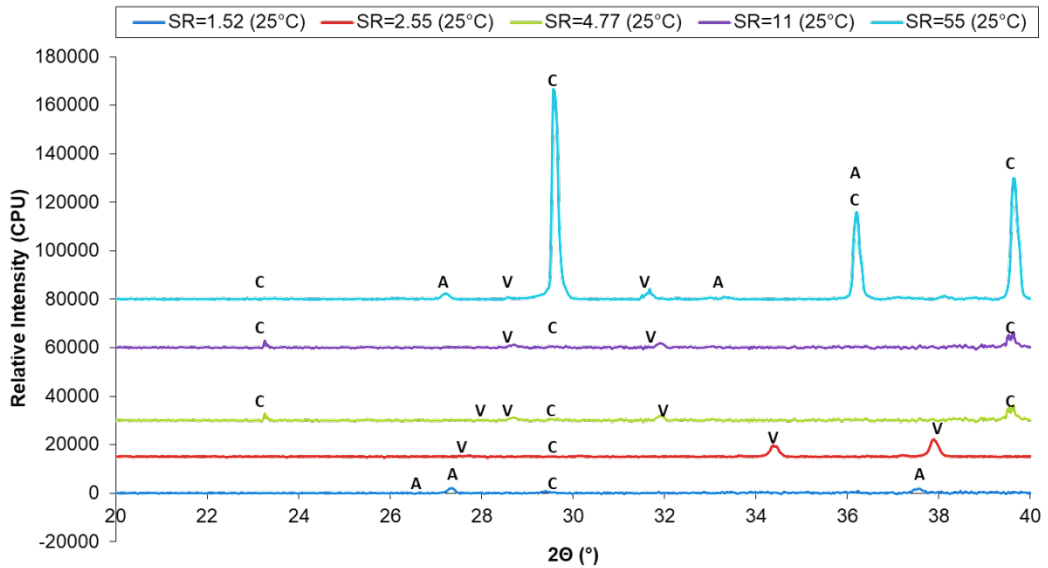
Figure 7.41: XRD patterns obtained ex-situ, for all RCE stainless steel samples at 25°C, after 24 hours. Key: C: calcite, V: vaterite, A: Aragonite. Arrows display some of the minor crystal phases and the relative intensity scale is arbitrary.
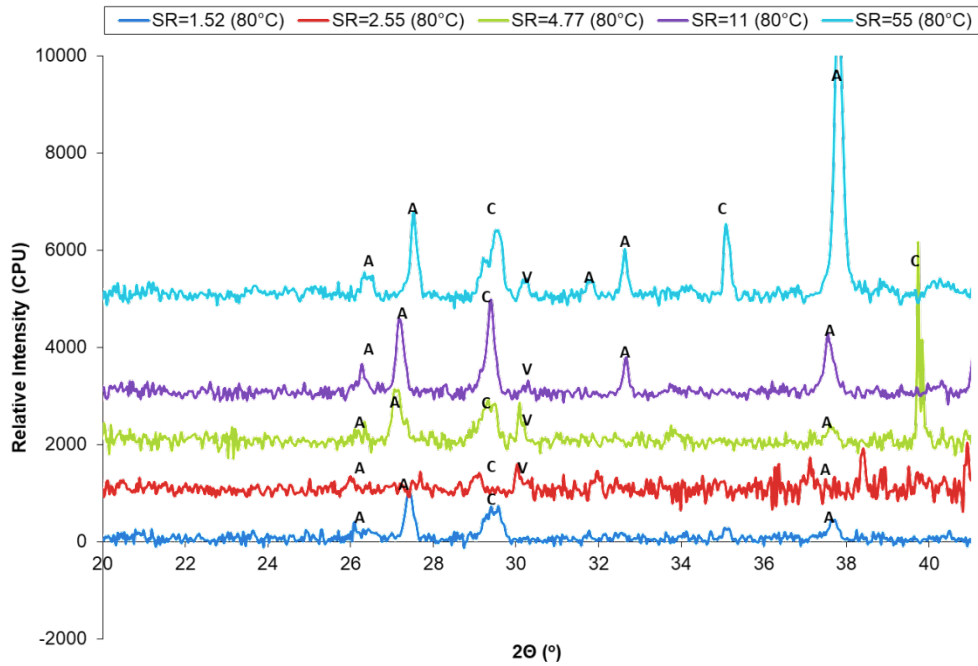
Figure 7.42: XRD patterns obtained ex-situ, for all RCE stainless steel samples at 80°C, after 24 hours. Key: C: calcite, V: vaterite, A: Aragonite. Arrows display some of the minor crystal phases and the relative intensity scale is arbitrary.

Figure 7.41 and Figure 7.42 illustrate the effect of temperature on surface deposition at stainless steel 316L. In general, it can be seen that vaterite and calcite are the most predominant crystals formed at 25°C, whilst aragonite and calcite are the most predominant phases at 80°C. Aragonite is commonly formed at higher temperatures so it was expected to precipitate mostly at 80°C.

Furthermore, a comparative analysis has been done for saturation ratio 55, at 25°C and 80°C (Figure 7.40). Results show that for the highest saturation ratio, no vaterite is identified at 25°C, but calcite and aragonite peaks are identified. This goes in agreement to the SEM images as the predominant phase observed was calcite and few tiny aragonite crystals. On the other hand at 80°C, calcite does not seem to be the predominant phase, as the aragonite peak (111) showed higher intensity. However, the peak's intensity might not necessarily quantify the amount of scale deposited. Alternatively, since SEM and XRD covered only a specific selected area of the RCE, it is possible that region of the sample contained more aragonite crystals than calcite.
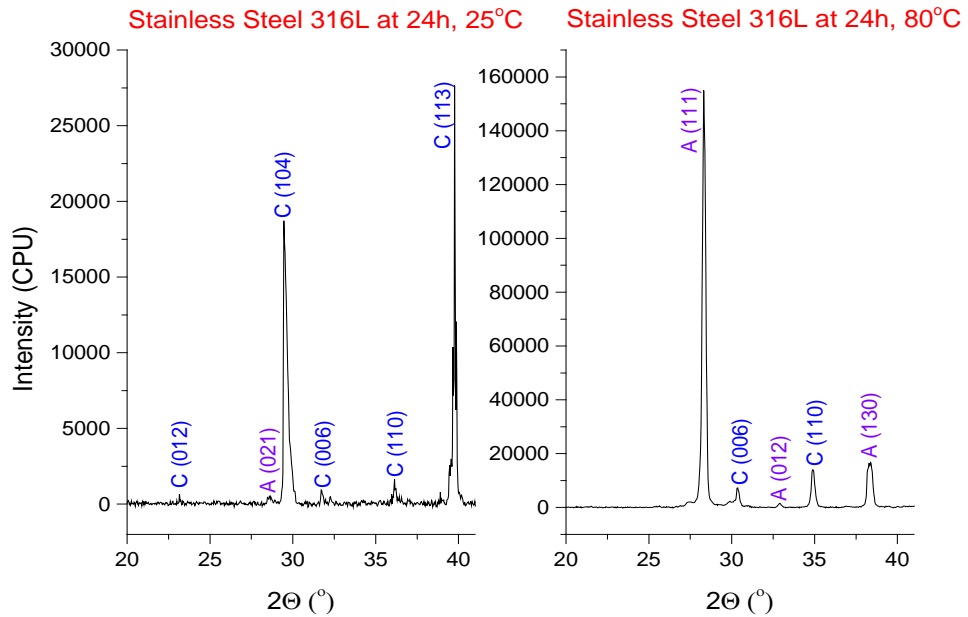
Figure 7.43: Comparison of CaCO$_3$ phases deposited on stainless steel after 24 hours, at different temperatures

Overall, stainless steel samples at ambient temperature were dominated by calcite crystals and some aragonite, but with temperature increase more aragonite phases have been detected suggesting a possible transition of calcite into aragonite or just an increase in aragonite as shown by the SEM images.

7.4.4 Effect of Hydrodynamics on Scale Deposition

One of the main advantages for using the RCE consists of permitting control of the flow rate during scale and corrosion processes, facilitating predictions for the real field in a laboratory scale.

In this study, the effect of flow velocity on surface scale deposition has been investigated over a range of Reynolds numbers as described in Table 5.3, simulating different levels of turbulent flow conditions.

It is generally known that like temperature, the flow velocity will have an effect on the deposition kinetics and changes in the morphology of CaCO$_3$ crystals deposits.

Figure 7.44 displays results showing the effect of flow rate as a function of supersaturation and time. The selected flow velocities varied between 300rpm to 3000rpm and tests were performed at 80°C where more scale deposition is expected.
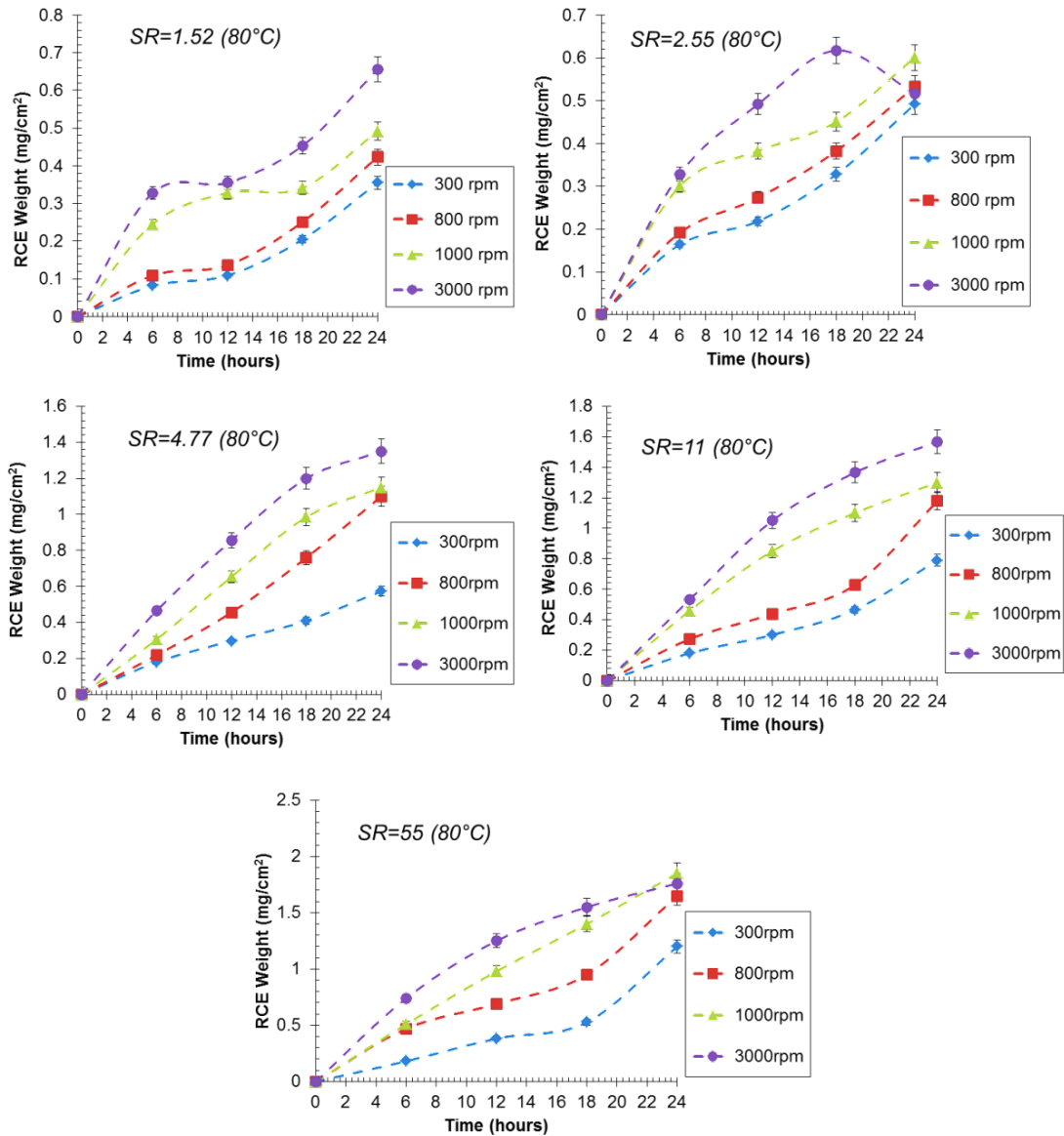
Figure 7.44: Effect of RCE velocity on SS 316L surfaces at 80°C over time, without application of electrical potential

Overall, it can be seen from Figure 7.44, that as the RCE speed increases the amount of scale deposited also increases. This is in good agreement with previous studies done for fouling on heat exchangers (349) (350), in which the mass of scale deposits increased with the flow hydrodynamics. As a consequence, a decrease in the crystal growth can also be observed at higher supersaturation levels due agglomeration at the surface leading to crystals transportation from the surface to the bulk solution.

Figure 7.45 illustrates examples of the $CaCO_3$ surface crystals formed under different regions of turbulence. SEM analyses correspond to the two lowest supersaturation case studies at 24 hours and 80°C.
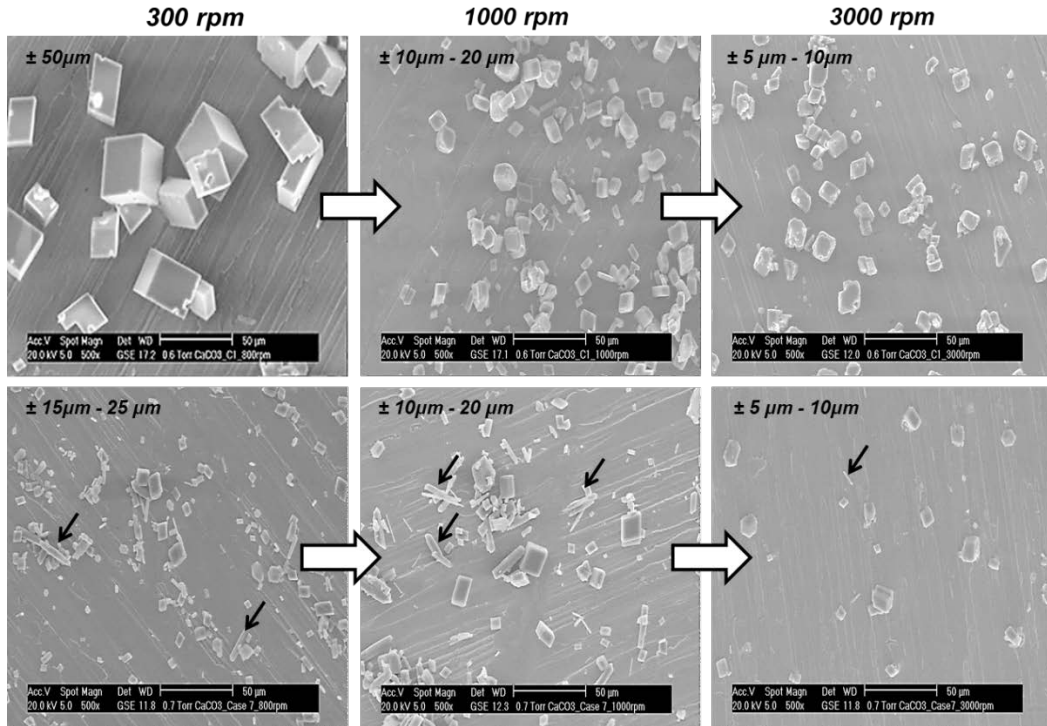
Figure 7.45: Effect of flow hydrodynamics on CaCO$_3$ deposition in SS 316L at 80°C, 24hours

It is noted that for SR=1.52 at 300rpm, well faceted rhombohedral crystals are deposited on SS 316L at the end of the test. When there is an increase in flow rates from 300rpm to 3000rpm, more calcite crystals appear to nucleate and grow at the surface of the metal, however their sizes seem to reduce significantly from 300rpm (± 50µm) to 1000rpm (± 10µm - 20µm) and then 3000rpm (± 5µm - 10µm).

Furthermore, at SR=2.55, the biggest crystals are obtained at the lowest flow rate. A mixture of rhomboheadral calcite and aragonite needle-like crystals (pointed with dark arrow in Figure 7.45) is observed at flow rates between 300rpm to 1000rpm. However, after 24 hours at 3000rpm, less calcite and aragonite needle crystals are adhered to the stainless steel surface. This may suggest that critical flow turbulence has been reached and particles are removed from surface to the bulk solution. In fact, if observing the mass deposition for case 2 in Figure 7.44, the same effect in drop of mass is observed. It can be conjectured that at extremely high flow rates, the dominant mechanism is diffusion-controlled thus more crystals are seen in bulk rather than at surface of the stainless steel.

It is worth noting that size characterisation based on SEM only gives an idea of the particle distribution across the surface area being analysed, it assumed that similar morphologies are found all over the metallic cylinder.

This information can be useful for predicting morphologies without performing experiments for a wider range of supersaturation regions. It seems that both crystal growth mechanisms and polymorphism will strongly depend on temperature and flow conditions when growing on stainless steel surfaces. Supersaturation continues to be the key driving force for crystallization, however, these two other parameters must be considered with the same relevance.

The relationship of different parameters on surface crystallisation deposition can be summarised by Figure 7.46.
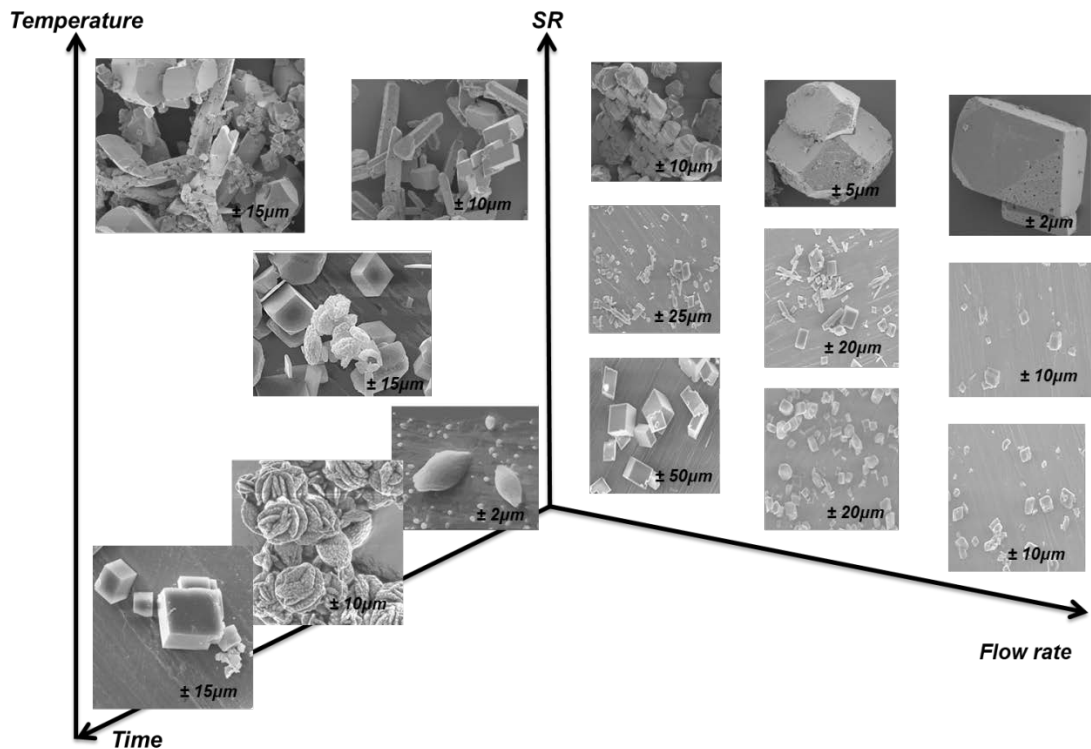
Figure 7.46: Summary of effects of supersaturation, temperature, time and flow hydrodynamic on $CaCO_3$ deposition in SS 316L

In the diagram above, it can be seen that at constant supersaturation the crystals deposited on stainless steel start growing from the least thermodynamic stable polymorph (i.e., vaterite) and slowly progress to calcite crystals. If temperatures are increased a polycrystalline surface is covered by different polymorphs but typically from the results obtained in this investigation, crystals would transform from vaterite to calcite and depending on the local supersaturation at the stainless steel, some of the calcite would convert to aragonite. Lastly, to summarise the effect of flow rate, it was observed that the higher the flow rate the fewer deposits were left at the surface of stainless steel. The strong possibility for this is due to hydrodynamic forces that

would remove scale over time from the stainless steel surface. Furthermore, high turbulence showed an impact on the reduction of particles over time.

7.4.5 Re-assessment of Bulk Crystallization Process

Samples from the bulk of crystallizing solutions with stainless steel RCE immersed were analysed post tests and results via SEM, XRD and particle size distribution (Mastersizer). Results shown in Figure 7.47 illustrated that kinetics occurring simultaneously with a passive metal are faster at the bulk solution, and therefore, the bulk precipitation kinetic results did not appear to be much different from the crystallizations using a batch reactor. It is worth noting that for carbon steel X-65 the bulk and surface interactions would be stronger and the deposition and precipitation rates are much faster due to corrosion reactions.

To summarise, the final check of crystal properties during the simultaneous precipitation and deposition (on stainless steel) experiments, concluded that the mechanisms of bulk crystallization are dominant (in absence of corrosion), and that scale deposition is mostly done by adhesion mechanisms rather than heterogeneous nucleation. Furthermore, this elucidates the fact that in absence of corrosion, the surface crystallisation mechanisms on stainless steel are identical to the bulk solution, as particles are typically transported from solution and adhered to the surface, rather than nucleating directly at the surface of the metal. This mechanism is more diffusion controlled rather than surface controlled.
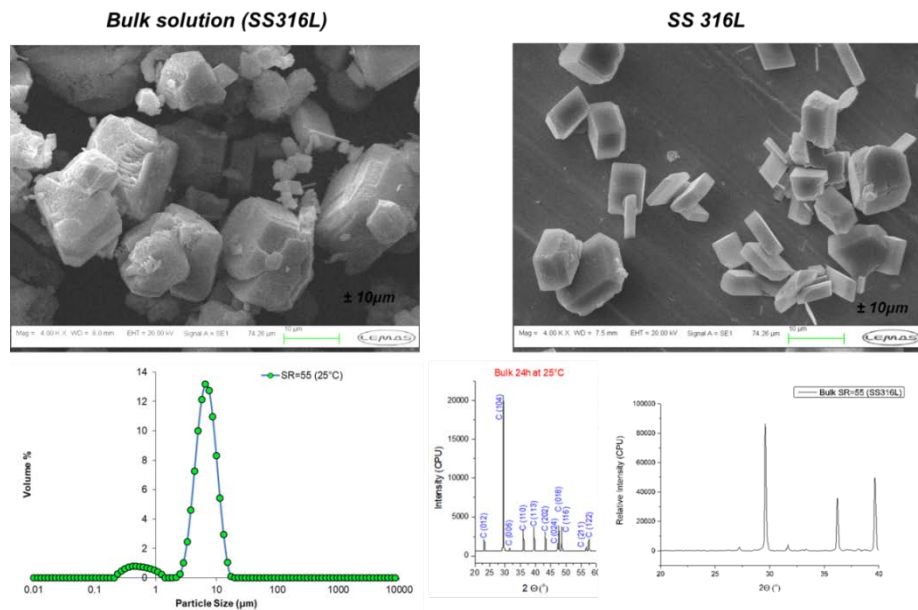
Figure 7.47: Bulk vs Surface crystal characterization for case 5 (SR=55) at 25°C

Lastly, the studies done in two different substrates elucidated the mechanisms involved during simultaneous scale and corrosion processes; emphasizing the importance of the nature of the substrate during $CaCO_3$ crystallization processes. The nucleation kinetics using carbon steel is much faster than using stainless steel. Therefore, $CaCO_3$ scale crystallization at stainless steel appears to provide identical nucleation and crystal growth kinetics as those encountered in the bulk of solution. This is due to the reactive crystallization process driven by diffusion-controlled reactions rather than a surface-controlled interaction as it was observed when carbon steel X-65 was utilized.

7.5 Closing Remarks

In this chapter a parametric study liking corrosion and surface scale deposition process was examined as a function of several factors such as: supersaturation, time, temperature, flow rates and metal surface.

Results have shown that surface crystallization of $CaCO_3$ in presence of corrosion over time is a complex process and depends on many factors other than the bulk supersaturation. The reason being that supersaturation is the thermodynamic driving force and not a kinetic parameter. Surface kinetics is dependent on several factors from surface roughness to type of metal and these may affect significantly the deposition rate over time.

The effect of flow rate has been assessed and results have shown that the higher the flow velocities the faster are the corrosion kinetics. However, the type of film formed was also affected by the increase in flow. Tests done on both carbon and stainless steel showed that for highly turbulent flow, some of the crystals can be removed from the steel surface over long periods of time.

Temperature showed a very strong influence on film formation kinetics for all case studies. At lower temperature no $FeCO_3$ was formed, but Fe_2O_3 was identified by XRD and $CaCO_3$ deposits were predominant across the samples. However, at higher temperature, a mixture of iron deposits with $CaCO_3$ crystals was observed in particular for the highest saturation ratio brines. This indicated that the local supersaturation created at the carbon steel surface promoted the deposition of $FeCO_3$ prior to adhesion of $CaCO_3$. This can also be linked to the fact that $FeCO_3$ is less soluble than $CaCO_3$ at high temperatures.

Crystal growth rate could be determined for corrosion products and scale products using Nesic and Sun model for $FeCO_3$ and cross-relating it to mass deposition rates. Results have shown that in presence of corrosion some mass gain can be observed however localized corrosion can be formed even when a film is relatively protective.

A film pathway has been proposed for samples deposited on stainless steel, in which the effect of flow velocity, supersaturation, temperature and time are clearly affecting the size, shape and amount of scale deposited over time.

Overall, the studies here presented emphasized the fact that thermodynamic predictions are not sufficient to simulate the scaling tendency at metal surfaces. This is due to the strong ionic and mechanistic interactions between bulk and surface components. This conclusion is of extreme relevance to the oilfield industry since mineral scale and corrosion processes tend to take place simultaneously. Therefore, it is crucial to implement the semi-empirical kinetic equations used in this study into the commercially available thermodynamic prediction software. This will result in a more accurate scale threat prediction and optimization of current treatment techniques used in the oil and gas facilities.

Chapter 8 - Conclusions and Suggestions for Future Work

Summary

This last chapter summarises the main results and outcomes from this research work, together with the re-assessment of the thesis aims and objectives and finishes with some suggestions for future work to be continued in this area.

8.1 Introduction

The work carried out in this PhD is a combination of modelling and experimental approaches to broadening the literature understanding on $CaCO_3$ crystallization processes and development of kinetic parameters that can be implemented in current commercially available thermodynamic scale prediction simulators, such as the MultiScale^{TM}.

The experimental analyses are conducted in dynamic conditions over a range of supersaturation and temperatures. These studies were subcategorised into $CaCO_3$ bulk spontaneous crystallization and surface crystallization processes; in order to better understand the mechanisms and kinetics involved during $CaCO_3$ precipitation and deposition. As part of this investigation, several theories were reviewed and implemented to assess the mechanistic surface approaches and characterize of growth of crystals over time. The modelling analyses intended to complement the experimental work carried out and provide a link between solution's speciation with kinetics involved during $CaCO_3$ bulk precipitation.

8.2 Conclusions of the Study

Each chapter plays an important part in this thesis and they are interdependent. The MultiScale modelling data was useful to create new brine compositions based on real field data and provide understanding of models behind thermodynamic prediction tools. Furthermore, the nucleation and crystal growth results obtained from spontaneous bulk crystallization in chapter 6 were useful to validate the thermodynamic prediction software and link experimental kinetic data to reassess the changes in supersaturation over time. In addition, results from surface crystallization processes provided insights into the different mechanisms that can take place during simultaneous processes of bulk precipitation and scale deposition/corrosion. Lastly, the assessment of different kinetic mechanisms enabled understanding in detail the effect of crystallizing environments on crystal's morphologies, size and stability. The findings of this PhD are summarised as follows:

8.2.1 Instrumentation for bulk and surface kinetics

A series of effective *in-situ* process analytical tools have been used to create a robust method development for characterising the early stages of crystallisation, i.e., measuring induction times for a range of low to high saturation brines. These tools

included pH electrode, ion selection electrode for detecting free calcium ions in solution, light transmittance turbidity probe and FBRM. It was concluded that for the range of supersaturation cases in study, the pH and calcium ion probes showed most consistent and reproducible results. Furthermore, several novel ex-situ techniques were used to characterise the crystals with regards to size (Mastersizer, Sysmex, and SEM), shape (SEM/EDXS) and internal structure (XRD). Furthermore, the spontaneous bulk crystallization was performed using a batch reactor whilst the combined bulk and surface crystallization studies were performed using the RCE. One of the key advantages of the RCE is that it can be efficienty run at high shear rate conditions, using a semi-batch system.

All of these apparatus together enabled studying and understanding the effects of processing conditions (supersaturation, temperature, flow rate, metal substrate, etc) on bulk and surface crystallization processes.

8.2.2 Nucleation & Growth Kinetics

The induction time for bulk crystallization was determined via in-situ measurements of calcium ions and pH. This combined method enabled acquiring and processing data for directly determining the de-supersaturation of solutions during the crystal growth process. To achieve that, experimental pH (carbonate ions determined via CO_2 equilibrium for a known pH) and calcium results were inserted in a thermodynamic software (MultiScale), and the resultant solution supersaturation was calculated. Therefore, the changes in bulk supersaturation during the crystallization process were determined as a function of time and the crystal evolution during this stage was analysed via SEM and XRD experiments. A robust model was created using modelling and experimental data to understand the kinetics of $CaCO_3$ in-situ.

The induction time data acquired showed an inversely proportional relationship to supersaturation. Furthermore, an increase in temperature suggested a decrease the measured induction time. However, this behaviour is particularly noticeable for lower saturated brines. These results are in agreement with the classic nucleation theory.

Table 6.6 to Table 6.9 present the induction periods determined by both pH and calcium ions tracking. The observations implied a slower nucleation rate for the low saturated brines, as opposed to faster nucleation rates for the higher saturated brines. For the lowest saturated brines, a thorough investigation of the induction time has been completed with help of post-test analyses such as SEM and Sysmex for detection of particle size over time. The pH method did not provide the expected

accuracy at low supersaturation, since changes in the bulk during crystal growth (i.e. detection of H^+ from dissociation of bicarbonate ions) could not be measured indirectly through pH.

The nucleation kinetics were determined via classic nucleation theory semi empirical equations and the respective calculated interfacial energies were found to be in the range of $0.92 *10^{-3}$ J/m^2 to $25.46*10^{-3}$ J/m^2 for a range of temperatures and saturation ratios. It was noted that the higher the temperature, the higher was the interfacial tension suggesting that mechanisms at higher temperature become more surface controlled (2D nucleation).

The effect of supersaturation and temperature on crystals morphology was also studied. Results have shown that vaterite tends to precipitate first both in bulk and at carbon steel surfaces. However, results from bulk experiments showed that after 24 hours all vaterite crystals transform into calcite. Conversely, experiments done in carbon steel have shown that vaterite, aragonite and calcite can co-precipitate at the same conditions. For lower saturated brines, the spiral growth mechanism (B&S model) appeared to be predominant, however for the higher saturated brines it was 2D nucleation.

In relation to particle shape and size, there was a clear observation that factors such as temperature and supersaturation dictate the final shape and size under specific conditions. So, at lower temperatures and at lower supersaturation conditions (Figure 6.30 to Figure 6.32), vaterite crystals would be the first ones to form followed by calcite crystals. Different shapes for vaterite have also been observed, some looking more flower-like and other looking more spherical crystals. When overgrown, vaterite crystals tend to become flat disc like particles and possessing a hollow typically in the centre due to local dissolution at the surface of the crystals. An increase in supersaturation showed to increase the amount of calcite formed at earlier stages of crystal growth as seen in Figure 6.33 and Figure 6.34.

As expected the increase in temperature contributed to the formation of more bulk crystals for the all supersaturation studied. Furthermore, at higher temperatures, in particular 80°C was observed the appearance of some aragonite needle-like crystals next to calcite crystals. Aragonite crystals have been known for remaining stable at high temperatures.

For growth rate analyses, the data was separated in two parts: low and high supersaturation, since this study covered two extremes of supersaturation. The calculated growth rates were plotted assuming surface controlled kinetics. The

values of the growth rate constants were extrapolated from the slope of the resulting straight lines and are summarised in Table 6.21. The results obtained were relatively smaller than those reported by Kralj et al (1990) at 40°C, however close to those reported for CaCO$_3$ precipitation in solution by Ellen and Mullin.

8.2.3 Bulk Precipitation versus Surface Deposition

Studies on surface kinetics were done as a function of the following parameters: bulk solution supersaturation, temperature, metal substrate, pH, flow rate and time. All of these factors have shown different mechanisms depending on testing parameters / conditions. Combining these results it could be concluded that the type of metal will strongly affect the bulk and surface interactions. For instance, corrosion and scale deposits were formed at low and high temperatures for carbon steel tests, whilst for stainless only CaCO$_3$ deposited at the surface.

This part of the work brings novelty as it is the first to show a parametric approach for understanding surface kinetics due to scale deposition and corrosion processes happening simultaneously. Two different metals have been selected for this study: carbon steel and stainless steel. Besides being two common industrial materials used in oilfield facilities, these provide the advantage of enabling assessing scale deposition on its own if using the stainless steel. Stainless steel is a passive metal and protects the surface against corrosion, for that reason no corrosion was observed during the tests.

The protective film must be characterized using other techniques than mass deposition to determine if it temporarily protects against corrosion or not. Interferometry analyses have shown identical peak depths at different temperatures. However, at 80°C the general corrosion rate was dropped to significant low values and remained stable, suggesting no corrosion threat was posed to the metal substrate.

High turbulent flow has been shown to increase the corrosion at the carbon steel and reduce the amount of scale deposits covering the metal substrate.

FeCO$_3$ appears to be more stable at higher temperatures when corrosion takes place in a non-CO$_2$ saturated environment.

The combined scale and corrosion processes enabled understanding that predicted scaling tendencies do not take into account the surface chemistry of steel (i.e., ferrous ions released from the metal), and therefore, the initial bulk saturation

tendency predicted may become less accurate if corrosion processes also occur simultaneously. For that reason, the model reviewed by Nesic has also been used to predict the rate of precipitation at the metal based on ions loss during corrosion. However, these models need to be combined and support both thermodynamic and kinetic aspects from bulk to surface and vice versa.

8.3 Review of Thesis Aims and Objectives

In accordance with the initial aims and objectives, this study has developed a robust method to investigate the influence of solution chemistry (e.g. composition and pH) on the formation, transformation and structure of calcium carbonate phases crystallising simultaneously in bulk solution (i.e. precipitation) and at metal surfaces (i.e. deposition). The experimental data was linked and rationalized with semi-empirical mathematical models for both bulk and surface crystallization theories and also with the thermodynamic scale prediction tool. This enabled obtaining an *in-situ* de-saturation profile and the crystal evolution pathways for the system in study could be assessed.

8.4 Relevance to the Academia and Industry

This study provided detailed knowledge on mechanistic approaches to understand the process of $CaCO_3$ scale formation and propagation in flowing systems. From the academic point of view, additional data is given as a function of critical crystallising parameters and this can be used to either validate similar studies. Furthermore, the kinetic and mechanistic models proposed new evolution pathways as a function of substrate and flow rate. The semi-empirical equations used to extract knowledge on crystallisation can be implemented to complement the current thermodynamic predictive softwares.

8.5 Limitations of this Study and Future Work Suggestions

This study has highlighted some important aspects about $CaCO_3$ simultaneous bulk precipitation and deposition kinetics. However a few implementations can be given for future work and these are proposed as:

- Assessment of bulk and surface kinetics and mechanisms in a continuous flow rig, instead of batch units for obtaining better approaches to the real field. This rig could be similar to a typical tube flow rig but assessment of scale should still be *in-situ* with focus on the same parameters such as temperature, substrate, pH, composition, flow rates, pressure and deposition rates, online XRD;

- Perform in-situ synchrotron X-ray diffraction (e.g., SAXS/WAXS) to assess nucleation and crystal growth for low saturated brine cases;

- Further studies of surface kinetic parameters such as wettability (contact angle), surface roughness, chemical composition, ductility and hardness to improve the understanding of scale formation an adhesion over a range of several metallic surfaces;

- Study the effect of scale inhibitors on deposition and precipitation for iron and calcium carbonate scale types;

- Carry on with molecular simulations of bulk nucleation for understanding the stability of three main polymorphs of $CaCO_3$ and results suggested that vaterite can be a metastable form during nucleation, leaving aragonite as the thermodynamically unstable and calcite remained stable

- With help of GULP optimise clusters with spherical radius for 5Å, 10 Å, 15 Å and 20 Å for each of calcium carbonate polymorphs: calcite, vaterite and aragonite.

Overall these are the main suggestions and main part of the work should focus on the design of an appropriate rig with continuous flow and made out of metals, which can have temperature, pressure, composition control via adapted specific probes such as pH, and that can be transported to a synchrotron facility for online X-ray diffraction. It seems that once these conditions are all put together, a proper kinetic and mechanistic model can then be created with help of physical and mathematical fundamentals.

References

1. Lucky, M. and Rogers, R. *Alternative Energy and Fuel News: Oil is Still World's Largest Energy Source, But Coal and Natural Gas are Gaining.* [Online]. 2013. [Accessed].

2. (EIA), E.I.A. *U.S Energy Information Administration.* 2013. Available from: http://www.eia.gov/forecasts/ieo/more_highlights.cfm

3. EP, T. *Offshore Profond - Control of very difficult conditions of deep.* 2012. Available from: http://total.com/fr/total-offshore-profond

4. EP, T. *Unconventional Gas - Resources for the future, Challenges.* 2012. Available from: http://total.com/en/brochure-gnc-en

5. Demadis, K.D., Mavredaki, E., Stathoulopoulou, A., Neofotistou, E. and Mantzaridis, C. Industrial water systems: problems, challenges and solutions for the process industries. *Desalination.* 2007, **213**(1-3), pp.38-46.

6. Crabtree, M., Eslinger, D., Fletcher, P., Johnson, A. and King, G. Fighting Scale—Removal and Prevention. *Oilfield Review.* 1999, pp.30-45.

7. Frenier, W. and Ziauddin, M. A Multifaceted Approach for Controlling Complex Deposits in Oil and Gas Production. *SPE Annual Technical Conference and Exhibition.* 2010, (SPE 132707), pp.1-24.

8. Moghadasi, J., Jamialahmadi, M., Müller-Steinhagen, H. and Sharif, A. Scale formation in oil reservoir and production equipment during water injection (kinetics of $CaSO_4$ and $CaCO_3$ crystal growth and effect on formation damage). *SPE International Oilfield Scale.* 2003, (SPE 82233), pp.1-12.

9. Dake, L.P. *Fundamentals of reservoir engineering.* First ed. London: Elsevier Science, 1978.

10. Moghadasi, J., Jamialahmadi, M., Müller-Steinhagen, H. and Sharif, A. Formation Damage Due to Scale Formation in Porous Media Resulting From Water Injection. *Proceedings of SPE International Symposium and Exhibition on Formation Damage Control.* 2004, pp.1-11.

11. Kroger, G., Pietsch, J. and Ufermann, K. *Environmental management in oil and gas exploration and production.* First ed. Oxford: Words and Publications, 1997.

12. Demadis, K.D., Mavredaki, E., Stathoulopoulou, A., Neofotistou, E. and Mantzaridis, C. Environmentally benign chemical additives in the treatment and chemical cleaning of process water systems: Implications for green chemical technology. *Desalination.* 2007, **213**(1-3), pp.257-265.

13. Ltd, B.H. *Flow Assurance Mineral Scale* [Online]. 2013. [Accessed]. Available from: https://www.bhge.com/products-services/upstream

14. Mullin, J.W. *Crystallization.* Fourth ed. Butterworth-Heinemann, 2001.

15. Jones, A.G. Design of crystallization process systems. In: *Crystallization Process Systems.* Oxford: Butterworth-Heinemann, 2002, pp.261-298.

16. Simkiss, K. Variations in the crystalline form of calcium carbonate precipitated from artificial sea water. *Nature.* 1964.

17. Bravais, M.A. *Etudes Cristallographiques.* Paris: Gauthier-Villars, 1866.

18. Hammond, C. *The Basics of Crystallography and Diffraction.* Third ed. Oxford: Oxford university Press, 2009.

19. Riedel, D. International tables for X-Ray crystallography. *Acta Crystallographica Section A Structural Science.* 1983, **39**.

20. Kashchiev, D. and van Rosmalen, G.M. Review: Nucleation in solutions revisited. *Crystal Research and Technology.* 2003, **38**(78), pp.555-574.

21. Roberts, K.J. *Understanding, Modelling and Predicting of Crystallisation and Precipitation on a Structural Basis.* University of Herriot-Watt, 1996.

22. Guinier, A. *X-Ray Diffraction in Crystals, Imperfect Crystals, and Amorphous Bodies.* NY: Dover Publications, Inc., 1994.

23.   Galwey, A. *Chemistry of solids : an introduction to the chemistry of solids and solid surfaces.* London: Chapman & Hall, 1967.

24.   Roelands, M.C.P. *Polymorphism in Precipitation Processes.* PhD. thesis, Delft University of Technology, 2005.

25.   Haleblian, J. and McCrone, W. Pharmaceutical applications of polymorphism. *Journal of pharmaceutical sciences.* 1969, **58**(8), pp.911-929.

26.   Bernstein, J., Davey, R.J. and Henck, J.-O. Concomitant Polymorphs. *Angewandte Chemie International Edition.* 1999, **38**(23), pp.3440-3461.

27.   Kashchiev, D. and Sato, K. Kinetics of crystallization preceded by metastable-phase formation. *The Journal of Chemical Physics.* 1998, **109**(19).

28.   Hammond, R.B., Pencheva, K. and Roberts, K.J. Structural variability within, and polymorphic stability of, nano-crystalline molecular clusters of l-glutamic acid and D-mannitol, modelled with respect to their size, shape and 'crystallisability'. *CrystEngComm.* 2012, **14**(3), pp.1069-1082.

29.   Bogdanowicz, M.J., Posner, G.H., Brunelle, J., Nozaki, H., Sterling, J.J., Dutra, G.A., Rapoport, H., Achiwa, K., Corey, E.J. and Matsui, M. Determining of Gibbs Energies for solid-solid phase transitions in electroche,ical double cells without liquid junction: calcite, aragonite and vaterite. *Journal of American Chemical Society.* 1976, **98**(8), pp.2364-2365.

30.   Laird, T. Handbook of Batch Process Design Edited by P. N. Sharratt. *Organic Process Research & Development.* 1998, **2**(4), pp.280-280.

31.   Garekani, H.a., Sadeghi, F., Badiee, a., Mostafa, S.a. and Rajabi-Siahboomi, a.R. Crystal habit modifications of ibuprofen and their physicomechanical characteristics. *Drug development and industrial pharmacy.* 2001, **27**(8), pp.803-809.

32.   Libbrecht, K.G. *The Snow Crystal Morphology Diagram.* [Online]. 2013. [Accessed 23/08/2014]. Available from: http://www.snowcrystals.com/science/Snowflake%20Morphology2.jpg

33.   Stahl, P.H. and Wermuth, C.G. *Handbook of Pharmaceutical Salts Properties, Selection and Use.* Zurich: Verlag Helvetica Chimica Acta, 2002.

34.   Myerson, A. *Handbook of Industrial Crystallization, Second Edition.* Butterworth-Heinemann, 2002.

35.   Yang, G., Kubota, N., Sha, Z., Louhi-Kultanen, M. and Wang, J. Crystal Shape Control by Manipulating Supersaturation in Batch Cooling Crystallization. *Crystal Growth & Design.* 2006, **6**(12), pp.2799-2803.

36.   Mersmann, A. Crystallization Technology Handbook. *Drying Technology.* 1995, **13**(4), pp.1037-1038.

37.   Klein, D.H. Kinetics of precipitation (Nielsen, Arne E.). *Journal of Chemical Education.* 1965, **42**(5), p.A428.

38.   Wagner, C. Kinetik der Phasenbildung. Von Prof. Dr. M. Volmer. (Bd. IV der Sammlung „Die chemische Reaktion", herausgegeben von K. F. Bonhoeffer.) XII und 220 S. Verlag Th. Steinkopff, Dresden und Leipzig 1939. Preis geh. RM. 19,—, geb. RM. 20,—. *Angewandte Chemie.* 1939, **52**(30), pp.503-504.

39.   Becker, R. and Döring, W. Kinetische Behandlung der Keimbildung in übersättigten Dämpfen. *Annalen der Physik.* 1935, **416**(8), pp.719-752.

40.   Kashchiev, D. Toward a better description of the nucleation rate of crystals and crystalline monolayers. *The Journal of Chemical Physics.* 2008, **129**(16), p.164701.

41.   Kashchiev, D. Nucleation. In: van der Eerden, J.P. and Bruinsma, O.S.L. eds. *Science and Technology of Crystal Growth.* Dordrecht: Springer Netherlands, 1995, pp.53-66.

42.   Kashchiev, D. *Nucleation. Basic Theory with Applications.* Oxford: Butterworth-Heinemann, 2000.

43.   Kashchiev, D. On the relation between nucleation work, nucleus size, and nucleation rate. *The Journal of Chemical Physics.* 1982, **76**(10), pp.5098-5102.

44. G. V. Samsonov, J.F.P., and L. F. Pryadko. *A Configurational Model of Matter.* Kiev, Russia: Springer, 1973.

45. Voort, E.V.d. and Hartman, P. Calculated interfacial tensions for the calcite cleavage rhombohedron and water. *Journal of Crystal Growth.* 1988, **89**, pp.603-607.

46. Urbina-Villalba, G. and García-Sucre, M. Brownian Dynamics Simulation of Emulsion Stability. *Langmuir.* 2000, **16**(21), pp.7975-7985.

47. Walton, A.G. and Whitman, D.R. Calculations of the Surface Energy for Some Orthorhombic Sulfates. *The Journal of Chemical Physics.* 1964, **40**(9), pp.2722-2724.

48. Hauser, E.R., Sogor, L. and Walton, A.G. Two-Dimensional Nucleation of Inorganic Crystals. *The Journal of Chemical Physics.* 1966, **45**(3), pp.1071-1072.

49. Hammond, R.B., Pencheva, K. and Roberts, K.J. A Structural−Kinetic Approach to Model Face-Specific Solution/Crystal Surface Energy Associated with the Crystallization of Acetyl Salicylic Acid from Supersaturated Aqueous/Ethanol Solution. *Crystal Growth & Design.* 2006, **6**(6), pp.1324-1334.

50. ter Horst, J.H. and Kashchiev, D. Determination of the nucleus size from the growth probability of clusters. *The Journal of Chemical Physics.* 2003, **119**(4), pp.2241-2241.

51. Garside, J. and Shah, M.B. Crystallization kinetics from MSMPR crystallizers. *Industrial & Engineering Chemistry Process Design and Development.* 1980, **19**(4), pp.509-514.

52. Oxtoby, D.W. Nucleation of First-Order Phase Transitions. *Accounts of Chemical Research.* 1998, **31**(2), pp.91-97.

53. Erdemir, D., Lee, A.Y. and Myerson, A.S. Nucleation of Crystals from Solution: Classical and Two-Step Models. *Accounts of Chemical Research.* 2009, **42**(5), pp.621-629.

54. Yau, S.T., Thomas, B.R. and Vekilov, P.G. Molecular mechanisms of crystallisation and defect formation. *Phys. Rev. Lett.* 2000, **85**, pp.353-356.

55. Kashchiev, D., Vekilov, P.G., Kolomeisky, A.B., M., P.V. and C., R.A. Kinetics of two-step nucleation of crystals. *The Journal of Chemical Physics.* 2005, **122**(24), p.244706.

56. Guo, C., Wang, J., Li, J., Wang, Z. and Tang, S. Kinetic Pathways and Mechanisms of Two-Step Nucleation in Crystallization. *The Journal of Physical Chemistry Letters.* 2016, **7**(24), pp.5008-5014.

57. Vekilov, P.G. The Two-Step Mechanism and The Solution-Crystal Spinodal for Nucleation of Crystals in Solution. In: *Kinetics and Thermodynamics of Multistep Nucleation and Self-Assembly in Nanoscale Materials.* John Wiley & Sons, Inc., 2012, pp.79-109.

58. Banerjee, S. and Briesen, H. Molecular dynamics simulations of glycine crystal-solution interface. *The Journal of Chemical Physics.* 2009, **131**(18), p.184705.

59. Wang, T., Cölfen, H. and Antonietti, M. Nonclassical Crystallization: Mesocrystals and Morphology Change of $CaCO_3$ Crystals in the Presence of a Polyelectrolyte Additive. *Journal of the American Chemical Society.* 2005, **127**(10), pp.3246-3247.

60. Meldrum, F.C. and Cölfen, H. Controlling mineral morphologies and structures in biological and synthetic systems. *Chemical reviews.* 2008, **108**(11), pp.4332-4432.

61. Vekilov, P.G., Skowronski, M., DeYoreo, J.J. and Wang, C.A. *Perspectives on Inorganic, Organic and Biological Crystal Growth: From Fundamentals to Applications: AIP Conference Proceedings.* 2007.

62. Meldrum, F.C. and Colfen, H. Crystallization and formation mechanisms of nanostructures. *Nanoscale.* 2010, **2**(11), pp.2326-2327.

63. Meldrum, F.C. and Cölfen, H. Controlling Mineral Morphologies and Structures in Biological and Synthetic Systems. *Chemical reviews.* 2008, **108**(11), pp.4332-4432.

64. Cölfen, H. and Antonietti, M. Mesocrystals and Nonclassical Crystallization. In: *Mesocrystals and Nonclassical Crystallization.* John Wiley & Sons, Ltd, 2008, pp.1-6.

65. Gebauer, D., Kellermeier, M., Gale, J.D., Bergstrom, L. and Colfen, H. Pre-nucleation clusters as solute precursors in crystallisation. *Chemical Society reviews.* 2014, **43**(7), pp.2348-2371.

66. Dai, L., Douglas, E.P. and Gower, L.B. Compositional analysis of a polymer-induced liquid-precursor (PILP) amorphous $CaCO_3$ phase. *Journal of Non-Crystalline Solids.* 2008, **354**(17), pp.1845-1854.

67. Barthe, S.C., Grover, M.a. and Rousseau, R.W. Observation of Polymorphic Change through Analysis of FBRM Data: Transformation of Paracetamol from Form II to Form I. *Crystal Growth & Design.* 2008, **8**(9), pp.3316-3322.

68. Singh, A., Puri, S. and Dasgupta, C. Growth Kinetics of Nanoclusters in Solution. *The Journal of Physical Chemistry B.* 2012, **116**(15), pp.4519-4523.

69. Li, H., Dzombak, D. and Vidic, R. Electrochemical Impedance Spectroscopy (EIS) Based Characterization of Mineral Deposition from Precipitation Reactions. *Industrial & Engineering Chemistry Research.* 2012, **51**(7), pp.2821-2829.

70. Nancollas, G.H. The growth of crystals in solution. *Advances in colloid and interface science.* 1979, **10**(1), pp.215-252.

71. Mougin, P., Wilkinson, D. and Roberts, K.J. In Situ Measurement of Particle Size during the Crystallization of l-Glutamic Acid under Two Polymorphic Forms: Influence of Crystal Habit on Ultrasonic Attenuation Measurements. *Crystal Growth & Design.* 2002, **2**(3), pp.227-234.

72. Garside, J., Mersmann, A. and Nyvlt, J. *Measurement of crystal and nucleation rates.* Second ed. Salisbury: IChemE, 2002.

73. Garside, J., Mersmann, A. and Nyvlt, J. *Measurement of Crystal Growth Rates.* First ed. European Federation of Chemical Engineering, 1990.

74. Varma, S., Chen, P.-C. and Unnikrishnan, G. Gas–liquid reactive crystallization for the synthesis of $CaCO_3$ nanocrystals. *Materials Chemistry and Physics.* 2011, **126**(1-2), pp.232-236.

75. Jones, A., Rigopoulos, S. and Zauner, R. Crystallization and precipitation engineering. *Computers & Chemical Engineering.* 2005, **29**(6), pp.1159-1166.

76. Hostomsky, J. and Jones, A.G. Calcium carbonate crystallization, agglomeration and form during continuous precipitation from solution. *Journal of Physics D: Applied Physics.* 1991, **24**(2), p.165.

77. Gilman, J.J. Direct Measurements of the Surface Energies of Crystals. *Journal of Applied Physics.* 1960, **31**(12), pp.2208-2218.

78. Van der Voort, E. and Hartman, P. Calculated interfacial tensions for the calcite cleavage rhombohedron and water. *Journal of Crystal Growth.* 1988, **89**(4), pp.603-607.

79. Teng, H.H., Dove, P.M. and DeYoreo, J.J. Reversed calcite morphologies induced by microscopic growth kinetics: insight into biomineralization. *Geochimica et Cosmochimica Acta.* 1999, **63**(17), pp.2507-2512.

80. Cao, B., Stack, A.G., Steefel, C.I., DePaolo, D.J., Lammers, L.N. and Hu, Y. Investigating calcite growth rates using a quartz crystal microbalance with dissipation (QCM-D). *Geochimica et Cosmochimica Acta.* 2018, **222**(Supplement C), pp.269-283.

81. Pietsch, W. An interdisciplinary approach to size enlargement by agglomeration. *Powder Technology.* 2003, **130**(1), pp.8-13.

82. Jones, A.G. Crystal agglomeration and disruption. In: *Crystallization Process Systems.* Oxford: Butterworth-Heinemann, 2002, pp.155-189.

83.   Wojcik, J.A. and Jones, A.G. Particle disruption of precipitated CaCO$_3$ crystal agglomerates in turbulently agitated suspensions. *Chemical Engineering Science.* 1998, **53**(5).

84.   Wang, D., Hamm, L.M., Giuffre, A.J., Echigo, T., Rimstidt, J.D., De Yoreo, J.J., Grotzinger, J. and Dove, P.M. Revisiting geochemical controls on patterns of carbonate deposition through the lens of multiple pathways to mineralization. *Faraday Discussions.* 2012, **159**(0), pp.371-386.

85.   Yoreo, J.J.D. and Vekilov, P.G. Principles of crystal nucleation and growth. *Reviews in Mineralogy and Geochemistry.* 2003, pp.57-94.

86.   Nielsen, M.H., Lee, J.R.I., Hu, Q., Yong-Jin Han, T. and De Yoreo, J.J. Structural evolution, formation pathways and energetic controls during template-directed nucleation of CaCO$_3$ *Faraday Discussions.* 2012, **159**, pp.105-121.

87.   Wang, J. and Becker, U. *Energetics and kinetics of carbonate orientational ordering in vaterite calcium carbonate*. American Mineralogist. 2012, 97, p.1427. [Accessed 2017-12-03t19:10:23.746+01:00]. Available from: https://www.degruyter.com/view/j/ammin.2012.97.issue-8-9/am.2012.3990/am.2012.3990.xml

88.   Addadi, L., Raz, S. and Weiner, S. Taking Advantage of Disorder: Amorphous Calcium Carbonate and Its Roles in Biomineralization. *Advanced Materials.* 2003, **15**(12), pp.959-970.

89.   Tester, C.C., Wu, C.-H., Weigand, S. and Joester, D. Precipitation of ACC in liposomes-a model for biomineralization in confined volumes. *Faraday Discussions.* 2012, **159**(0), pp.345-356.

90.   Gago-Duport, L., Briones, M.J.I., Rodríguez, J.B. and Covelo, B. Amorphous calcium carbonate biomineralization in the earthworm's calciferous gland: pathways to the formation of crystalline phases. *Journal of structural biology.* 2008, **162**(3), pp.422-435.

91.   Deng, H., Wang, S., Wang, X., Du, C., Shen, X., Wang, Y. and Cui, F. Two competitive nucleation mechanisms of calcium carbonate biomineralization in response to surface functionality in low calcium ion concentration solution. *Regen Biomater.* 2015, **2**(3), pp.187-195.

92.   Jordan, M., Ishkov, O., Vazquez, O. and Mackay, E. Scale Squeeze Placement Options in Subsea Multi-Lateral Horizontal Wells Completed With Sliding Sleeve Technology. In: *SPE International Oilfield Scale Conference and Exhibition, 11-12 May, Aberdeen, Scotland, UK, 2016/5/11/*. SPE: Society of Petroleum Engineers, 2016.

93.   Sawada, K. The mechanisms of crystallization and transformation of calcium carbonates. *Pure and Applied Chemistry.* 1997, **69**(5), pp.921-928.

94.   Bewernitz, M.A., Gebauer, D., Long, J., Colfen, H. and Gower, L.B. A metastable liquid precursor phase of calcium carbonate and its interactions with polyaspartate. *Faraday Discussions.* 2012, **159**(0), pp.291-312.

95.   Finney, A.R. and Rodger, P.M. Probing the structure and stability of calcium carbonate pre-nucleation clusters. *Faraday Discussions.* 2012, **159**(0), pp.47-60.

96.   Kitamura, M. Crystallization and Transformation Mechanism of Calcium Carbonate Polymorphs and the Effect of Magnesium Ion. *Journal of Colloid and Interface Science.* 2001, **236**(2), pp.318-327.

97.   Sawada, K. *The mechanisms of crystallization and transformation of calcium carbonates.* Pure and Applied Chemistry. 1997, 69, p.921. [Accessed 2017-12-03t19:00:03.472+01:00]. Available from: https://www.degruyter.com/view/j/pac.1997.69.issue-5/pac199769050921/pac199769050921.xml

98.   Stalker, R., Graham, G. and Simpson, C. The Impact of Inorganic Scale Deposits and Their Removal on General CO$_2$ Corrosion Rates and Corrosion

Inhibitor Performance. *SPE International Symposium on Oilfield Corrosion.* 2004, (SPE 87554), pp.1-11.

99. Taheri, A., Masoudi, R., Zahedzadeh, M., Ataei, A. and Fakhri, H. Simulation and Experimental Studies of Mineral Scale Formation Effects on Performance of an Iranian Carbonate Oil Reservoir under Water Injection. In: *2008/1/1/.* SPE: Society of Petroleum Engineers, 2008.

100. Beniash, E., Aizenberg, J., Addadi, L. and Weiner, S. Amorphous calcium carbonate transforms into calcite during sea urchin larval spicule growth. *Proceedings of the Royal Society B: Biological Sciences.* 1997, **264**(1380), pp.461-465.

101. Hasson, D., Avriel, M., Resnick, W., Rozenman, T. and Windreich, S. Mechanism of calcium carbonate heat-transfer surfaces. *Industrial & Engineering Chemistry Research.* 1968, **7**(1), pp.59-65.

102. Ras, H.S. and Ghizellaoui, S. Determination of Anti-Scale Effect of Hard Water by Test of Electrodeposition. *Procedia Engineering.* 2012, **33**(2011), pp.357-365.

103. UK, S.s. *What is Hard Water and Why is it Bad?* [Online]. 2001. [Accessed 16/02/14]. Available from: http://www.softwatershop.co.uk/hardwater.htm

104. Ball, P. Scale-up and scale-down of membrane-based separation processes. *Membrane Technology.* 2000, **2000**(117), pp.10-13.

105. Collins, I.R., Hedges, B., Harris, L.M., Fan, J.C. and Fan, L.D.G. The Development of a Novel Environmentally Friendly Dual Function Corrosion and Scale Inhibitor. In: *2001/1/1/.* SPE: Society of Petroleum Engineers, 2001.

106. Online, D.I. *Membrane filter cartridge for ultra-filtration - Xiga 55 - Pentair X-Flow.* [Online]. 2003. [Accessed 16/02/14]. Available from: http://www.directindustry.com/prod/pentair-x-flow/membranes-filters-cartridges-ultra-filtration-71363-625188.html

107. Addepalli, S., Eiroa, D., Lieotrakool, S., François, A.-L., Guisset, J., Sanjaime, D., Kazarian, M., Duda, J., Roy, R. and Phillips, P. Degradation Study of Heat Exchangers. *Procedia CIRP.* 2015, **38**(Supplement C), pp.137-142.

108. Amiri, M., Moghadasi, M., Amiri, M. and Moghadasi, J. Prediction the amount of barium sulfate scale formation in Siri oilfield using OLI ScaleChem software. *Asian Journal of Scientific Research.* 2010, **3**(4), pp.230-239.

109. Frenier, W.W., Consultants, F.C. and Ziauddin, M. A Multifaceted Approach for Controlling Complex Deposits in Oil and Gas Production. *SPE Annual Technical Conference and Exhibition.* 2010, (SPE 132707), pp.1-24.

110. Stumm, W. and Morgan, J.J. Aquatic Chemistry : Chemical Equilibria and Rates in Natural Waters. 2013.

111. Zen, E.A. Carbonate equilibria in the open ocean and their bearing on the interpretation of ancient carbonate rocks. *Geochimica et Cosmochimica Acta.* 1960, **18**.

112. Brantley, S.L., Kubibki, J. and White, A.F. *Kinetics of Water-rock Interaction.* New York: Springer, 2008.

113. Martell, A.E. and Smith, R.M. *Critical Stability Constants.* Boston, MA: Springer US, 1982.

114. Harned, H.S. and Davis, R. The Ionization Constant of Carbonic Acid in Water and the Solubility of Carbon Dioxide in Water and Aqueous Salt Solutions from 0 to 50°. *Journal of the American Chemical Society.* 1943, **65**(10), pp.2030-2037.

115. Plummer, L.N. and Busenberg, E. The solubilities of calcite, aragonite and vaterite in CO_2-H_2O solutions between 0^oC and 90^oC, and evaluation of the aqueous model for the system $CaCO_3$-CO_2-H_2O. *Geochimica et Cosmochimica Acta.* 1982, **46**(6), pp.1011-1040.

116. Langdon, C., Takahashi, T., Sweeney, C., Chipman, D., Goddard, J., Marubini, F., Aceves, H., Barnett, H. and Atkinson, M.J. Effect of calcium

carbonate saturation state on the calcification rate of an experimental coral reef. *Global Biogeochemical Cycles.* 2000, **14**(2), pp.639-654.

117. Barry, J.P., Buck, K.R., Lovera, C., Kuhnz, L. and Whaling, P.J. Utility of deep sea CO_2 release experiments in understanding the biology of a high-CO_2 ocean: Effects of hypercapnia on deep sea meiofauna. *Journal of Geophysical Research: Oceans.* 2005, **110**(C9), pp.n/a-n/a.

118. Feely, R.A., Sabine, C.L., Lee, K., Berelson, W., Kleypas, J., Fabry, V.J. and Millero, F.J. Impact of Anthropogenic CO_2 on the $CaCO_3$ System in the Oceans. *Science.* 2004, **305**(5682), pp.362-366.

119. Marubini, F., Barnett, H., Langdon, C. and Atkinson, M.J. Dependence of calcification on light and carbonate ion concentration for the hermatypic coral Porites compressa. *Marine Ecology Progress Series.* 2001, **220**, pp.153-162.

120. Gattuso, J.-p., Gao, K., Lee, K., Rost, B., Schulz, K.G., Océanographie, L., Océanologique, O. and Pierre, U. *Seawater carbonate chemistry Approaches and tools to manipulate the carbonate chemistry*. 2010, pp.41-52.

121. Green, D.W. and Perry, R.H. *Perry's Chemical Engineers' Handbook.* 7th ed. New York: McGraw-Hill, 1997.

122. Chen, Z., Xiao, S., Chen, F., Chen, D., Fang, J. and Zhao, M. Calcium carbonate phase transformations during the carbonation reaction of calcium heavy alkylbenzene sulfonate overbased nanodetergents preparation. *Journal of Colloid and Interface Science.* 2011, **359**(1), pp.56-67.

123. Clarkson, J.R., Price, T.J. and Adams, C.J. Role of metastable phases in the spontaneous precipitation of calcium carbonate. *Journal of the Chemical Society, Faraday Transactions.* 1992, **88**(2), pp.243-243.

124. Tai, C.Y. and Chen, F.B. Polymorphism of $CaCO_3$, precipitated in a constant-composition environment. *AIChE Journal.* 1998, **44**(8), pp.1790-1798.

125. Chen, P.-C., Tai, C.Y. and Lee, K.C. Morphology and growth rate of calcium carbonate crystals in a gas-liquid-solid reactive crystallizer. *Chemical Engineering Science.* 1997, **52**(21-22), pp.4171-4177.

126. Brečević, L. and Nielsen, A.E. Solubility of amorphous calcium carbonate. *Journal of Crystal Growth.* 1989, **98**(3), pp.504-510.

127. Nancollas, G.H. and Sawada, K. Formation of scales of calcium carbonate polymorphs: The influence of magnesium ion and inhibitors. *Journal of Petroleum Technology.* 1982, **34**(March).

128. Wada, N., Kanamura, K. and Umegaki, T. Effects of Carboxylic Acids on the Crystallization of Calcium Carbonate. *Journal of Colloid and Interface Science.* 2001, **233**(1), pp.65-72.

129. Euvrard, M., Membrey, F., Filiatre, C., Pignolet, C. and Foissy, A. Kinetic study of the electrocrystallization of calcium carbonate on metallic substrates. *Journal of Crystal Growth.* 2006, **291**(2), pp.428-435.

130. Revelle, R. Physico-chemical factors affecting the solubility of calcium carbonate in sea water. *Journal of Sedimentary Research.* 1934, **4**(3), pp.103-110.

131. Helalizadeh, A., Müller-Steinhagen, H. and Jamialahmadi, M. Mixed salt crystallisation fouling. *Chemical Engineering and Processing: Process Intensification.* 2000, **39**(1), pp.29-43.

132. Straub, F.G. Solubility of Calcium Sulfate and Calcium Carbonate at Temperatures between 182°C and 316°C. *Industrial & Engineering Chemistry.* 1932, **24**(8), pp.914-917.

133. Ogino, T., Suzuki, T. and Sawada, K. The formation and transformation mechanism of calcium carbonate in water. *Geochimica et Cosmochimica Acta.* 1987, **51**(10), pp.2757-2767.

134. Carlson, W.D. and William, D.C.S. Aragonite-Calcite Nucleation Kinetics : An Application and Extension of Avrami Transformation Theory. *The Journal of Geology.* 1983, **91**(1), pp.57-71.

135.   Chen, S.F., Yu, S.-h., Jiang, J., Li, F. and Liu, Y. Polymorph discrimination of CaCO$_3$ mineral in an ethanol/water solution: Formation of complex vaterite superstructures and aragonite rods. *Chemistry of Materials.* 2006, (7), pp.115-122.

136.   Ward, M.D. and McCleverty, J.a. Non-innocent behaviour in mononuclear and polynuclear complexes: consequences for redox and electronic spectroscopic properties. *Journal of the Chemical Society, Dalton Transactions.* 2002, (3), pp.275-288.

137.   Ward, M.D. Snapshots of Crystal Growth. *Science.* 2005, **308**(5728), pp.1566-1567.

138.   Spanos, N. and Koutsoukos, P.G. The transformation of vaterite to calcite: effect of the conditions of the solutions in contact with the mineral phase. *Journal of Crystal Growth.* 1998, **191**(4), pp.783-790.

139.   Ogino, T., Suzuki, T. and Sawada, K. The rate and mechanism of polymorphic transformation of calcium carbonate in water. *Journal of Crystal Growth.* 1990, **100**(1-2), pp.159-167.

140.   Kralj, D., Brečević, L. and Kontrec, J. Vaterite growth and dissolution in aqueous solution III. Kinetics of transformation. *Journal of Crystal Growth.* 1997, **177**, pp.248-257.

141.   Vekilov, P.G., Feeling-Taylor, A.R., Petsev, D.N., Galkin, O., Nagel, R.L. and Hirsch, R.E. Intermolecular interactions, nucleation, and thermodynamics of crystallization of hemoglobin C. *Biophysical journal.* 2002, **83**(2), pp.1147-1156.

142.   Andreassen, J.-P. Formation mechanism and morphology in precipitation of vaterite—nano-aggregation or crystal growth? *Journal of Crystal Growth.* 2005, **274**(1-2), pp.256-264.

143.   webmineral. *Calcium Carbonate Properties Calcite Aragonite Vaterite*, 2013.

144.   Gower, L.B. Biomimetic model systems for investigating the amorphous precursor pathway and its role in biomineralization. *Chemical reviews.* 2008, **108**(11), pp.4551-4627.

145.   Davies, C.W. *Ion association.* Washington: Butterworths, 1962.

146.   Kralj, D., Brečević, L. and Nielsen, A.E. Vaterite growth and dissolution in aqueous solution I. Kinetics of crystal growth. *Journal of Crystal Growth.* 1990, **104**, pp.793-800.

147.   Petrotech, E. *MultiScale manual: Expro Petrotech ® Analysis Services E.* 2001.

148.   Sandengen, K. Prediction of mineral scale formation in wet gas condensate pipelines and in meg (mono ethylene glycol) regeneration plants. 2006, (September).

149.   Flaten, E.M. *The effect of MEG (mono ethylene glycol) on the precipitation kinetics of calcium carbonate related to natural gas production from subsea wells.* thesis, 2010.

150.   Morse, J.W., Arvidson, R.S. and Lüttge, A. Calcium Carbonate Formation and Dissolution. *Chemical reviews.* 2007, **107**(2), pp.342-381.

151.   Dove, P.M. and Jr, M.F.H. Calcite precipitation mechanisms and inhibition by orthophosphate: In situ observations by Scanning Force Microscopy. *Geochimica et Cosmochimica Acta.* 1993, **45**, pp.705-714.

152.   Hossain, F.M., Murch, G.E., Belova, I.V. and Turner, B.D. Electronic, optical and bonding properties of CaCO$_3$ (calcite). *Solid State Communications.* 2009, **149**(29-30), pp.1201-1203.

153.   Han, Y.S., Hadiko, G., Fuji, M. and Takahashi, M. Factors affecting the phase and morphology of CaCO$_3$ prepared by a bubbling method. *Journal of the European Ceramic Society.* 2006, **26**(4-5), pp.843-847.

154.   Nielsen, M.H., Lee, J.R.I., Hu, Q., Yong-Jin Han, T. and De Yoreo, J.J. Structural evolution, formation pathways and energetic controls during

template-directed nucleation of CaCO₃. *Faraday Discussions.* 2012, **159**, pp.105-105.

155. Li, S., Yu, L., Geng, F., Shi, L., Zheng, L. and Yuan, S. Facile preparation of diversified patterns of calcium carbonate in the presence of DTAB. *Journal of Crystal Growth.* 2010, **312**(10), pp.1766-1773.

156. Vergaro, V., Carata, E., Panzarini, E., Baldassare, F., Dini, L. and Ciccarella, G. Synthesis of calcium carbonate nanocrystals and their potential application as vessels for drug delivery. *AIP Conference Proceedings.* 2015, **1667**(1), p.020014.

157. Ben Amor, Y., Bousselmi, L., Bernard, M.C. and Tribollet, B. Nucleation-growth process of calcium carbonate electrodeposition in artificial water—Influence of the sulfate ions. *Journal of Crystal Growth.* 2011, **320**(1), pp.69-77.

158. Dyer, S.J. and Graham, G.M. The effect of temperature and pressure on oilfield scale formation. *Journal of Petroleum Science and Engineering.* 2002, **35**(1), pp.95-107.

159. Rukuni, T.T. The Effect of Temperature and Pressure on the separation of Calcium Carbonate and Barium Sulphate from a Mixed Sludge. *Journal of Chemical Engineering & Process Technologyy.* 2012.

160. Söhnel, O. and Garside, J. *Precipitation: Basic principles and industrial applications.* Oxford: Butterworth-Heinemann, 1992.

161. García, A.V., Thomsen, K. and Stenby, E.H. Prediction of mineral scale formation in geothermal and oilfield operations using the Extended UNIQUAC model. *Geothermics.* 2006, **35**(3), pp.239-284.

162. Baraka-Lokmane, S. and Sorbie, K.S. Effect of pH and scale inhibitor concentration on phosphonate–carbonate interaction. *Journal of Petroleum Science and Engineering.* 2010, **70**(1), pp.10-27.

163. Wada, N., Yamashita, K. and Umegaki, T. Effects of divalent cations upon nucleation, growth and transformation of calcium carbonate polymorphs under conditions of double diffusion. *Journal of Crystal Growth.* 1995, **148**(3), pp.297-304.

164. Dobberschütz, S., Nielsen, M.R., Sand, K.K., Civioc, R., Bovet, N., Stipp, S.L.S. and Andersson, M.P. The mechanisms of crystal growth inhibition by organic and inorganic inhibitors. *Nature communications.* 2018, **9**, p.1578.

165. Ghizellaoui, S., Euvrard, M., Ledion, J. and Chibani, A. Inhibition of scaling in the presence of copper and zinc by various chemical processes. *Desalination.* 2007, **206**(1), pp.185-197.

166. Aizenberg, J., Black, A.J. and Whitesides, G.M. Oriented Growth of Calcite Controlled by Self-Assembled Monolayers of Functionalized Alkanethiols Supported on Gold and Silver. *Journal of the American Chemical Society.* 1999, **121**(18), pp.4500-4509.

167. Chen, T., Neville, A., and M. Yuan,. Assessing the effect of Mg^{2+}+ on CaCO₃ scale formation-bulk precipitation and surface deposition. . *Journal of Crystal Growth.* 2005, **275**(1-2), pp.1341-1347.

168. Devos, O., Jakab, S., Gabrielli, C., Joiret, S., Tribollet, B. and Picart, S. Nucleation-growth process of scale electrodeposition – influence of the magnesium ions. *Journal of Crystal Growth.* 2009, **311**(18), pp.4334-4342.

169. Wada, N., Yamashita, K. and Umegaki, T. Effects of Silver, Aluminum, and Chrome Ions on the Polymorphic Formation of Calcium Carbonate under Conditions of Double Diffusion. *Journal of Colloid and Interface Science.* 1998, **201**(1), pp.1-6.

170. Keysar, S., Semiat, R., Hasson, D. and Yahalom, J. Effect of surface roughness on the morphology of calcite crystallizing on mild steel. *Journal of Colloid and Interface Science.* 1994, **162**, pp.311-319.

171. Andritsos, N.A.J.K.K.P.G. Crystallization and deposit formation of lead sulfide from aqueous solutions I. Deposition rates. *Journal of Colloid and Interface Science.* 1991, **145**(1), pp.158-169.
172. Quddus, A. Effect of hydrodynamics on the deposition of CaSO$_4$ scale on stainless steel. *Desalination.* 2002, **142**(1), pp.57-63.
173. Trippa, G. and Jachuck, R.J.J. Process Intensification: Precipitation of Calcium Carbonate Using Narrow Channel Reactors. *Chemical Engineering Research and Design.* 2003, **81**(7), pp.766-772.
174. Karabelas, A.J. Scale formation in tubular heat exchangers—research priorities. *International Journal of Thermal Sciences.* 2002, **41**(7), pp.682-692.
175. Andritsos, N., Karabelas, A.J. and Koutsoukos, P.G. Morphology and Structure of CaCO$_3$ Scale Layers Formed under Isothermal Flow Conditions. *Langmuir.* 1997, **13**(10), pp.2873-2879.
176. Revie, R.W. *Thermodynamics: Corrosion tendancy and electrode potentials, Corrosion and corrosion control.* John Wiley & Sons Ltd, 2000.
177. Cecile Barthe, S. *Investigation and modeling of the mechanisms involved in batch cooling crystallization and polymorphism through efficient use of the FBRM.* 2018.
178. Morizot, A.P. and Neville, A. Insights into electrodeposition of an inhibitor film and its inhibitive effects on calcium carbonate deposition. *Journal of Colloid and Interface Science.* 2002, **245**(1), pp.40-49.
179. Al Nasser, W.N., Shaikh, a., Morriss, C., Hounslow, M.J. and Salman, a.D. Determining kinetics of calcium carbonate precipitation by inline technique. *Chemical Engineering Science.* 2008, **63**(5), pp.1381-1389.
180. Wu, W. and Nancollas, G.H. Determination of interfacial tension from crystallization and dissolution data: a comparison with other methods. *Advances in colloid and interface science.* 1999, **79**(2-3), pp.229-279.
181. Bargir, S., Dunn, S., Jefferson, B., Macadam, J. and Parsons, S. The use of contact angle measurements to estimate the adhesion propensity of calcium carbonate to solid substrates in water. *Applied Surface Science.* 2009, **255**(9), pp.4873-4879.
182. Hui, F. and Lédion, J. Evaluation methods for the scaling power of water. *JOURNAL EUROPEEN D HYDROLOGIE.* 2002, **1**, pp.1-27.
183. MacAdam, J. and Parsons, S.A. Calcium carbonate scale formation and control. *Re/Views in Environmental Science & Bio/ ….* 2004, **1**(Chapman 1992), pp.159-169.
184. Jaouhari, R., et al. Influence of Water Composition and Substrate on Electrochemical Scaling. *Journal of The Electrochemical Society.* 2000, **147**(6), pp.2151-2161.
185. Amor, M.B., Zgolli, D., Tlili, M.M. and Manzola, a.S. Influence of water hardness, substrate nature and temperature on heterogeneous calcium carbonate nucleation. *Desalination.* 2004, **166**, pp.79-84.
186. Herz, A., Malayeri, M.R. and Müller-Steinhagen, H. Fouling of roughened stainless steel surfaces during convective heat transfer to aqueous solutions. *Energy Conversion and Management.* 2008, **49**(11), pp.3381-3386.
187. Rankin, B.H. and Adamson, W.L. Scale formation as related to evaporator surface conditions. *Desalination.* 1973, **13**, pp.63-87.
188. Brondel, D., Edwards, R., Hayman, A., Hill, D., Mehta, S. and Semerad, T. Corrosion in the oil industry. *Oilfield Review.* 1994, **6**(2), pp.4-18.
189. Mitchell, C.A., Yu, L. and Ward, M.D. *J. Am. Chem. Soc.* 2001, **123**, p.10830.
190. Nauli, S., Farr, S., Lee, Y.-j., Kim, H.-y., Faham, S. and Bowie, J.U. Polymer-driven crystallization. 2007, pp.2542-2551.
191. Lang, M., Grzesiak, A.L. and Matzger, A.J. The Use of Polymer Heteronuclei for Crystalline Polymorph Selection. *Journal of the American Chemical Society.* 2002, **124**(50), pp.14834-14835.

192. Hou, H., Xie, Y. and Li, Q. Large-Scale Synthesis of Single-Crystalline Quasi-Aligned Submicrometer CuO Ribbons. *Crystal Growth & Design.* 2005, **5**(1), pp.201-205.

193. Lee, I.S., Lee, A.Y. and Myerson, A.S. Concomitant polymorphism in confined environment. *Pharmaceutical research.* 2008, **25**(4), pp.960-968.

194. Goodwin, A.L., Michel, F.M., Phillips, B.L., Keen, D.A., Dove, M.T. and Reeder, R.J. Nanoporous Structure and Medium-Range Order in Synthetic Amorphous Calcium Carbonate. *Chemistry of Materials.* 2010, **22**(10), pp.3197-3205.

195. D.C. Popescu, S. Cavalli, A.K., M.S. FERNANDEZ, J.L. Arias and Sommerdijk, N.A.J.M. *Biomineralization: from Paleontology to Materials Science* 2007.

196. Aizenberg, J. Patterned crystallization of calcite in vivo and in vitro. *Journal of Crystal Growth.* 2000, **211**(1-4), pp.143-148.

197. Zettler, H.U., Wei, M., Zhao, Q. and MÜller-Steinhagen, H. Influence of Surface Properties and Characteristics on Fouling in Plate Heat Exchangers. *Heat Transfer Engineering.* 2005, **26**(2), pp.3-17.

198. Cheong, W.C., Neville, A., Gaskell, P. and Abbott, S. Using Nature to Provide Solutions to Calcareous Scale Deposition. *Proceedings of SPE International Oilfield Scale Conference.* 2008, (May), pp.28-29.

199. Tomson, M., Fan, C., Lu, H., Zhang, P., Alsaiari, H.A. and Kan, A.T. Integration of Kinetics Into Scale Prediction Software. In: *SPE International Symposium on Oilfield Chemistry, 2009/1/1/, The Woodlands. Texas.* SPE: Society of Petroleum Engineers, 2009.

200. Amiri, M. and Moghadasi, M. Prediction the amount of barium sulfate scale formation in Siri oilfield using OLI ScaleChem software. *Asian Journal of Scientific Research.* 2010, **3**(4), pp.230-239.

201. Prisyazhniuk, V.A. Physico-chemical principles of preventing salts crystallization on heat-exchange surfaces. *Applied Thermal Engineering.* 2009, **29**(14), pp.3182-3188.

202. Greenlee, L.F., Testa, F., Lawler, D.F., Freeman, B.D. and Moulin, P. The effect of antiscalant addition on calcium carbonate precipitation for a simplified synthetic brackish water reverse osmosis concentrate. *Water Research.* 2010, **44**(9), pp.2957-2969.

203. Kashchiev, D. Magic Cluster Sizes in Nucleation of Crystals. *Crystal Growth & Design.* 2012, **12**(6), pp.3257-3262.

204. Meldrum, F.C. Calcium carbonate in biomineralisation and biomimetic chemistry. *International Materials Reviews.* 2003, **48**(3), pp.187-224.

205. Li, Q., Fernandez-Martinez, A., Lee, B., Waychunas, G.A. and Jun, Y.-S. Interfacial Energies for Heterogeneous Nucleation of Calcium Carbonate on Mica and Quartz. *Environmental science & technology.* 2014, **48**(10), pp.5745-5753.

206. Jaho, S., Athanasakou, G.D., Sygouni, V., Lioliou, M.G., Koutsoukos, P.G. and Paraskeva, C.A. Experimental Investigation of Calcium Carbonate Precipitation and Crystal Growth in One- and Two-Dimensional Porous Media. *Crystal Growth & Design.* 2016, **16**(1), pp.359-370.

207. Zhang, Y., Shaw, H., Farquhar, R. and Dawe, R. The kinetics of carbonate scaling—application for the prediction of downhole carbonate scaling. *Journal of Petroleum Science and Engineering.* 2001, **29**(2), pp.85-95.

208. Neville, A. and Morizot, A.P. A combined bulk chemistry/electrochemical approach to study the precipitation, deposition and inhibition of $CaCO_3$. *Chemical Engineering Science.* 2000, **55**, pp.4737-4743.

209. Becker, J.R. *Corrosion and scale handbook.* Tulsa (Okla.): PennWell, 1998.

210. Koch, G.H., Brongers, M.P.H., Thompson, N.G., Virmani, Y.P. and Payer, J.H. *Corrosion Cost and Preventative Strategies in the United States.* Turner-Fairbank Highway Research Center, 2002.

211. Perez, N. *Electrochemistry and corrosion science.* 2004.
212. E.E., S. and R.A., B. *Fundamentals of Electrochemical Corrosion.* ASM International, 2000.
213. Lyon, S.B. 2.17 - Corrosion in Natural Waters*. In: *Shreir's Corrosion.* Oxford: Elsevier, 2010, pp.1094-1106.
214. Frankel, G.S. and Cottis, R.A. 2.01 - Principles of Corrosion in Liquids. In: *Shreir's Corrosion.* Oxford: Elsevier, 2010, pp.725-730.
215. Popoola, L.T., Grema, A.S., Latinwo, G.K., Gutti, B. and Balogun, A.S. Corrosion problems during oil and gas production and its mitigation. *International Journal of Industrial Chemistry.* 2013, **4**(1), p.35.
216. Talbot, D. and Talbot, J. *Corrosion Science and Technology.* Boca Raton: CRC Press., 1997.
217. Schumacher, M.M. Corrosion of metals in marine environments, an overview. In, 1979, pp.1-23.
218. Kermani, M.B. and Harrop, D. The Impact of Corrosion on Oil and Gas Industry. 1996.
219. Amani, M. and Hjeij, D. A Comprehensive Review of Corrosion and its Inhibition in the Oil and Gas Industry. In: *SPE Kuwait Oil and Gas Show and Conference*, *2015/10/11/, Mishref, Kuwait.* SPE: Society of Petroleum Engineers, 2015.
220. Asmara, Y.P., Juliawati, A., Sulaiman, A. and Jamiluddin. Mechanistic model of stress corrosion cracking (scc) of carbon steel in acidic solution with the presence of H 2 s. *IOP Conference Series: Materials Science and Engineering.* 2013, **50**(1), p.012072.
221. Kermani, M.B. and MacCuish, R.G. Materials Assessment for Sour Service Applications. In: *SPE Annual Technical Conference and Exhibition*, *1990/1/1/, New Orleans, Louisiana.* SPE: Society of Petroleum Engineers, 1990.
222. Jackobson, G. *Testing for localized corrosion.* [Online]. 2014. [Accessed 01/12/2014]. Available from: http://www.nace.org/Corrosion-Central/Corrosion-101/Testing-for-Localized-Corrosion
223. Intrater, J. A Review of: "Corrosion Inspection and Monitoring, Pierre R. Roberge". *Materials and Manufacturing Processes.* 2007, **22**(7-8), pp.958-958.
224. Revie, R.W. and Uhlig, H. Thermodynamics: Corrosion Tendency and Electrode Potentials. In: *Corrosion and Corrosion Control.* NY: John Wiley & Sons Ltd, 2000.
225. Marcus, P. *Corrosion Mechanisms in Theory and Practice.* Second ed. NY: Marcel Dekker, Inc., 2002.
226. Waard, C.D. and Milliams, D.E. Carbonic Acid Corrosion of Steel. *Corrosion.* 1975, **31**(5), pp.177-181.
227. Bockris, J.O.M. and Potter, E.C. The Mechanism of Hydrogen Evolution at Nickel Cathodes in Aqueous Solutions. *The Journal of Chemical Physics.* 1952, **20**(4), pp.614-628.
228. Nešić, S. Key issues related to modelling of internal corrosion of oil and gas pipelines – A review. *Corrosion Science.* 2007, **49**(12), pp.4308-4338.
229. Möller, D. *Chemistry for Environmental Scientists.* Walter de Gruyter GmbH & Co KG, 2015.
230. Möller, H., Boshoff, E.T. and Froneman, H. The corrosion behaviour of a low carbon steel in natural and synthetic seawaters. *Journal of the Southern African Institute of Mining and Metallurgy.* 2006, **106**(8), pp.585-592.
231. J. Lipkowski and P.N. Ross. *Structure of Electrified Interfaces.* New York: VCH Publishers Inc, 1993.
232. Zaragoza-Ayala, A.E., Acuna, N., Aldana, J. and Solis, W. Pitting Corrosion Behaviour of 316L Stainless Steel in Tropical SeaWater. In: *CORROSION 96*, *1996/1/1/, Denver, Colorado.* NACE: NACE International, 1996.

233. Stern, M. and Geary, A.L. Electrochemical polarization I. A theoretical analysis of the shape of polarization curves. *Journal of The Electrochemical Society.* 1957, **104**(1), pp.56-63.

234. Syrett, B.C. and Wing, S.S. Effect of Flow on Corrosion of Copper-Nickel Alloys in Aerated Sea Water and in Sulfide-Polluted Sea Water. *Corrosion.* 1980, **36**(2), pp.73-85.

235. Dougherty, J.A. A Review of the Effect of Organic Acids on CO2 Corrosion. In: *CORROSION 2004, 2004/1/1/, New Orleans, Louisiana.* NACE: NACE International, 2004.

236. Nazari, M.H. and Allahkaram, S.R. The effect of acetic acid on the CO_2 corrosion of grade X70 steel. *Materials & Design.* 2010, **31**(9), pp.4290-4295.

237. Crolet, J.L., Thevenot, N. and Dugstad, A. Role of Free Acetic Acid on the CO_2 Corrosion of Steels. In: *CORROSION 99, 1999/1/1/, San Antonio, Texas.* NACE: NACE International, 1999.

238. George, K., Nesic, S. and de Waard, K. Electrochemical Investigation and Modeling of Carbon Dioxide Corrosion of Carbon Steel in the Presence of Acetic Acid. In: *CORROSION 2004, 2004/1/1/, New Orleans, Louisiana.* NACE: NACE International, 2004.

239. Dugstad, A. Mechanism of protective film formation during CO_2 corrosion of carbon steel. *CORROSION 98.* 1998, (31).

240. Dugstad, A. Mechanism of Protective Film Formation During CO_2 Corrosion of Carbon Steel. In: *CORROSION 98, 1998/1/1/, San Diego, California.* NACE: NACE International, 1998.

241. Soror, T.Y. Scale and Corrosion Prevention in Cooling Water Systems Part I: Calcium Carbonate. *The Open Corrosion Journal.* 2009, **2**(1), pp.45-50.

242. Kvarekval, J., Nyborg, R. and Seiersten, M. Corrosion Product Films on Carbon Steel in Semi-Sour CO_2/H_2S Environments. In: *CORROSION 2002, 2002/1/1/, Denver, Colorado.* NACE: NACE International, 2002.

243. Dugstad, A. Mechanism of Protective Film Formation During CO_2 Corrosion of Carbon Steel. *NACE International.* 1998.

244. Dugstad, A. Internal corrosion in dense phase CO_2 transport pipelines - state of the art and the need for further R&D. *Corrosion.* 2012, (C2012-0001452), pp.1-14.

245. Pessu, F., Barker, R. and Neville, A. The Influence of pH on Localized Corrosion Behavior of X65 (UNS K03014) Carbon Steel in CO_2-Saturated Brines. In: *2015/5/12/.* NACE: NACE International.

246. Creek, F. *Predictive modelling of scale, corrosion & inhibitor dosages for cooling waters.* Inc. Kimberton, 1999.

247. DeWaard, C., Milliams, D.E. and Lotz, U. Predictive Model for CO_2 Corrosion Engineering in Wet Natural Gas Pipelines. *Corrosion 91.* 1991, (577).

248. Nordsveen, M., Nešić, S., Nyborg, R. and Stangeland, A. A Mechanistic Model for Carbon Dioxide Corrosion of Mild Steel in the Presence of Protective Iron Carbonate Films—Part 1: Theory and Verification. *Corrosion.* 2003, **59**(5), pp.443-456.

249. Sun, W. and S. Nesic, B. Revisited: Kinetics of Iron Carbonate Scale Precipitation in CO2 Corrosion. *NACE International.* 2006.

250. Akbar, A., Hu, X., Neville, A. and Wang, C. The influence of flow rate and inhibition on the protective layer under erosion-corrosion conditions using rotating cylinder electrode. *NACE International.* 2011, (11274), pp.1-12.

251. Kermani, M.B. and Morshed, A. Carbon Dioxide Corrosion in Oil and Gas Production—A Compendium. *Corrosion.* 2003, **59**(8), pp.659-683.

252. Yang, Y., Brown, B., Nešić, S., Gennaro, M. and Molinas Agnellini, B. *Mechanical strength and removal of a protective iron carbonate layer formed on mild steel in CO_2 corrosion.* 2010.

253.   Yang, Y., Brown, B., Nesic, S., Elena Gennaro, M. and Molinas Agnellini, B. *Effect of adhesion on strength of iron carbonate film on film removal in CO_2 corrosion.* 2010.

254.   J.L. Crolet, N.T.S.N. Role of Conductive Corrosion Products in the Protectiveness of Corrosion Layers. *Corrosion Science.* 1998, **54**(3), pp.194-203.

255.   Newman, J. and Thomas-Alyea, K.E. *Electrochemical Systems.* Third ed. New Jersey: Prentice-Hall, 1991.

256.   Finšgar, M. and Jackson, J. Application of corrosion inhibitors for steels in acidic media for the oil and gas industry: A review. *Corrosion Science.* 2014, **86**(Supplement C), pp.17-41.

257.   Nešić, S. and Lee, K.-L.J. A Mechanistic Model for Carbon Dioxide Corrosion of Mild Steel in the Presence of Protective Iron Carbonate Films—Part 3: Film Growth Model. *Corrosion.* 2003, **59**(7), pp.616-628.

258.   Waard, C.d., Lotz, U. and Dugstad, A. *Influence of liquid flow velocity on carbon dioxide corrosion: A semi-empirical model.* NACE International, Houston, TX (United States), 1995.

259.   Marie, A., K. Halvorsen and T. Søntvedt. CO_2 Corrosion Model for Carbon Steel Including a Wall Shear Stress Model for Multiphase Flow and Limits for Production to Avoid Mesa Attack. *CORROSION 99.* 1999, **42**.

260.   Fosbøl, P.L., Thomsen, K. and Stenby, E.H. Review and recommended thermodynamic properties of $FeCO_3$. *Corrosion Engineering, Science and Technology.* 2010, **45**(2), pp.115-135.

261.   Mishra, B., Al-Hassan, S., Olson, D.L. and Salama, M.M. Development of a Predictive Model for Activation-Controlled Corrosion of Steel in Solutions Containing Carbon Dioxide. *Corrosion.* 1997, **53**(11), pp.852-859.

262.   Nesic, S., Nordsveen, M., Maxwell, N. and Vrhovac, M. Probabilistic modelling of CO_2 corrosion laboratory data using neural networks. *Corrosion Science.* 2001, **43**(7), pp.1373-1392.

263.   Nesic, S. and Vrhovac, M. A neural network model for CO_2 corrosion of carbon steel. *The Journal of Corrosion Science and Engineering.* 1999, pp.1-13.

264.   DeWaard, C. and Lotz, U. Prediction of CO_2 Corrosion of Carbon Steel. *Corrosion 93.* 1993, (69).

265.   Nešić, S., Nordsveen, M., Nyborg, R. and Stangeland, A. A Mechanistic Model for Carbon Dioxide Corrosion of Mild Steel in the Presence of Protective Iron Carbonate Films—Part 2: A Numerical Experiment. *Corrosion.* 2003, **59**(6), pp.489-497.

266.   Nešić, S., Solvi, G.T. and Enerhaug, J. Comparison of the Rotating Cylinder and Pipe Flow Tests for Flow-Sensitive Carbon Dioxide Corrosion. *Corrosion.* 1995, **51**(10), pp.773-787.

267.   Kahyarian, A., Singer, M. and Nesic, S. *Modeling of Uniform CO_2 Corrosion of Mild Steel in Gas Transportation Systems: a Review.* 2016.

268.   Barker, R.J. *Erosion-corrosion of carbon steel pipework on an offshore oil and gas facility.* Ph.D. thesis, University of Leeds, 2012.

269.   Alsaiari, H.A., Kan, A. and Tomson, M. Effect of Calcium and Iron (II) Ions on the Precipitation of Calcium Carbonate and Ferrous Carbonate. *SPE.* 2010.

270.   Greenberg, J. and Tomson, M. Precipitation and dissolution kinetics and equilibria of aqueous ferrous carbonate vs temperature. *Applied Geochemistry.* 1992, **7**(2), pp.185-190.

271.   Johnson, M.L. *Ferrous carbonate precipitation kinetics: A temperature ramped approach.* thesis, Rice University, 1991.

272.   Elgaddafi, R., Naidu, A., Ahmed, R., Shah, S., Hassani, S., Osisanya, S.O. and Saasen, A. Modeling and experimental study of CO_2 corrosion on carbon steel at elevated pressure and temperature. *Journal of Natural Gas Science and Engineering.* 2015, **27**(Part 3), pp.1620-1629.

273. Van Hunnik, E., B.F. Pots and E. Hendriksen. The formation of protective $FeCO_3$ corrosion product layers in CO_2 corrosion. *NACE International.* 1996.

274. Sun, W. and Nešić, S. A Mechanistic Model of Uniform Hydrogen Sulfide/Carbon Dioxide Corrosion of Mild Steel. *Corrosion.* 2009, **65**(5), pp.291-307.

275. Sun, W., Chokshi, K., Nesic, S. and Gulino, D. *A STUDY OF PROTECTIVE IRON CARBONATE SCALE FORMATION IN CO_2 CORROSION.* 2017.

276. Sun, W. *Kinetics of Iron Carbonate and Iron Sulfide Scale Formation in CO_2/H_2S Corrosion.* Ph.D. thesis, Ohio University, 2006.

277. Woollam, R.C. and Nesic, S. *Review of Kinetics Models for Ferrous Carbonate ($FeCO_3$) Precipitation.* Ohio University.

278. Sun, W.S.N. and Woollam, R.C. The effect of temperature and ionic strength on iron carbonate ($FeCO_3$) solubility limit. *Corrosion Science.* 2009, **51**(6), pp.1273-1276.

279. Toledo, M. *PerfectIon guidebook - Mettler Toledo.* 2011, pp.1-49.

280. Verdoes, D., Kashchiev, D. and van Rosmalen, G.M. Determination of nucleation and growth rates from induction times in seeded and unseeded precipitation of calcium carbonate. *Journal of Crystal Growth.* 1992, **118**(3-4), pp.401-413.

281. Xyla, A.G., Giannimaras, E.K. and Koutsoukos, P.G. The precipitation solutions of calcium carbonate in aqueous. *Colloids and Surfaces A: Physicochemical and Engineering Aspects.* 1991, **53**, pp.241-255.

282. Rodriguez-Blanco, J.D., Shaw, S., Bots, P., Roncal-Herrero, T. and Benning, L.G. The role of pH and Mg on the stability and crystallization of amorphous calcium carbonate. *Journal of Alloys and Compounds.* 2012, **536**, pp.S477-S479.

283. Zhang, Y. and Dawe, R. The kinetics of calcite precipitation from a high salinity water. *Applied Geochemistry.* 1998, **13**(2), pp.177-184.

284. Andreassen, J.-P., Beck, R. and Nergaard, M. Biomimetic type morphologies of calcium carbonate grown in absence of additives. *Faraday Discussions.* 2012, **159**(0), pp.247-261.

285. Hanhoun, M., Montastruc, L., Azzaro-Pantel, C., Biscans, B., Frèche, M. and Pibouleau, L. Simultaneous determination of nucleation and crystal growth kinetics of struvite using a thermodynamic modeling approach. *Chemical Engineering Journal.* 2013, **215-216**(Complete), pp.903-912.

286. Lioliou, M.G., Paraskeva, C.a., Koutsoukos, P.G. and Payatakes, A.C. Heterogeneous nucleation and growth of calcium carbonate on calcite and quartz. *Journal of Colloid and Interface Science.* 2007, **308**(2), pp.421-428.

287. Spanos, N. and Koutsoukos, P.G. Kinetics of precipitation of calcium carbonate in alkaline pH at constant supersaturation. Spontaneous and seeded growth. *The Journal of Physical Chemistry B.* 1998, **5647**(98), pp.6679-6684.

288. Koutsoukos, P.G. and Klepetsanis, P.G. Calcium Carbonate Crystal Growth And Dissolution Inhibitors. *Corrosion.* 2007, (07052), pp.1-17.

289. Pine Research, I. *Rotating Cylinder Electrode (RCE) Guide*, 2013.

290. Neville, A.T.H. and Morizot, A.P. Electrochemical assessment of calcium carbonate deposition using a rotating disc electrode (RDE). *Journal of Applied Electrochemistry.* 1999, **29**(4), pp.455-462.

291. Morizot, A., Neville, A. and Hodgkiess, T. Studies of the deposition of $CaCO_3$ on a stainless steel surface by a novel electrochemical technique. *Journal of Crystal Growth.* 1999, **199**, pp.738-743.

292. Mohamed, H., El-Lateef, H., Maharram Abbasov, V., Imran Aliyeva, L. and Allahverdi Ismayilov, T. *Corrosion Protection of Steel Pipelines Against CO_2 Corrosion-A Review.* 2012.

293. Beavers, J.A. and Thompson, N.G. External corrosion of oil and natural gas pipelines. *American Society of Mechanical Engineers Handbook.* 2006, **13**(C), pp.1-12.

294. Palomar-Pardave, M., Gonzalez, I., Romero-Romo, M. and Oropeza, M. *MES 23: Electrochemistry, Nanotechnology, and Biomaterials.* 1 ed. Pennington, USA: The Electrochemical society, 2008.

295. Yang, Q., Liu, Y., Gu, A., Ding, J. and Shen, Z. Investigation of induction period and morphology of CaCO 3 fouling on heated surface. *Chemical Engineering Science.* 2002, **57**, pp.921-931.

296. Instruments, M. *Basic of principles of particle-size analysis*. 2003, 44, pp.1-8. Available from: http://cat.inist.fr/?aModele=afficheN&cpsidt=14620810

297. Malkin, A.J. and McPherson, A. Light scattering investigation of the nucleation processes and kinetics of crystallization in macromolecular systems. *Acta Crystallographica D.* 1994, **50**, pp.385-395.

298. Instruments, M. *Sysmex FPIA-2100 Bringing shape to the world of particle characterisation.* 2001.

299. J. Goldstein, D.N., D. Joy, C, Lyman, P. Echlin, E. Lifshin, L. Sawyer, and J. Michael. *Scanning Electron Microscopy and X-Ray Microanalysis.* New York, 2003.

300. Gopi, D., Ramya, S., Rajeswari, D. and Kavitha, L. Corrosion protection performance of porous strontium hydroxyapatite coating on polypyrrole coated 316L stainless steel. *Colloids and surfaces. B, Biointerfaces.* 2013, **107**, pp.130-136.

301. Electronics, R.C.o.M. *Rhos Testing Lab* [Online]. 2013. [Accessed]. Available from: http://www.rohs-cmet.in/content/icp-oes

302. Singh, D.N. and Kumar, A. A Fresh Look at ASTM G 1-90 Solution Recommended for Cleaning of Corrosion Products Formed on Iron and Steels. *Corrosion.* 2003, **59**(11), pp.1029-1036.

303. Reddy, M.M., Plummer, L.N. and Eneous, H.E.R. Crystal growth of calcite from calcium bicarbonate solutions at constant PCO_2 and 25°C: a test of a calcite dissolution model. *Geochimica et Cosmochimica Acta.* 1980, **45**(1281-1289).

304. Ma, Y.F., Gao, Y.H. and Feng, Q.L. Effects of pH and temperature on $CaCO_3$ crystallization in aqueous solution with water soluble matrix of pearls. *Journal of Crystal Growth.* 2010, **312**(21), pp.3165-3170.

305. Njegić-Dzakula, B., Falini, G., Brecević, L., Skoko, Z. and Kralj, D. Effects of initial supersaturation on spontaneous precipitation of calcium carbonate in the presence of charged poly-L-amino acids. *Journal of Colloid and Interface Science.* 2010, **343**(2), pp.553-563.

306. Zarga, Y., Ben Boubaker, H., Ghaffour, N. and Elfil, H. Study of calcium carbonate and sulfate co-precipitation. *Chemical Engineering Science.* 2013, **96**, pp.33-41.

307. Pytkowicz, R.M., Disteche, A. and Disteche, S. Calcium carbonate solubility in seawater at in situ pressures. *Earth and Planetary Science Letters.* 1967, **2**, pp.430-432.

308. Gal, J.Y., Bollinger, J.C., Tolosa, H. and Gache, N. Calcium carbonate solubility: a reappraisal of scale formation and inhibition. *Talanta.* 1996, **43**, pp.1497-1509.

309. Carter, E.R. Kinetic Model for Solid- State Reactions. *The Journal of Chemical Physics.* 1961, **35**(1137), pp.75-116.

310. Frade, J.R. and Cable, M. Reexamination of the Basic Theoretical Model for the Kinetics of Solid-State Reactions. *Journal of the American Ceramic Society.* 1992, **75**(7), pp.1949-1957.

311. Kazmlerczak, F., Tomron, M.B. and Nancollas, H. Crystal Growth of Calcium Carbonate. A controlled Composition Kinetic Study. *Journal Physical Chemistry.* 1982, **86**(1), pp.103-107.

312. Tai, C.Y. and Chen, P.C. Nucleation, agglomeration and crystal morphology of calcium carbonate. *AIChE Journal.* 1995, **41**(1).

313. Sohnel, O. and Mullin, J.W. PRECIPITATION OF CALCIUM CARBONATE. *Journal of Crystal Growth.* 1982, **60**, pp.239-250.

314. Söhnel, O., Mullin, J.W., Engineering, B. and Place, T. A method for the determination of precipitation induction periods. *Journal of Crystal Growth.* 1978, **44**(4), pp.377-382.

315. Kashchiev, D., Verdoes, D. and van Rosmalen, G.M. Induction time and metastability limit in new phase formation. *Journal of Crystal Growth.* 1991, **110**(3), pp.373-380.

316. Söhnel, O. and Garside, J. Solute clustering and nucleation. *Journal of Crystal Growth.* 1988, **89**(2), pp.202-208.

317. Markgraf S A, R.R.J. High-temperature structure refinements of calcite and magnesite. *American Mineralogist.* 1985, **70**, pp.590-600.

318. Davey, R.J., Allen, K., Blagden, N., Cross, W.I., Lieberman, H.F., Quayle, M.J., Righini, S., Seton, L. and Tiddy, G.J.T. Crystal engineering? Nucleation, the key step. *CrystEngComm.* 2002, **4**(47), pp.257-257.

319. Bragg, W.L. Crystal Structure of Aragonite. *Acta Crystallographica Section A Structural Science.* 1925, **61**, pp.425-425.

320. Brečević, L. and Kralj, D. On calcium carbonates: from fundamental research to application. *Croatica Chemica Acta.* 2007, **80**, pp.467-484.

321. Andreassen, J.-P., Flaten, E.M., Beck, R. and Lewis, A.E. Investigations of spherulitic growth in industrial crystallization. *Chemical Engineering Research and Design.* 2010, **88**(9), pp.1163-1168.

322. Andreassen, J.-P. and Hounslow, M.J. Growth and aggregation of vaterite in seeded-batch experiments. *AIChE Journal.* 2004, **50**(11), pp.2772-2782.

323. Flaten, E.M., Seiersten, M. and Andreassen, J.-P. Induction time studies of calcium carbonate in ethylene glycol and water. *Chemical Engineering Research and Design.* 2010, **88**(12), pp.1659-1668.

324. Koutsoukos, P.G. and Kontoyannis, C.G. Precipitation of calcium carbonate in aqueous solutions. *Journal of the Chemical Society, Faraday Transactions 1.* 1984, **80**(5), pp.1181-1181.

325. Manoli, F. and Dalas, E. Spontaneous precipitation of calcium carbonate in the presence of chondroitin sulfate. *Journal of Crystal Growth.* 2000, **217**(4), pp.416-421.

326. Pitzer, K.S. Thermodytriarnics of Electrolytes. I. Theoretical Basis and General Equations. *The Journal of Physical Chemistry.* 1973, **77**(2), pp.268-277.

327. Beck, R., Nergaard, M. and Andreassen, J.P. Crystal growth of calcite at conditions of gas processing in solvent mixtures of monoethylene glycol and water. *Transactions of Tianjin University.* 2013, pp.79-85.

328. Davies, C.W. and Shedlovsky, T. Ion Association. *Journal of The Electrochemical Society.* 1962, **111**(3), pp.85C-85C.

329. De Yoreo, J.J., Zepeda-Ruiz, L.a., Friddle, R.W., Qiu, S.R., Wasylenki, L.E., Chernov, a.a., Gilmer, G.H. and Dove, P.M. Rethinking Classical Crystal Growth Models through Molecular Scale Insights: Consequences of Kink-Limited Kinetics. *Crystal Growth & Design.* 2009, **9**(12), pp.5135-5144.

330. Amjad, Z. *The science and technology of industrial water treatment.* 2010.

331. Cheong, W.C., Gaskell, P.H. and Neville, A. Substrate effect on surface adhesion/crystallisation of calcium carbonate. *Journal of Crystal Growth.* 2013, **363**, pp.7-21.

332. Neville, A., Hodgkiess, T. and Morizot, A.P. Surface scales in sea water systems: effects of their formation on corrosion behaviour of engineering steels. *British Corrosion Journal.* 1997, **32**(4), pp.277-282.

333. Joshi, G. *Elucidating Sweet Corrosion Scales.* PhD. thesis, University of Manchester, 2015.

334. Scully, J.R. Polarization Resistance Method for Determination of Instantaneous Corrosion Rates. *Corrosion.* 2000, **56**(2), pp.199-218.

335. Gao, K., Yu, F., Pang, X., Zhang, G., Qiao, L., Chu, W. and Lu, M. Mechanical properties of CO_2 corrosion product scales and their relationship to corrosion rates. *Corrosion Science.* 2008, **50**(10), pp.2796-2803.

336. Xu, L., Lu, M., Zhang, L. and Chang, W. EFFECT OF TEMPERATURE ON WET CO_2 CORROSION OF 3%Cr PIPELINE STEEL. *Corrosion.* 2012, (C2012-0001348).

337. Wang, J. Effect of temperature to crevice corrosion of austentic and duplex stainless steel in deepwater. *NACE International.* 2012, (C2012-0001361), pp.1-11.

338. Fang, H. *Low Temperature and High Salt Concentration Effects on General CO_2 Corrosion for Carbon Steel.* thesis, University of Ohio, 2006.

339. Zeng, Z., Lillard, R.S. and Cong, H. Effect of Salt Concentration on the Corrosion Behavior of Carbon Steel in CO2 Environment. *Corrosion.* 2016, **72**(6), pp.805-823.

340. Takabe, H., Amaya, H., Otome, Y., Ueda, M., Kondo, K., Ohe, T. and Nakatsuka, S. The effect of alloying elements on environmental cracking resistance of stainless steels in CO_2 environments with and without small amount of H_2S. *NACE International.* 2012, (C2012-0001277), pp.1-15.

341. Nancollas, G.H. and Reddy, M.M. The kinetics of crystallization of scale-forming minerals. *SPE.* 1974, pp.117-126.

342. Burns, R.M. The Corrosion of Metals—I. Mechanism of Corrosion Processes. *Bell System Technical Journal.* 1936, **15**(1), pp.20-38.

343. Chen, T., Neville, A., Sorbie, K. and Zhong, Z. Using in situ synchrotron radiation wide angle X-ray scattering (WAXS) to study $CaCO_3$ scale formation at ambient and elevated temperature. *Faraday Discussions.* 2007, **136**, pp.355-355.

344. Tolaieb, B., Bingham, R. and Neville, A. Barium Sulfate Kinetics on Steel Surfaces at Different Supersaturation Ratios. *CORROSION 2013.* 2013, (2751).

345. Alsaiari, H., Kan, A. and Tomson, M. Molar Ratio of Ca^{2+} to Fe^{2+} in the Supersaturated Solution of Iron Carbonate and Calcium Carbonate and in the Precipitate: Relation and Interpretation. *SPE International Symposium on Oilfield Corrosion.* 2009, **11**, pp.1-18.

346. Faraoun, H.I., Zhang, Y.D., Esling, C. and Aourag, H. Crystalline, electronic, and magnetic structures of θ-Fe_3C, χ-Fe_5C_2, and η-Fe_2C from first principle calculation. *Journal of Applied Physics.* 2006, **99**(9), p.093508.

347. Wood, I.G., Vocadlo, L., Knight, K.P., Dobson, D.P., Marshall, M.G., Price, G.B.D. and Brodholt, J. Thermal expansion and crystal structure of cementite, Fe_3C, between 4 and 600 K determined by time-of-flight neutron powder diffraction. *Journal of Applied Crystallography.* 2004, **37**, pp.82-90.

348. Labille, S.C., Morizot, A.P., Neville, A. and Graham, G.M. *An Electrochemical Approach For The Protection Of Metal Surfaces From Formation Of Calcium Carbonate Using Bulk " Jar Tests Tests ".* 2001, pp.2001-2001.

349. Hasson, D. *Fouling of heat transfer equipment.* McGraw-Hill, 1981.

350. Andritsos, N., Karabelas, A.J. and Koutsoukos, P.G. Morphology and structure of $CaCO_3$ scale layers formed under isothermal flow conditions. *Langmuir.* 1997, **7463**(6), pp.2873-2879.